UNIVERSITÉ DU LUXEMBOURG

PhD-FSTM-2025-073
The Faculty of Science, Technology and Medicine

DISSERTATION

Defence held on 14 July 2025 in Esch-sur-Alzette

to obtain the degree of

DOCTEUR DE L'UNIVERSITÉ DU LUXEMBOURG EN PHYSIQUE

by

Sevan GHARABEIKI

Born on 26 March 1995 in Tehran (Iran (Islamic Republic of))

LUMINESCENCE INVESTIGATION OF VOLTAGE LOSSES IN CHALCOPYRITE SOLAR CELLS

Dissertation defense committee

Prof. Dr. Susanne SIEBENTRITT, dissertation supervisor
Professor, UNIVERSITÉ DU LUXEMBOURG

Prof. Dr. Alex REDINGER, Chairman
Professor, UNIVERSITÉ DU LUXEMBOURG

Prof. Dr. Jürgen CHRISTEN
Professor, UNIVERSITÄT MAGDEBURG

Prof. Dr. Thomas KIRCHARTZ
Professor, FORSCHUNGSZENTRUM JÜLICH

Prof. Dr. Selina OLTHOF
Professor, UNIVERSITÄT WUPPERTAL

Table of Contents

List of frequently used symbols

p_0	Net hole concentration (cm^{-3})
n_0	Net electron concentration (cm^{-3})
n_i	Intrinsic carrier density (cm^{-3})
N_c	Effective density of states for electrons in conduction band (cm^{-3})
N_v	Effective density of states for holes in valance band (cm^{-3})
N_D	Donor concentration (cm^{-3})
N_A	Acceptor concentration (cm^{-3})
E_F	Fermi level energy (eV)
E_C	Conduction band edge (eV)
E_V	Valance band edge (eV)
E_i	Intrinsic Fermi level (eV)
δn	Excess generated electrons concentration (cm^{-3})
δp	Excess generated holes concentration (cm^{-3})
n	Total electron concentration under excitation (cm^{-3})
p	Total hole concentration under excitation (cm^{-3})
E	Photon energy (eV)
E_g	Band gap energy (eV)
V_{OC}	Open circuit voltage (V)
J_{SC}	Short circuit current density (mA/cm^2)
FF	Fill factor
$\Delta\mu$	Quasi Fermi level splitting (eV)
$\Phi_{PL}(E)$	PL emission spectrum ($1.cm^{-2}s^{-1}eV^{-1}$)
$\Phi_{EL}(E)$	EL emission spectrum ($1.cm^{-2}s^{-1}eV^{-1}$)
V_{in}	Interval voltage (V)
V_{bi}	Bias voltage (V)

$QE(E)$	External quantum efficiency spectrum
$A(E)$	Absorptance spectrum
$R(E)$	Reflectance spectrum
$T(E)$	Transmittance spectrum
$\Phi_{Sun}(E)$	Sun spectrum AM 1.5 g (1.cm^{-2}s^{-1}eV^{-1})
$\Phi_{BB}(E)$	Black body emission spectrum (1.cm^{-2}s^{-1}eV^{1})
n_{id}	Diode ideality factor
R_{SH}	Shunt resistance
R_S	Series resistance
J_{MPP}	Maximum power point (MPP) current (mA/cm^2)
V_{MPP}	Maximum power point (MPP) voltage (V)
$\eta(x)$	Charge collection efficiency function
τ_{eff}	Effective lifetime (ns)
E_g^{loc}	Local band gap (eV)
$\overline{E_g}$	Average band gap (eV)
E_U	Urbach energy (eV)
$A^{PL}(E)$	Absorptance spectrum from PL measurements
$A^{dir}(E)$	Absorptance spectrum from direct measurements
$QE^{EL}(E)$	External Quantum efficiency spectrum from EL measurements
$QE^{dir}(E)$	External Quantum efficiency spectrum from direct measurements
σ_A	Absorptance edge broadening parameter (eV)
σ_g	Band gap fluctuation (inhomogeneities) parameter (eV)
σ_{QE}	External quantum efficiency broadening parameter (eV)
F_0^{SQ}	Shockley-Queisser radiative saturation flux density (cm^{-2}s^{-1})
F_0^{rad}	Radiative saturation flux density (cm^{-2}s^{-1})
F_{Gen}^{Sun}	Sun generation flux density (cm^{-2}s^{-1})

F_{Gen}^{SQ}	Shockley-Queisser Sun generation flux density ($cm^{-2}s^{-1}$)
$\alpha(E)$	Absorption co-efficient (cm^{-1})
$\alpha^{loc}(E, E_g)$	Local absorption coefficient (cm^{-1})
T	Temperature (K)
J_0^{rad}	Radiative saturation current density ($A.cm^{-2}$)
J_0^{SQ}	Shockley-Queisser radiative saturation current density ($A.cm^{-2}$)
J_{SC}^{SQ}	Shockley-Queisser Short circuit current density ($A.cm^{-2}$)
Y_{PL}	Photoluminescence quantum yield
Y_{EL}	Electroluminescence quantum yield
V_{OC}^{SQ}	Shockley-Queisser V_{OC} limit (V)
$qV_{OC}^{SQ} = \Delta\mu^{SQ}$	Shockley-Queisser quasi Fermi level splitting limit (eV)
$\Delta\mu^{rad}$	Radiative $\Delta\mu$ limit (eV)
$\delta\Delta\mu^{rad}$	Radiative $\Delta\mu$ loss (eV)
$\delta\Delta\mu^{Gen}$	Generation $\Delta\mu$ loss (eV)
$\delta\Delta\mu^{nr}$	Non-radiative $\Delta\mu$ loss (eV)
V_{OC}^{rad}	Radiative V_{OC} limit (V)
δV_{OC}^{rad}	Radiative V_{OC} loss (V)
δV_{OC}^{SC}	Short circuit V_{OC} loss (V)
δV_{OC}^{nr}	Non-radiative V_{OC} loss (V)
F_{Gen}^{Laser}	Laser generation flux density ($cm^{-2}s^{-1}$)
F_{inc}^{Laser}	Laser incident flux density ($cm^{-2}s^{-1}$)
$A(E_{laser})$	Absorptance at laser photon energy
γ_{el}	Average depth of electrostatic potential fluctuations (eV)

List of constants

k_B	Boltzmann constant	1.38×10^{-23} J·K $^{-1}$
h	Planck's constant	6.626×10^{-34} J.s
q	Elementary charge	1.602×10^{-19} C
c	Light velocity in vacuum	2.998×10^{8} m/s
e	Euler's number i.e. exp(1)	2.71828
ε_0	Vacuum permittivity	8.853×10^{-12} F/m

List of abbreviations

CIGSe	$Cu(In,Ga)Se_2$
EL	Electroluminescence
PL	Photoluminescence
EDX	Energy-Dispersive X-ray analysis
CL	Cathodoluminescence
SQ	Shockley-Queisser
DOS	Density of states
VB	Valance band
CB	Conduction band
SRH	Shockley-Read-Hall
SCR	Space-charge region
QNR	Quasi-neutral region
MPP	Maximum power point
PCE	Power conversion efficiency of a solar cell
SLG	Soda lime glass
AFM	Atomic force microscopy
KPFM	Kelvin probe force microscopy
FM-KPFM	Frequency- modulation Kelvin probe force microscopy
AM-KPFM	Amplitude-modulation Kelvin probe force microscopy
GB	Grain boundaries
HSG	Hockey stick gradient
BGG	Band gap graded
NG	Non graded
PDT	Post deposition treatment
TRPL	Time resolved photoluminescence

SEM	Scanning electron microscopy
SOA	State-of-the-art
CGI	$\frac{Cu}{Ga+In}$
GGI	$\frac{Ga}{Ga+In}$

Abstract

Chalcopyrite-based solar cells have achieved remarkable power conversion efficiencies of up to 23.6% for absorbers with a band gap near 1.1 eV. However, this efficiency is still around 10 percentage points below the Shockley-Queisser (SQ) theoretical limit. One of the main reasons for this efficiency gap is deficit in the open circuit voltage V_{OC} relative to the SQ-V_{OC} limit.

The SQ predictions are entirely based on an idealized solar cell model that makes several important assumptions. One assumption is that the absorptance $A(E)$ and external quantum efficiency $QE(E)$ is unity for energies higher than band gap and zero in the sub-band gap energy range, meaning that $A(E)/QE(E)$ is a step function. This implies that only photons with energies higher than the band gap are completely absorbed, contributing to the generation of electron-hole pairs, and all photogenerated electron-hole pairs are fully extracted through the contacts. Another key assumption is that charge recombination occurs exclusively through band-to-band radiative recombination mechanism, with non-radiative recombination pathways entirely absent in the device.

However, in practice, the behavior of actual devices deviates significantly from this idealized SQ assumptions. First, instead of exhibiting a sharp step-like transition at the band gap energy, the $A(E)$ and $QE(E)$ spectra of real devices show a gradual increase near the absorption edge, leading to spectral broadening. This broadening causes radiative V_{OC} losses. Second, real solar cells often suffer from incomplete light absorption and charge collection inefficiencies, which further contribute to V_{OC} losses. Finally, unlike the SQ model, along with the radiative band-to-band transition, undesirable non-radiative recombination also occurs within the actual devices, both in the bulk and at interfaces, resulting in detrimental non-radiative V_{OC} losses.

In this thesis, simulations were conducted to evaluate the effects of band gap inhomogeneities, Urbach tails and absorber thickness on the absorption edge broadening and radiative losses. Notably, it was found that band gap distribution along with the reduced absorber thickness have significant contribution to the broadening and radiative losses, while Urbach tails only show a minor effect within the typical range of Urbach energy values observed for CIGSe absorbers.

Moreover, comprehensive experimental analyses are performed to quantitatively evaluate the V_{OC} losses caused by all non-idealities in Cu(In,Ga)Se_2 CIGSe solar cell. Two distinct approaches are employed for this purpose. The first method relies on purely optical analysis, where $A(E)$ and photoluminescence (PL) spectra are used to evaluate quasi Fermi level splitting ($\Delta\mu$) (analogious to V_{OC}) losses of CIGSe absorbers relative to SQ limit. The second method relies on optoelectronic analysis, where V_{OC} losses are extracted through a combination of electroluminescence (EL) and direct $QE(E)$ measurements.

The primary focus of this work is to study the influence of the band gap gradient on the radiative losses in CIGSe solar cells. Experimental findings indicate that absorbers with a graded band gap exhibit stronger broadening at the absorption onset and suffer from 5 -16 meV additional radiative losses compared to the ungraded absorbers. These findings are further supported by a meta-analysis and a review of published data, which consistently show that the presence of a band gap gradient contributes significantly to absorption edge broadening.

This thesis also investigates the impact of alkali ions incorporation on the sub-bandgap Urbach tails and grain boundaries in CIGSe absorbers. PL measurements are used to evaluate the extent of Urbach tails, while Kelvin probe force microscopy (KPFM) is employed to extract the band bending across the grain boundaries. The main objective of these measurements is to determine whether there is any relationship between the reduction in Urbach tails and changes in band bending at grain boundaries. Consistent with previously published results, the PL results show that alkali incorporation reduces the extent of tail states. However, KPFM measurements indicate that decrease in the tail states is not correlated with the changes in the grain boundary band bending. Instead, excitation-dependent PL measurements suggest that the reduction in the Urbach tails is primarily due to the flattening of the electrostatic potential fluctuations within the material.

1 Introduction

Global electricity consumption is dramatically increasing each year. In 2024 the total electricity demand was around 29,000 TWh [1]. Predictions are expecting an increase of approximately 3,500 TWh in electricity consumption from 2024 to 2027 [1]. This amount of increase corresponds to annual growth rate of around 4% over this period [1].

This substantial growth in electricity consumption is primarily caused by several key factors, including expanding industrial activities, advancements in the electrification technology, growing energy requirements for data centers, and the rising demand for air conditioning and cooling systems [1]. It is predicted that photovoltaic technology would cover about 50% of this expected increase in electricity consumption [1]. Therefore, a collective global effort is underway to develop more efficient solar cells. Numerous companies, research institutions and universities continue to announce record-breaking device efficiencies each year. This ongoing research and competition among academic and industrial leaders reflects the importance of the photovoltaic technology for future of the electricity generation.

According to the most recent reports, wafer based silicon (Si) technology has dominant share in the photovoltaic market, accounting for approximately 98% of global supply [2]. The remaining 2% share is covered by thin-film photovoltaic technologies [2]. The Cu(In,Ga)Se2 CIGSe solar cells belong to the thin-film category.

CIGSe is a p-type, direct band gap semiconductor. This semiconductor shows favorable optoelectronic characteristics for solar cell applications. Notably, it has a high absorption coefficient ($>10^4$ cm^{-1}) [3], allowing for efficient light absorption in a thin-film with few micrometer thickness. The band gap of CIGSe absorbers can be tuned by adjusting the Ga concentration within the material. The band gap of this material increases from approximately 1.0 eV in pure $CuInSe_2$ (CISe) to about 1.7 eV in pure $CuGaSe_2$ (CGSe) material [4, 5]. This band gap tunability is a key advantage and has recently gained significant attention for applications in tandem devices [5-8]. Moreover, CIGSe solar cells have been proven to be stable against environmental influences [9].

Over the past five decades, the power conversion efficiency of the CIGSe devices has increased significantly from 5.7% to 23.6% [10, 11]. In CIGSe solar cells, two key strategies have played

a crucial role in improving efficiencies: (i) the introduction of a graded band gap profile and (ii) the incorporation of alkali elements into the absorber layer.

The band gap gradient uses the tunable band gap properties of CIGSe absorbers by intentionally increasing the band gap near the back and front surfaces [12, 13]. Such a gradient architecture drives minority carriers (here electrons) away from the interfaces, thereby decreasing interface non-radiative recombination losses, improving the open circuit voltage V_{OC} and overall efficiency of devices [13].

Alkali ions also have a significant role in enhancing the efficiency of CIGSe devices. Since the 1990s, sodium (Na) addition has been used in CIGSe solar cells to improve the device performance [14-16]. Later, heavier alkali ions such as potassium (K) [17], rubidium (Rb) [11, 18, 19], and cesium (Cs) [20] have also been introduced into the CIGSe absorbers, resulting the power conversion efficiencies to surpass 20% [11, 17, 19]. The primary effects of these alkalis are increase in net p-type doping concentration [21-23] and a reduction in detrimental non-radiative recombination losses (i.e., lifetime improvement) [24, 25], which directly leads to enhancements in V_{OC} and overall device efficiency.

Despite significant achievements in CIGSe technology, the efficiency of the CIGSe solar cells remains considerably lower than the theoretical maximum predicted Shockley–Queisser (SQ) efficiency limit [26]. For a material with a band gap of around 1.1 eV, the SQ model predicts an efficiency of approximately 33% for a single-junction solar cell under one sun illumination [26, 27]. Currently, the efficiency of CIGSe devices with a similar band gap is about 10 percentage points lower than this theoretical prediction [11].

One primary reason for this loss in the efficiency of CIGSe solar cells is a deficit in the V_{OC} with respect to the SQ limit. Therefore, improving the V_{OC} is an essential step for pushing the performance of these devices closer to their theoretical efficiency limit.

Further improving the CIGSe device performance requires advanced characterization techniques to identify performance limitations and underlying losses in efficiency. In this thesis, luminescence-based characterization techniques are employed to investigate the V_{OC} limitations in $Cu(In,Ga)Se_2$ (CIGSe) devices.

Moreover, this work also studies the influence of alkali elements on the sub-band gap tail states and grain boundaries in CIGSe absorbers.

This thesis contains 6 main chapters, in the following, a brief overview of each chapter is provided.

Chapter 2 of this thesis presents literature review and discusses the fundamental principles and equations related to semiconductors and solar cells. Additionally, it also introduces the CIGSe absorber, discussing its crystal structure, tail states, defect properties, and the beneficial effects of alkali incorporation.

Chapter 3 provides a detailed overview of the sample deposition and characterization technics. All CIGSe absorbers in this thesis were prepared using multistage co-evaporation deposition method. The details of deposition process are discussed extensively in this chapter. Moreover, key characterization techniques, including electroluminescence (EL) and photoluminescence (PL) measurements, are also introduced. In particular, the calibration procedures and experimental setups for both EL and PL analyses are presented in this chapter. Furthermore, other experimental methods, such as current–voltage (J–V) measurements, quantum efficiency (QE) analysis, and UV-Vis photospectrometry measurements, are also covered in **Chapter 3**.

Chapter 4 of this thesis provides a theoretical framework which allows us to understand the limitations in the V_{OC} of photovoltaic devices.

The ideal SQ model assumes that a solar cell has step-function-like $A(E)$ and $QE(E)$ spectra [26]. This assumption means that only photons with energies higher than the material's band gap are absorbed, while those with lower energies are not absorbed in the material. Moreover, this model neglects charge collection losses and considers that all photogenerated carries are completely extracted out of the device [26]. Additionally, SQ model also assumes that the charge recombination mechanism is entirely through radiative recombination and it does not consider the contribution of unfavorable non-radiative recombination effect [26].

However, real world devices exhibit completely different behavior. Real solar cells suffer from radiative V_{OC} losses due to absorption edge broadening [28], generation and short circuit [28] V_{OC} losses due to incomplete light absorption and charge collection losses, and most

importantly, most photovoltaic technologies show significant V_{OC} losses due to non-radiative recombination effect [28, 29] .

In this chapter, using theoretical calculations, effect of all these non-ideal behaviors on the V_{OC} will discussed.

These theoretical calculations are based on two different approaches: (i) based on optoelectrical analysis, which employs EL and $QE(E)$ spectra to evaluate losses in the V_{OC}. (ii) The purely optical measurements, which use PL and $A(E)$ spectra to assess losses in the quasi-Fermi level splitting ($\Delta\mu$). While the optoelectrical method is well-studied and widely employed in the literature [28, 30-32], the optical method has not received much attention to date.

It is important to note that these two approaches are conceptually similar, and the ($\Delta\mu$) and its associated losses are analogous to the V_{OC} and its losses. However, for optoelectrical model completed devices are required to perform analysis, whereas optical measurements can be carried out on absorber materials alone, without need to have a full device structure.

It is important to mention that these methods are not exclusive to CIGSe technology and can be effectively applied to other photovoltaic technologies as well. CIGSe devices represent a model system in this work for performing a comprehensive analysis of V_{OC} losses.

In **Chapter 4**, simulations are also performed to investigate the influence of band gap inhomogeneities, sub-band gap tail states (i.e., Urbach tails), and absorber thickness on the shape of the absorptance spectrum $A(E)$. Furthermore, contribution of each effect to the radiative losses will be quantified using theoretical equations.

In **Chapter 5**, with the use of theoretical framework of **Chapter 4**, the $\Delta\mu$ and V_{OC} values along with their associated losses are experimentally quantified for CIGSe samples. Specifically, $\Delta\mu$ losses are extracted using experimentally measured $A(E)$ and absolute PL spectra. It will be shown that individual loss components can be summed up to determine the final $\Delta\mu$ value. Similarly, V_{OC} losses in complete solar cells are analyzed through a combination of quantum efficiency (QE) measurements and absolute EL measurements.

This chapter primarily studies the impact of the band gap gradient on the radiative losses. Notably, experimental results of this chapter reveal that samples with a band gap gradient

exhibit more pronounced absorption edge broadening and increased radiative losses compared to samples without band gap gradient. A meta-analysis of published data further supports this observation, indicating that band gap gradients can lead to additional radiative losses in CIGSe absorbers.

Furthermore, **Chapter 6** investigates the influence of alkali ions on the V_{OC} and sub-band gap Urbach tails of CIGSe samples.

Previous studies have shown that alkali ions can reduce the extent of Urbach tails, i.e., decrease the Urbach energy [33, 34]. This chapter first confirms these findings by demonstrating that alkali incorporation leads to a measurable reduction in Urbach energies. Subsequently, the origins of this decrease are investigated.

In this chapter, the potential contribution of electrostatic potential fluctuations and grain boundaries to the formation of tail states are investigated.

Band bending at grain boundaries is measured for absorbers containing different alkali elements to examine whether alkali incorporation changes the band bending. The aim of this chapter is to investigate whether changes in the GB band bending are correlated with the reduction in Urbach tails.

Additionally, the strength of electrostatic potential fluctuations within the material is evaluated by intensity dependent PL measurements.

All grain boundary analyses were performed using Kelvin Probe Force Microscopy (KPFM). These measurements were conducted by my colleague, **Muhammad Uzair Farooq**, under the supervision of **Prof. Alex Redinger**.

The measurements of **Chapter 6** shows that grain boundaries do not have contribution to the tail states, and decrease in the tail states with alkali addition is due to flattening of electrostatic potential fluctuations.

Finally, **Chapter 7** provides an overview of the key findings and summarizes main results throughout this thesis.

2 Background and literature review

This chapter provides an introduction to the fundamental concepts of semiconductors and solar cells, along with an overview of the properties of $Cu(In,Ga)Se_2$ (CIGSe) absorber materials. This chapter is divided into five main sections:

In **Section 2.1** the basic principles of semiconductors, including light absorption, electron-hole pair generation, and charge carrier recombination processes are discussed. Subsequently, In **Section 2.2**, the working principle of solar cells are covered. This section includes discussions about the current-voltage characteristics, introduction of key parameters for characterizing solar cells, and a brief overview of the Shockley-Queisser model [26], which predicts the maximum efficiency of a single-junction solar cells. All the fundamental concepts in these sections are well-documented in standard semiconductor textbooks, and in this thesis, they are explained with reference to sources [3, 35-39].

Section 2.3 introduces tail states in semiconductors, a topic that is discussed extensively in **Chapter 6** of this thesis, focusing particularly on CIGSe absorbers.

Section 2.4 presents the equations and formulas related to photoluminescence (PL) and electroluminescence (EL) measurements. Both EL and PL measurements are the primary characterization tools used in this thesis. These measurements are essential methods for the detailed quantification of V_{OC} losses in photovoltaic devices.

Finally, **Section 2.5** discusses the properties of CIGSe absorbers and devices. This section covers the crystal structure, defects, device structure, and the beneficial impact of alkali elements on the absorbers.

It is important to note that frequently appeared constants, symbols, and abbreviations are summarized at the beginning of this thesis.

2.1 Basic semiconductor knowledge

2.1.1 Fundamentals of semiconductors

In a semiconductor material with a defined band gap (E_g), the hole (p_0) and electron concentration (n_0) are given by the following equations:

$$n_0 = N_c \exp\left(-\frac{E_c - E_F}{k_B T}\right) \qquad (\boldsymbol{Eq\ 2.1})$$

$$p_0 = N_v \exp\left(-\frac{E_F - E_v}{k_B T}\right) \qquad (\boldsymbol{Eq\ 2.2})$$

Here, k_B is Boltzmann constant, T denotes the temperature, E_F the Femi level energy, E_c represents the conduction band edge, E_v the valence band edge, and N_c and N_v represent the effective density of states (DOS) for electrons in the conduction band (CB) and holes in the valence band (VB), respectively.

The N_c and N_v can be expressed as:

$$N_c = 2\left(\frac{2\pi m_n k_B T}{h^2}\right)^{\frac{3}{2}} \ and \quad N_v = 2\left(\frac{2\pi m_p k_B T}{h^2}\right)^{\frac{3}{2}} \qquad (\boldsymbol{Eq\ 2.3})$$

Where h is Planck's constant, and m_n and m_p are effective masses of electron and holes, respectively.

Depending on the semiconductor type — p type, n type or intrinsic semiconductor — the Fermi level energy position can be located close to the valence band, near to the conduction band or in the middle of the band gap energy. **Fig 2. 1** schematically illustrate the Fermi level position in the p-type, n-type and intrinsic semiconductors.

It is often helpful to define the intrinsic carrier concentration n_i according to the following formula:

$$n_0 p_0 = N_C N_V \exp\left(-\frac{E_g}{k_B T}\right) = n_i^2 \qquad (\boldsymbol{Eq\ 2.4})$$

Therefore,

$$n_i = \sqrt{N_C N_V} \exp\left(-\frac{E_g}{2k_B T}\right) \qquad (\boldsymbol{Eq\ 2.5})$$

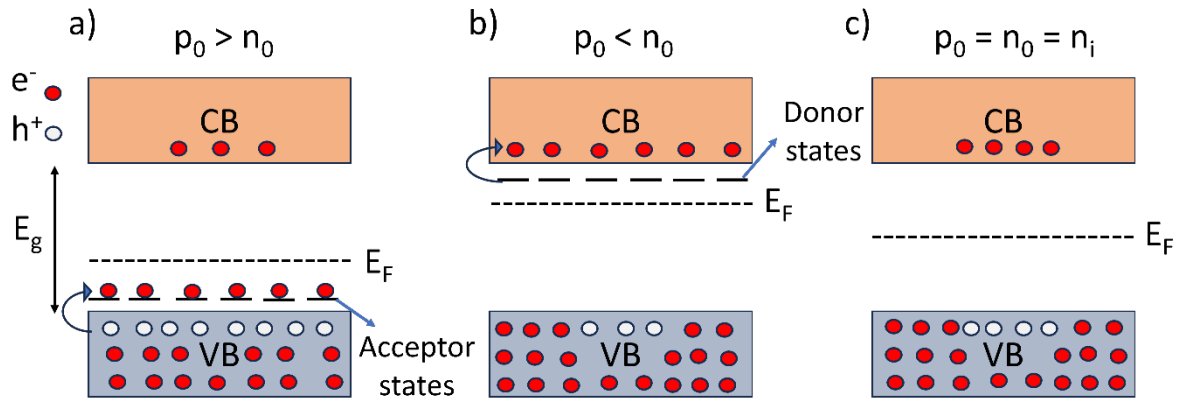

Fig 2. 1 Schematic diagram showing Fermi level position, acceptor and donor states in **a)** p-type **b)** n-type and **c)** intrinsic semiconductors. In the intrinsic semiconductor material the Fermi level position is in the middle of the band gap (E_g).

It is important to highlight that, for optoelectronic applications, semiconductor materials are often doped by introducing acceptor or donor states. This allows to manipulate the Fermi energy level position, either by moving it close to the valence band (VB) by introducing the acceptor states or moving it near to the conduction band (CB) by adding donor states.

By introducing acceptor levels near the valence band (**Fig 2. 1a**), the electrons from VB can jump into the acceptor states and leave behind holes in the VB (i.e, increase the hole concentration in VB). Therefore, the Fermi level gets closer to the VB. On the other hand, by introducing donor states close to the CB, the donors can release electrons into the CB and increase the electron concentration in the CB. In this case the Fermi level gets closer to the CB.

The donors and acceptors concentration in a semiconductor materials are denoted by N_D and N_A, respectively.

For a p-type semiconductor if $N_A \gg n_i$, it can be written:

$$N_A \approx p_0 \; and \; n_0 = \frac{n_i^2}{N_A} \qquad (\boldsymbol{Eq\ 2.6})$$

Similarly, for n-type semiconductor if $N_D >> n_i$:

$$N_D \approx n_0 \; and \; p_0 = \frac{n_i^2}{N_D} \qquad (\boldsymbol{Eq\ 2.7})$$

In a semiconductor material, these acceptor and donor states can be introduced extrinsically through addition of impurity atoms in the material, or can arise intrinsically through formation of defect states. In the case of CIGSe, these states are primarily formed in the material by intrinsic defects. A detailed discussion on acceptor and donor states, defects, and doping concentration in CIGSe will be provided in **Section 2.5.1**.

2.1.2 Photons absorption and electron-hole pair generation

When a semiconductor is exposed to an external excitation source—such as solar radiation, laser light, electron beam, or an applied bias voltage—excess charge carriers are generated within the material. In solar cells, these excess carriers are generated by solar irradiance, which spans from the infrared (IR) to the ultraviolet (UV) energy range. The spectral photon flux density of standard solar radiation (Φ_{Sun}) is given by the AM 1.5 g spectrum [40], and it is shown in **Fig 2. 2**.

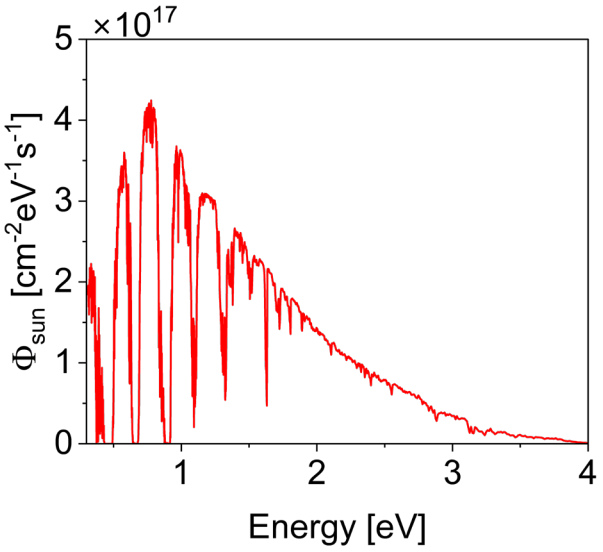

Fig 2. 2 Spectral photon flux density for Sun emission under AM 1.5 g standard emission condition. This spectrum is extracted from NREL website [40].

Light consists of particles called photons, each carrying a certain energy (E_{ph}) determined by photon wave frequency (*f*), i.e, $E_{ph} = hf$. When a semiconductor is exposed to an external light source, such as Sun or a laser radiation, the incident photons can be absorbed in the material. These absorbed photons generate electron-hole pairs by exciting electrons from the VB to the CB. This process results in the excess electrons in the CB and excess holes in the VB.

However, it is important to highlight that not all incident photons across the entire energy range are absorbed in the semiconductor material. Part of the photons might get absorbed within the material and part of them can get reflected from surface and interfaces.

To further discuss the light absorption, let's consider a semiconductor under incident Sun light. The Φ_{Sun} spectrum in **Fig 2. 2** is incident spectral photon flux density, which gives the number of incident photons per unit time, per unit energy, per unit area (i.e, has unit of $cm^{-2}eV^{-1}s^{-1}$).

When photons reach to the surface of a semiconductor, a portion is reflected. The reflected spectral photon flux density $\Phi_R(E)$ can be written as:

$$\Phi_R(E) = \Phi_{Sun}(E) \cdot R(E) \qquad (\boldsymbol{Eq\ 2.8})$$

Here, $R(E)$ is the reflectance spectrum. The $R(E)$ depends on the energy of the incident photons, and it is simply defined as the ratio of the number of reflected photons over the number of incident photons. This $R(E)$ spectrum can be determined experimentally using a photospectrometry measurements (see **Section 3.6**).

Furthermore, the remaining photons penetrate and get absorbed at different depths within the semiconductor. The spectral photon flux density at a depth of *x* inside the material, denoted as $\Phi_\gamma(x, E)$, can be expressed using Beer-Lambert's law:

$$\Phi_\gamma(x, E) = \Phi_{Sun}(E) \cdot \big(1 - R(E)\big) \cdot e^{-\alpha(E)x} \qquad (\boldsymbol{Eq\ 2.9})$$

Here, $\alpha(E)$ is the absorption coefficient.

Using this equation, the transmitted photon flux density $\Phi_T(E)$ from a material of thickness d is given by:

$$\Phi_T(E) = \Phi_{Sun}(E) \cdot \big(1 - R(E)\big) \cdot e^{-\alpha(E)d} \qquad (\boldsymbol{Eq\ 2.10})$$

The remaining photons that are neither reflected nor transmitted are absorbed within the material. Thus, the absorbed photon flux density $\Phi_A(E)$ is given by:

$$\Phi_A(E) = \Phi_{Sun}(E) - \Phi_T(E) - \Phi_R(E) \qquad (\boldsymbol{Eq\ 2.11})$$

By combining Eq 2.10, Eq 2.8 and Eq 2.11, the $\Phi_A(E)$ can be expressed as:

$$\Phi_A(E) = \Phi_{Sun}(E) \cdot \big(1 - R(E)\big) \cdot (1 - e^{-\alpha(E)d}) \qquad (\boldsymbol{Eq\ 2.12})$$

The ratio of the absorbed photons over the incident photons at each energy in a semiconductor material is described by the absorptance spectrum, $A(E)$. Therefore, according to Eq 2.12, the $A(E)$ can be defined as:

$$A(E) = \frac{\#absorbed\ photons}{\#incident\ photons} = \frac{\Phi_A(E)}{\Phi_{Sun}(E)} = \big(1 - R(E)\big) \cdot (1 - e^{-\alpha(E)d}) \qquad (\boldsymbol{Eq\ 2.13})$$

Furthermore, returning to Eq 2.9, the $\Phi_\gamma(x, E)$ indicate that how many photons are available at the depth x within the semiconductor. By differentiating this equation with respect to x, the rate at which photons are lost as they penetrate deep into the material can be determined. This photon loss rate, corresponds to the local absorption rate $R_j(x, E)$, with unit of $cm^{-3}s^{-1}eV^{-1}$, and can be expressed as:

$$R_j(x, E) = -\frac{\partial \Phi_\gamma(x, E)}{\partial x} = \alpha(E) \cdot \Phi_{Sun}(E) \cdot \big(1 - R(E)\big) \cdot e^{-\alpha(E)x} \qquad (\boldsymbol{Eq\ 2.14})$$

Considering that each absorbed photon generates one electron–hole pair, the carrier generation rate must equal to the absorption rate of the photons. In this case, the generation rate of electron-hole pairs $G_{e-h}(x, E)$, at a specific photon energy interval and at the depth *x*, is given by:

$$G_{e-h}(x, E) = R_j(x, E) = \alpha(E) \cdot \Phi_{Sun}(E) \cdot \big(1 - R(E)\big) \cdot e^{-\alpha(E)x} \qquad (\boldsymbol{Eq\ 2.15})$$

Or simply, by defining the generation function $g(x, E)$ as:

$$g(x, E) = \alpha(E) \cdot \big(1 - R(E)\big) \cdot e^{-\alpha(E)x} \qquad (\boldsymbol{Eq\ 2.16})$$

The Eq 2.15 can be simplified into:

$$G_{e-h}(x, E) = \Phi_{Sun}(E)\ \cdot g(x, E) \qquad (\boldsymbol{Eq\ 2.17})$$

Furthermore, it is very useful to calculate the total generation flux density F_{Gen}^{Sun}, which corresponds to the total number of electron hole pairs generated per unit area per unit time (with unit of $cm^{-2}s^{-1}$), this can be obtained by integrating the $G_{e-h}(x,E)$ over the material thickness and entire photon energy interval. Thus using Eq 2.15, the F_{Gen}^{Sun} can be written as:

$$F_{Gen}^{Sun} = \int_0^{\infty}\int_0^{d} G_{e-h}(x,E)\,dxdE = \int_0^{\infty} \Phi_{Sun}(E)\cdot\big(1-R(E)\big)\cdot(1-e^{-\alpha(E)d})dE \quad (\boldsymbol{Eq\ 2.18})$$

Using definition of $A(E)$ from Eq 2.13, the F_{Gen}^{Sun} can be further simplified into the following form:

$$F_{Gen}^{Sun} = \int_0^{\infty} A(E)\Phi_{Sun}(E)dE \quad (\boldsymbol{Eq\ 2.19})$$

In the **Chapter 4** and **Chapter 5**, the importance of this generation flux will be explored more extensively.

In the presence of an external excitation source such as Sun or laser, a single Fermi level is not sufficient to describe the excess electron and hole concentrations. Instead, quasi-Fermi levels are introduced, allowing the excess electron and hole concentration to be expressed as:

$$n = n_0 + \delta n = N_c \exp\left(-\frac{E_c - E_{Fn}}{k_B T}\right) \quad (\boldsymbol{Eq\ 2.20})$$

$$p = p_0 + \delta p = N_v \exp\left(-\frac{E_{Fp} - E_v}{k_B T}\right) \quad (\boldsymbol{Eq\ 2.21})$$

Here, the E_{Fn} and E_{Fp} represent the quasi-Fermi levels of electrons and holes, respectively. The δn and δp are excess electron and hole concentrations, respectively. Since, the electrons and holes are generated in pairs, the $\delta n = \delta p$.

Furthermore, The difference between them is called quasi-Fermi level splitting and in this thesis it is denoted by $\Delta\mu$:

$$\Delta\mu = E_{Fn} - E_{Fp} \quad (\boldsymbol{Eq\ 2.22})$$

In the schematic diagram shown in **Fig 2. 3**, the optical generation process in a semiconductor is illustrated. When excess electron-hole pairs are generated within the material, the quasi-

Fermi level for electrons, E_{Fn} , shifts closer to the conduction band edge (CB), indicating an increase in the electron concentration. Similarly, the quasi-Fermi level for holes, E_{Fp} moves closer to the valence band edge (VB), which means a higher hole concentration. The quasi-Fermi level splitting $\Delta\mu$ strongly depends on the excitation intensity. With the increase in the excitation intensity, more charge carriers are generated, leading to increased electron and hole concentrations in the CB and VB, respectively. As a result, the $\Delta\mu$ becomes larger.

In a p-type semiconductor material like CIGSe, under low excitation conditions ($p_0 \gg \delta p = \delta n$), the hole Fermi level remains approximately at the same position as the equilibrium Fermi level (i.e, $E_{Fp} \cong E_F$), because the low excitation does not significantly change the hole carrier concentration. Therefore, in the low excitation condition, the $\Delta\mu$ is primarily effected by the electron concentration and electron quasi-Fermi level E_{Fn}.

On the other hand, under high excitation condition, when the excess generated hole concentration is comparable to net doping concentration (i.e., $p_0 \approx \delta p = \delta n$), the hole Fermi level also shifts downward (See **Fig 2. 3**).

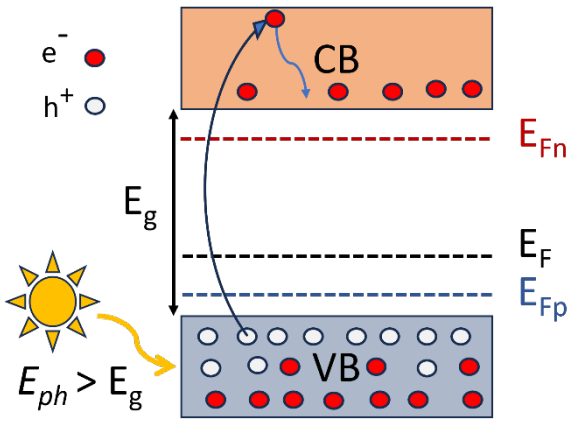

Fig 2. 3 Schematic diagram showing electron-hole generation process in a p-type semiconductor with external excitation light. This figure illustrates optical generation under high excitation where both quasi Fermi levels are shifted.

In this section, the discussion mainly focused on the optical excitation. However, excess charge carriers can also be generated through other excitation sources, such as incident electrons.

Regardless of the excitation method, the concentration of excess electrons and holes can be described by their quasi-Fermi levels.

Later, in **Section 2.2**, it will be shown that the quasi-Fermi level splitting ($\Delta\mu$) is a crucial parameter for evaluating the performance of solar cells.

2.1.3 Charge carrier recombination

The opposite mechanism of the electron-hole pair generation is charge carrier recombination process. This recombination can occur through either radiative or non-radiative pathways. When the excess charge carriers are generated within the material, the excited electrons in the CB and generated holes in the VB would not stay there forever. In an operational photovoltaic devices, these photogenerated pairs are extracted and directed toward external load to perform electrical work. However, in cases where a semiconductor alone is under excitation, or when a solar cell is illuminated under open circuit condition (i.e., no external load connected), the excess free electrons in the CB recombine with holes in the VB. These recombination can be through both radiative and non-radiative mechanisms.

This section discusses both types of radiative and non-radiative recombination processes, along with their relevant equations and formulas.

Radiative recombination:

A semiconductor material has an $A(E)$ spectrum, and behaves like a gray body. Unlike a black body, which absorbs and emits photons across all energy ranges, the gray body absorption and emission are governed by its $A(E)$ spectrum.

Under thermal equilibrium without external excitation sources, a semiconductor absorbs gray-body radiation from its environment (i.e, $A(E)\Phi_{\mathrm{BB}}(E)$). This absorption leads to the generation of electron–hole pairs, which subsequently recombine, resulting in the emission of gray-body radiation from semiconductor. Since the system remains in equilibrium, the radiative generation rate should be counterbalanced by the radiative recombination rates. Therefore, in thermal equilibrium condition, with no external excitation source, for radiative generation rate (G_{rad}^{0}) and radiative recombination rate (R_{rad}^{0}), it can be written [3]:

$$G_{rad}^{0} = R_{rad}^{0} = B_{rad} n_0 p_0 \qquad (\boldsymbol{Eq\ 2.23})$$

Here, B_{rad} is called the radiative recombination coefficient, which has a unit of cm^3s^{-1}, and it can be calculated by knowing the absorption coefficient $\alpha(E)$ of the material [41-43].

However, in steady state condition, when the material is under external excitation source such as Sun or incident laser radiation, the $\Delta\mu$ within the material leads to increase in the carrier concentration in both CB and VB. In this case, the net radiative recombination rate can be expressed as:

$$R_{rad}^{net} = B_{rad}(np - n_0p_0) \qquad (\boldsymbol{Eq\ 2.24})$$

For a p-type material under low excitation condition, as I mentioned previously in **Section 2.1.1,** $p \approx p_0 \approx N_A$. Therefore, the Eq 2.24 can be transformed into [44]:

$$R_{rad}^{net} \approx B_{rad}N_A(n - n_0) = B_{rad}N_A\delta n \qquad (\boldsymbol{Eq\ 2.25})$$

Here, the radiative recombination lifetime τ_{rad} can be defined according to following formula:

$$\tau_{rad} \approx \frac{1}{B_{rad}N_A} \qquad (\boldsymbol{Eq\ 2.26})$$

It is clear that, the radiative lifetime is inversely proportional to the B_{rad} and carrier concentration N_A. For CIGSe absorbers the carrier concentrations around 10^{15} cm^{-3} to 10^{17} cm^{-3} are reported [11, 22, 45, 46]. On the other hand, the B_{rad} is reported to be in the order of 10^{-10} cm^3s^{-1} or 10^{-11} cm^3s^{-1} [41, 47]. These values for B_{rad} and N_A leads to τ_{rad} in the range of µs for CIGSe absorbers [41, 47].

Non-radiative recombination:

Non-radiative recombination in a semiconductor can arise from defect assisted recombination mechanism known as Shockley-Read-Hall (SRH) recombination [48, 49], or from Auger-Meitner [50-52] recombination processes.

The Auger-Meitner recombination is normally considered for indirect semiconductors such as Si [52], or for semiconductors with very high doping concentration [3, 47]. For direct CIGSe semiconductor, this recombination mechanism has negligible contribution to the overall recombination processes in the material [47]. Therefore, detailed mechanisms and formulas of Auger-Meitner recombination are not discussed here.

On the other hand, Shockley-Read-Hall (SRH) recombination plays a crucial role in the overall recombination processes in the CIGSe absorbers. This type of recombination can occur both within the bulk of the material and at its surfaces or interfaces.

In the bulk, when defect states are present within the band gap of the material, the net SRH recombination rate can be expressed as [3, 48, 49]:

$$R_{SRH}^{net} = \frac{np - n_0 p_0}{\tau_n \left(p + N_V \mathrm{e}^{-\left(\frac{E_V - E_t}{k_B T}\right)} \right) + \tau_p \left(n + N_C \mathrm{e}^{-\left(\frac{E_t - E_C}{k_B T}\right)} \right)} \qquad (\boldsymbol{Eq\ 2.27})$$

Here, τ_p and τ_n are called SRH lifetime for electrons and holes, respectively. E_t is the defects energy level.

In the low excitation condition (i.e., $N_A \gg \delta n$), for a p-type material the Eq 2.24 is transformed into the following form:

$$R_{SRH}^{net} \approx \frac{N_A \delta n}{\tau_n \left(N_A + N_V \mathrm{e}^{-\left(\frac{E_V - E_t}{k_B T}\right)} \right)} \qquad (\boldsymbol{Eq\ 2.28})$$

In this case, the SRH lifetime (τ_{SRH}) would be same as the electron lifetime τ_n :

$$\tau_{SRH} \approx \tau_n = \frac{1}{\sigma_n v_{th} N_t} \qquad (\boldsymbol{Eq\ 2.29})$$

Here, σ_n is capture cross section of electrons, v_{th} is thermal velocity and N_t represents the defect density.

Furthermore, SRH recombination can also take place at surfaces and interfaces. The disruption of the lattice symmetry at the surface regions can lead to higher defect concentration and recombination centers at these regions, which can increase the non-radiative recombination activities at the surfaces/interfaces.

For a surface recombination rate, the SRH equation (Eq 2.27) can be modified into the following form [3]:

$$R_{SRH,surface}^{net} = \frac{S_p S_n (np - n_0 p_0)}{S_n \left(p + N_V \mathrm{e}^{-\left(\frac{E_V - E_t}{k_B T}\right)} \right) + S_p \left(n + N_C \mathrm{e}^{-\left(\frac{E_t - E_C}{k_B T}\right)} \right)} \qquad (\boldsymbol{Eq\ 2.30})$$

Here, the S_n and S_p are electron and hole surface recombination velocities, respectively, with units of cm.s^{-1}.

For a p-type semiconductor, under low excitation condition (i.e., $N_A \gg \delta p = \delta n$), this equation can be simplified into the following form:

$$R_{SRH,surface}^{net} \approx \frac{S_n N_A \delta n}{\left(N_A + N_V \mathrm{e}^{-\left(\frac{E_V - E_t}{k_B T}\right)} \right)} \qquad (\boldsymbol{Eq\ 2.31})$$

Therefore, in a p-type semiconductor such as CIGSe, surface recombination is primarily dominated by the electron surface recombination velocity (S_n).

These SRH non-radiative recombination processes are known to be harmful for photovoltaic device performance. In **Chapter 4** and **Chapter 5**, the impact of non-radiative recombination activities on the V_{OC} and device performance will be discussed extensively.

Furthermore, it is essential to employ effective passivation strategies for surfaces and interfaces to mitigate surface recombination velocities. In **Section 2.5.2**, more details regarding the surface passivation approaches for CIGSe absorbers are discussed.

2.2 p-n junction and of solar cells

In the previous sections, the fundamentals of semiconductors, photon absorption, charge generation, and recombination processes were introduced. In this section, the photovoltaic effect and the basic principles of solar cells will be presented. The following discussions are based on references [3, 36, 38, 39].

The operation of a solar cell is based on the photovoltaic effect, where incident solar energy is converted into the electrical energy. A solar cell device consists of an active absorber material where light is absorbed, and excess charge carriers are generated. In the CIGSe solar cells, the p-type CIGSe semiconductor serves as the absorber layer.

However, carrier generation alone is not enough to produce electrical power. The photogenerated charge carries needs to be separated and collected through the device to generate current flow. In order to separate the excess electron-hole pairs, an internal asymmetry within the photovoltaic device is required. In the CIGSe devices, this asymmetry is established by a p–n junction, which enables effective charge carrier separation. Therefore, in this section a brief overview of the p–n junction is provided.

2.2.1 Basic equations and essential parameters of solar cells

A p-n junction is formed when a p-type material and a n-type material are brought together into contact. Such a junction can generally be classified into two configurations: (i) Homojunction, where the two contacting semiconductors are from identical semiconductors. (ii) Heterojunction, where two dissimilar semiconductor materials are in contact. Notably, CIGSe solar cells are based on heterojunction structure, where the p-type CIGSe material is in contact with dissimilar n-type buffer and window layers. Therefore following discussions are based on heterojunction configuration.

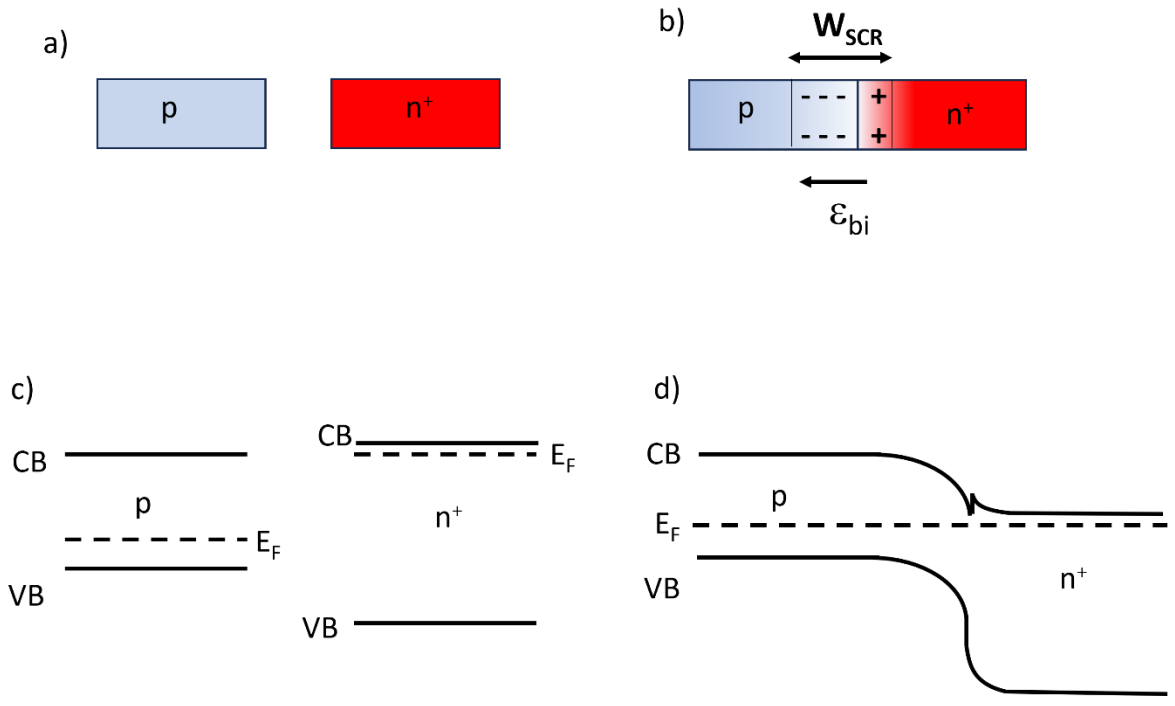

Fig 2. 4 a) Separate p-type and n-type semiconductors, **b)** p-type and n-type materials after the p-n junction formation, **c)** Band structure of separate p-type and n-type materials before junction formation, and **d)** Band structure after the p-n hetero junction formation.

Fig 2. 4 a and **b** illustrate a schematic representation of p-n heterojunction formation. In the case of CIGSe devices, the n-type window layer is highly doped, with its donor concentration ($N_{D,n}$) significantly higher than the acceptor concentration of p-type CIGSe material ($N_{A,p}$) (i.e., $N_{D,n} \gg N_{A,p}$). Therefore, here the p-n^+ configuration is presented, where n^+ denotes the highly doped n-type material.

It is also important to mention that, this model is a simplified approach. Here the effect of buffer layer is not considered. The original CIGSe device structure is more complicated and will be discussed in **section 2.5.2**.

In the p-n junction, since the electron concentration is higher in the n-type region and lower in the p-type region, electrons diffuse from the n-region to the p-region. Similarly, holes from the p-type material diffuse toward the n-region. As a result of this diffusion process, positively charged fixed donor states stay on the n-type side, and fixed negatively charged acceptor states remain on the p-type side (**Fig 2. 1b**). These ionized donor and acceptor states are fixed and immobile. As a result, this redistribution of charge carriers creates a region called **space-charge region (SCR)** or **depletion region**, which is depleted of free charge carriers.

Additionally, within the SCR, an internal electric field is formed, this built-in electrical field prevents further diffusion of charge carriers from each side. The electric potential associated with this electrical field is called the **built-in potential (V_{bi})**. The area outside the SCR, where electrical field is not present, is referred as **quasi-neutral region (QNR)**.

Furthermore, **Fig 2. 4 c** illustrates the band diagram of p-type and n-type material separately, before the formation of heterojunction. In this case, the n-type material has a higher band gap than the p-type material. Once again I would like to mention that the p-type material here represents the absorber layer, while the highly doped n-type material corresponds to the window layer in a solar cell. The high band gap of n-type region allows photons to pass through and reach the p-type absorber.

Fig 2. 4 d presents the band diagrams when two type of semiconductors are in contact. As explained previously in **Section 2.1.1**, in the p-type material, the Fermi level is located near the valence band edge (VB), while in the n-type material, this Fermi level is closer to the conduction band edge (CB). After the junction formation, under equilibrium conditions, the

Fermi level remains at a constant energy level throughout the entire p-n junction structure, ensuring equilibrium condition with no net carrier flow.

The width of the space charge region (SCR) on each side of the junction inversely depend on the square root of the doping concentration of that side. Since the n region is highly doped here, the SCR predominantly extends into the p-side, while its width in the n-side becomes very narrow and can be considered negligible.

In this case, the width of the space charge region (W_{SCR}) can be expressed with the following equation:

$$W_{SCR} = \sqrt{\frac{2\varepsilon_p \varepsilon_0 V_{bi}}{qN_{A,p}}} \qquad (\boldsymbol{Eq\ 2.32})$$

Where ε_0 is the vacuum electrical primitivity, ε_p is the relative electrical permittivity of p side. $N_{A,p}$ represent the acceptor concentration on the p-side, and V_{bi} is the built-in potential.

The equivalent electrical circuit of this simple p-n junction solar cell is presented in **Fig 2. 5**.

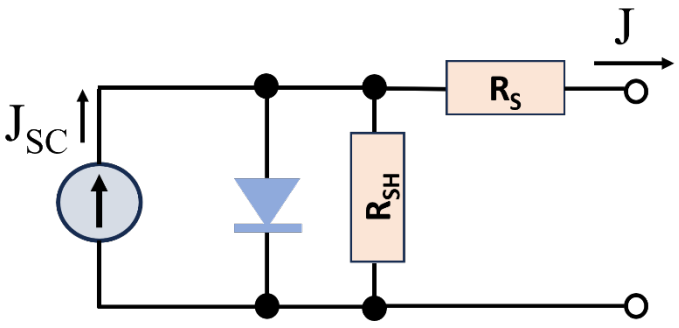

Fig 2. 5 Equivalent electrical circuit of a solar cell device based on p-n junction structure. Under dark condition J_{SC} vanishes. The external load is not included in electrical circuit.

In the absence of the incident light (i.e., under dark condition), this solar cell behaves like a diode. Therefore, a diode equation can be used to describe the electrical behavior of a solar cell under dark condition.

Under the dark condition, when the p-type side is connected to the positive terminal and the n-type side to the negative terminal, the diode is in a forward bias condition. In this state, the

width of the space charge region gets narrower, allowing mobile electrons from the n-region to diffuse into the p-region, and similarly, holes from the p-region to diffuse into the n-region. This carrier movement generates a current flow.

Under the dark conditions (i.e., with no incident light), the diode equation for a solar cell can be expressed as:

$$J(V) = J_0 \left[\exp\left(\frac{q(V - JR_S)}{n_{id} k_B T} \right) - 1 \right] + \frac{(V - JR_S)}{R_{SH}} \qquad (\boldsymbol{Eq\ 2.33})$$

Here, $J(V)$ is the diode current density, V applied bias voltage, n_{id} is called diode ideality factors, R_S series resistance, R_{SH} shunt resistance, and J_0 is saturation current density.

R_{SH} is related to the parallel path for current flow, while R_S represents the series resistance associated with the diode. The R_S and R_{SH} in the equivalent diode circuit are shown in **Fig 2. 5**.

The J_0 is closely related to both radiative and non-radiative recombination activities within the device. Higher recombination rate would leads to higher J_0 values. As will be shown shortly, increase in the J_0 can negatively impact the device performance.

n_{id} also depends on the recombination activities within the device. For an ideal diode, the ideality factor is unity (*i.e,* $n_{id} = 1$). However, in the real cases, n_{id} has values between 1 to 2. The ideality factor n_{id} indicates how the diode's J-V profile deviates from the ideal diode J-V curve.

Now, let's consider this simple solar cell under Sun radiation.

With the presence of illumination, the diode equation is shifted down by the photocurrent density J_{ph}. For a solar cell under Sun radiation, the illuminated diode equation can be expressed as:

$$J(V) = J_0 \left[\exp\left(\frac{q(V - JR_S)}{n_{id} k_B T} \right) - 1 \right] + \frac{(V - JR_S)}{R_{SH}} - J_{ph}(V) \qquad (\boldsymbol{Eq\ 2.34})$$

Under illumination, when the solar cell is under short circuit condition (i.e., V = 0), the current flowing through the device is called short circuit current density J_{SC}. This J_{SC} is important parameter for characterizing solar cells.

In the cases with negligible R_S and infinitely large R_{SH}, if the $J_{ph}(V)$ is independent of applied voltage, the $J_{ph}(V)$ in Eq 2.34 can be replaced with short circuit current density J_{SC}. Therefore, the light J-V curve would be same as dark one but shifted down with short-circuit current density J_{SC}.

For J_{SC}, it can be written:

$$J_{SC} = \int_0^{\infty} QE(E)\Phi_{Sun}(E)dE \qquad (\boldsymbol{Eq\ 2.35})$$

Here, the $QE(E)$ is called the external quantum efficiency of solar cell, and it can be defined as the ratio of the collected charge carriers over the number of incident photons.

$$QE(E) = \frac{\#\ collected\ e-h\ pairs}{\#\ incident\ photons} \qquad (\boldsymbol{Eq\ 2.36})$$

Notably, the quantum efficiency $QE(E)$ spectrum is closely interconnected to the $A(E)$ with the charge collection function.

The $QE(E)$ can be expressed as:

$$QE(E) = \int_0^{d} g(E,x)\eta(x)dx \qquad (\boldsymbol{Eq\ 2.37})$$

Where the $g(E,x)$ is the generation function defined in Eq 2.16, and $\eta(x)$ is charge collection function.

Under the short circuit condition, $\eta(x)$ depends only on the depth x inside the material. However, under applied bias, it can depend also on the voltage [3].

In an ideal scenario with complete charge collection conditions, where all optically generated electron and hole pairs are extracted from junctions, the $\eta(x)$ is unity. Therefore, the $QE(E)$ would transform into the following form.

$$QE(E) = \int_0^d g(E,x)dx \qquad (\boldsymbol{Eq\ 2.38})$$

$$= \int_0^d \alpha\,[1 - R(E)]\exp(-\alpha x)dx$$

By performing this integral over the thickness *d* of the absorber, the $QE(E)$ can be written as:

$$QE(E) = A(E) = [1 - R(E)]\,[1 - \exp(-\alpha d)]\ \ if\ \ \eta(x) = 1 \qquad (\boldsymbol{Eq\ 2.39})$$

The right-hand side of this equation is the same Beer-Lambert's law for $A(E)$, as discussed earlier in Eq 2.13. Therefore, it can be concluded that in the cases where the collection efficiency is ideal (i.e., $\eta(x) = 1$) , the $A(E)$ and $QE(E)$ would have identical spectral profile.

Another important parameter for a solar cell, is **open-circuit voltage V_{OC}** parameter. This voltage is measured when the device is in the open circuit condition and no net current is flowing over it (i.e., *J = 0*).

In a simplified case, with assumptions $n_{id} = 1$, $R_{SH} = \infty$ and $R_S = 1$, the V_{OC} can be expressed into the following form.

$$V_{OC} = \frac{k_B T}{q} \ln\left(1 + \frac{J_{SC}}{J_0}\right) \qquad (\boldsymbol{Eq\ 2.40})$$

Or,

$$V_{OC} \approx \frac{k_B T}{q} \ln\left(\frac{J_{SC}}{J_0}\right) \quad when\ \ J_{SC} \gg J_0 \qquad (\boldsymbol{Eq\ 2.41})$$

As mentioned earlier J_0 depends on the radiative and non-radiative recombination rate within the solar cell. With an increase in the non-radiative recombination rate, the J_0 also increases, leading to a reduction in the V_{OC} values. More detailed description regarding the effect of non-radiative recombination on the V_{OC} will be explained in the **Chapter 4** and **Chapter 5**.

Notably, the measured V_{OC} is the difference between the hole and electron quasi-Fermi levels at the p-side and n-side metallic contacts, respectively. In the ideal cases, without the presence of interface recombination activities, the open-circuit voltage V_{OC} is related to $\Delta\mu$ according to the following formula:

$$V_{OC} = \frac{\Delta\mu}{q} \qquad (\boldsymbol{Eq\ 2.42})$$

However, non-radiative recombination activities on the interface regions can reduce the charge carrier concentration at the interfaces, thereby pushing down the quasi-Fermi level of minority carriers (here E_{Fn}) at the interfaces below the corresponding bulk E_{Fn} values [29, 53-55]. As a result, the measured V_{OC} falls below the bulk $\Delta\mu$ limit.

Fig 2. 6, illustrates the illuminated and dark J-V curve of a solar cell. Here, the illuminated curve is same as the dark curve but shifted down by J_{SC} (see Eq 2.34 and its related discussions). The V_{OC} and J_{SC} position on the curve is shown in this figure.

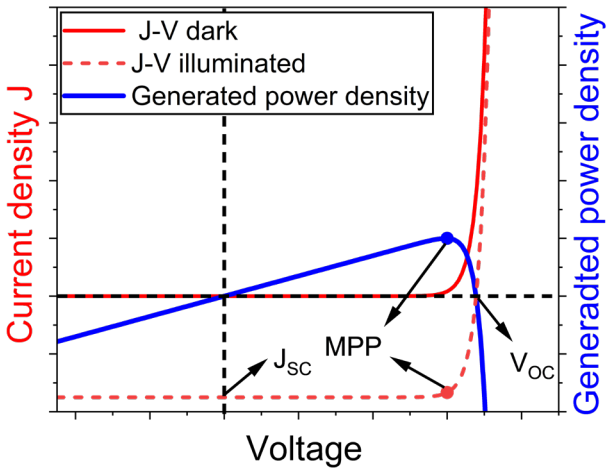

Fig 2. 6 Schematic diagram illustrating the dark and illuminated J-V curves of a solar cell, along with the power density at each voltage point. V_{OC}, J_{SC} and MPP are indicated in this figure.

The generated power density by a solar cell is defined as the product of the current density and voltage. At a certain point on the J-V profile, the device has its maximum power output. This point is referred to as the maximum power point (MPP). The current density and voltage associated with this point are denoted as J_{MPP} and V_{MPP}, respectively. These parameters are used to define the fill factor (FF) parameter, which is:

$$FF = \frac{J_{MPP} \times V_{MPP}}{J_{SC} \times V_{OC}} \qquad (\boldsymbol{Eq\ 2.43})$$

The efficiency of device, denoted as PCE, can be expressed as the maximum power density divided by incident illuminated power (P_{in}). The illuminated power P_{in} under AM 1.5 g standard illumination condition is 1000 W/m^2. Therefore, for PCE it can be written:

$$PCE = \frac{J_m \times V_m}{P_{in}} = \frac{J_{SC} \times V_{OC} \times FF}{P_{in}} \qquad (\boldsymbol{Eq\ 2.44})$$

Overall, the three key parameters for characterizing a solar cell are J_{SC}, V_{OC}, and FF. With these parameters, the power conversion efficiency (PCE) of the photovoltaic devices can be determined, and decrease in the one of them leads to a reduction in the overall efficiency of a solar cell.

2.2.2 Schockley-Queisser V_{OC} limit

In the previous section, it was mentioned that the V_{OC} is a crucial parameter for a solar cell.

The maximum achievable V_{OC} for an ideal solar cell can be calculated using the detailed balance model developed by Shockley and Queisser in 1961 (SQ model) [26].

This SQ model has three key assumptions for the ideal solar cell:

i- The $QE(E)$ spectra of this solar cell is defined by Heaviside step function, which has a transition point at the band gap energy (i.e., $QE(E) = 1$ for $E > E_g$ and $QE(E) = 0$ for $E < E_g$).

This step function $QE(E)$ means that all photons with energies above the band gap are fully absorbed, generating electron hole pairs, and all photogenerated carriers are collected from the device. In contrast, photons with energies below the band gap are not absorbed and do not contribute to charge generation process.

ii- The only available recombination mechanism in the photovoltaic device is spontaneous band to band radiative recombination, and non-radiative recombination pathways such as SRH and Auger recombination are not present in the device.

Based on these two assumptions, the J_{SC} for idealized SQ-solar cell can be expressed as :

$$J_{SC}^{SQ} = q \int_{E_g}^{\infty} \Phi_{Sun}(E) dE \qquad (\boldsymbol{Eq\ 2.45})$$

And J_0 for SQ device is given by:

$$J_0^{SQ} = q \int_{E_g}^{\infty} \Phi_{BB}(E) dE \qquad (\boldsymbol{Eq\ 2.46})$$

Subsequently, the V_{OC} limit for SQ model can be extracted from following equation:

$$V_{OC}^{SQ} \approx \frac{k_B T}{q} \ln\left(\frac{\int_{E_g}^{\infty} \Phi_{Sun}(E) dE}{\int_{E_g}^{\infty} \Phi_{BB}(E) dE}\right) \qquad (\boldsymbol{Eq\ 2.47})$$

iii- This model also assumes no ohmic and contact losses, in this case the Shockley-Queisser $\Delta\mu$ limit, denoted as $\Delta\mu^{SQ}$, would be same as qV_{OC}^{SQ} (i.e., $qV_{OC}^{SQ} = \Delta\mu^{SQ}$)

This model considers very simplified and idealized case for a photovoltaic device. Under real conditions, the $QE(E)$ spectra of solar cells do not behave like Heaviside step function, instead they show gradual increase from energies lower than the band gap to energies above the band gap (i.e $QE(E)$ shows broadening). Furthermore, along with the radiative recombination, non-radiative activities are also present in the device.

In **Chapter 4** and **Chapter 5** of this thesis, the effect of all non-idealities on the V_{OC} of solar cells will be covered extensively. These non-idealities involve the broadening of the absorption edge, incomplete absorption, incomplete charge collection, and presence of non-radiative recombination activities.

The SQ model also enables the calculation of maximum efficiency limit for single junction solar cells.

By considering J_{SC}^{SQ} and V_{OC}^{SQ} with Eq 2.45 and Eq 2.47, and by using the following FF equation[1] for an ideal diode (i.e. diode with $n_{id} = 1$, $R_{SH} = \infty$ and $R_S = 1$) [3]:

$$FF^{SQ} = \frac{\frac{qV_{OC}^{SQ}}{k_B T} - \ln\left(\frac{qV_{OC}^{SQ}}{k_B T} + 1\right)}{\frac{qV_{OC}^{SQ}}{k_B T} + 1} \qquad (\boldsymbol{Eq\ 2.48})$$

[1] The ***Eq 2.48*** is derived from ***Eq 2.202*** of ref [3] R. Scheer and H.-W. Schock, *Chalcogenide photovoltaics: physics, technologies, and thin film devices*. John Wiley & Sons, 2011..

The efficiency of SQ-solar cell can be calculated using Eq 2.44.

By performing the calculations the maximum theoretical efficiency of a photovoltaic device with an absorber material with band gap of 1.1 eV at the temperature of 25 °C would approximately be 33% under standard AM 1.5 g Sun illumination.

2.3 Urbach tails in a semiconductor

Urbach tails in a semiconductor material are referred to a joint density of states (DOS) that exhibit exponential decay from the band edges into the band gap [56]. The decay constant of this exponential tails is denoted as the **Urbach energy** (E_U). This E_U quantifies the extent of the DOS within the band gap. Higher E_U values indicate that the DOS extends further deep into the band gap.

In **Fig 2. 7**, schematic diagram for DOS in an ideal semiconductor with no tail states and a semiconductor with Urbach tails are presented. In the ideal case, the DOS of the VB and CB within the band gap is zero [35, 56]. However, when the Urbach tails are present, the DOS of VB and CB shows exponential decay into the band gap [35, 56].

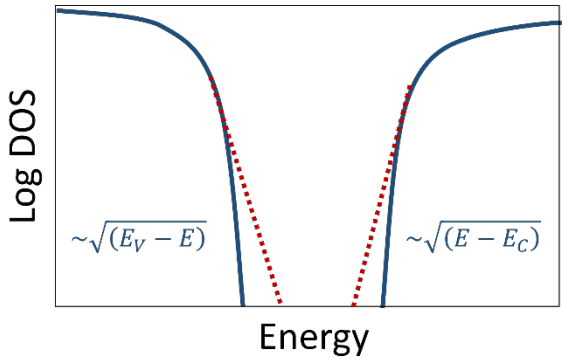

Fig 2. 7 Illustrates the density of states (DOS) for an ideal semiconductor compared to the DOS of semiconductor exhibiting Urbach tails. Continues line show when the Urbach tails are not present and DOS follows square root behavior, while dotted lines show the case when Urbach tails are present. This figure is plotted according to Figure 2.11 of Dr. Omar Ramirez's PhD thesis *[57]*.

These Urbach tails were first reported by Franz Urbach in 1953 for silver bromide (AgBr) crystals [58], it was observed that these tail states are temperature-sensitive, and higher temperatures can increase the extent of these Urbach tails (i.e., increase the Urbach energy).

The absorption coefficient *α(E)* of a material is directly related to the density of states (DOS) available for optical transition [56]. Therefore, to assess the extent of the Urbach decay (i.e, Urbach energy), it is essential to quantify the absorption coefficient, *α(E)*, in the energy ranges deep within the band gap energy.

The *α(E)* follows the behavior of the joint DOS. Therefore, in an ideal semiconductor without Urbach tails, the *α(E)* is zero within the band gap and follows a square-root dependence for photon energies above the band gap [35, 56]. However, in a real semiconductors, due to disorders and defects, *α(E)* does not sharply fall to zero below the band gap energy. Instead, it exhibits an exponential decay profile and Urbach tailing behavior [35, 56, 59].

The *α(E)* behavior of a direct semiconductor with presence of tail states can be explained with the following model proposed earlier by Kirchartz and Rau [30]:

$$\alpha(E) = \begin{cases} \alpha_0 \sqrt{\dfrac{E - E_g}{kT}} & , \quad E > E_g + \dfrac{E_U}{2} \\ \alpha_0 \, exp\left(\dfrac{E - E_g}{E_U}\right) \sqrt{\dfrac{E_U}{2ekT}} & , \quad E < E_g + \dfrac{E_U}{2} \end{cases} \qquad (\boldsymbol{Eq\ 2.49})$$

This equation clearly shows the square root behavior of *α(E)* for energies higher than band gap and exponential decay dependence for energy ranges lower than the band gap. In this model the α_0 is a constant that depends on the optical properties of material. For direct semiconductors like CIGSe, α_0 values in the order of $10^4 cm^{-1}$ are reported [3].

Using Eq 2.49, in **Fig 2. 8** the increase in the Urbach energy is simulated by considering $E_g = 1.1\ eV$ and $\alpha_0 = 10^4 cm^{-1}$. This instructive figure shows that as the E_U increase, the low energy slope of $\alpha(E)$ in the logarithmic scale becomes flatter.

These tail states can contribute to defect assisted SRH recombination mechanism and also can contribute to the sub band gap radiative recombination processes [33]. In **Section 2.2**, I briefly mentioned that increase in the non-radiative recombination activities decreases the V_{OC} of the photovoltaic devices and reduce their efficiency. Notably, later in **Chapter 4**, I will show that sub band gap absorptions can also lead to broadening in the $A(E)$ and $QE(E)$ spectrum, which in turn induces radiative losses in the V_{OC} of solar cells.

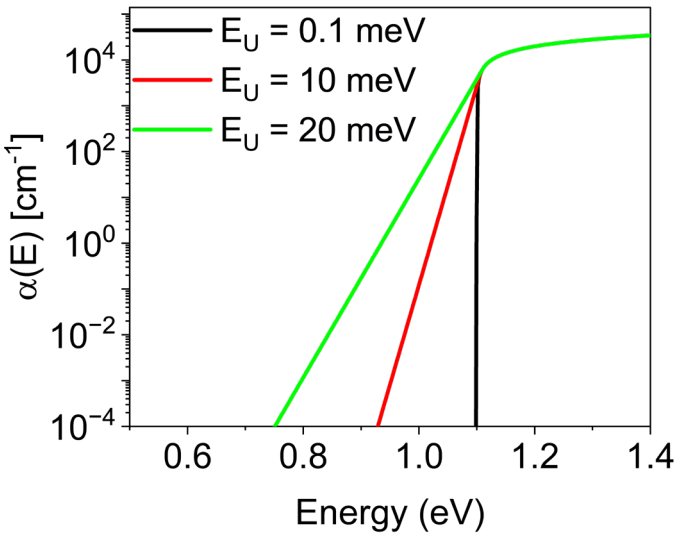

Fig 2. 8. $\alpha(E)$ for E_U values of 0.1 meV, 10meV, and 20 meV extracted from model described in Eq 2.49.

The Urbach tails are partly caused by thermal disorders (i.e, lattice vibration), and as reported for different materials, with an increase in the semiconductor's temperature, the Urbach energy also increases [58-63]. Furthermore, static structural disorders and defects in the crystal structure, such as vacancies and grain boundaries can have additional contribution to the Urbach tails [59, 63-65]. Moreover, these defect states can get charged and interact with each other through Coulombic interactions, this effect induces electrostatic potential fluctuations of the band edges, which cause further distortion of the band edges and lead to increase in the density of states within the forbidden band gap, ultimately causing an increase in the Urbach energies [34, 65-67].

Chapter 6 of this thesis investigates the tail states in the CIGSe absorbers. Using PL measurements, the absorption coefficient $\alpha(E)$ of CIGSe samples is quantified in the energy ranges deep into the band gap, and the Urbach energies are determined from the exponential decay of $\alpha(E)$ in the sub-band gap region.

More details regarding the experimental quantification of Urbach energy are explained in the results chapters.

2.4 Luminescence from semiconductor

Luminescence in semiconductors refers to the emission of light resulting from the radiative recombination of excess electron-hole pairs. Photoluminescence (PL) emission occurs when these excess carriers are generated optically, whereas electroluminescence (EL) emission arises when the forward bias is applied and excess carriers are injected through the junction.

EL measurements are performed on fully processed solar cell devices, as they require a p-n junction structure and metallic contacts to apply bias voltage. In contrast, PL measurements can be conducted directly on the bare absorber layers, without the need for a complete device structure. This makes PL a valuable and efficient technique for evaluating the absorbers quality before the fabrication of full functional devices.

Chapter 5 of this thesis explores EL and PL measurements to analyze V_{OC} losses in CIGSe solar cells, while **Chapter 6** focuses on PL measurements to investigate sub-bandgap absorption properties and tail states in the CIGSe absorbers.

This section provides a brief discussion of the theoretical background of these measurement techniques, highlighting their similarities and differences. Additionally, in **Chapter 3,** the details of the EL and PL experimental setups, including the calibration procedures for absolute measurements will be provided.

2.4.1 Photoluminescence

The PL emission spectrum $\Phi_{\mathrm{PL}}(E)$, represents the spectral photon flux density with the unit of $\frac{\#photons}{cm^2 eVs}$, and it is described by Planck's generalized law of radiation [68]:

$$\Phi_{\mathrm{PL}}(E) = \frac{2\pi}{h^3 c^2} \frac{A(E)\, E^2}{\exp\left(\frac{E - \Delta\mu}{k_{\mathrm{B}} T}\right) - 1} \qquad (\boldsymbol{Eq\ 2.50})$$

This law, establishes a direct connection between PL signal, $A(E)$ and $\Delta\mu$.

This formulation was first introduced in Würfel's 1982 publication [68], where a detailed derivation of Planck's generalized law is provided.

By considering Boltzmann's approximation, where $E - \Delta\mu \gg k_{\mathrm{B}}T$, the Eq 2.50 can be rearranged and simplified into the following form:

$$\Phi_{\mathrm{PL}}(E) \approx A(E)\frac{2\pi}{h^3c^2}E^2 \exp\left(-\frac{E}{k_{\mathrm{B}}T}\right)\exp\left(\frac{\Delta\mu}{k_BT}\right) \qquad (\boldsymbol{Eq\ 2.51})$$

Here, using the definition of the blackbody radiation spectrum $\Phi_{\mathrm{BB}}(E)$, the Eq 2.51 can be expressed as:

$$\Phi_{\mathrm{PL}}(E) \approx A(E)\Phi_{\mathrm{BB}}(E)\exp\left(\frac{\Delta\mu}{k_BT}\right) \qquad (\boldsymbol{Eq\ 2.52})$$

In this thesis, all PL measurements were performed under the conditions where the Boltzmann's approximation is valid.

The primary purpose of the PL measurements in this thesis is to find the numerical value of $\Delta\mu$ for CIGSe material. Furthermore, with the use of PL spectra, ultra-low values of $A(E)$ in the sub-band gap energy ranges can be accurately determined. This $A(E)$ spectrum can be subsequently used for quantification of Urbach energies.

In this section, just the theory behind PL measurements is covered, while the detailed methods for calibration of PL setup, including both spectral and laser intensity calibration, are introduced in **Chapter 2**. Additionally, $\Delta\mu$ and $A(E)$ extraction methods are extensively discussed in **Chapter 4** and **Chapter 5** of this thesis.

2.4.2 Electroluminescence

The EL emission spectrum, $\Phi_{\mathrm{EL}}(E)$, is linked to the internal voltage V_{in} and $QE(E)$ spectrum of photovoltaic device via Rau's optoelectronic reciprocity relation [69]:

$$\Phi_{\mathrm{EL}}(E) = QE(E)\Phi_{\mathrm{BB}}(E)\left[\exp\left(\frac{V_{in}}{k_BT}\right) - 1\right] \qquad (\boldsymbol{Eq\ 2.53})$$

Here, the V_{in} is analogous to the $\Delta\mu$. However, it is different from the applied voltage bias. In the ideal scenario, with no charge transport losses, and negligible interface/surface recombination, the V_{in} would be same as the applied voltage. However, in reality, with presence of interface recombination activities and transport losses, the V_{in} would have lower values than the applied bias voltage.

In the cases where the $V_{in} \gg k_B T$, the Eq 2.53 can be rearranged into the simplified form:

$$\Phi_{\mathrm{EL}}(E) \approx QE(E)\Phi_{\mathrm{BB}}(E) \exp\left(\frac{V_{in}}{k_B T}\right) \qquad (\boldsymbol{Eq\ 2.54})$$

Notably, this equation is analogous to Planck's generalized law. If $QE(E)$ is replaced by the absorptance spectrum $A(E)$ and V_{in} by the $\Delta\mu$, the Planck's generalized law can be recovered.

In **Chapter 3**, more details regarding the calibration procedure of EL setup will be discussed. Furthermore, in **Chapter 5**, the EL theory and reciprocity relation is used to quantify the V_{OC} losses in CIGSe devices.

2.5 CIGSe absorbers

2.5.1 Crystal structure, defects and band gap

Cu(In,Ga)Se_2 (CIGSe) is an inorganic compound semiconductor made of the elements from groups I, III, and VI of the periodic table. This semiconductor contains copper (Cu) from group I elements, indium (In) and gallium (Ga) both from group III, and selenium (Se) from group VI.

It is worth mentioning that alloys of this material with incorporating Ag, S and Te have also been developed for the photovoltaic applications. Examples include (Ag,Cu)(In,Ga)Se_2 [11, 70, 71], Cu(In,Ga)S_2 [72-74], Cu(In,Ga)$(Se,S)_2$ [20] and CuIn$(Se,Te)_2$ [75]. However, in this thesis only the Cu(In,Ga)Se_2 CIGSe compounds are investigated. Therefore, only the properties of CIGSe will be discussed in the following section.

CIGSe compound crystalizes in a special form of tetragonal crystal structure known as chalcopyrite structure. The chalcopyrite crystal structure of the CIGSe compound is illustrated in **Fig 2. 9**. In this crystal structure, each Cu atom is bonded to four Se atoms, and each Se atom is bounded with two Cu atoms and two In or Ga atoms.

Fig 2. 9 also illustrates the lattice parameters of the CIGSe chalcopyrite structure. In the tetragonal structure, the lattice parameters are expressed as $a = b \neq c$ [35].

In the CIGSe crystal, these lattice parameters are influenced by the concentrations of In and Ga. For pure CuInSe_2 (CISe), the calculated lattice parameters are approximately $a = b \approx$

5.78 Å and $c \approx 11.62$ Å [76]. The introduction of Ga into the compound typically reduces all the lattice parameter values, with pure $CuGaSe_2$ (CGSe) having $a = b \approx 5.61$ Å and $c \approx 11.00$ Å [76]. Therefore, for an alloy compound with both Ga and In atoms, the lattice parameters will be expected to have values between those of CISe and CGSe compounds.

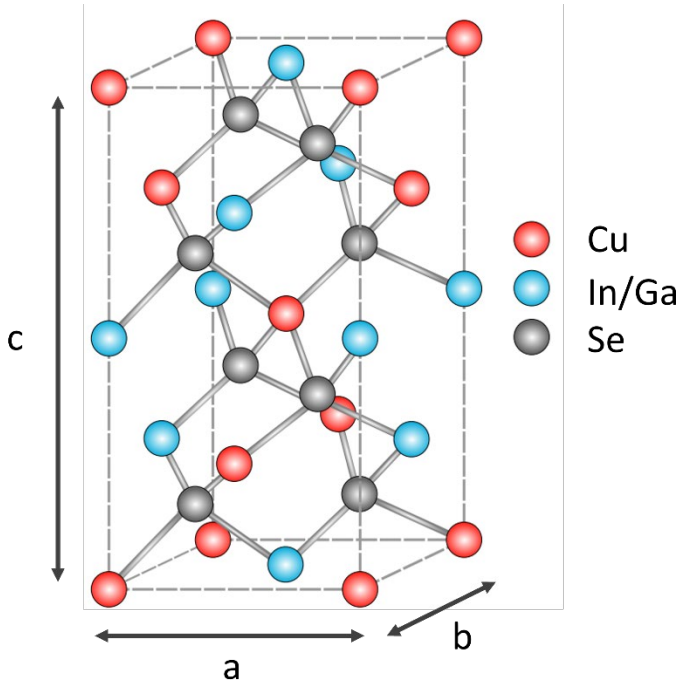

Fig 2. 9 Represents the chalcopyrite crystal structure of the CIGSe semiconductor. This figure with some minor modifications is directly taken from the PhD thesis of Dr. Max Wolter *[77]*.

Moreover, one of the advantages of CIGSe compounds is that their band gap can be manipulated by changing the Ga concentration. For pure CISe semiconductor, a band gap of around 1.04 eV has been reported, while for pure CGSe, the band gap energy was reported to be around 1.68 eV [4, 78].

For the CIGSe semiconductor compounds, the band gap energy can be determined using the following empirical equation [4, 78]:

$$E_g = (1-x)E_g^{CISe} + xE_g^{CGSe} - bx(x-1) \qquad (\boldsymbol{Eq\ 2.55})$$

Here, x represents the $\frac{Ga}{Ga+In}$ or GGI ratio, E_g^{CISe} and E_g^{CGSe} are band gap values for pure CISe and pure CGSe, with values of approximately 1.04 eV and 1.7 eV, respectively. The constant *b* is the ‘*’optical bowing coefficient”* according to ref [78], and has values around 0.11 to 0.24 for polycrystalline CIGSe semiconductors [78].

In a semiconductor material, the band gap can be increased either by lowering the valence band (VB) position or by shifting up the conduction band (CB) energy position. In CIGSe, increasing the Ga concentration primarily affects the CB energy level, shifting it to higher levels, while the VB position remains relatively unchanged [79]. It has been reported that CB and VB energy levels can be also manipulated by alloying CIGSe with sulfur (S) or silver (Ag) [80-82]. However, discussions related to the compounds with Ag and S are beyond the scope of this thesis and are not covered here.

This ability to tune the band gap is a valuable characteristic of the CIGSe absorbers. As will be demonstrated in the subsequent **Section 2.5.2**, this property can be used to engineer the band gap energy across the thickness of the CIGSe absorbers, enabling the effective surface/interface passivation.

Furthermore, it is important to mention that the complex quaternary CIGSe semiconductor does not always exhibit a perfect chalcopyrite lattice structure. Crystallographic defects are commonly present in CIGSe and can significantly influence its electrical, optical, and structural characteristics. The important crystallographic defects the CIGSe absorbers can summarized into the following categories;

Voids: In the CIGSe absorbers, empty spaces are commonly observed in the crystal structure [83, 84]. These empty volumes, known as voids, occur when number of atoms are missing from the lattice.

Dislocations: The dislocations or line defects are referred to the one dimensional misalignment of crystal planes [35, 85]. In the CIGSe polycrystalline absorbers this dislocation concentrations are reported to be around 10^{10} cm^{-2} to $10^{11}cm^{-2}$ [86, 87].

Grain boundaries (GBs): In most cases, CIGSe absorbers are grown as polycrystalline thin films [11, 17, 81, 88-90]. Unlike single-crystalline materials, polycrystalline semiconductors

consist of multiple grains, which have the same chalcopyrite crystal structure but different crystal orientations. The interfaces between these grains are called grain boundaries (GBs), which separate grains with distinct crystallographic orientations [85]. At these GBs, the periodic symmetry of the crystal lattice is interrupted. This effect leads to the formation of trap states on the GB regions [35, 91]. These states can trap free charge carriers and become charged [92], leading to formation of band bending (i.e., electronic barriers) at the grain boundary position [91-93]. Additionally, the defect states associated with the GBs can act as recombination centers and enhance non-radiative SRH recombination rate [91], ultimately reducing the overall efficiency of the solar cells. In **Chapter 6** of this thesis, the electronic barriers at the CIGSe GBs will be investigated using Kelvin-probe force microscopy (KPFM) measurements. More details regarding the KPFM measurements will be provided in the upcoming **Chapter 3**.

Point defects: These defects are localized imperfections where individual atoms are either missing, displaced, or placed in inappropriate lattice positions within the crystal structure. The important types of point defects in CIGSe include [94, 95]:

- **Vacancies**: Occur when atoms are missing from their regular lattice positions, creating empty lattice sites. Vacancies in CIGSe are V_{Cu}, V_{In}, V_{Ga}, and V_{Se}.
- **Antistites**: Arise when atoms occupy incorrect lattice positions, such as Cu atoms sitting on In sites (Cu_{In}) or vice versa (In_{Cu}). Similarly, Cu_{Ga} , Ga_{Cu}.
- **Interstitials**: These defects are referred to the cases where atoms occupy empty position between the regular lattice sites. In the CIGSe absorbers these defects are In_i, Cu_i, Ga_i, Se_i.
- **Defect complexes**: This type of defects are formed when two or more point defects are combined together, these point defects can have interaction with each other and create new energy levels. Such as combination of V_{Se} and V_{Cu} (V_{Se} -V_{Cu}).

Notably, the electronic properties of CIGSe absorbers are mainly influenced by point defects. presence of these point defects have influence on the doping concentration of CIGSe absorbers. For instance, V_{Cu}, Cu_{In} and Cu_{Ga} induces defect states close to the VB which act as a acceptor states trapping electrons from VB and increasing the hole concentration of CIGSe absorbers

[95]. On the other hand defects like In_{Cu} or Ga_{Cu} introduce donor states near the CB which can donate electrons to the CB [95].

For the photovoltaic applications, normally Cu-poor materials are prepared ($\frac{Cu}{In+Ga}$ (CGI) <1) [18, 19, 70, 96]. In contrast, Cu-rich phases often exhibit deep-level defects [95, 97] and high surface recombination velocities [54, 96], which negatively impact their efficiency and overall performance.

In the Cu poor CIGSe absorbers both donor states and acceptor states are available in high concentrations [98, 99]. Therefore, the CIGSe absorbers are compensated semiconductors. In the simplified case, by considering the defect exhaustion, the doping concentration can be expressed as $p \approx N_A - N_D$ [36].

2.5.2 Device structure, band structure and band gap gradient

In **Fig 2. 10a**, the structure of CIGSe solar cells and their band structures are illustrated.

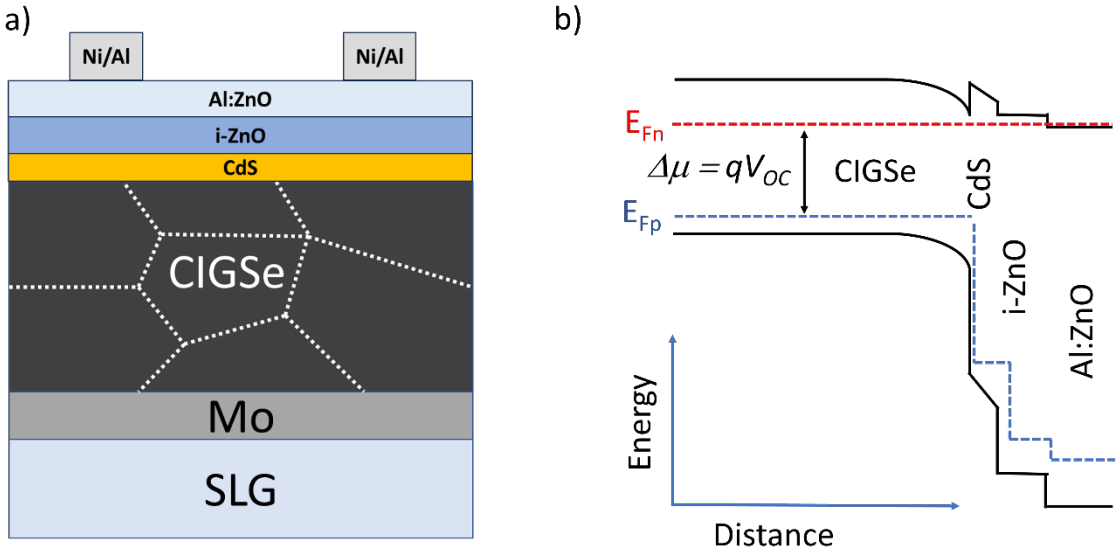

Fig 2. 10 a) CIGSe device architecture. **b)** band structures and band alignments in the CIGSe solar cells (without metallic contacts). This band alignment figure is plotted according to the previous published reports [55, 100, 101]. Here the solar cell is under V_{OC} condition.

Traditionally, soda lime glass (SLG) is used as a substrate for CIGSe absorbers [13, 102], although other substrates such as steel foils and polymers have also been employed [13, 101]. The SLG substrate contains sodium (Na), which can diffuse into the CIGSe layer during the

growth process. The presence of Na has been shown to improve the solar cell efficiency by increasing the V_{OC} of devices. This effect will be further discussed in **Section 2.5.3**.

The CIGSe layer is deposited on the Mo metallic back contact. Various deposition techniques have been employed for CIGSe growth, including co-evaporation [6, 11, 17, 19, 101, 102], sputtering [88, 89], and solution-based printing methods [103, 104].

In this thesis, the co-evaporation method is used for deposition, and the thickness of CIGSe samples investigated in this thesis is around 1.5 μm to 2 μm. More details regarding the co-evaporation process will be provided in **Chapter 3**.

Following the absorber layer, a buffer layer of with approximately 50 nm thickness is deposited. The standard buffer in CIGSe devices is CdS, which is also used in this work. However, alternative buffer layers such as Zn(O,S) have been successfully developed in other studies [105].

The device is completed by final deposition of an intrinsic ZnO (i-ZnO) and aluminum-doped ZnO (Al:ZnO) window layers, followed by Ni/Al metallic contacts coating.

Fig 2. 10 b presents the band alignment of CIGSe devices under V_{OC} condition. Here, the V_{OC} is given by the difference between hole quasi fermi level on the p-side and electron quasi fermi level on the n-side contacts. This figure presents the $\Delta\mu$ for the case with no interfacial recombination. In the presence of interfacial recombination at CIGS/CdS interface, the electron fermi level would bend down at interface, therefore the measured V_{OC} would be smaller than bulk $\Delta\mu$ in this case [55].

Further details on the deposition processes for CIGSe absorbers and other layers will be provided in **Chapter 3**.

In the CIGSe solar cells, it is essential to effectively passivate charge carrier recombination at surface and interface regions.

On the front surface, the buffer layer can partially mitigate front surface recombination activities [13]. However, near the Mo back contact, where CIGSe is directly in contact with metallic Mo, high surface recombination activity is observed.

To address this issue, various surface passivation strategies have been developed to reduce both surface and interface recombination. A well-known and widely adopted approach in CIGSe solar cells is the introduction of a band gap gradient within the absorber layer [13]. This strategy involves increasing the band gap energy (i.e., increasing Ga concentration) near both the front and back interfaces in the absorber.

A band gap gradient toward the rear surface has a back surface field effect, repelling photogenerated electrons away from the Mo contact and thereby reducing non-radiative recombination losses at the back interface [13]. This back-surface gradient can also improve carrier collection efficiency [13]. Similarly, if the buffer layer does not provide sufficient front-side passivation, a band gap gradient toward the front contact can also be introduced to suppress front surface recombination velocity [13].

As discussed in **Section 2.5.1**, the band gap of CIGSe can be tuned by adjusting the gallium (Ga) content. By varying the Ga concentration through the absorber depth, a desired band gap profile can be achived. More details regarding the deposition process and band gap engineering are provided in **Section 3.1**.

In the literature, three main types of band gap profiles are typically reported: (i) uniform band gap profile (no-gradient) [6, 106], (ii) Double graded band gap profile (V-shape gradient)[13, 17, 46, 107] and (iii) Hockey-stick gradient profile [11, 107].

These profiles are schematically illustrated in **Fig 2. 11**. In the graded band gap structures, the absorption onset is determined by the region with the lowest band gap energy, commonly referred to as the *notch* [13]. In the samples with uniform band gap, this notch region extends throughout all the absorbers thickness. However, in the two other cases, the notch is in the region where absorber has its minimum band gap.

As will be discussed later in **Chapters 4** and **Chapter 5**, the depth and thickness of this notch region can significantly influence the absorption properties of CIGSe absorbers.

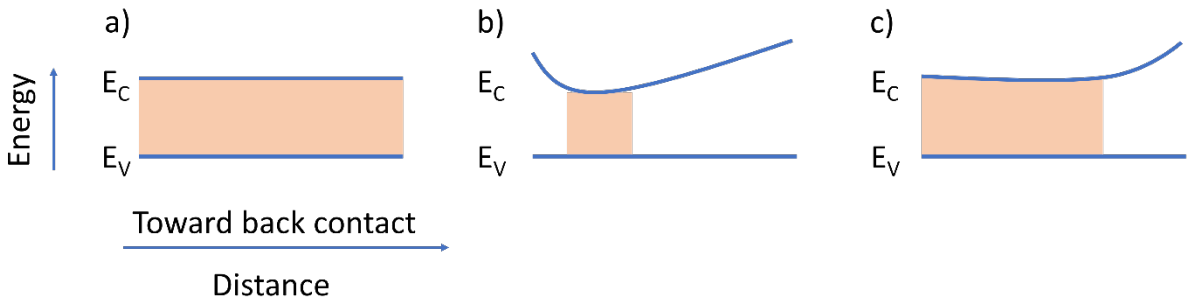

Fig 2. 11 Illustrates CIGSe absorbers with **a)** Homogeneous band gap **b)** Double graded or V-shape band gap **c)** Hockey stick (HS) band gap profile. In all cases region with minimum band gap region (i.e., notch) is highlighted.

In addition to the gradient approach, the back surface can also be passivated using selective contact that has a proper band alignment, which can block the electrons and transport holes [100, 108, 109], or employing tunneling layer at the back contact was also reported to be effective for back side passivation [110].

Notably, Dr. Taowen Wang from our laboratory has developed other passivation methods based on back surface selective contacts [100, 108, 109]. However, in this thesis, the gradient profile is primarily used as the passivation strategy. Therefore, passivation strategies based on selective contacts are not explained here.

2.5.3 Effect of alkali elements on CIGSe absorbers

The incorporation of alkali metals is a key factor in enhancing the efficiency of CIGSe devices [6, 17-19, 65, 111]. These alkali elements can be categorized into light and heavy alkali atoms [65]. Sodium (Na), a light alkali, is typically introduced from soda-lime glass (SLG) substrates. The SLG contains Na atoms that diffuse into the CIGSe layer during the growth process [112]. On the other hand, heavy alkalis such as potassium (K), rubidium (Rb), and cesium (Cs) are primarily introduced externally through post-deposition treatment (PDT) process [17, 18, 24, 65, 113]. In the PDT process, after the growth of CIGSe, heavy alkali fluoride (Alk-F) compounds are evaporated onto the surface of the absorbers, allowing them to diffuse into the CIGSe absorber. More details regarding the PDT process are explained in **Chapter 3**.

Alkali ions primarily enhance the *Voc* of CIGSe devices, resulting in increased power conversion efficiency. The beneficial effects of alkali ions can be summarized as follows:

(i) **Increasing p-type doping level**: It has long been long known that Na can enhance the hole carrier concentration in the CIGSe absorbers [21, 23, 113, 114]. As the hole concentration increases, the equilibrium Fermi level (E_F) shifts closer to the VB. This effect would result in a larger $\Delta\mu$ and, consequently, a higher open-circuit voltage (V_{OC}) under illumination (See Eq 2.21 and Eq 2.22).

Among the various mechanisms proposed to explain the Na-induced increase in hole concentration, two primary models have received particular attention. The first model involves **donor state passivation** mechanism, where Na is believed to neutralize donor-like defects, particularly indium-on-copper antistites (In_{Cu}) [15, 23, 115]. This passivation mechanism reduces the donor concentration in the compensated CIGSe absorber (i.e, reduces N_D), thereby increasing the net p-type doping. Notably, Colombara et al. proposed the so-called *Revani diffusion model* for this mechanism [115], which suggests that Na pushes In_{Cu} defects from the grain interiors toward the grain boundaries, effectively lowering this donor type defect concentration within the grains.

The second mechanism is based on the formation of copper vacancies (V_{Cu}) [116]. As the CIGSe absorber cools down after the growth process, the solubility of Na atoms decreases inside the grains. This reduction in solubility results in the out-diffusion of Na atoms from the grain interiors toward the grain boundaries or the surfaces. This out-diffusion process leaves behind (V_{Cu}), which act as **acceptor states** and thus contribute to the increase in p-type doping.

The incorporation of heavy alkalis can also enhance the p-type doping level in CIGSe absorbers. Recent reports have shown that the addition of K, Rb and Cs can enhance the hole concentration [21, 45, 71, 117-119]. However, for heavy alkali ions, the exact mechanisms responsible for this increase in doping remain unclear up to now.

(ii) Mitigation of non-radiative recombination: The alkali elements can also decrease the SRH non-radiative recombination rate (i.e, increase the lifetime) in the CIGSe absorbers [24, 25, 120-122]. This non-radiative recombination centers can be located within the bulk or on the surface of the material.

The alkali elements can **reduce the extent of tail states** (i.e., reduce the Urbach energy) [18, 33, 34, 65, 121], as mentioned previously, these tail states can have contribution to the SRH recombination activities (See also ref [33]), therefore passivation of tail states can reduce the SRH recombination rate. Notably, in polycrystalline CIGSe absorbers, it has been reported that samples with no alkali elements exhibit Urbach energies around 17 meV [33]. The addition of sodium (Na) can reduce the Urbach energy to approximately 12 meV, and further reduction to around 11 meV were observed through the incorporation of Rb heavy alkali [33]. A similar decreasing trend in Urbach energies has also been observed in single-crystalline CIGSe absorbers [34].

Moreover, alkali ions are predominantly accumulated at the GBs regions [65, 123-126], where their presence is believed to effectively neutralize charged defects, reduce the electronic barrier, and suppress non-radiative recombination activities in these regions [65]. This hypothesis is supported by some KPFM measurements, which revealed a reduction in the band bending at grain boundary sites with the addition of heavy alkalis [65, 127].

In addition to their effect on grain boundaries, both heavy and light alkali elements can also interact with the surfaces and interfaces, leading to the passivation of non-radiative recombination centers at these region [120, 128-130]. Notably, recent studies suggest that Rb can undergo an exchange mechanism with Cu at the surface by substituting Cu atoms [129]. This mechanism contributes to improvement of CdS/CIGSe junction quality and a reduction in the interface defect density.

There are also reports showing the light alkali Na can segregate near the Mo back contact and reduce the non-radiative recombination velocity in this region [120].

Further details regarding the beneficial impact of alkali ions on the CIGSe device performance will be covered in **Chapter 6**.

2.5.4 Urbach tails and V_{OC} losses in CIGSe devices

As discussed earlier in **Section 2.3**, Urbach tails can engage in the radiative and non-radiative activities which can in turn lower the V_{OC} of devices. Furthermore, **Section 2.5.3** highlighted that the E_U in CIGSe absorbers can be manipulated by incorporating alkali ions.

Notably, some previous publications have observed a linear relationship between the V_{OC} deficit (V_{OC}^{def}) and E_U for CIGSe and Perovskite solar cells [33, 131].

Here, V_{OC}^{def} is defined as the difference between the measured V_{OC} and the V_{OC}^{SQ} limit:

$$V_{OC}^{def} = V_{OC}^{SQ} - V_{OC} \qquad (\boldsymbol{Eq\ 2.56})$$

The **Fig 2. 12** presents an empirical linear trent between the V_{OC}^{def} and E_U for state of the art (SOA) CIGSe devices [33]. Interestingly, it can be observed that all SOA CIGSe samples, except one with no alkali, follow this linear trend.

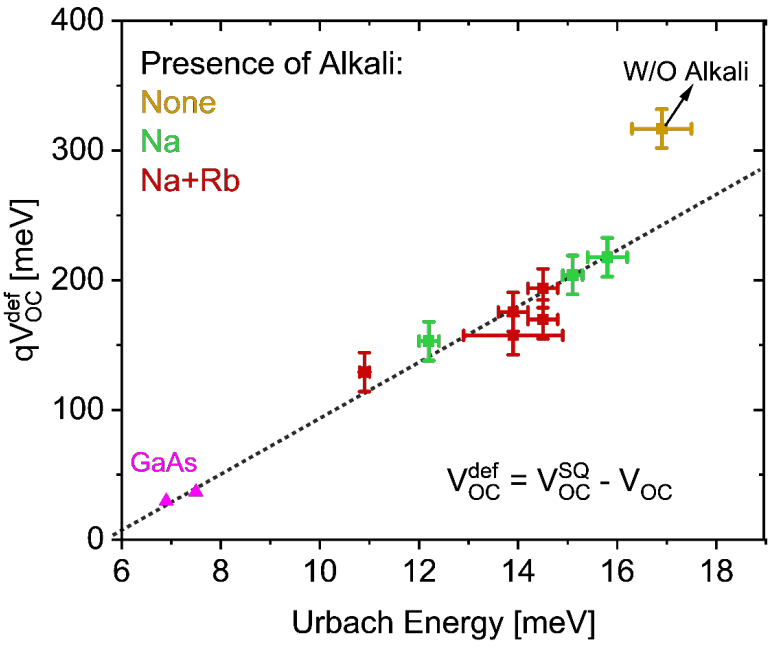

Fig 2. 12 linear relationship between Urbach energy and V_{OC}^{def}, here the presence of alkali is represented by a color code. Additionally GaAs samples with lowest reported Urbach energies are

used as a reference point. This Figure with some modifications are taken from Wolter et al [33] under CC BY 4 license. Also it was used in my published work [132].

In **Fig 2. 12**, It is evident that the absorber with no alkali incorporation exhibit the highest Urbach energies. A significant reduction in E_U, down to approximately 12 meV, is observed in samples with Na, while an even lower value of around 11 meV is achieved when Na and Rb are both introduced into the absorber.

It has been proposed that both radiative and non-radiative recombination via Urbach tail states are the dominant limitations mechanism to the V_{OC} in SOA CIGSe absorbers. When a device exhibits a higher V_{OC}^{def} than predicted by the empirical line, it indicates that additional loss mechanisms beyond the Urbach tails contribute to its reduced V_{OC}.

Chapter 6 of this thesis explores the impact of alkali elements on the GBs and Urbach tails. In particular, the possible contribution of charged GBs to the Urbach tails are investigated in this chapter. The Urbach energies of samples with no alkali, with Na and Na+Rb are quantified using PL analysis, while electronic barrier across the GBs are analyzed through Kelvin probe force microscopy (KPFM) measurements. Details of KPFM measurements are provided in **Section 3.8**.

2.6 Summary of Chapter 2

So far, this chapter has covered the fundamental concepts related to the semiconductors and solar cells, along with the corresponding equations and formulas. Additionally, the basic principles of EL and PL measurements were also introduced.

Furthermore, the crystal structure, solar cell architecture, band gap gradient profiles, defects and beneficial impact of alkalis in the CIGSe absorbers were all discussed in this chapter.

The next **Chapter 3** will focus on the deposition processes and solar cell fabrication and characterization methods, while **Chapter 4** and **Chapter 5** will use EL and PL formulas to investigate the V_{OC} and $\Delta\mu$ losses in CIGSe solar cells.

Additionally, in **Chapter 6** the PL measurements will be used to investigate the effect of Rb and Na alkalis on the tail states and $\Delta\mu$ of CIGSe absorbers.

3 Sample growth and characterization methods

In this chapter, the deposition and characterization methods used throughout this thesis will be introduced.

The CIGSe absorbers investigated in this thesis were prepared in two different laboratories. **Chapter 5** focuses on the analysis of CIGSe samples deposited in the Laboratory for Photovoltaics (LPV) at the University of Luxembourg. I personally performed the deposition of these samples. Furthermore, **Chapter 6** focuses on surface and grain boundary studies of CIGSe samples prepared in PVcomB laboratory at Helmholtz-Zentrum Berlin (HZB).

At the beginning of this chapter, in **Section 3.1** and **Section 3.2**, the deposition process of the CIGSe absorbers and the device fabrication are discussed. The samples prepared in our laboratory (LPV) exhibit rough surfaces. In the **Section 2.5.4**, I briefly mentioned that AFM/KPFM measurements were conducted to investigate the grain boundaries in CIGSe films. For surface and grain boundary analysis, smooth surface morphology is essential. The rough surfaces are known to be detrimental for KPFM measurements by inducing topographical artifacts, which can cause errors in the extracted KPFM data [133, 134] . To avoid this issue requirement, we collaborated with PVcomB, where optimized deposition recipe was developed to prepare CIGSe absorbers with smooth surfaces.

A key factor influencing the surface roughness of the CIGSe samples is the amount of Cu supplied during the deposition process. In this chapter, deposition process and the impact of Cu-rich growth conditions on the final surface roughness will be discussed extensively.

Furthermore, the subsequent sections of this chapter introduce the optical characterization techniques, including photoluminescence (PL), transmittance, and reflectance, as well as optoelectrical analysis methods such as electroluminescence (EL), J-V, and external quantum efficiency (QE) measurements. These methods are the primary tools in this thesis for investigating the V_{OC} losses in solar cells.

While this chapter focuses on introducing the experimental setups and methodologies, the detailed equations and analysis of V_{OC} losses will be discussed in **Chapter 4** and **Chapter 5**.

Additionally, other characterization techniques used in this study, such as cathodoluminescence (CL), Kelvin probe force microscopy (KPFM), time-resolved PL (TRPL), and secondary ion mass spectrometry (SIMS) measurements, are also briefly explained.

3.1 CIGSe Co-evaporation

3.1.1 Co-evaporation in LPV

In **Chapter 5**, all the investigated CIGSe samples are prepared in laboratory for photovoltaics (LPV), and all the deposition processes were performed using co-evaporation method in Veeco Gen 930 molecular beam epitaxy (MBE) machine.

The investigated samples in **Chapter 5** are prepared either on transparent **SLG substrates** or on **Mo-coated SLG** substrates. Transparent SLG substrates are used for transmittance and reflectance analysis, while Mo/SLG substrates are employed for device fabrication.

Fig 3. 1 schematically illustrates the MBE machine and its key components. This machine is equipped with elemental sources of Cu, In, Ga, and Se, as well as NaF and RbF for post-deposition treatment (PDT). The base pressure of the MBE machine is approximately in the range of 10^{-9} mTorr.

The deposition rate for each element is controlled by its temperature. For Se, a cracker source is used, and its flux can be adjusted by temperature and also with a needle valve attached to the cracker. The deposition rate for each element is routinely monitored using a Beam Flux Monitor (BFM) and a Quartz Crystal Microbalance (QCM). The BFM monitors the pressure of the evaporated particles. These instruments together help to maintain consistent deposition rates across different processes, ensuring the deposition reproducibility.

During the PVD deposition process, the substrate set temperature is monitored by a thermocouple connected to the heater without touching the substrates. Additionally, the absorber's surface temperature is measured using a pyrometer that is mounted outside the machine, directly observing the absorbers through a transparent viewport. Usually, in our MBE machine, pyrometer measures slightly lower temperature than the substrate set temperature (around 50-70 °C lower).

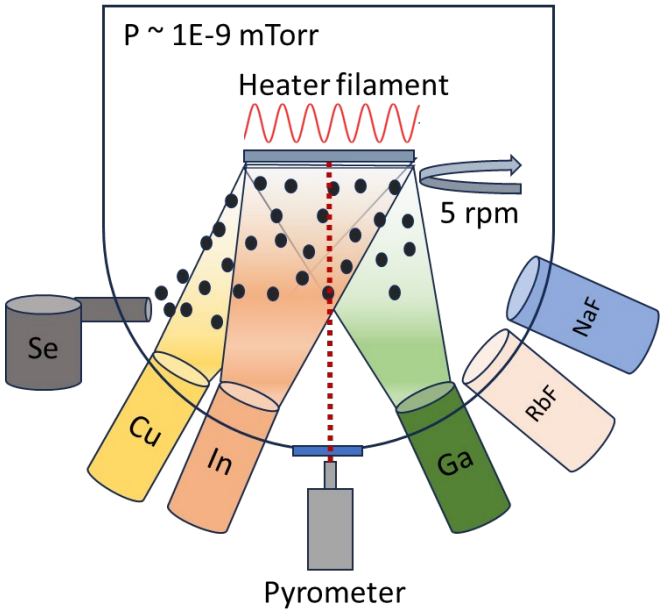

Fig 3. 1 Schematic diagram showing the molecular beam epitaxy (MBE) machine and its key components.

The investigated samples in **chapter 5** have either graded band gap profile or uniform band gap through their thickness.

In the **Section 2.5.2**, the Ga compositional gradient in the CIGSe absorbers has already been discussed. It was mentioned that high-efficiency CIGSe solar cells are typically prepared with a V-shaped band gap gradient profile, where the band gap increases toward both the back and front contacts (see **Fig 2. 11 b** and ref [12, 13, 17, 19, 101]).

For samples with a V shape band gap gradient, a three-stage co-evaporation deposition method is employed [12]. **Fig 3. 2** schematically illustrates the temperature profile and deposition process of 3-stage deposition method.

Before starting the deposition, all substrates undergo a cleaning procedure, which involves annealing step at 500 °C for 20 minutes. The substrates are then cooled down to the set temperature of 356 °C. Subsequently, a Se annealing step is performed on the Mo substrates to form $MoSe_2$. It has been reported that the presence of this thin $MoSe_2$ layer can form an ohmic contact at the Mo/CIGSe interface [101, 135, 136]. It is worth mentioning that, the entire deposition process is carried out under a selenium-rich atmosphere, with Se supplied in excess to prevent its loss during growth process.

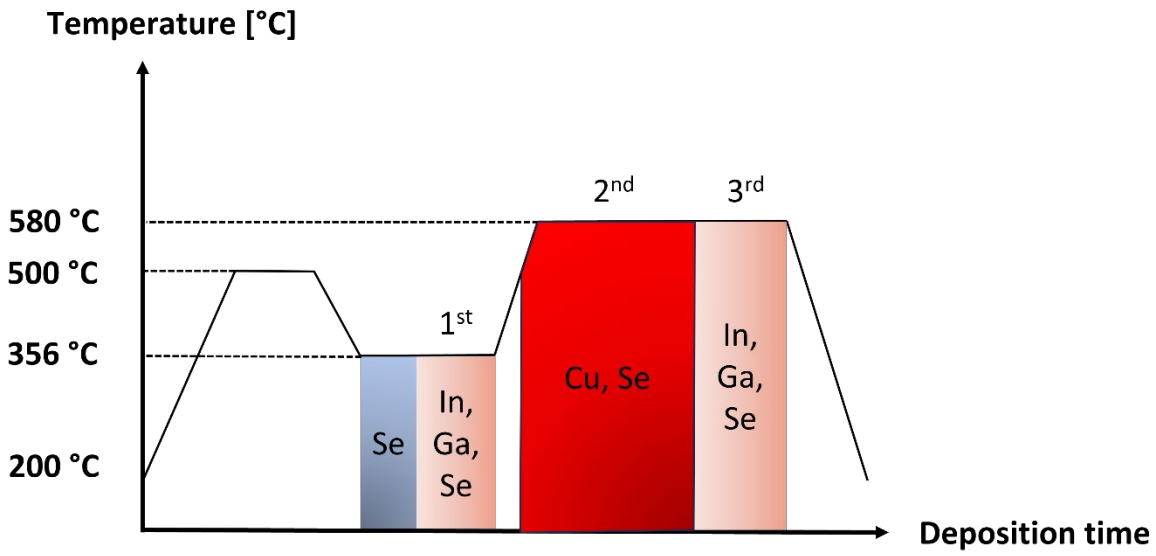

Fig 3. 2 The growth process of 3-stage deposition method. Temperature profile and supply of elements during each stage.

Subsequently, in the 1st stage, In and Ga are co-evaporated together at the substrate temperature of 356°C, forming a precursor layer with the $(In,Ga)_2Se_3$ composition. In the second stage, the substrate temperature is increased, and Cu is provided to the precursor film to form the chalcopyrite phase. The Cu is usually supplied in excess to achieve Cu-rich phase (CGI > 1), which improves grain size and absorbers quality [137]. However, as I mentioned in the previous **Section 2.5.1**, for solar cell applications, normally absorbers with Cu-poor composition are preferred. Therefore, in the 3rd stage (i.e., last stage), the Cu supply is stopped, and In and Ga are resupplied again to achieve the final Cu-poor composition (CGI < 1). It is worth mentioning that the In and Ga deposition rates are not necessarily the same in the first and last stage.

The substrate set temperature during the 2nd and 3rd stages reaches to its maximum point around 580 °C. After finishing the last stage, the prepared absorbers are cooled down in the Se atmosphere to 200°C.

In this three-stage process, due to the lower diffusivity of Ga compared to In [138], a higher Ga concentration remains near the front and back contacts, creating a V-shaped Ga distribution profile over the thickness, this effect results in an increase in the band gap energy towards both surfaces (see **Fig 2. 11 b**).

For three stage growth process, the deposition process is controlled using pyrometer reading and heater output power signal [139, 140]. The pyrometer measures the heat emission from absorber surface (black body radiation). The detected thermal radiation is influenced by the material's thickness, leading to an interference pattern in the pyrometer reading.

Fig 3. 3 illustrates the pyrometer and heater output power profile during 3-stage growth profile. It can be observed that during the first stage of growth (t_1), thickness interference effect causes oscillations in the pyrometer reading temperature (T_{Pyro}) [141, 142]. The duration of the first stage in our processes is controlled by number of T_{Pyro} oscillations which is typically 3 oscillations.

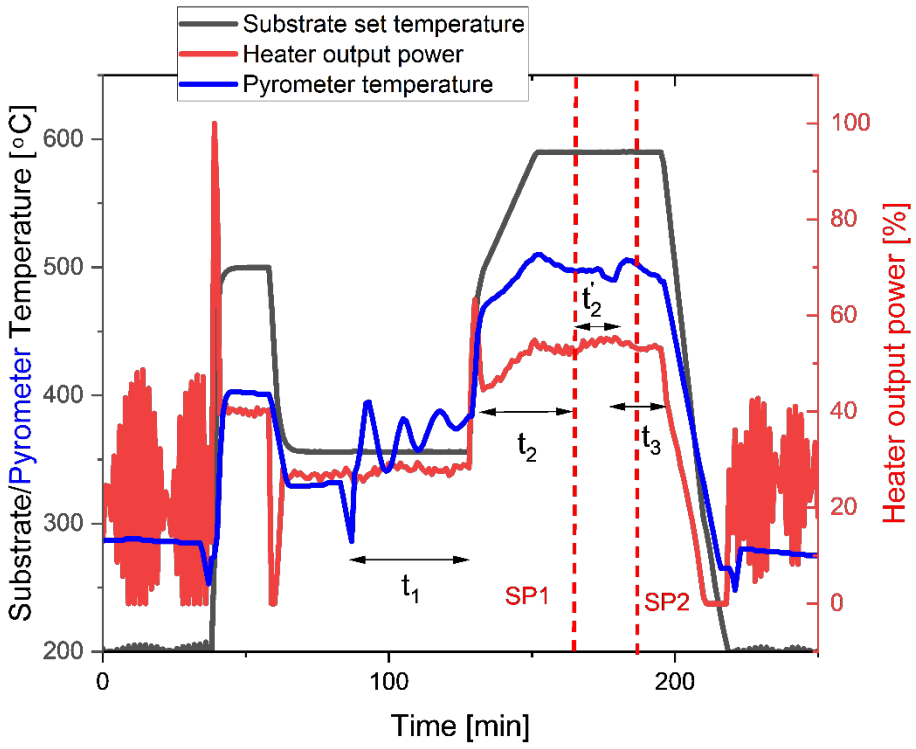

Fig 3. 3 Representing profiles of heater set temperature, pyrometer temperature and heater output power during 3-stage deposition process. Red dashed lines show stochiometric points (SP)

Furthermore, in the second stage the process is primarily controlled by heater output power signal. In the 2nd stage, with the supply of excess Cu and formation of CuSe phases, the emissivity of the layer increases [139, 141], which leads to enhanced radiative heat loss. This effect leads to increase in the heater output power to keep the substrates at constant set

temperature during this step. Therefore, by monitoring the changes in the heater output power, it is possible to detect the point where material transforms to the Cu-rich phase.

In **Fig 3. 3**, the second stage is divided into two parts: from the starting point to the first stoichiometric point (SP1 with CGI ≈1), denoted as t_2, and from SP1 to the point where the heater output power reaches to its maximum value, denoted as t_2'.

When material reaches to its first stochiometric point SP1, with further Cu supply, heater output power starts to increase, which indicates that the material is transforming to Cu-rich phase, and CuSe phases are forming in the absorbers. The Cu supply continues for a certain duration t_2' until the end of the second stage, where the output power reaches to its maximum point. The CGI concentration at this point (denoted here as y_{2nd}) can be estimated using the formula $y_{2nd} \approx (t_2 + t_2') / t_2$. In our processes we usually use estimated $y_{2nd} \approx 1.2$.

In the last stage of the deposition, In and Ga are deposited again for a certain duration t_3. During this stage, the heater output power starts decreasing. The CIGSe absorbers return to the stoichiometric point again (SP2), and then the deposition of In and Ga goes further than SP2 to achieve the final-poor composition (CGI < 1).

In **Chapter 5**, in addition to the Ga graded samples, some absorbers with uniform Ga composition (i.e., uniform band gap) are also investigated.

Samples that have a constant Ga distribution through their depth were prepared using a process known as the Cu-rich-off (CURO) process [143]. This deposition method has two main stages: initially the Cu, In, Ga, and Se are co-evaporated onto the substrates together at a substrate set temperature of 580°C. In this stage, the Cu is supplied in excess to promote Cu-rich growth. Subsequently, the Cu supply is cut off, and In and Ga fluxes are continued to achieve a final Cu-poor composition. Since In and Ga are supplied at the same deposition rate throughout the process, this process results in a flat distribution of Ga and thus flat band gap profile across the thickness. **Fig 3. 4** schematically illustrates the time progression and temperature profile of the CURO growth processes.

Controlling the stoichiometry, particularly the CGI ratio, is a challenging aspect of this process. However, through repeated depositions, I was able to develop an optimized recipe for my study.

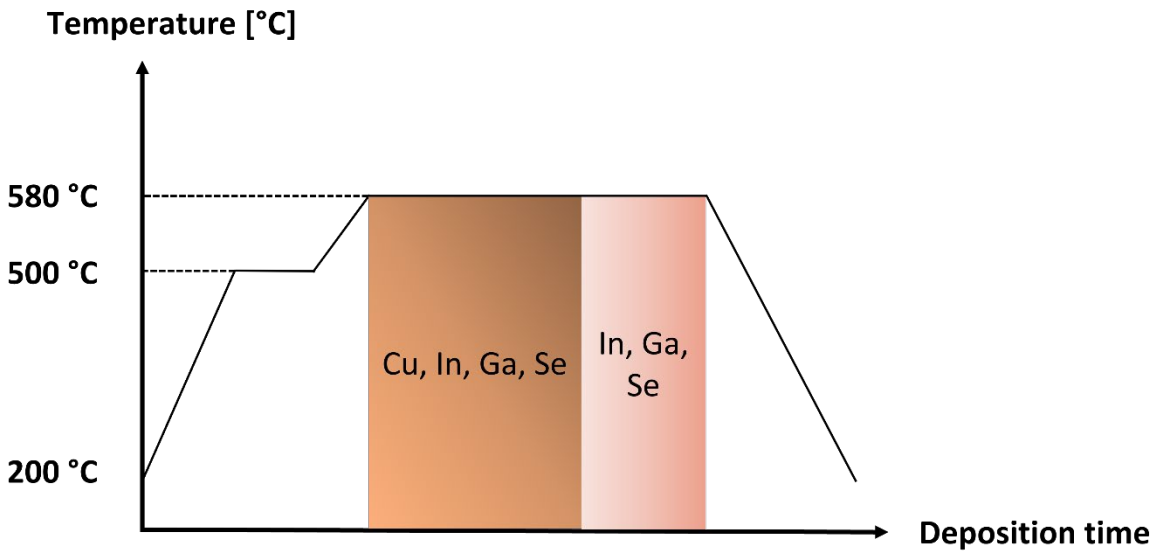

Fig 3. 4 Temperature profile and deposition process for Cu-rich-off (CURO) growth method

The duration of three-stage process is approximately 3.5 hours, while the CURO process takes only 70 minutes.

In **Chapter 5**, Secondary Ion Mass Spectroscopy (SIMS) measurements, along with cross-sectional Cathodoluminescence (CL) analyses are presented for some selected samples. These results clearly show a graded band gap profile for the samples processed with the 3-stage method, and a constant band gap for the samples prepared using the CURO deposition recipe.

3.1.2 CIGSe growth in PVcomB

For the purpose of grain boundaries and KPFM measurements, it is essential to prepare samples with smooth surfaces. Presence of high surface roughness can induce artifacts which can lead to inaccuracies in the KPFM data interpretation [133, 134] (see also **Section 2.5.3**).

At PVcomB, Helmholtz-Zentrum Berlin, our colleagues successfully developed a growth process that results in smooth CIGSe surfaces, this process is optimized for CIGSe/perovskite tandem devices [7]. In **Chapter 6** of this study, samples from PVComB are investigated. The MBE machine in PVcomB has similar components to our machine (See **Fig 3. 1**). However, these samples were grown using a slightly modified three-stage process than we use in our laboratory.

For these samples, in the first stage, in the presence of Se, instead of supplying In and Ga simultaneously, Ga and In were evaporated sequentially, following a Ga-In-Ga-In sequence at the substrate set temperature of 300°C [117, 144]. The rest of the process is similar to the conventional three-stage method that is already explained in **Section 3.1.1**.

The maximum substrate set temperature reaches 530°C during the 2^{nd} and 3^{rd} stage of this process [117]. For the process control, in addition to the pyrometer and heater output power signal, laser light scattering (LLS) is also employed. The CIGSe process control with light scattering has been reported in previous studies [145, 146]. This LLS method relies on scattered laser light intensity for process control. Through a transparent viewport a laser light is directed on the absorber surface and the scattered light is detected. In the second stage, when the CIGSe composition passes the stochiometric point (i.e, CGI > 1), the roughness of the film starts to increase, thus it effects the scattered laser light signal, resulting in an increase in the LLS signal. With this change in the LLS signal the process can be more reliably controlled [146].

Previous reports indicate that the amount of Cu supplied during the 2^{nd} stage of the three-stage co-evaporation process is a key factor influencing the final roughness of the films [137], and the surface roughness depends on the CGI concentration at the end of the 2^{nd} stage (y_{2nd}) [137]. During this stage, excess Cu leads to increase in the grain size and formation of $CuSe_x$ on the surface of CIGSe absorbers, which in turn increases the surface roughness of absorbers.

With our colleagues from PVcomB, we studied the effect of Cu-excess growth on the roughness of the final absorbers by examining CIGSe samples with varying durations of the second stage. We investigated samples with y_{2nd} of 1.05, 1.3, and 1.5, with these y_{2nd} values being estimated through combination of laser light scattering (LLS), heater output power and pyrometer signals [117, 146].

Fig 3. 5 illustrates the AFM image of CIGSe absorbers with estimated y_{2nd} of 1.05, 1.3 and 1.5. It can be observed that the sample with the lower y_{2nd} have smaller grain size, and grain size increases with more Cu supply in the 2^{nd} stage (i.e higher y_{2nd} values).

Moreover, **Fig 3. 6** illustrates the mean roughness measured by AFM measurements, It can be observed that the surface roughness increases with increase in y_{2nd}. Therefore, for further

KPFM analysis the samples prepared with CGI concentration of 1.05 at the end of 2nd stage (i.e., y_{2nd} ~ 1.05) were used.

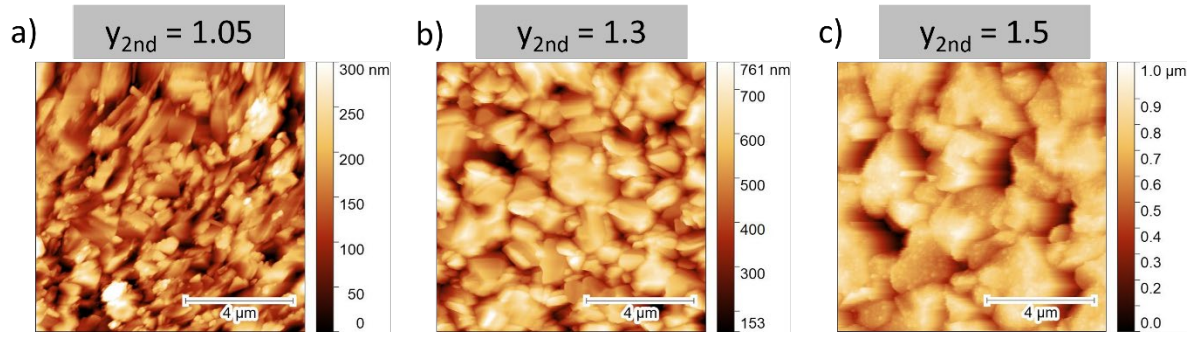

Fig 3. 5 Topography image (AFM image) of CIGSe samples grown in PvComB. with y_{2nd} of **a)** 1.05, **b)** 1.3 and **c)** 1.5. Here, y_{2nd} represent the CGI concentration at the end of the 2nd stage. (These measurements were provided by **Uzair Muhammad Farooq**)

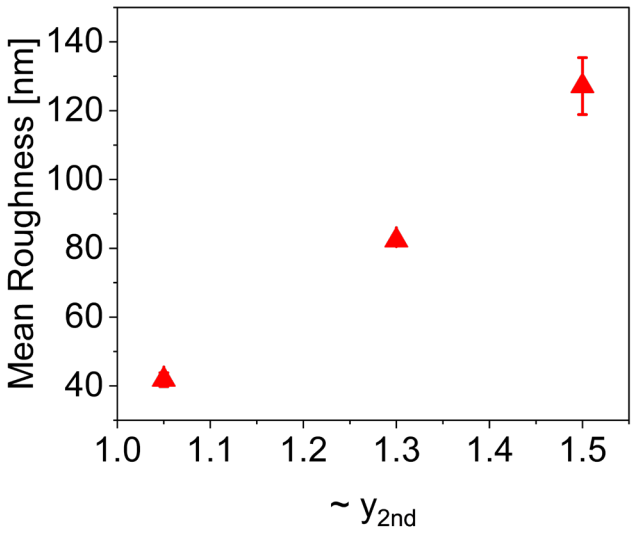

Fig 3. 6 Mean roughness measured for the samples with y_{2nd} of 1.05, 1.3 and 1.5.

Furthermore, for the purpose of Urbach tails and grain boundary studies, CIGSe absorbers with no alkali elements, with Na, and with both Na and Rb are prepared using the PVcomB deposition process.

As mentioned previously in **Section 2.5.2**, standard SLG substrates contain significant amount of Na that can diffuse into the CIGSe layer during the high temperature deposition process. Therefore, for samples that have Na, the growth was performed on Mo coated SLG substrates.

On the other hand, for samples with no Na, a SiN_xO_y barrier layer was deposited on the SLG to prevents the Na diffusion.

Additionally, for samples containing Rb, the Rb is supplied to the absorbers through a post-deposition treatment (PDT). In the case of RbF PDT, two different approaches were employed:

The first approach is the **in-situ RbF PDT**. In this method, directly after the growth process, the substrate set temperature was reduced to 280°C, and the Se pressure was decreased to one-sixth of the growth Se pressure. RbF was then evaporated for 10 minutes onto the substrates surface along with Se.

The second PDT method is **ex-situ PDT**. For the ex-situ PDT process, after the growth, the absorbers were removed of the deposition reactor and broken into two pieces. One piece served as a reference sample, while the other was placed back into the deposition reactor and underwent RbF PDT at the substrate set temperature of 480°C. The RbF rate, Se rate and duration of the ex-situ PDT is same as in-situ PDT process.

After the growth process, the samples were stored in a dark boxes and sealed in a vacuum bag to minimize the exposure to light and air before being transported to our laboratory.

3.2 From absorbers to solar cells

The CIGSe device structure has already been discussed in **section 2.5.2**.

To complete the CIGSe absorbers into the final devices, a CdS buffer layer with thickness of ~50 nm is deposited on the top of absorbers. Before CdS deposition, all the absorbers are cleaned either in a diluted ammonia solution or in a 5% KCN solution. This cleaning step is essential to etch away the surface oxides and excess RbF PDT remnants. The CdS deposition occurs through a chemical reaction at 67°C in an aqueous solution containing 2 mmol CdSO4, 50 mmol thiourea, and 1.5 mol ammonia, typically taking about 8 minutes.

After CdS deposition, the intrinsic zinc oxide (i:ZnO) and aluminum doped zinc oxide (Al:ZnO) layers are deposited on the top of the CIGSe/CdS stack using RF magnetron sputtering.

Finally, solar cell devices are completed by final deposition of Ni:Al metallic grids by e-beam evaporator.

All these processes were performed by **Dr. Michele Melchiorre** in our laboratory.

3.3 Photoluminescence and electroluminescence measurements

The theory behind the PL and EL emission has been already covered in **section 2.4**. In the following discussions, the PL and EL setup components and calibration processes are mainly introduced.

It is worth mentioning that both the EL and PL measurements in this thesis are employed to assess the $\Delta\mu$ and V_{OC} losses in CIGSe absorbers. In this section, the focus is solely on the introduction of the EL and PL experimental setups. The theory and equations has already been covered in **Section 2.4**. In **Chapter 4** and **Chapter 5,** the detailed quantification of $\Delta\mu$ and V_{OC} losses will be presented.

3.3.1 Photoluminescence (PL) measurements

For PL measurements in our laboratory, a home-built PL setups are used. In this thesis, the PL measurements were performed on both absorber materials and solar cells.

In our laboratory we have two PL setups, I refer them here as the PL setup-1 and PL setup-2, the schematic diagram of each PL setup is illustrated in **Fig 3. 7** and **Fig 3. 8**, respectively.

The PL setup-1 is equipped with a red laser that has a wavelength of 660 nm. The diameter of this laser beam is ~ 2.2 mm. This diameter has been measured by CCD camera.

The emitted PL signal from the sample is collected by two parabolic mirrors installed in off-axis configuration. The PL emission signal is directed from parabolic mirror-2 into the spectrometer through an optical fiber (See **Fig 3. 7**).

To block the possible laser light reflection into the spectrometer, a long pass filter on the path of the emitted PL signal is placed.

In PL setup-1, the spectrometer has grating density of 100 lines/mm and 300 lines/mm. For all measurements performed in setup-1, an optical fiber with diameter of 550 um and spectrometer grating of 100 lines/mm is used.

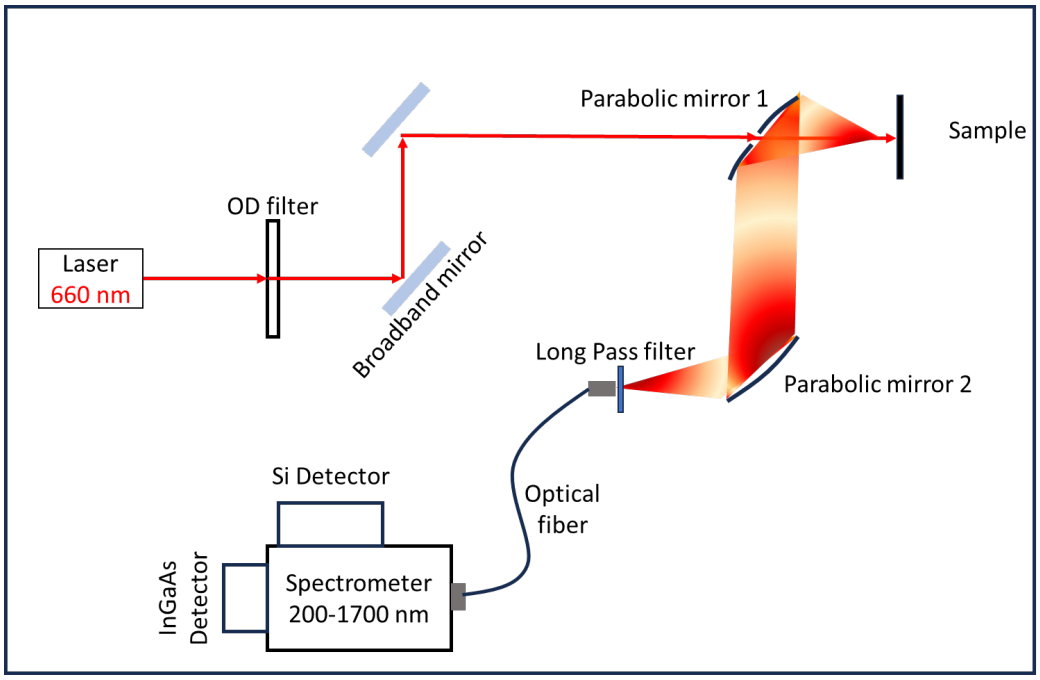

Fig 3. 7 PL setup-1 and its components. The laser light is passed through parabolic mirror 1 and reaches to sample. the emitted light is collected by two parabolic mirrors in off-axis position.

Additionally, we have also another PL setup which is equipped with 637 nm diode laser (PL setup-2). The PL setup-2 has dual configuration, it can operate similarly to setup-1 configuration, but also it can accommodate a beam expander in a slightly different configuration.

The **Fig 3. 8** illustrates **setup-2** with a beam expander. The beam expander increases the laser beam diameter to approximately 8 mm, enabling uniform illumination of a solar cells with area around 0.25 cm^2. This beam expander is essential for measuring samples with window layers, as it ensures that the entire cell area is illuminated. Without the beam expander, the cell is illuminated only partially, and a significant part of the cell would remain under dark. Since the window layer is conductive, this uneven illumination creates a potential difference between the illuminated and dark regions, leading to a current flow towards the dark areas. This effect can lower the measured $\Delta\mu$.

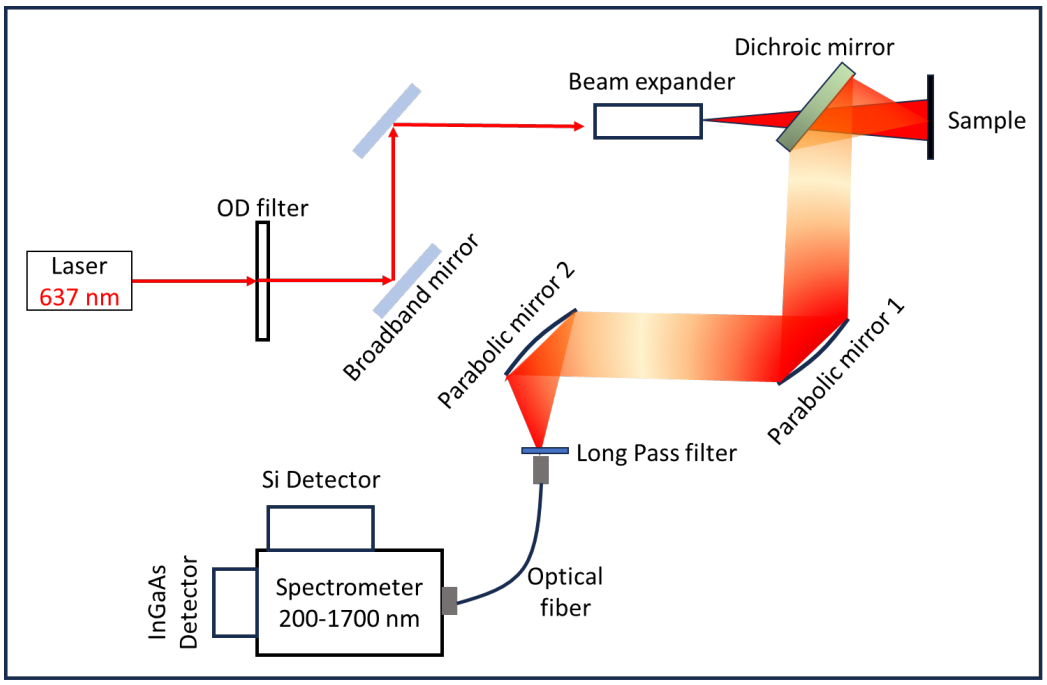

Fig 3. 8 PL setup-2 and its components. It is equipped with beam expander and dichroic mirror. The expanded laser beam is passed through dichroic mirror and reaches to sample. the PL signal is reflected through dichroic mirror and is collected with parabolic mirrors.

In the beam expander configuration, Setup-2 is equipped with a dichroic mirror placed between beam expander and sample. This mirror passes the laser light that reaches the sample while simultaneously reflecting the PL emission signal towards the parabolic mirrors.

The PL signal is subsequently directed through parabolic mirrors toward the spectrometer using a 550 µm fiber. For the measurements in the setup-2, a spectrometer grating with either100 lines/mm or 150 lines/mm is used.

Both PL setup1 and PL setup 2 are equipped with Si and InGaAs detectors. The InGaAs array detector (model DU490 A 1.7) is manufactured by Oxford Instruments and operates within a wavelength range of approximately 800 nm to 1700 nm, as specified by the manufacturer. The Si detector (model DU420A-BEX2-DD), also from Oxford Instruments, effectively covers a photon wavelength range of approximately 300 nm to 1000 nm. The CIGSe samples in this thesis have maximum PL emission around 1.1 eV. Therefore, for these samples, the InGaAs detector is primarily used, which is well-suited for recording the PL spectra in these energy ranges.

Before conducting the measurements, the alignment is performed for the optical setup. In this context, alignment means ensuring that the incident laser beam and the collection point of the PL signal are at the same position on the sample. To achieve this, first a CCD camera at the sample position is placed, and the location of the laser spot is recorded. Next, the optical fiber is disconnected from the spectrometer and connected to a halogen lamp, in this step the halogen lamp is coupled into the setup from the reverse optical path, which simply means that the halogen lamp emission travels from spectrometer side through parabolic mirrors and reaches to sample position. Subsequently, the lamp's spot position is recorded on the CCD camera. This spot position represents the PL signal collection point on the sample. The alignment process involves adjusting the mirrors and optical components to overlap the lamp spot with the laser spot. Subsequently, the PL setup needs to be calibrated for measurements.

The calibration process involves both spectral and intensity calibration. Spectral calibration is necessary to convert the raw detector data into a spectrum with appropriate units, while intensity calibration is performed to determine the number of incident photons and the number of photons emitted from the sample.

Let's start first with the spectral calibration.

The initial PL spectra recorded by the detector provides the raw number of counts, which have no meaningful physical units. To obtain a meaningful spectrum with an appropriate unit, spectral correction must be performed.

The spectral calibration is carried out using a known spectrum of a halogen lamp. In the first step of the spectral calibration, halogen lamp spectrum is measured in the detector, and then a calibration function (η_{cal}) can be determined using the following equation:

$$\eta_{cal} = \frac{\phi_{lamp}}{\phi_{lamp}^{measured}} \qquad (\boldsymbol{Eq\ 3.1})$$

The ϕ_{lamp} is the lamp spectrum provided by the halogen lamp manufacturer, and it has unit of ($cm^{-2}\ s^{-1}\ nm^{-1}$). $\phi_{lamp}^{measured}$ is the measured halogen lamp spectrum recorded in the detector, and it has unit of counts.

To extract the spectral photon flux density of a sample ($\varphi_{\mathrm{PL}}(\lambda)$), this calibration function η_{cal} is subsequently multiplied to directly measured raw PL counts of the sample ($\phi_{sample}^{measured}$):

$$\varphi_{\mathrm{PL}}(\lambda) = \eta_{cal}\phi_{sample}^{measured} \qquad (\boldsymbol{Eq\ 3.2})$$

Here, $\varphi_{\mathrm{PL}}(\lambda)$ has a unit of ($cm^{-2}\ s^{-1}\ nm^{-1}$). However, in all calculations, the unit of energy eV is preferred over the nm. Therefore, to convert nm to eV, it is essential to apply the transform Jacoby according to the following formula:

$$\varphi_{\mathrm{PL}}(E) = \varphi_{\mathrm{PL}}(\lambda)\ \frac{d\lambda}{dE} \qquad (\boldsymbol{Eq\ 3.3})$$

Up to this point, a meaningful PL spectrum with a unit of $cm^{-2}\ s^{-1}\ eV^{-1}$ is determined. However, the $\varphi_{\mathrm{PL}}(E)$ is not an absolute spectrum yet. To accurately quantify both the number of incident photons on the absorber and the number of photons emitted as the PL signal, intensity calibration must still be performed.

For the intensity calibration, the laser power is initially measured using a power meter. The incident flux of the laser (F_{inc}^{Laser}), with unit of $cm^{-2}eV^{-1}$, can be determined according to the following equation:

$$F_{inc}^{Laser} = \frac{2P_{laser}\ \lambda_{Laser}}{\pi w^2 hc} \qquad (\boldsymbol{Eq\ 3.4})$$

In this equation, λ_{Laser} denotes laser wavelength, and w is laser beam radius.

The laser beam follows a Gaussian intensity distribution, and F_{Laser}^{Inc} represents the laser flux at the peak of this distribution. Due to the Gaussian profile of the laser intensity, the factor of 2 is necessary in the Eq 3.4 for calculating the overall incident photon flux from the measured laser power.

To determine the intensity calibration factor, the measured laser flux in Eq 3.4 must be compared to the flux recorded by the detector. Therefore, in the next step, a spectralon (a perfect reflector) is placed at the sample position, and the laser spectrum is recorded in the detector. Here also the initial measurements from detector provides the laser spectrum in units of raw counts. To obtain photon flux density of laser ($\Phi_{\mathrm{Laser}}(E)$) with a meaningful unit of

$cm^{-2}s^{-1}eV^{-1}$, again the calibration factor η_{cal} needs to be applied to directly measured laser spectrum from detector (see Eq 3.2).

Furthermore, the integrated laser spectrum over the all photon energy ranges (i.e., $\int_0^\infty \Phi_{\text{Laser}}(E)dE$) should match the calculated laser flux F_{inc}^{Laser} from Eq 3.4. Therefore, by having the laser spectrum and directly measured F_{inc}^{Laser}, the intensity calibration factor δ can be determined through the following equation:

$$F_{inc}^{Laser} = \delta \int_0^\infty \Phi_{\text{Laser}}(E)dE \qquad (\boldsymbol{Eq\ 3.5})$$

This calibration factor can be subsequently multiplied to the measured PL spectrum $\varphi_{\text{PL}}(E)$ in Eq 3.3 to obtain the absolute PL spectrum $\Phi_{\text{PL}}(E)$:

$$\Phi_{\text{PL}}(E) = \delta\varphi_{\text{PL}}(E) \qquad (\boldsymbol{Eq\ 3.6})$$

This absolute spectrum is subsequently used to extract the $\Delta\mu$ of CIGSe samples.

To minimize uncertainty, δ is usually extracted for different laser fluxes, and for final measurement average of δ is used. Overall, the uncertainty in δ determination can result around 5 meV errors in final $\Delta\mu$ determination.

In this section, I also want to briefly discuss the analysis method and data treatment.

All PL data analysis is performed in the LPV-Viewer software, which is a home-made python-based program.

The InGaAs detector in PL setup-1 consists of two interconnected diodes, each with different sensitivity. To improve measurement accuracy, in certain cases, data point from only one of the diodes are used, excluding the contribution of the second diode from the PL spectra. **Fig 3. 9** presents the original PL spectra of a CIGSe sample alongside the spectra that includes data points from only a single diode. It can be observed that in regions where the PL signal decreases (i.e., at the high-energy and low-energy wings), the difference in sensitivity between the two diodes introduces noise artifacts, which can be effectively removed by considering only the data points from a single diode.

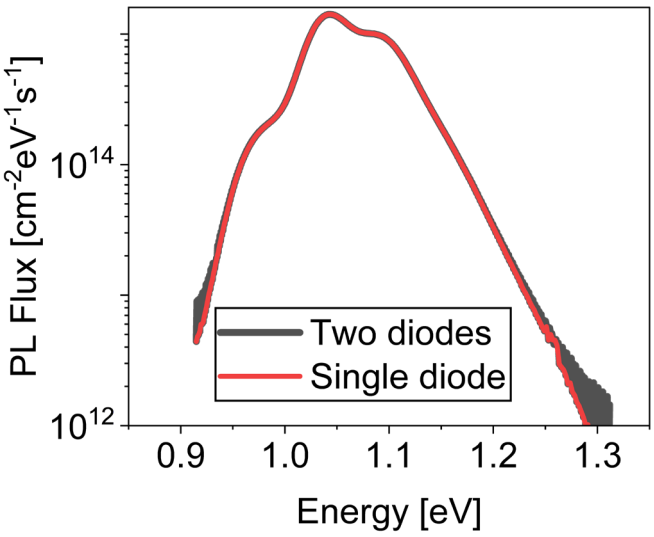

Fig 3. 9 The PL spectra of sample A2 with single and double diode of InGaAs detector points (This sample will be investigated in Chapter 6)

3.3.2 Electroluminescence measurements

At a certain stage of my work, it became necessary to develop an electroluminescence (EL) setup.

Using the configuration similar to PL Setup-1, I installed a prism mirror to mount the solar cells horizontally. By applying a forward bias through a 4-probe contact configuration with Keithley 2400 source meter, I could successfully detect the EL signal emitted from the CIGSe solar cells.

The similarity of EL and PL measurements were already discussed in **Section 2.4**. The key difference between PL and EL is the excitation source: instead of using an external laser source to excite the sample, a forward bias is applied across the solar cell junctions. In this thesis, the CIGSe solar cells are investigated using absolute EL measurements, meaning that the EL photon flux emitted from the solar cells is quantified.

To achieve absolute measurements, spectral and intensity calibrations are first performed in the PL configuration, as described in **Section 3.3.1**.

The intensity calibration factor determined in Eq 2.35 can also be employed for EL measurements to determine the absolute EL photon flux density emitted out of the solar cells.

Furthermore, since the injected current density is known, and it is being recorded using source meter, the number of injected charge carriers can also be quantified.

Further details regarding the determination of internal voltage V_{in} through EL measurements are provided in **Chapter 4** and **Chapter 5** of this thesis.

3.4 Current Voltage measurements

Current-voltage (J-V) measurement is a standard tool used to assess the performance a solar cell. With these measurements the important photovoltaic parameters of solar cells including V_{OC}, J_{SC}, FF and PCE can be quantified.

In this thesis, the J-V measurements are conducted in a class AAA solar simulator equipped with a Xenon short-arc lamp, providing a simulated AM 1.5 sun emission. The solar cell is mounted on a metallic stage with temperature controller, the temperature of the cells is maintained at 25°C during the measurements.

4-probe contact configuration for the J-V measurements are used for applying bias voltage, and the resistivity of the contacts is measured before each scan and kept within the range of 1-2 ohms. The contact probes are connected to the Keithley 2400 source meter. With this source meter a sweep voltage is applied in the range of -0.5 V to 0.8 V, then at each voltage point the current is recorded. The J-V measurements for all solar cells are recorded both under dark and illuminated conditions.

Prior to the measurements, a reference Si solar cell is measured. This reference cell, which has certified J-V characteristics under AM 1.5 g illumination, is measured to ensure that key parameters, including J_{SC}, V_{OC} and FF are same as the certified values.

In our laboratory, the CIGSe solar cells with the areas of approximately 0.5 cm² or 0.25 cm² are fabricated. The absorbers are grown on square substrates with inch × inch size, allowing to make 8 or 16 solar cells using the 0.5 cm² or 0.25 cm² area configurations, respectively. Most of the cells investigated in this thesis have an area of around ~ 0.25 cm². Before performing J-V measurements, the area of each cell is determined using an optical microscope. The area measurement has errors of about 0.01 cm². This error can impact the accuracy of the short-circuit current density (J_{SC}) determination. To mitigate this effect, the current density obtained

from J-V measurements is usually cross -checked with the current density calculated from integrating the $QE(E)$ spectrum of the solar cell over the AM1.5 spectrum (see Eq 2.35).

Fig 3. 10 a and **b** show the solar cells fabricated with area configurations of 0.5 cm² and 0.25 cm², respectively. **Fig 3. 10 c** illustrates the sample mounted in the J-V setup, along with the 4-probe contact configuration.

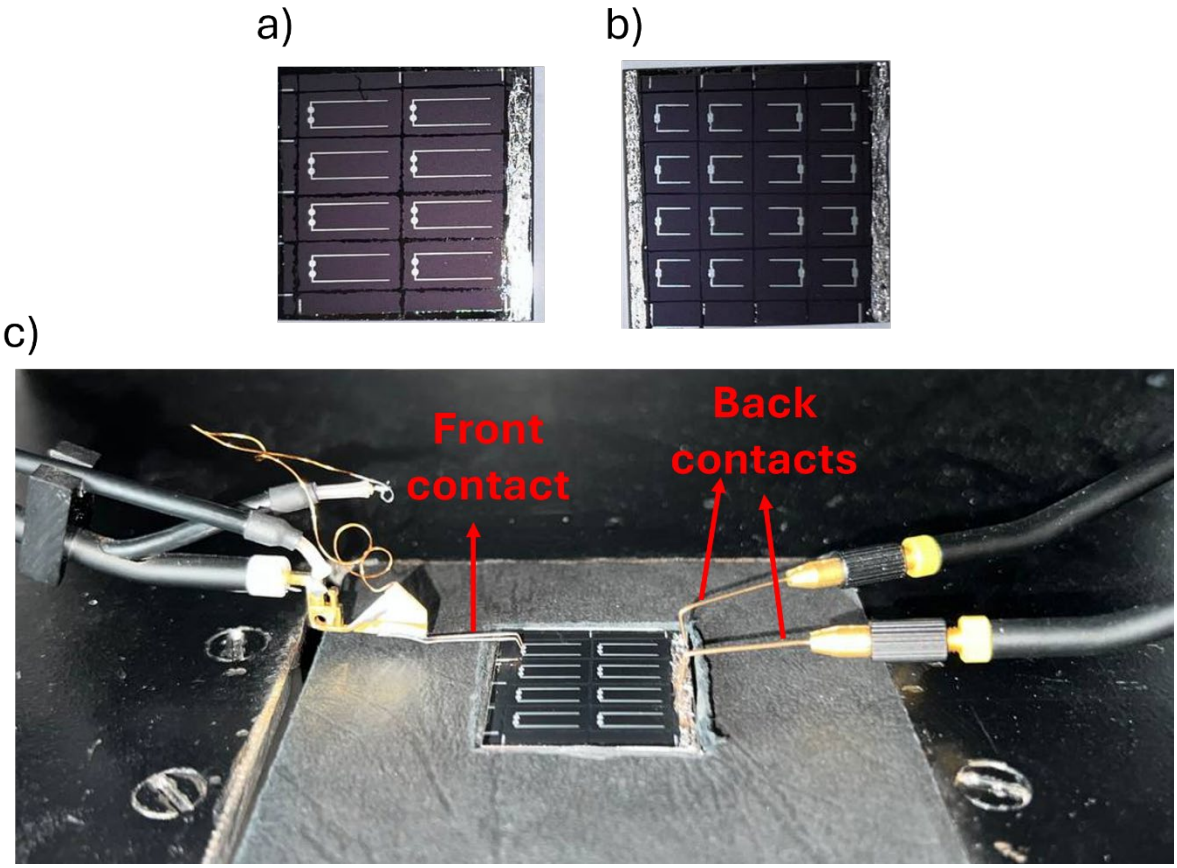

Fig 3. 10 the CIGSe solar cells **a)** with 0.5 cm2 area and **b)** with 0.25 area. **c)** CIGSe solar cell under solar simulator. The contacts on back contact and front contact are indicated in this figure.

3.5 Capacitance-Voltage measurements

The capacitance-Voltage (C-V) measurements were performed to extract the p-type doping concentration of the CIGSe solar cells. The details of C-V measurements are explained in the reference [147].

In the previous chapter, the formation of the p-n junction and the SCR was explained in **Section 2.2**. The segregation of positive and negative charges in the SCR creates a capacitance within the junction.

The doping concentration of absorbers can be determined by measuring the capacitance of the p-n junction under different applied voltages. In this section, the equations related to C-V measurements are summarized.

For CIGSe solar cells a Schottky contact model with n^+- p configuration can be considered. For the depletion width of a Schottky contact the Eq 2.32 can be transformed into the following form:

$$W = \sqrt{\frac{2\varepsilon\varepsilon_0(V_{bi} - V_{DC})}{qN_A}} \qquad (\boldsymbol{Eq\ 3.6})$$

Where the ε is the dielectric constant of the sample (here 13.6 according to [3]), V_{DC} is applied DC voltage, q is elementary charge and N_A is doping concentration of p-type CIGSe sample (Acceptor density).

For the CV measurements, a DC voltage in the range of -0.5 V to 0.5 V is applied along with a small, controlled AC voltage with amplitude of 0.03 V and with frequency of ~ 630 kHz. The capacitance of the solar cells is measured using Agilent inductance-capacitance-resistance (LCR) meter. All measurements were conducted at low temperature (Below 170 K) to prevent the possible deep defects contribution to the capacitance.

For the measured capacitance, the following equation can be written :

$$\frac{1}{C^2} = \frac{2(V_{bi} - V_{DC})}{q\varepsilon\varepsilon_0 A^2 N_A} \qquad (\boldsymbol{Eq\ 3.7})$$

Here, A is the device area.

Subsequently, the N_A can be extracted by using the following equation:

$$N_A = N_{CV} = -\frac{2}{q\varepsilon\varepsilon_0 A^2}\left[\frac{d(C^{-2})}{dV_{DC}}\right] = -\frac{C^3}{q\varepsilon\varepsilon_0 A^2}\left(\frac{dC}{dV_{DC}}\right)^{-1} \qquad (\boldsymbol{Eq\ 3.8})$$

Prior to the measurements, the samples were stayed in a dark condition for 24 hours to avoid possible contribution of metastable defects in extracted doping values.

All the CV measurements and analysis were performed with the assistance of **Dr. Mohit Sood**.

3.6 Transmittance reflectance measurements

Transmittance and reflectance measurements are performed using Perkin Lambda 950 UV-Vis-NIR spectrometer, equipped with tungsten and deuterium lamps, that covers a wavelength range of 175 nm to 3300 nm.

It is important to highlight that transmittance measurements are performed exclusively on absorbers deposited on transparent SLG substrates (see **Section 3.1.1**).

This measurements involves directing monochromatic light onto the sample and collecting the transmitted or reflected light with an integrating sphere at each photon wavelength. A photomultiplier detector is used to detect the transmitted/reflected light in the UV-Vis range, while a PbS detector is used for the NIR range. According to the manufacturer, the resolution of the measurements in the UV-Vis range is 0.05 nm, and in the NIR range is 0.2 nm [148].

Before measurements, an autozero process is performed to establish a baseline and correction for any background noise. For transmittance measurements, autozeroing is done by placing the bare SLG substrate, without the absorber layer, in the substrate holder position. After this, the transmittance spectrum is measured with the absorber/SLG configuration.

For reflectance measurements, autozeroing is performed using a perfect reflector (Spectralon) placed in the sample position.

In transmittance measurements, light passes through both the absorber and the substrate before reaching the integrating sphere and detector. It is observed that the SLG substrate influences the transmitted light spectrum. Therefore, for calibration and the autozero process in transmittance measurements, the autozero is performed with SLG substrate to remove the possible influence of SLG on the final transmittance spectra.

In contrast, in the reflectance measurements, the incident light directly interacts with the absorber and is then reflected into the integrating sphere. In this case, the effect of the substrate

is negligible. Although the possible contribution of CIGSe/SLG interface cannot be ruled out. Consequently, a perfect reflector (Spectralon) is used for the autozero process as a reference, and the reflectance measurements are calibrated using this perfect reflector.

At the end of the analysis, the so called "open beam" measurements are always conducted for both reflectance and transmittance. This step involves measuring transmittance and reflectance without placing a sample in the holder position. This step ensures that the extracted data is free from unwanted background noise. If any background is detected, the measured transmittance or reflectance spectrum is correct by subtracting the background. In the most cases, the impact of this background is negligible.

In **Fig 3. 11** we show a UV-Vis measurements on a CIGSe sample deposited on glass SLG, where the transmittance $T(E)$ and reflectance $R(E)$ spectra are measured separately and absorptance spectra is extracted by using $A(E) = 1 - T(E) - R(E)$.

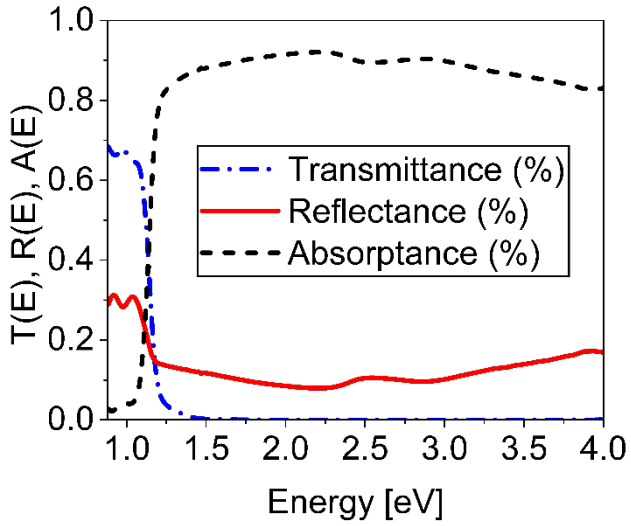

Fig 3. 11 UV-Vis measurements showing Transmittance (T), Reflectance (R), and Absorptance (A) spectra for CIGSe B-NG sample (This sample will be discussed in **Chapter 5**). Adapted from my preprint [149]

3.7 External quantum efficiency (QE) measurements

External quantum efficiency $QE(E)$ measurements are employed for quantification of the J_{SC} losses across different photon energy ranges. Additionally, by analyzing the $QE(E)$ spectrum and applying Rau's reciprocity principle (Eq 2.53)[28, 69], the maximum attainable open-

circuit voltage (V_{OC}), known as the radiative limit (V_{OC}^{rad}), can be determined [28]. In this section, only the $QE(E)$ measurement method is discussed. Detailed discussions on V_{OC}^{rad}, V_{OC} losses, and broadening of the $QE(E)$ spectrum will be covered in **Chapter 4** and **Chapter 5** .

Here, I just summarize the key points. Further information regarding the $QE(E)$ analysis can be found in reference [147, 150].

The $QE(E)$ measurement gives the number of collected charge carriers per incident photons (see Eq 2.36). In our laboratory, we measure $QE(E)$ spectra using a home-built setup. In this setup, first the incident light is passed through a chopper and reaches to a grating monochromator. Then the monochromatic light beam is directed through optical components and prism mirrors on the sample. The equipment uses two lamp sources, the Xenon lamp and Tungsten lamp. With the combination of these two lamps, we can effectively cover the measurements in the photon spectral range of 300 nm to 1600 nm.

In these measurements, the incident photons first generate a current density in the absorbers. This current is then transformed to a voltage using a current-to-voltage converter. The resulting voltage is subsequently amplified using a lock-in amplifier. Finally, the amplified signal is transformed back into a current and converted into the $QE(E)$ output at the final stage.

The calibration of the $QE(E)$ setup is performed using Silicon (Si) and InGaAs reference diodes. The Si diode covers the photon wavelengths in the range of 300-1100 nm and InGaAs diode is used for the wavelength ranges of 1100-1600 nm.

This Si and InGaAs references have a known $QE(E)$ spectrum provided by Physikalisch Technische Bundesanstal (PTB)[2]. In the first step of calibration process, the measured $QE(E)$ spectra of diodes in our setup is compared to the ones provided by PTB using the following formula:

$$QE_{ref} = QE_{PTB}\,\frac{dI_{SC,ref}(E)}{dI_{SC,PTB}(E)} \qquad (\boldsymbol{Eq\ 3.9})$$

[2] Is national metrology institute of Federal Republic of Germany

The $I_{SC,ref}$ is the short circuit current of the reference diodes measured in our setup, and $I_{SC,PTB}$ is the short circuit current of the reference diodes provided by PTB.

In the next step, the short-circuit current of our CIGSe solar cells ($I_{SC,sample}$) is measured at each wavelength. Subsequently, the $QE(E)$ spectra of the solar cell is extracted using the following equation:

$$QE_{Sample} = QE_{ref} \frac{dI_{SC,sample}(E)}{dI_{SC,ref}(E)} \qquad (\boldsymbol{Eq\ 3.10})$$

Fig 3. 12 illustrates a typical $QE(E)$ spectrum of a CIGSe solar cell. For this cell, an additional reflectance measurements were also performed using the UV-Vis spectrometer. In the high energy ranges, where the transmittance is negligible, the $A(E)$ can be approximated by $A(E) \approx 1 - R(E)$. Thus, by comparing the $1 - R(E)$ and $QE(E)$ spectra, possible collection losses can be identified.

In **Chapter 4** and **Chapter 5** more details regarding the $QE(E)$ spectrum analysis will be provided.

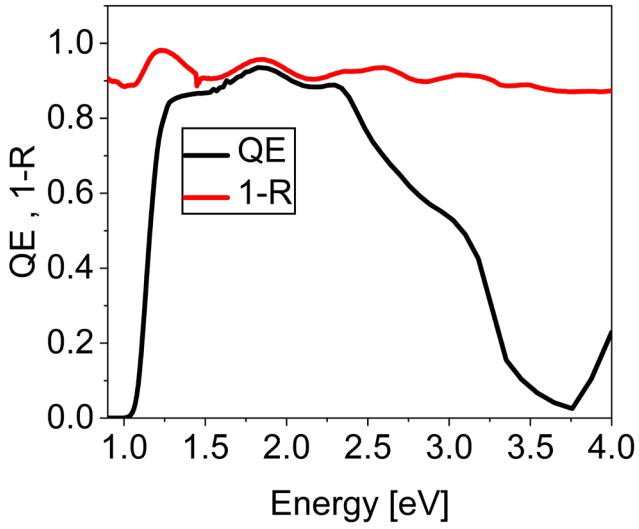

Fig 3. 12 $QE, 1 - R(E)$ for a CIGSe sample. (This sample is F-BGG sample, will be discussed in **Chapter 5**)

3.8 Grain boundary (GB) characterization

The Atomic force microscopy (AFM) and Kelvin probe force microscopy (KPFM) measurements were all performed to study grain boundary (GB) properties of CIGSe samples in **Chapter 6**.

All the AFM/KPFM measurements were performed by **Muhammad Uzair Farooq** from Scanning Probe Microscopy (SPM) laboratory under supervision of **Prof. Dr. Alex Redinger**. Following details about the KPFM measurements are provided by Uzair. More details about the KPFM equipment can be found in my published paper [132] and references [133, 134]. Here, only the GB analysis is summarized.

Prior to the AFM/ KPFM measurements, all the CIGSe samples went through an Ammonia washing step for 30 seconds using 1 Molar diluted Ammonia solution. This step is necessary, since it etches off the RbF PDT remnants, and also it can remove possible surface oxides from the surface [151].

After ammonia cleaning, the absorbers were rinsed with deionized (DI) water. While still with water on the top, they were transferred to a nitrogen-filled environment, where they remained until the water had completely evaporated. Subsequently, the dried samples were sealed in nitrogen-filled boxes and transported to the AFM/KPFM setup, where all AFM and KPFM measurements were conducted under nitrogen environment. These steps were carefully followed to minimize air exposure and surface oxidation, which could potentially influence the KPFM analysis.

The AFM measurements provide the topography map, while KPFM measurements generate the contact potential difference (CPD) map. This CPD map can be calibrated and converted to the work function map using a reference calibration sample with a known work function. In this thesis, all KPFM measurements were calibrated using a highly oriented pyrolytic graphite (HOPG) which has a work function of 4.6 eV.

In KPFM measurements, changes in the work function are detected, and the band bendings are quantified from the local variations in work function at the GBs positions [133, 134].

It is important to highlight that KPFM analysis on polycrystalline absorbers are highly sensitive to the operational mode of analysis. Two main modes are commonly used in KPFM measurements: Amplitude Modulation (AM) and Frequency Modulation (FM) [133].

AM-KPFM is sensitive to the electrostatic force between the tip and the absorber surface[133, 134]. This mode is more susceptible to the geometrical artifacts and surface roughness, which can induce artifacts and inaccuracies in the measured work function and potentially lead to misinterpretation of the extracted results [133, 134].

In contrast, FM-KPFM is more sensitive to the gradient of the electrostatic force, making it less affected by surface geometry and topographical features [133, 134]. As a result, FM-KPFM provides more reliable results for work function measurements.

Notably, most published studies analyzing grain boundaries (GBs) in CIGSe samples rely on the AM-KPFM measurements [65, 123, 127, 152-154]. In contrast, in this thesis FM-KPFM measurements were employed to minimize the impact of geometrical artifacts and improve the extracted band bending accuracies.

In **Fig 3. 13** , as an example, a band bending analysis of a selected GB is illustrated. In **Fig 3. 13 a** the topographic AFM map for this grain boundary is presented, and the corresponding simultaneously acquired work function map is provided in **Fig 3. 13 b**.

For band bending analysis, the GB region is first identified using the topography image (**Fig 3. 13 a**), where a straight line is drawn across the selected GB. This line is then transferred to the simultaneously measured work function map (i.e., KPFM map). By monitoring the changes in the work function along this line, the band bending (i.e., ΔCPD) can be extracted.

In **Fig 3. 13 c**, the line profile across this selected GB is presented. The height profile here is indicated in blue. At the GB position, the height profile exhibits a valley-like shape, which corresponds to the location of the GB. Furthermore, the change in the CPD is also shown in this figure with red curve.

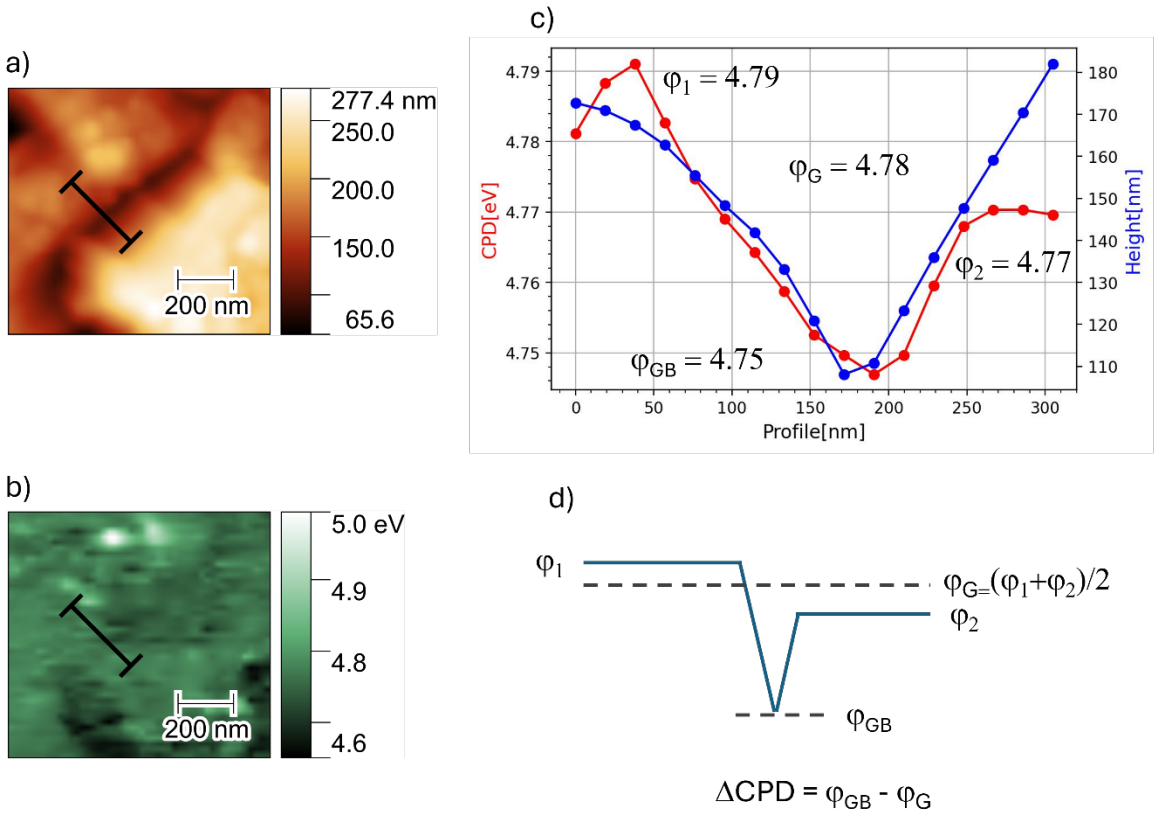

Fig 3. 13 Band bending extraction for a selected GB from A1 sample. This sample will be investigated in **Chapter 6**. **a)** Topography map with a selected line across the GB. **b)** The work function map measured simultaneously from the same region. **c)** corresponding line profile showing change in the height and work function for the selected GB. **d)** Schematic diagram showing the downward band bending extraction method. (This figure is slightly modified version of Fig. S9 from my published work [132] taken under **CC BY 4 license**)

It can be observed that the CPD (or work function) initially decreases at the GB position and then increases, forming a valley-shaped pattern. This behavior indicates that the grain boundary exhibits a negative potential barrier (i.e., downward band bending).

To quantify the band bending, the measured work function at the GB position is compared to the work function values of the neighboring grain facets.

In **Fig 3. 13 d**, a schematic illustration of downward band bending is shown. Here, φ_1 and φ_2 correspond to the work functions of facets 1 and 2, respectively. The average facet work function can be calculated using $\varphi_G = \frac{\varphi_1+\varphi_2}{2}$. The work function at the GB position (i.e., at

the minimum point of the height profile) is denoted as φ_{GB}. The contact potential difference (ΔCPD) of GB, which represent the band bending, is simply the difference between the average facet work function φ_G and the φ_{GB} (i.e, $\Delta CPD = \varphi_{GB} - \varphi_G$).

All the parameters, including φ_1 , φ_2 , φ_G and φ_{GB} for the selected GB are presented in **Fig 3. 13 c**. For this GB, the band bending is approximately -30 meV. The negative sign indicates downward band bending. Similar calculations can be performed for upward band bending (positive values), where the change in work function shows peaks instead of valleys. In Chapter 6, an example of upward band bending will be discussed (see **Fig 6. 11**).

For work function changes that do not exhibit clear trends like valleys or peaks at the GB position, and where the change from grain to grain can be attributed to different work functions of the facets, we assume no band bending (i.e., neutral GBs with 0 meV band bending).

In **Chapter 6**, more GBs from absorbers with different alkali ions will be presented.

3.9 Scanning electron microscope (SEM), Energy dispersive X-ray (EDX) and Cathodoluminescence (CL) measurements

The SEM images were captured using the FESEM Hitachi SU-70 system with an acceleration voltage of 7 kV. These measurements were conducted by **Dr. Michele Melchiorre**.

The elemental composition of the samples were analyzed using a SEM Zeiss EVO10 system (LaB6 detector) and an Oxford Instruments UltimMax40 SDD EDX detector. The measurements were performed at an acceleration voltage of 20 kV. Standardization for each element was conducted using pure elemental standards at the same acceleration voltage.

3.10 Cathodoluminescence measurements

In addition to SEM measurements performed in our laboratory, a dedicated CL-SEM setup was used to record the cathodoluminescence (CL) emission of some selected CIGSe samples. This CL results will be discussed mainly in **Chapter 5**. All CL measurements were performed by our colleagues at the **Centre for Gallium Nitride** at the **University of Cambridge**.

The following details for CL measurements are provided by **Yucheng Hu** from University of Cambridge.

The CL-SEM setup uses an iDus InGaAs 1.7 detector. For exciting samples, an electron beam with an acceleration voltage of 5 kV, a probe current of 10 nA, and a aperture of 100 μm were used. All measurements were carried out at the room temperature, and each measurement was performed with exposure time of 250 ms.

The CL measurements were conducted on both the planar surface and cross-section of the samples.

Data processing and analysis also were performed by our colleagues from Cambridge university, using the open-source Python packages HyperSpy [155] and LumiSpy [156].

3.11 Time resolved photoluminescence measurements (TRPL)

Time-resolved photoluminescence (TRPL) measurements are a useful technique for evaluating the quality of absorber materials. The carrier lifetime extracted from these measurements provides insights into the non-radiative recombination rate within the absorbers. In general, a longer extracted lifetime indicates higher material quality and lower non radiative recombination rate, which often corresponds to an increased $\Delta\mu$ and V_{OC}. In this section, I will describe the details of TRPL measurements and the data processing methods.

The TRPL measurements were all conducted using a pulsed laser excitation source with a wavelength of 640 nm (~1.94 eV). In our setup, the pulse repetition frequency can be adjusted within a 0.02 Mhz to 2 Mhz. This frequency is adjusted based on the lifetime of the samples. For recording the decay profile of the luminescence, a time-correlated single-photon counting (TCSPC) system is used in the TRPL setup.

The number of incident photons per pulse is determined using the following equation:

$$\frac{\#photons}{pulse} = \frac{P_{Av}}{E_{ph}.f_{rep}} \qquad (\boldsymbol{Eq\ 3.11})$$

Here, P_{Av} represents the average laser power, E_{ph} denotes the photon energy of the laser, and f_{rep} is the pulse repetition frequency.

The excess minority carrier concentration (δn) at initial time (t = 0 s) can be estimated using the following equation:

$$\delta n = \frac{P_{Av}.\alpha}{E_{ph}.f_{rep}.A} \qquad (\boldsymbol{Eq\ 3.12})$$

Where the α is the absorption coefficient of the absorber at laser energy. For CIGSe absorbers $\alpha \approx 5 \times 10^4 \text{cm}^{-1}$ is considered according to ref [3]. The α in this equation is included because, unlike the steady state PL measurements the photogenerated charge carriers are not in steady state anymore. Therefore, homogeneous charge carrier distribution cannot be assumed over the material thickness. In this case, a represents the effective depth at which charge carriers are generated.

The injection level used for TRPL measurements in this thesis is approximately 1×10^{16} cm^{-3}, this injection level is slightly higher than the doping concentration of CIGSe samples determined from C-V analysis (See **Fig 6. 9** in **Chapter 6**).

The carrier lifetime in the material is influenced by different recombination mechanism. The effective carrier lifetime (τ_{eff}) in the material can be expressed by the following equation [42, 47, 157]:

$$\frac{1}{\tau_{eff}} = \frac{1}{\tau_{rad}} + \frac{1}{\tau_{SRH}} + \frac{1}{\tau_{Auger}} \qquad (\boldsymbol{Eq\ 3.14})$$

τ_{rad} is the radiative lifetime, τ_{SRH} is same SRH lifetime explained in **section 2.1.3**. For a p-type. τ_{Auger} is the Auger lifetime. It is evident that the effective lifetime (τ_{eff}) is limited by the mechanism with the shortest lifetime value.

The Auger lifetime depends on the charge carrier concentration, and for CIGSe absorbers it is reported to have values within the range of a few microseconds [47], while for the radiative lifetime τ_{rad} values around 1μs to 3 μs has been reported [41, 42]. In most of the cases, CIGSe absorbers suffer from a high non-radiative recombination rate (i.e, high SRH recombination rate). Therefore, Eq 3.14 is dominated by the non-radiative lifetime. However, in high-quality CIGSe absorbers, with low SRH recombination activities, the effective lifetime is determined by both radiative and non-radiative lifetimes.

In an ideal scenario, the excess generated charge carriers would exhibit a single-exponential decay, with the decay constant corresponding to the τ_{eff} [158]. However, in reality, TRPL measurements show more complicated decay profile, often deviating from single exponential decay model.

In **Fig 3. 14** the TRPL decay of an investigated CIGSe sample from **Chapter 6** is illustrated. It can be observed that the TRPL decay shows initially a fast decay component, followed by a longer decay. In all investigated samples in **Chapter 6,** a similar decay profile can be observed.

For analyzing this TRPL curve, initially the background is subtracted, and then the decay profile is fitted using biexponential decay model:

$$\Phi_{PL}(t) = A_1 \exp\left(-\frac{t}{\tau_1}\right) + A_2 \exp\left(-\frac{t}{\tau_2}\right) \qquad (\boldsymbol{Eq\ 3.13})$$

Here, the $\Phi_{PL}(t)$ is TRPL decay flux and A_1 and A_2 are perfactors for each exponential component. The τ_1 is short decay lifetime and τ_2 is longer decaying lifetime.

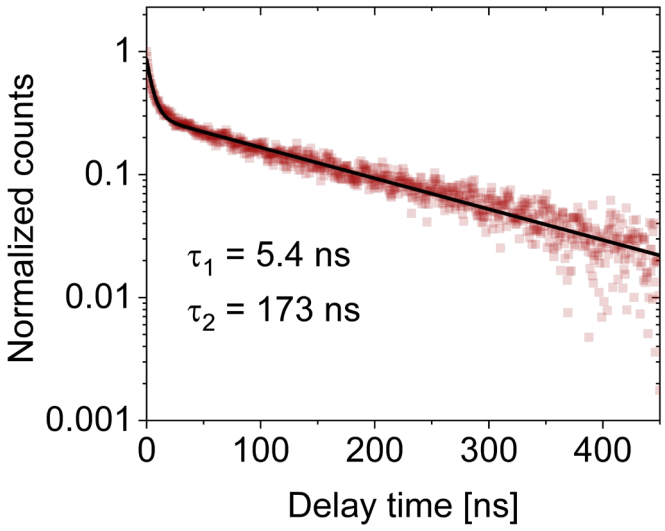

Fig 3. 14 The TRPL decay (red color) along with the biexponential fit (black line) for CIGSe B2 sample. This B2 sample will be discussed in **Chapter 6**. This figure is modified version of Fig S.5 from my published work taken under **CC BY 4** license [132].

An example of biexponential decay fit is also presented in **Fig 3. 14**. The τ_1 and τ_2 are affected by multiple factors, such as injection level [158], surface/interface recombination activities [106, 158], degradation [159], and trapping or detrapping effects [160]. Therefore, analyzing

the exact mechanism behind the TRPL decay is often challenging. A detailed investigation of the carrier lifetime is beyond the scope of this thesis, and more comprehensive studies about the CIGSe lifetime measurements can be found in the referenced literature [106, 158-161].

In this thesis, the TRPL measurements are primarily used as a qualitative analysis tool to assess the impact of alkali incorporation on device and absorber performance. To enable a meaningful comparison of samples with different alkalis, these measurements were conducted under similar excitation conditions for all investigated samples.

For analyzing the TRPL curve, I used a method proposed in earlier studies [157, 158, 162], where the longer decay time of the biexponential curve (here τ_2) is used to compare different samples.

In bi-exponential fit, the fast decay component (τ_1) has been attributed to various factors, including high injection conditions [158] and possible contribution of charge separation effects due to the presence of a buffer layer [161, 163].

As mentioned earlier, the injection level in our TRPL measurements is slightly higher than carrier concentration of absorbers. Therefore, the initial fast decay in the investigated samples might primarily result from the high-injection condition at the beginning of the measurement. At later delay times, the concentration of excess charge carriers decreases, and the decay falls into the low-injection condition, where monoexponential decay dominates the TRPL decay profile.

Further details on the differential equations governing TRPL decay profiles have been discussed in the published reports [158], and are not the primary focus of this thesis. Here, just a simplified approach is used to compare the CIGSe samples with different alkalis.

3.12 Secondary ion mass spectrometry (SIMS) measurements

To investigate the elemental distribution profile throughout the depth of the CIGSe films, Secondary Ion Mass Spectrometry (SIMS) measurements were conducted by Dr Natalia Valle at the at Luxembourg Institute of Science and Technology. The following details of the measurements are provided by **Dr. Nathalie Valle**.

The SIMS analysis were performed using the CAMECA SC-Ultra setup. A focused Cs^+ ion beam with an energy of 1 keV was utilized to sputter the samples' surface. The sputtered region had an area of 250 µm × 250 µm. However, the detected elements (here Cu, In, Ga, Se) are only from the central region, with a diameter of 60 µm.

The SIMS measurements for selected CIGSe samples are discussed in **Chapter 5**. It is important to note that the presented SIMS measurements are not absolute and cannot be used to quantify the concentration of elements throughout the material's depth. The SIMS measurements in this thesis are primarily employed to study the Ga distribution profile of the CIGSe absorbers.

4 Theoretical analysis of V_{OC} losses for a photovoltaic absorber material

As mentioned earlier in **Section 2.2.2**, the maximum V_{OC} for an ideal solar cell is given by the Shockley-Queisser (SQ) limit (i.e., detailed balance model). For an idealized photovoltaic device, the $A(E)$ or $QE(E)$ is defined by Heavyside step function, where only incident photons with energies higher the band gap are fully absorbed, while those with energies below the band gap energy are not absorbed at all. The step like shape of $QE(E)$ also means complete charge extraction from the device, without any collection losses. However, in reality, absorber materials do not exhibit a perfectly sharp transition at the absorption edge. The softening of the absorption edge and sub band gap absorptions would lead to radiative V_{OC} losses relative to the SQ limit. Additionally, incomplete absorption and potential charge collection losses cause further decrease in the maximum attainable V_{OC}, even in the ideal absorbers with no nonradiative recombination activities. Therefore, the maximum efficiency and V_{OC} limit of real solar cells can no longer be quantified using the SQ formalism.

To quantify the maximum V_{OC} limit of a solar cell with non-step like $A(E)/QE(E)$ spectra, the detailed balance model needs to be generalized in a way that incorporates also the actual shape of the $A(E)/QE(E)$ spectra in the calculations. Here, in this chapter, the primarily focus is on the *generalized detailed balance model* , which enables the determination of the maximum V_{OC} limit and V_{OC} losses of real photovoltaic devices with non-step-like $A(E)/QE(E)$ spectra [28, 32].

This chapter is divided into two main sections. In **Section 4.1**, the theoretical calculations that generalize the detailed balance model for a non-step-like $A(E)/QE(E)$ spectra are discussed. This generalization is performed through two different approaches: (i) The **optoelectrical approach**, which has been widely used in the previous published studies [28, 31, 32, 69, 164], and relies on the optoelectronic reciprocity principle (Eq 2.54). This approach needs detailed knowledge of the $QE(E)$ spectrum, and it enables to determine the maximum attainable (V_{OC}) limit, denoted as the radiative V_{OC} limit (V_{OC}^{rad}). (ii) The purely **optical approach**, based on Planck's generalized law of radiation (Eq 2.52). Through this method, the maximum achievable $\Delta\mu$, known as the radiative $\Delta\mu$ limit ($\Delta\mu^{rad}$), can be obtained using the $A(E)$

spectrum. The advantage of this method is that the $\Delta\mu$ analysis can be performed directly on the absorber material without requiring a complete solar cell devices. Unlike the optoelectrical approach, the optical model has not been widely covered in the literature.

In **Section 4.1**, the theory and formulas of generalized detailed balance model are mainly introduced. In **Chapter 5,** these models are applied to experimentally measured $A(E)$ and $QE(E)$ spectra to quantify $\Delta\mu$ and V_{OC} losses for CIGSe samples from our laboratory.

Additionally, the second part of this chapter (**Section 4.2**) contains simulations, where the influence of the band gap inhomogeneities and tail states on the $A(E)$ shape and the radiative $\Delta\mu$ limit will be discussed. Notably, in these simulations, I will discuss that both band gap inhomogeneities and sub-band gap tail states contribute to the softening of the absorption edge. However, their effects are distinct: The influence of tail states is primarily in the energy ranges significantly below the band gap, and their contribution to the $A(E)$ broadening and radiative losses is smaller than that of band gap fluctuations. Furthermore, this chapter will also cover the effect of absorption thickness (i.e., thickness of material) on the $A(E)$ broadening.

It is important to note that a manuscript has been prepared based on the results of this chapter. At the time of writing, the manuscript is under peer review, and the preprint is available online [149]. All upcoming results are reproduced from this preprint under **CC BY 4** license.

4.1 Generalized detailed balance model

The detailed balance principle states that, under thermal equilibrium, every microscopic process per unit of time is counterbalanced by its corresponding reverse process [165]. In **Section 2.2.2**, I have already discussed the Shockley-Queisser model [26], which enables to determine the maximum achievable efficiency for a single junction solar cell with an ideal, step-function-like $A(E)$ or $QE(E)$ spectrum. Shockley and Queisser, in their paper, referred to this maximum efficiency limit as the *detailed balance limit* [26].

The primary limitation on the solar cell efficiency arises from this detailed balance principle. According to this principle, in thermal equilibrium, the photon flux density emitted by the semiconductor due to charge carrier recombination must be equal to the rate at which charge carriers are generated [26].

The Shockley-Queisser (SQ) model assumes that all photogenerated charge carriers recombine at the same rate as they are generated, and this recombination is occurring exclusively through radiative spontaneous emission. This model also considers that non-radiative recombination pathways, such as Shockley-Read-Hall [48, 49] or Auger-Meitner recombination [51, 52], are not present in the material [26, 166].

Once again, it is important to mention that an important assumption of the SQ model is that all photons with energies above the band gap energy are fully absorbed, generating electron-hole pairs, and all photogenerated charge carriers are perfectly extracted from the absorber [26, 166]. On the other hand, photons with sub band gap energy are not absorbed in the absorber. This implies that the material has a step function like $A(E)$ and $QE(E)$ spectra (See **Fig 4. 1).**

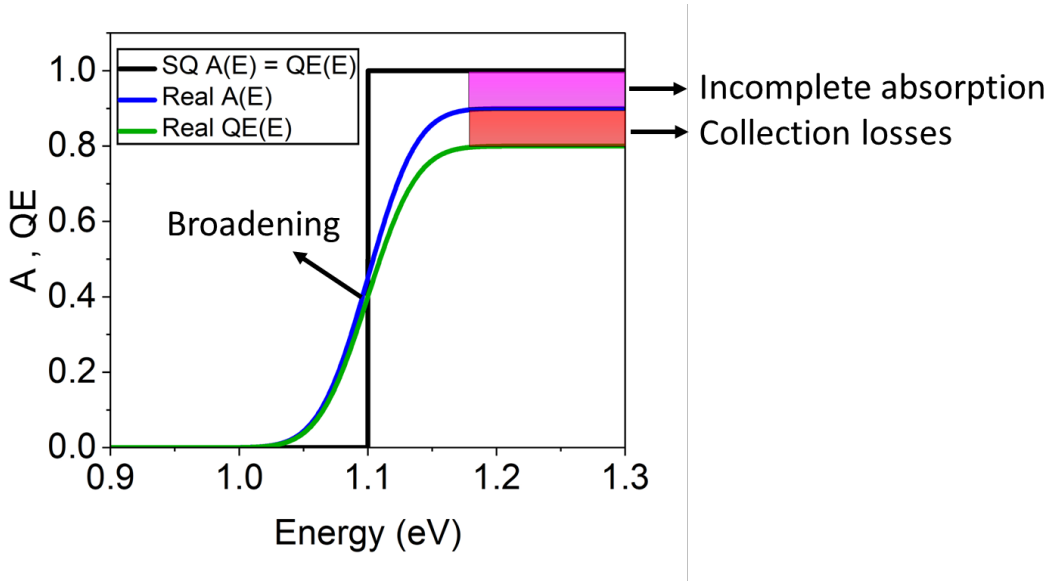

Fig 4. 1 Schematic diagram illustrating the comparison between the SQ model of $A(E)/QE(E)$ spectrum and the $A(E)/QE(E)$ spectra in a real solar cell device.

However, it is important to mention that in the real world, absorber materials do not show the characteristics of an ideal SQ solar cell. First of all, the absorption onset of a real semiconductor is not sharp [28, 166, 167]. Instead, band gap fluctuations—caused by compositional or electrostatic potential variations—as well as Urbach tails, lead to a gradual increase in the *A(E)* edge rather than steep step like transition (i.e, $A(E)$ edge broadens) [77, 166-168]. Secondly, real solar cells generally suffer from absorption losses due to reflection effect. Consequently, $A(E)$ becomes less than unity for energies above the band gap energy. Additionally, charge

collection losses causes $QE(E)$ spectrum to fall below $A(E)$. **Fig 4. 1** schematically illustrates the difference between $A(E)/QE(E)$ spectra of real solar cells and ideal SQ case. In this chapter, through mathematical equations, it will be demonstrated how the broadening of $A(E)/QE(E)$, along with the absorption and collection losses, can decrease the maximum achievable V_{OC} limit below its SQ limit. Lastly, not all charge carriers in a real solar cells recombine through radiative recombination mechanism; a significant portion of photogenerated charge carriers recombine through non-radiative recombination processes.

Therefore, for a real photovoltaic devices, understanding the origins of these losses is essential, and it is important to distinguish different mechanism that are responsible for V_{OC} losses.

In this section, the generalization of the detailed balance model is explained to understand the origin of each loss mechanism in $\Delta\mu$ and V_{OC} with respect to the SQ limit. In **Section 4.1.1** only the optical approach is discussed, which requires detailed knowledge of $A(E)$ shape for $\Delta\mu$ loss analysis. Then, in **Section 4.1.2**, the optoelectrical approach is covered, where $QE(E)$ spectrum is utilized to quantify the V_{OC} losses for a complete photovoltaic devices.

Notably, these two approaches are completely analogous. In **Section 2.4**, the analogy between V_{OC}, $\Delta\mu$, and the relationship between $QE(E)$ and $A(E)$ has already been introduced. Here, it will be shown that the analysis of $\Delta\mu$ and V_{OC} losses also follow similar equations in both optical and optoelectrical models, allowing for analogous calculations to be performed.

4.1.1 Generalized detailed balance based on optical approach

The maximum achievable limit for $\Delta\mu$ in the case of non-step-function like $A(E)$ is called the radiative $\Delta\mu$ limit, denoted here as $\Delta\mu^{rad}$ [28, 31, 69, 166]. This $\Delta\mu^{rad}$ has lower values than the SQ limit. This difference is primarily attributed to the deviation of $A(E)$ shape from ideal step function model.

The broadening of $A(E)$ spectrum results in a radiative $\Delta\mu$ losses, denoted here as $\delta\Delta\mu^{rad}$. In the upcoming discussion, it will be shown that this loss mechanism is mainly caused by enhanced equilibrium radiative emission resulting from increased sub-band gap absorption and emission.

Additionally, the incomplete absorption would lead to generation $\Delta\mu$ losses, labeled as $\delta\Delta\mu^{Gen}$. This loss primarily arises because of the reflection effect or insufficient absorber thickness, which decrease the number of absorbed photons and, consequently, reduce the density of photogenerated electron-hole pairs, ultimately leading to a further drop in the $\Delta\mu$ below its SQ limit.

This separation of the loss mechanisms is not a novel concept; this approach, was first developed in the published work of Rau et al [28]. However, their calculations were entirely based on optoelectrical measurements, where they used $QE(E)$ spectra to obtain V_{OC} losses. In contrast, here in this section, the focus will be on the purely optical measurements, relying on $A(E)$ and $\Delta\mu$. The optical approach enables us to investigate these loss mechanisms without processing the absorber materials into complete devices. Additionally, by conducting analysis only on the absorbers rather than full devices, the possible influence of charge collection effects are excluded.

To determine radiative $\Delta\mu$ limit ($\Delta\mu^{rad}$) and respective $\Delta\mu$ losses, the generalization of the detailed balance model needs to be carried out to accommodate a non-step-function like $A(E)$ into the SQ-like equations (Eq 2.47). For this purpose, the Planck's generalized law of radiation (Eq 2.52) [29, 68, 169] can be used as a starting point for performing the required calculations. As mentioned earlier, this law establishes a direct connection between PL emission spectrum, $A(E)$ spectrum, and $\Delta\mu$ of the material.

By considering the Planck's generalized law (Eq 2.52), and integrating it over all photon energies, it can be written:

$$\int_0^\infty \Phi_{\mathrm{PL}}(E)\,dE = \exp\left(\frac{\Delta\mu}{k_{\mathrm{B}}T}\right)\int_0^\infty A(E)\Phi_{BB}(\mathrm{E})dE \qquad (\boldsymbol{Eq\ 4.1})$$

The left-hand side of this equation is an integral over the PL spectral emission, which simply gives the total photon flux density out of the samples. In the detailed balance situation, in the radiative limit condition (i.e, $\Delta\mu = \Delta\mu^{rad}$), the only recombination mechanism is spontaneous emission [26, 166], which implies that all photogenerated electron-hole pairs recombine radiatively. Therefore, the flux density emitted out of the semiconductor must be the same as the generation flux density [26, 166].

Light absorption and charge carrier generation processes has already been discussed in **Section 2.1.2**. For a solar cell under the standard 1 sun illumination condition (**Fig 2. 2**), the sun generation flux density F_{Gen}^{Sun} has been introduced in Eq 2.19 (i.e., $F_{Gen}^{Sun} = \int_0^\infty A(E)\Phi_{Sun}(E)dE$) [40].

Therefore, by considering the radiative limit ($\Delta\mu = \Delta\mu^{rad}$), where the radiative emission is balanced with the generation flux density, the left-hand side of Eq 4.1 can be replaced with F_{Gen}^{Sun} (Eq 2.19), leading to:

$$\int_0^\infty A(E)\Phi_{Sun}(E)dE = \exp\left(\frac{\Delta\mu^{rad}}{k_B T}\right)\int_0^\infty A(E)\Phi_{BB}(\mathrm{E})dE \qquad (\boldsymbol{Eq\ 4.2})$$

Thus, $\Delta\mu^{rad}$would be:

$$\Delta\mu^{rad} = k_B T ln\frac{\int_0^\infty A(E)\Phi_{Sun}(E)dE}{\int_0^\infty A(E)\Phi_{BB}(\mathrm{E})dE} \qquad (\boldsymbol{Eq\ 4.3})$$

$$= k_B T\ ln\frac{F_{Gen}^{sun}}{F_0^{rad}}$$

In the equation above (Eq 4.3), the denominator of the logarithmic term, is represents the integral over equilibrium emission (i.e., integral over $A(E)\Phi_{BB}(\mathrm{E})$). This integral is referred to the radiative saturation flux density, denoted here as F_0^{rad}.

With this method, now the generalization of detailed balance model has been completed for a non-step function like $A(E)$ spectrum, and according to Eq 4.3, $\Delta\mu^{rad}$ can be obtained with detailed knowledge of the $A(E)$ shape and temperature of the absorber material. It is evident that substituting the $A(E)$ with a Heaviside function recovers the SQ-$\Delta\mu$ limit (qV_{OC}^{SQ}) (see **Fig 4. 1** and Eq 2.47)[26].

It is also important to highlight that these calculations assume that absorbers have a perfect reflector at the back side, where the radiative emission occurs only from the front side of the absorber [26, 27]. In the cases where the radiative emission occurs from both the front and

back sides of the absorber, a factor of 2 should be included in the denominator of the logarithmic term of Eq 4.3 (i.e, $\Delta\mu^{rad} = k_B T\, ln\frac{F_{Gen}^{sun}}{2F_0^{rad}}$) [26, 27].

Although Eq 4.3 allows the extraction of $\Delta\mu^{rad}$ from any measured *A(E)* spectrum, this equation does not provide any information regarding the origins of $\Delta\mu$ losses with respect to the SQ limit (qV_{OC}^{SQ}). Therefore, it is essential to understand how $A(E)$ broadening and incomplete photon absorptions contribute to the $\Delta\mu$ losses. Thus, it is necessary to employ a practical approach to separate different loss mechanisms with respect to the qV_{OC}^{SQ}.

Similar to the work of Rau et al. [28], where they used a mathematical expansion to separate these loss mechanisms for V_{OC}, an analogous method can also be employed here to obtain $\Delta\mu$ losses. Therefore, a mathematical expansion to Eq 4.3 is applied to break it down into the following form [28]:

$$\Delta\mu^{rad} = k_B T ln\left(\frac{F_{Gen}^{SQ}}{F_0^{SQ}} \times \frac{F_{Gen}^{sun}}{F_{Gen}^{SQ}} \times \frac{F_0^{SQ}}{F_0^{rad}}\right) \qquad (\boldsymbol{Eq\ 4.4})$$

$$= qV_{OC}^{SQ} - \delta\Delta\mu^{Gen} - \delta\Delta\mu^{rad}$$

Here, F_{Gen}^{SQ} and F_0^{SQ} are generation flux and radiative saturation flux for SQ type absorbers (i.e., step like $A(E)$), respectively:

$$F_{Gen}^{SQ} = \int_{E_g}^{\infty} \Phi_{Sun} dE \qquad (\boldsymbol{Eq\ 4.5})$$

$$F_0^{SQ} = \int_{E_g}^{\infty} \Phi_{BB} dE \qquad (\boldsymbol{Eq\ 4.6})$$

The first term in Eq 4.4 simply represents the SQ limit (qV_{OC}^{SQ}) for a material with well-defined band gap energy (E_g). The second and third components of this equation correspond to the $\Delta\mu$ losses with respect to this SQ limit.

Here, the second term of Eq 4.4 is called generation $\Delta\mu$ loss:

$$\delta\Delta\mu^{Gen} = -k_{\mathrm{B}}T\ln\left(\frac{F_{Gen}}{F_{Gen}^{SQ}}\right) = k_{\mathrm{B}}Tln\left(\frac{\int_{E_g}^{\infty}\Phi_{Sun}(E)dE}{\int_{0}^{\infty}A(E)\Phi_{Sun}(E)dE}\right) \qquad (\boldsymbol{Eq\ 4.7})$$

This loss mechanism mainly arises from the incomplete light absorption and is primarily due to incoming light reflection or insufficient absorption in very thin absorber layers. It simply means that not all photons with energies above the band gap are absorbed. Consequently, fewer photons contribute to the charge carrier generation within the material, thus reducing the $\Delta\mu$.

The last term in Eq 4.4 refers to the radiative $\Delta\mu$ loss:

$$\delta\Delta\mu^{rad} = -k_{\mathrm{B}}T\ln\left(\frac{F_0^{SQ}}{F_0^{rad}}\right) = k_{\mathrm{B}}Tln\left(\frac{\int_{0}^{\infty}A(E)\Phi_{BB}(\mathrm{E})dE}{\int_{E_g}^{\infty}\Phi_{BB}(\mathrm{E})dE}\right) \qquad (\boldsymbol{Eq\ 4.8})$$

This loss mechanism mainly stems from the broadening of the absorption edge. As $A(E)$ becomes broader, sub-band gap states start contributing to photon absorption and radiative emission. Additionally, the $\Phi_{BB}(\mathrm{E})$ spectrum also increases in the low energy ranges. Consequently, the $A(E)\Phi_{BB}(\mathrm{E})$ term gains more weight in the low and sub band gap regions, leading to a significant increase in this loss component. In the subsequent sections of this chapter, I will use simulations to illustrate how the band gap inhomogeneities, Urbach tails and reduced absorber thickness affect the broadening of $A(E)$ and $\delta\Delta\mu^{rad}$ values.

Up to this point, the entire focus was exclusively on the cases where non-radiative recombination pathways were absent in the material, and recombination mechanism was solely due to spontaneous radiative recombination. However, it is crucial to note that in a real absorber material, not all photogenerated electron-hole pairs recombine radiatively. In solar cells, the Shockley-Read-Hall recombination activities through deep defects or at the interfaces and surfaces [3, 48, 49], along with potential Auger recombination activities [52], further reduces $\Delta\mu$ to values lower than $\Delta\mu^{rad}$. In this scenario, $\Delta\mu$ of an absorber can be expressed as [28-30, 69]:

$$\begin{aligned}\Delta\mu &= qV_{OC}^{SQ} - \delta\Delta\mu^{Gen} - \delta\Delta\mu^{rad} - \delta\Delta\mu^{nr} \\ &= \Delta\mu^{rad} - \delta\Delta\mu^{nr}\end{aligned} \qquad (\boldsymbol{Eq\ 4.9})$$

Where $\delta\Delta\mu^{nr}$ is the non-radiative loss and simply can be written as:

$$\delta\Delta\mu^{nr} = -k_{\mathrm{B}}T\ln(Y_{PL}) \qquad (\boldsymbol{Eq\ 4.10})$$

Here, Y_{PL} is the photoluminescence quantum yield (PLQY) or external radiative efficiency (ERE) [29, 170]. It is expressed as the ratio of the emitted photon flux density from the sample to the generation flux density F_{Gen}^{Sun} (Eq 2.19):

$$Y_{PL} = \frac{\int_0^{\infty} \Phi_{\mathrm{PL}}(E)\,dE}{F_{Gen}^{Sun}} \qquad (\boldsymbol{Eq\ 4.11})$$

In the experimental conditions, Y_{PL} is determined using a laser flux instead of the solar spectrum. The intensity calibration process for the laser flux has already been explained in **Section 3.3.1**. In this chapter the focus is solely on the theoretical equations. **Chapter 5** will provide more details regarding the experimental determination of Y_{PL}.

This $\delta\Delta\mu^{nr}$ is the primary recombination activity is the photovoltaic devices. The Y_{PL} for state-of-the-art CIGSe absorbers is typically more than 1% [11, 46]. However, for samples in this thesis, the measured Y_{PL} is much smaller. In the best case, with the RbF PDT, the Y_{PL} reaches approximately 0.2 %.

4.1.2 Generalized detailed balance based on optoelectrical approach

In the previous section, the generalized detailed balance model based on optical approach was discussed. It was shown that determining the radiative $\Delta\mu$ limit ($\Delta\mu^{rad}$) and respective losses requires the accurate knowledge of $A(E)$ shape. Several methods exist for $A(E)$ determination, the most convenient method is measuring the transmittance/reflectance spectra using UV-Vis measurements (**see Section 3.6**). However, CIGSe samples are generally prepared on opaque Mo substrates, which hinders the transmittance measurements. Despite this limitation, $A(E)$ spectra can still be extracted using alternative techniques, such as ellipsometry. Nevertheless, ellipsometry measurements can be challenging due to the factors such as Ga gradient or surface roughness in the CIGSe samples [171].

Furthermore, for some cases, the study needs to be extended beyond the absorber material to evaluate the overall performance of the photovoltaic device itself. Therefore, instead of doing only optical measurements, optoelectrical analysis can be performed to assess V_{OC} losses in the solar cells.

In this section, the theoretical framework of V_{OC} losses in solar cells will be covered based on optoelectrical measurements. It is important to highlight that the generalization of the SQ model based on optoelectrical approach has been extensively discussed in the previous published reports [28, 30, 31, 164]. All the V_{OC} loss calculations introduced in the following discussion were first reported by Rau et al [28]. Here, the key equations relevant to this model are summarized.

Similar to the optical approach (Eq 4.3) , the radiative V_{OC} limit (V_{OC}^{rad}) can be extracted for a complete solar cell using an analogous equation [28, 69, 172]:

$$V_{OC}^{rad} = \frac{k_B T}{q}\, ln \frac{\int_0^\infty QE(E)\Phi_{Sun} dE}{\int_0^\infty QE(E)\Phi_{BB}(\mathrm{E}) dE} = \frac{k_B T}{q} \ln\left(\frac{J_{SC}}{J_0^{rad}}\right) \qquad (\boldsymbol{Eq\ 4.12})$$

Here, J_{SC} is short circuit current density which was introduces in Eq 2.35, and J_0^{rad} is radiative saturation current density which is completely analogous to F_0^{rad} that was already defined in Eq 4.3.

By writing the mathematical expansion proposed by Rau et al [28]. The V_{OC} losses with respect to SQ limit can be obtained using the following formula:

$$V_{OC}^{rad} = \frac{k_B T}{q}\, ln\left(\frac{J_{SC}^{SQ}}{J_0^{SQ}} \times \frac{J_{SC}}{J_{SC}^{SQ}} \times \frac{J_0^{SQ}}{J_0^{rad}}\right) \qquad (\boldsymbol{Eq\ 4.13})$$

$$= V_{OC}^{SQ} - \delta V_{OC}^{SC} - \delta V_{OC}^{rad}$$

Similar to the generation $\Delta\mu$ loss ($\delta\Delta\mu^{Gen}$), short circuit V_{OC} loss (δV_{OC}^{SC}) [28] is defined here, which primarily arises from incomplete light absorption and charge collection losses:

$$\delta V_{OC}^{SC} = -\frac{k_B T}{q}\, ln\left(\frac{J_{SC}}{J_{SC}^{SQ}}\right) \qquad (\boldsymbol{Eq\ 4.14})$$

and similar to radiative $\Delta\mu$ losses ($\delta\Delta\mu^{rad}$), the broadening of $QE(E)$ spectra would result in the radiative V_{OC} loss (δV_{OC}^{rad}) [28]:

$$\delta V_{OC}^{rad} = -\frac{k_B T}{q}\, ln\left(\frac{J_0^{SQ}}{J_0^{rad}}\right) \qquad (\boldsymbol{Eq\ 4.15})$$

Moreover, with the presence of non-radiative recombination channels, for V_{in} it can be written:

$$V_{in} = V_{OC}^{rad} + \frac{k_B T}{q} \ln(Y_{EL}) \qquad (\boldsymbol{Eq\ 4.16})$$

Where Y_{EL} corresponds to the electroluminescence (EL) quantum yield:

$$Y_{EL} = \frac{q \int_0^\infty \Phi_{EL}(E)\, dE}{J} \qquad (\boldsymbol{Eq\ 4.17})$$

Here, J is injected current density across the junction. Notably, the one sun equivalent measurement is carried out with injection current density equal to J_{SC} [30].

Compared to the optical approach in **Section 4.1.1**, in optoelectrical analysis, $A(E)$ is substituted by $QE(E)$ spectrum. In **Section 2.2.1** I have already shown that $QE(E)$ is directly related to $A(E)$ spectrum through charge collection efficiency. Moreover, in optoelectrical approach, the flux densities are replaced by current densities. All the current densities here are completely analogous with their corresponding flux densities that have been already explained in the **Section 4.1.1**. However, it is important to note that, unlike the flux densities which depend solely on the absorption properties, current densities are affected by both light absorption and charge collection efficiency.

4.2 Simulations for non-step like *A(E)* spectra

Up to this point, the generalization of the detailed balance model has enabled the extraction of radiative losses (both $\delta\Delta\mu^{rad}$ and δV_{OC}^{rad}) for a non-ideal $A(E)$ spectrum, which exhibits gradual increase at the absorption edge rather than step function like transition.

The broadening of $A(E)$ is a complex phenomenon influenced by various factors, including band gap fluctuations [167]. In the CIGSe absorbers these fluctuations can arise from alloy disorder due to In and Ga inhomogeneous distribution [33, 34, 41], variation in the Cu composition and Cu-poor composition [41], as well as presence of charged defects that induce electrostatic potential fluctuations [33, 34, 41]. All these effects can distort the band edges and contribute to this broadening. Additionally, presence of the Urbach tails can further contribute to broadening and radiative losses .

In this section, to enhance the understanding about the influence $A(E)$ broadening on the radiative losses, simulations were performed to analyze the effects of band gap inhomogeneities and sub-band gap tail states on the $A(E)$ shape. Part of the upcoming equations and models, based on Gaussian band gap fluctuations, have been already developed in the previous published reports [30, 41, 166, 167]. However, here the primary focus would be to integrate these fluctuations with Urbach tails, and to show that the Urbach tails and band gap fluctuations contribute differently to the broadening of $A(E)$. Urbach tails predominantly have influence on the energy ranges significantly lower than band gap. On the other hand, band gap inhomogeneities (fluctuations) primarily affect $A(E)$ shape near the absorption onset. Notably, the effect of Urbach tails on $A(E)$ shape and its broadening has not been covered extensively in the previous published reports.

Moreover, within this section, the contribution of Gaussian type band gap distribution and Urbach tails on the $\delta\Delta\mu^{rad}$ will be quantified for each simulated $A(E)$ spectrum using the generalized detailed balance model. Additionally, at the end of this section, the impact of the absorber thickness on the shape of $A(E)$ and its broadening will be discussed. Notably, it will be shown that along with the band gap fluctuations and Urbach tails, the decrease in the absorber thickness would further enhance the broadening of $A(E)$ spectrum.

All the loss analyses presented in this section are based on the optical approach, utilizing the simulated $A(E)$ spectrum for calculations (See **Section 4.1.1**).

Lastly, it is worth mentioning that a MATLAB-based scripts (MATLAB version 9.11.0.1809720 (R2021b)) were used for the upcoming simulations and calculations.

4.2.1 Effect of band gap inhomogeneities on the $A(E)$

In the first part of the simulations, only a semiconductor with presence of Gaussian band gap fluctuations is considered. Shortly in **Section 4.2.2**, the effect of exponential Urbach decay will be also incorporated in the simulations.

Based on the previous reports [41, 166, 167], instead of defining a single band gap energy for a material, a distribution of band gap energy can be considered. Using a Gaussian distribution model, at each localized point on the absorber, a Gaussian distribution of a local band gap energy (E_g^{loc}) around mean value of $\overline{E_g}$ can be defined [41, 166, 167]:

$$P\left(E_g^{loc}\right) = \frac{1}{\sigma_g\sqrt{2\pi}} \exp\left(-\frac{\left(E_g^{loc} - \overline{E_g}\right)^2}{2\sigma_g^2}\right) \qquad (\boldsymbol{Eq\ 4.18})$$

The term ‘’local band gap E_g^{loc}’’ here represents a well-defined band gap in a narrow-localized region on the absorber surface. Here, a probability distribution model for the local band gaps E_g^{loc} is assumed, where σ_g represents the standard deviation that quantifies the degree of lateral band gap inhomogeneities around the mean band gap value $\overline{E_g}$. By this definition, increase in σ_g indicates stronger lateral fluctuations of the band gap energy.

In the next step of the simulations, at each local position $\boldsymbol{x}$ on the absorber, a local absorptance $A^{loc}\left(E, E_g^{loc}(\boldsymbol{x})\right)$ is defined [167]. Subsequently, the final $A(E)$ spectrum of the absorber can be obtained by taking an average integral of all $A^{loc}\left(E, E_g^{loc}(\boldsymbol{x})\right)$ over the absorber area (a) [167]:

$$A(E) = \frac{1}{a}\int_a A^{loc}\left(E, E_g^{loc}(\boldsymbol{x})\right) d\boldsymbol{x} \qquad (\boldsymbol{Eq\ 4.19})$$

In the case of Gaussian probability distribution for E_g^{loc} (i.e., Eq 4.18), this average integral can be substituted with an integral over the Gaussian probability distribution. Thus, using Eq 4.18, the simulated $A(E)$ spectrum can be expressed as [30, 166, 167]:

$$A(E) = \int_0^\infty A^{loc}\left(E, E_g^{loc}\right) P\left(E_g^{loc}\right) dE_g^{loc} \qquad (\boldsymbol{Eq\ 4.20})$$

With this approach, instead of conducting a direct averaging, the integration is performed over all possible values of E_g^{loc}, each weighted by its probability of occurrence.

In the further steps of the simulations, a model for the local absorptance $A^{loc}\left(E, E_g^{loc}\right)$ needs to be defined. In a very simple approximation, it can be considered that each localized point on the absorber surface has a well-defined local band gap E_g^{loc}, and its $A^{loc}\left(E, E_g^{loc}\right)$ exhibits a step-function-like behavior [30, 166, 167]:

$$A^{loc}\left(E, E_g^{loc}\right) = \begin{cases} 1, & E > E_g^{loc} \\ 0, & E < E_g^{loc} \end{cases} \qquad (\boldsymbol{Eq\ 4.21})$$

In this model, each point on the absorber surface is represented as a vertical column with a step-function-like absorptance spectrum that absorbs light along its depth

For this simple approximation, the integral over the Gaussian probability distribution (Eq 4.20) would lead to error function like solution for $A(E)$ spectrum. Detailed solution of this integral is described in **Appendix A1** (see also references [30, 166, 167]):

$$A(E) = \frac{1}{2}\mathrm{erfc}\left(\frac{\overline{E_g} - E}{\sqrt{2}\sigma_g}\right) \qquad (\boldsymbol{Eq\ 4.22})$$

In **Fig 4. 2 a** the simulated $A(E)$ spectra for $\overline{E_g} = 1.1\ eV$ with σ_g values in the range of 0 meV to 60 meV are illustrated. Here, for the case with no lateral fluctuations (i.e., $\sigma_g = 0$), the $A(E)$ spectrum represents the SQ model (i.e, step function $A(E)$). On the other hand, increase in the σ_g (i.e, more lateral band gap inhomogeneities) would result stronger broadening for the simulated $A(E)$ spectrum.

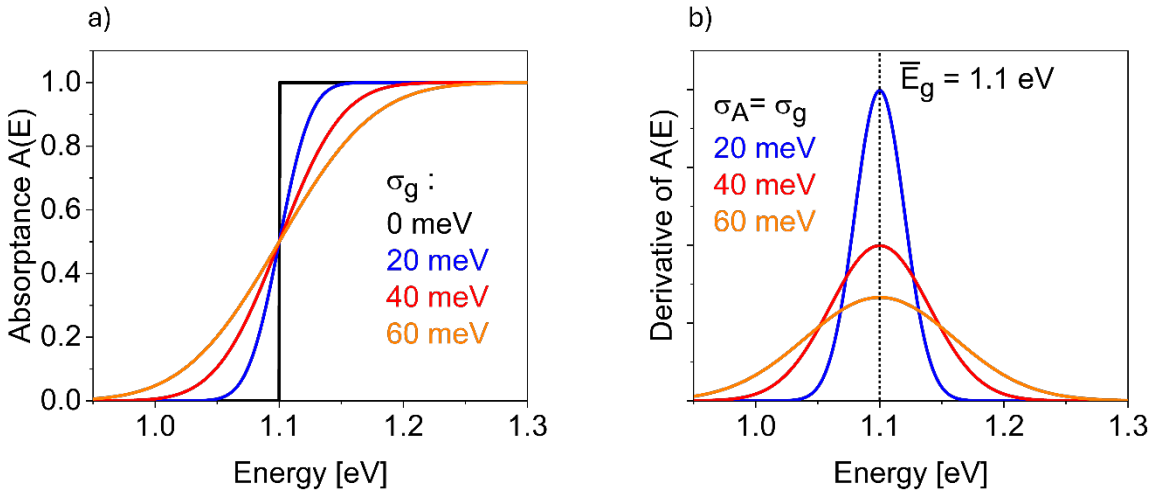

Fig 4. 2 a) $A(E)$ spectra modeled as an error function centered around $\overline{E_g} = 1.1\ eV$ (Eq 4.22). **b)** The first derivative of these error-function-like $A(E)$ spectra, displays a Gaussian distribution with broadening of $\sigma_g = \sigma_A$. (For each σ_g, a color code is assigned).

For any experimentally measured or simulated $A(E)$ spectrum, it is often a useful approach to fit its first derivative with a Gaussian distribution function. The broadening of this Gaussian fit (denoted as σ_A) provides insights into the degree of deviation from the ideal step-function. For the simulated $A(E)$ spectra with error function model, it is evident that their derivative has a

Gaussian shape, with σ_A value same as defined fluctuation parameter σ_g, and with inflection point at the average band gap energy $\overline{E_g}$ (see **Fig 4. 2 b**).

It is worth mentioning that even though this error function model is defined only for lateral band gap inhomogeneities, this approach offers a useful approximation for analyzing the broadening of any experimentally measured $A(E)$ spectrum. In **Chapter 5**, it will be demonstrated that this valuable approach can also be effectively applied to evaluate the broadening of $A(E)$ spectrum in CIGSe samples with a compositional gradient in depth, where along with the observed lateral variations in the band gap, there are also intentional changes in the band gap throughout the depth of the material.

In the next step, the theoretically extracted equations in **Section 4.1.1** are employed to quantify the $\Delta\mu$ losses for simulated $A(E)$ spectra. Once again, it is worth emphasizing that obtaining the radiative limit, $\Delta\mu^{rad}$, requires only the $A(E)$ spectrum and the absorber temperature T (See Eq 4.3). However, calculating $\Delta\mu$ losses relative to the SQ-limit requires additional information regarding the reference band gap energy (E_g), where the SQ limit of this E_g serves as the reference point for evaluating the $\Delta\mu$ losses (see Eq 4.7 and Eq 4.8). In this section, all loss analyses are performed using the mean band gap value $\overline{E_g}$ as the reference band gap energy (i.e., $E_g = \overline{E_g} = 1.1\ eV$), and the temperature in all calculations is set to **296 K**.

It is important to highlight that in these simulations, a complete absorption at the energy ranges well above the band gap is considered (see **Fig 4. 2 a**). Consequently, $\delta\Delta\mu^{Gen}$ due to incomplete absorption is negligible. Therefore, $\Delta\mu^{rad}$ can be simply obtained using $\Delta\mu^{rad} = qV_{OC}^{SQ} - \delta\Delta\mu^{rad}$.

Fig 4. 3 presents the obtained $\Delta\mu^{rad}$ and $\delta\Delta\mu^{rad}$ values for this simplified error-function model. Here, σ_g increases from 0 meV to 100 meV.

In addition to the performed calculations, the results in **Fig 4. 3** are compared with the existing literature methods to validate their accuracy. In **Appendix A2**, I demonstrate that the methods used in this section align perfectly with previously proposed calculations in published work of Rau and Werner [166].

Additionally, some published papers use approximation $\delta\Delta\mu^{rad} \sim \frac{\sigma_g^2}{2kT}$ to estimate radiative losses [167, 168, 173]. However, in **Appendix A2**, I also show that this approximation tends to overestimate the radiative losses and it is only a good approximation for σ_g values smaller than 50 meV.

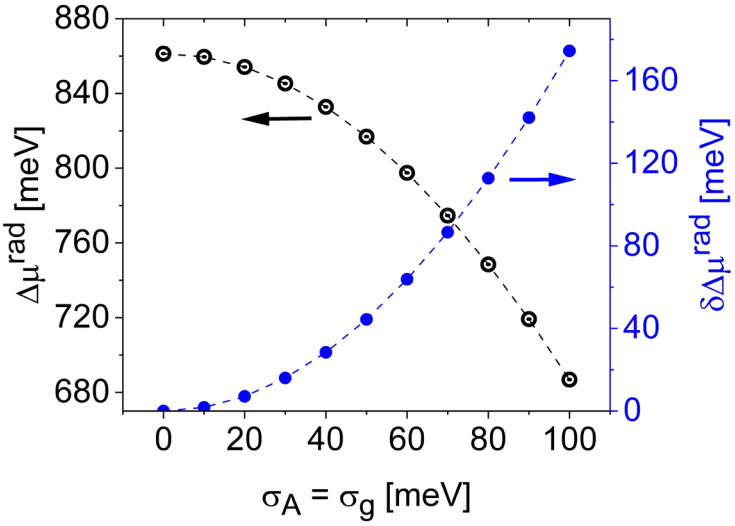

Fig 4. 3 depicts the calculated $\Delta\mu^{rad}$ and $\delta\Delta\mu^{rad}$ values for simulated error-function like $A(E)$ spectra with σ_g in the range of 0 meV to 100 meV. It can be observed that with an increase in σ_g, $\delta\Delta\mu^{rad}$ increases and $\Delta\mu^{rad}$ decreases.

Overall, the simulated spectra and calculated $\delta\Delta\mu^{rad}$ values indicate that stronger band gap inhomogeneities (i.e., larger σ_g) enhances the broadening of $A(E)$ edge, ultimately increasing $\delta\Delta\mu^{rad}$. This loss mechanism leads to lower $\Delta\mu^{rad}$, which in turn reduces V_{OC} and the overall efficiency of the final devices.

4.2.2 Effect of Urbach tails on the *A(E)*

Up to now, only the effect of band gap inhomogeneities are considered, which was represented by the Gaussian distribution of E_g^{loc}, and the $A(E)$ spectrum was modeled with simple error function like model. Although this simplified approach offers a valuable and practical model for $A(E)$ spectrum, it does not provide any information about the influence of sub-band gap Urbach tails and absorbers thickness on the $A(E)$ shape and its broadening. Therefore, instead of using simplified step function model for $A^{loc}\left(E, E_g^{loc}\right)$ (Eq 4.21), a more accurate model

needs to be employed that includes the combined role of Urbach tails and absorber thickness in the simulations.

For this purpose, a more realistic assumption is considered, where the $A(E)$ can be extracted from the absorption co-efficient of a direct semiconductor. In this case, a local absorption co-efficient α^{loc} is first defined at each localized position on the absorber surface. The α^{loc} can be defined based on earlier model described in Eq 2.49. In this model, the α^{loc} shows square root increase for energies above the E_g^{loc}, and Urbach decay behavior (i.e., exponential decay) below it [30, 67, 174]:

$$\alpha^{loc}\left(E, E_g^{loc}\right) = \begin{cases} \alpha_0 \sqrt{\dfrac{E - E_g^{loc}}{k_B T}} & , \quad E \geq E_g^{loc} + \dfrac{E_U}{2} \\ \alpha_0 \, exp\left(\dfrac{E - E_g^{loc}}{E_U}\right) \sqrt{\dfrac{E_U}{2ek_B T}} & , \quad E < E_g^{loc} + \dfrac{E_U}{2} \end{cases} \qquad (\boldsymbol{Eq\ 4.23})$$

In this equation, E_U represents the Urbach energy, and α_0 is a constant. For the upcoming simulations, $\alpha_0 = 10^4 cm^{-1}$ is considered, which aligns well with the reported α_0 values of CIGSe absorbers [3]. It is essential to mention that the square root scaling factor is included for the Urbach decay term to ensure that the overall $\alpha^{loc}\left(E, E_g^{loc}\right)$ function is well behaved and continuous at the transition energy point.

Now, the local absorptance model $A^{Loc}\left(E, E_g^{loc}\right)$ needs to be defined for a given $\alpha^{loc}\left(E, E_g^{loc}\right)$. To achieve this, the Beer-Lambert's law (Eq 2.13 with $R(E) = 0$) can be employed, which allows to define $A^{loc}\left(E, E_g^{loc}\right)$ using the following equation [30, 175]:

$$A^{loc}\left(E, E_g^{loc}\right) = 1 - \exp(-\alpha^{loc} d) \qquad (\boldsymbol{Eq\ 4.24})$$

Here, *d* is the thickness of the absorber material.

In this section, the effect of different thicknesses on the $A(E)$ broadening is excluded, and in all upcoming simulations a constant thickness of *d = 2* µm is considered. In the next **Section 4.2.3**, more details regarding the thickness effect will be discussed.

In the next step, by performing the same integral as in the previous case (Eq 4.20), the overall $A(E)$ can be acquired by integrating the newly defined $A^{loc}(E, E_g)$ (Eq 4.24) over the Gaussian probability distribution of E_g^{loc}.

This model also considers that absorber material has two-dimensional lateral band gap inhomogeneities, where each localized point on the material absorbs photons through its depth. However, unlike the previous case, here on each surface point on the absorber, the local absorptance $A^{Loc}(E, E_g)$ is defined by Beer-Lambert's law rather than the step-function model.

In **Fig 4. 4 a**, simulated $A(E)$ spectra are presented for E_U values in the range of 0 meV to 20 meV. It is important to highlight that for these simulations, fixed values of $\sigma_g = 40$ meV, $\overline{E_g} = 1.1\ eV$ and T = 296 K are considered. As expected, increase in the E_U leads to a flattening of the low-energy slope of $A(E)$ spectrum in logarithmic scale.

Similar to error function model, the first derivative of the $A(E)$ can be evaluated to quantify the degree of broadening of $A(E)$. In the upcoming discussions in **Fig 4. 8**, it will be shown that the first derivative slightly deviates from the Gaussian shape. However, a Gaussian fit can still be reliably employed to compare the σ_A for each $A(E)$.

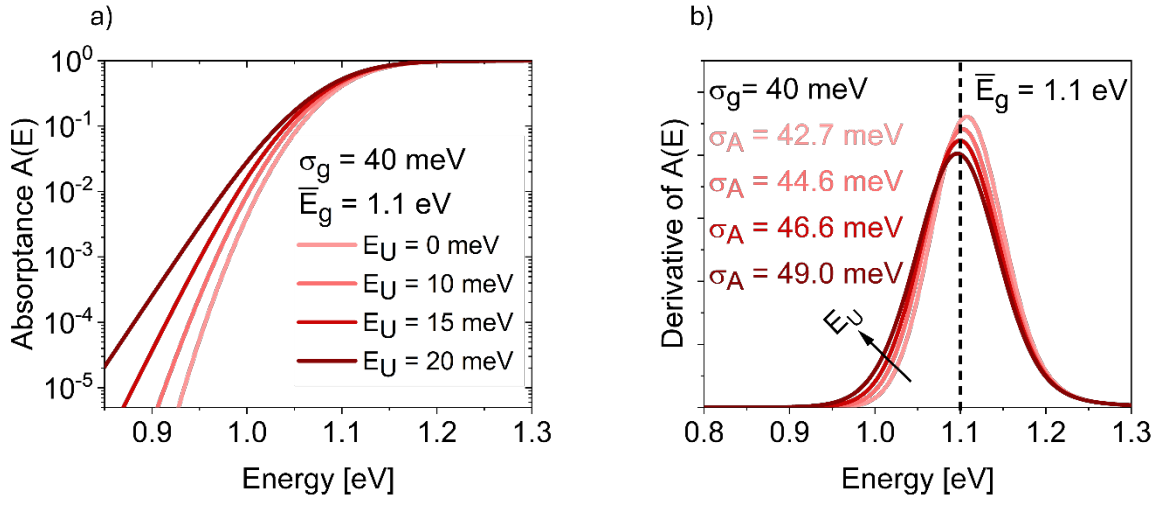

Fig 4. 4 a) Simulated $A(E)$ spectra for E_U ranging from 0 meV to 20 meV. **b)** first derivative of these simulated $A(E)$ spectra and their extracted σ_A values from a separate Gaussian fit to each derivative curve. Each E_U is represented by different color code.

Fig 4. 4 b illustrates the first derivative of each simulated $A(E)$ spectrum, along with the corresponding σ_A values extracted from the Gaussian fits.

Here, in **Fig 4. 4 b**, it can be observed that the inflection point slightly deviates from the average band gap energy ($\overline{E_g} = 1.1\ eV$). Notably, unlike the error function model, when both effect of tails states and fluctuations are combined, the square root dependence of *α(E)*, absorber thickness, and Urbach tails have all effect on the position of inflection point.

Fig 4. 4 b illustrates that at $E_U = 0$ meV, the inflection point is slightly higher than $\overline{E_g}$. This deviation primary arises because of the reduced absorption due to the square root dependence of the *α(E)* for energies above the band gap. However, as E_U increases, sub band gap absorption increases, and this inflection point shifts towards lower energies.

Furthermore, it can be also clearly observed that the extracted σ_A increases with the increase in E_U (**Fig 4. 4 b** inset). Here, unlike the error function approach, σ_A is no longer equal to σ_g. Instead, in this case, σ_A exhibits a more complicated dependence on multiple factors; it is not solely influenced by σ_g but also by the absorber thickness and Urbach energy.

An interesting observation here is that even in the cases with no Urbach tails (i.e, $E_U = 0$ meV), the σ_A has larger values than σ_g. This discrepancy primarily arises due to the finite thickness of the absorber. In the upcoming **Section 4.2.3**, I will demonstrate that as the thickness increases to sufficiently large values, this model converges to the error function model, where $\sigma_g = \sigma_A$.

At this point, a simulation method is introduced that incorporates both the influence of Gaussian band gap inhomogeneities and Urbach tail states. Now, these simulated $A(E)$ spectra can be utilized to extract the $\Delta\mu^{rad}$ and $\delta\Delta\mu^{rad}$ for different σ_g and E_U values using Eq 4.3 and Eq 4.8.

Fig 4. 5 a depicts the variation of $\Delta\mu^{rad}$ across σ_g values ranging from 0 meV to 60 meV, and E_U values in the range of 0 meV to 20 meV. Moreover, **Fig 4. 5 b** visually represent a color map that shows the rise in $\delta\Delta\mu^{rad}$ as both σ_g and E_U increases. Here, for each E_U and σ_g, $\delta\Delta\mu^{rad}$ is calculated separately.

Chalcopyrite absorbers have E_U values in the range of 11 meV to 20 meV [33, 34, 168]. In **Fig 4. 5**, it can be observed that within this specific range of E_U, the tail states have only a small contribution to the radiative losses.

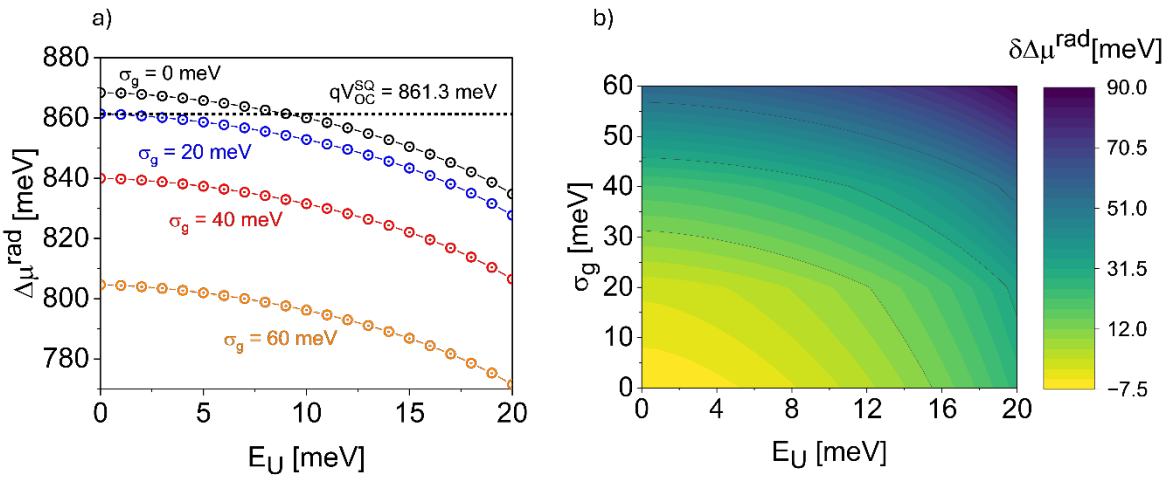

Fig 4. 5 $\Delta\mu^{rad}$ and $\delta\Delta\mu^{rad}$ calculated for simulated $A(E)$ spectra based on realistic direct band gap absorption co-efficient (i.e., according to Eq 4.23and Eq 4.24). **a)** Illustrates the quantified $\Delta\mu^{rad}$ values for σ_g in the range of 0 meV to 60 meV and E_U in the range of 0 meV to 20 meV. Each σ_g is represented by a different color code. Dotted line illustrates the qV_{OC}^{SQ} limit for $\overline{E_g} = 1.1$ eV **b)** Color map illustrating the dependence of the $\delta\Delta\mu^{rad}$ on the σ_g and E_U.

As mentioned previously, for calculating the $\delta\Delta\mu^{rad}$, it is essential to specify a reference band gap energy (E_g) (see Eq 4.8). Here, in **Fig 4. 5 b**, the $\delta\Delta\mu^{rad}$ is obtained with respect to $\overline{E_g} = 1.1\ eV$ (i.e., $E_g = \overline{E_g} = 1.1\ eV$ in Eq 4.8).

In these simulations, an interesting observation is that in certain ranges with low E_U and σ_g values, the radiative losses ($\delta\Delta\mu^{rad}$) become negative (**Fig 4. 5 b**). This implies that, within this specific range, the $\Delta\mu^{rad}$ surpasses the Shockley-Queisser (SQ) limit (see **Fig 4. 5 a**). At the first glance, this may seem surprising. However, this phenomenon arises primarily due to gradual increase of $A(E)$ and reduced absorption compared to SQ model (i.e step function) for energies above the band gap energy.

To further discuss this effect, in **Fig 4. 6a,** the $A(E)$ spectrum is simulated for the case of $E_U = 0$ meV and $\sigma_g = 0$ meV using square root dependence of $\alpha(E)$ (SQRT model). Additionally this SQRT model is compared with the step function SQ spectrum. It is evident that for the SQRT model, $A(E)$ spectrum exhibits a gradual increase for energies above the band gap, leading to lower absorption than SQ-model within the specific energy ranges above the band gap. This behavior is primarily due to the square-root behavior of the $\alpha(E)$ for energies above the band gap (see Eq 4.23 and Eq 4.24).

In Eq 4.9, it can be seen that calculating $\delta\Delta\mu^{rad}$ requires multiplying $A(E)$ spectrum by $\Phi_{BB}(\mathrm{E})$. In this special case where $E_U = 0$ meV and $\sigma_g = 0$ meV , the gradual increase of $A(E)$ above the band gap reduces the $A(E) \times \Phi_{BB}(\mathrm{E})$ values compared to the case where $A(E)$ is step function (i.e SQ model). Consequently, this particular $A(E)$ shape leads to decrease of F_0^{rad} below the F_0^{SQ}, ultimately leading to a negative value for radiative loss (see again Eq 4.9).

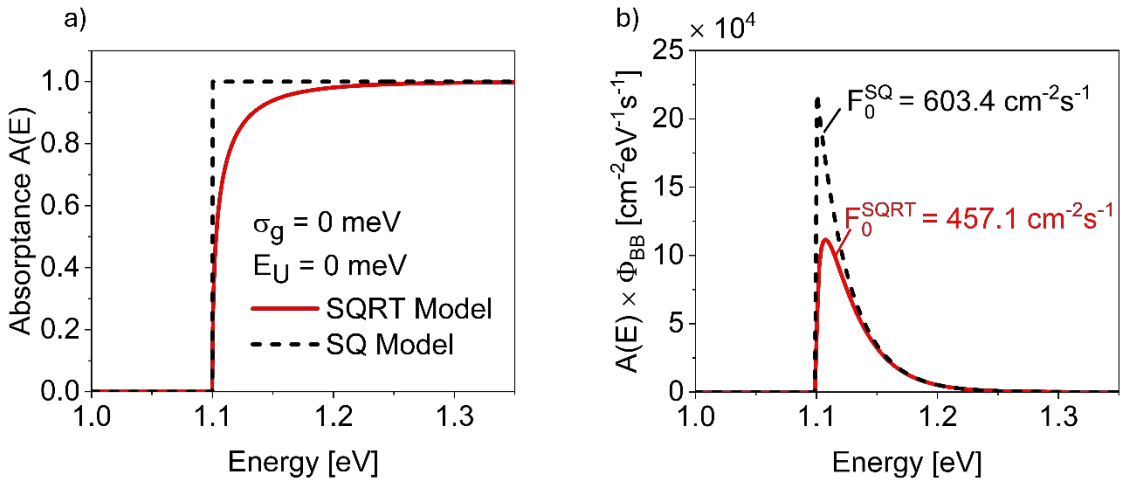

Fig 4. 6 a) $A(E)$ simulated from SQRT and SQ model. SQRT model represents the $A(E)$ spectra simulated using Eq 4.23 and Eq 4.24, with $E_U = 0$ meV and $\sigma_g = 0$ meV. SQ model refers to step function spectrum. **b)** Depicts the $A(E) \times \Phi_{BB}(\mathrm{E})$ spectra for both models. The F_0^{rad} values are determined by calculation of the covered area under these spectra, using $F_0^{rad} = \int_0^{\infty} A(E)\Phi_{BB}(\mathrm{E})dE$. Here, F_0^{SQRT} and F_0^{SQ} represent F_0^{rad} values derived from SQRT and SQ absorptance model, respectively. For both spectra $\overline{E_g} = 1.1\ eV$ is considered. For the SQRT model, thickness of 2 µm is used.

In the **Fig 4. 6 b**, the equilibrium emission spectra (i.e., $A(E) \times \Phi_{BB}(\mathrm{E})$) for both SQ and SQRT models are illustrated. It can be observed that the SQRT model exhibits a smaller area covered under its curve compared to the SQ model. Since the radiative saturation flux density (F_0^{rad}) is simply the integral of $A(E) \times \Phi_{BB}(\mathrm{E})$ spectrum (see Eq 4.3), a smaller area would correspond to a lower F_0^{rad} compared to F_0^{SQ}. Consequently, according to Eq 4.8, this effect results negative values for $\delta\Delta\mu^{rad}$.

Up to now, the contributions of both Urbach tails and Gaussian band gap fluctuations have been investigated. It is crucial to distinguish Gaussian fluctuations from exponential Urbach

tails. Therefore, before finishing this section, I would like to further discuss the influence of fluctuations and Urbach tail states on the broadening of $A(E)$.

Fig 4. 7 depicts a simulated $A(E)$ spectra using the direct semiconductor *α(E)* spectrum (Eq 4.23). To visualize the effects of exponential Urbach tails and band gap fluctuations, four different cases are investigated here: (I) no fluctuations and negligible Urbach energy, (II) only Urbach tails, (III) only fluctuations, and (IV) the combined influence of both fluctuation and Urbach tail effects.

Since the first derivative of each spectrum needs to be investigated for quantifying σ_A, for the first case, a small Urbach energy (0.1 meV) is included to ensure the continuity of $A(E)$ derivative at the transition energy.

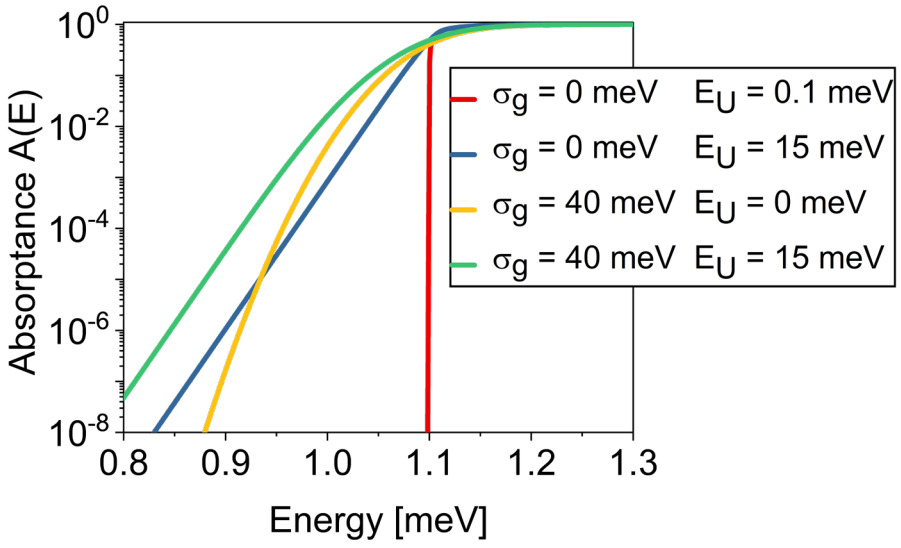

Fig 4. 7. Simulated $A(E)$ spectra with considering the direct semiconductor *α(E)*. Models with and without Gaussian band gap fluctuations, as well as with and without E_U are compared here. Simulation were performed by combining the effect of Gaussian fluctuations with absorption coefficient of direct semiconductor (see Eq 4.20, Eq 4.23 and Eq 4.24). For all cases, the thickness is 2 μm and $\overline{E_g} = 1.1\ eV$.

Before discussing the derivative of each spectrum, comparing the simulated $A(E)$ for last two cases (**Fig 4. 7**), it can be seen that the influence of the Urbach tails is mainly observed at the energy ranges deep inside the bandgap. In this range, the $A(E)$ spectra show perfectly

exponential Urbach decay behavior. On the other hand, at higher energy ranges, the $A(E)$ is mainly influenced by Gaussian band gap fluctuations.

This observation is crucial for experimental quantification of the Urbach energy. In experimental measurements, it is essential to consider energies deep below the band gap energy for Urbach energy extraction to avoid any possible influence from band gap fluctuations.

In **Fig 4. 8**, the first derivative of simulated $A(E)$ spectra for each case is presented. In order to evaluate the broadening of $A(E)$ (i.e, σ_A), a Gaussian fit is applied to each derivative curve.

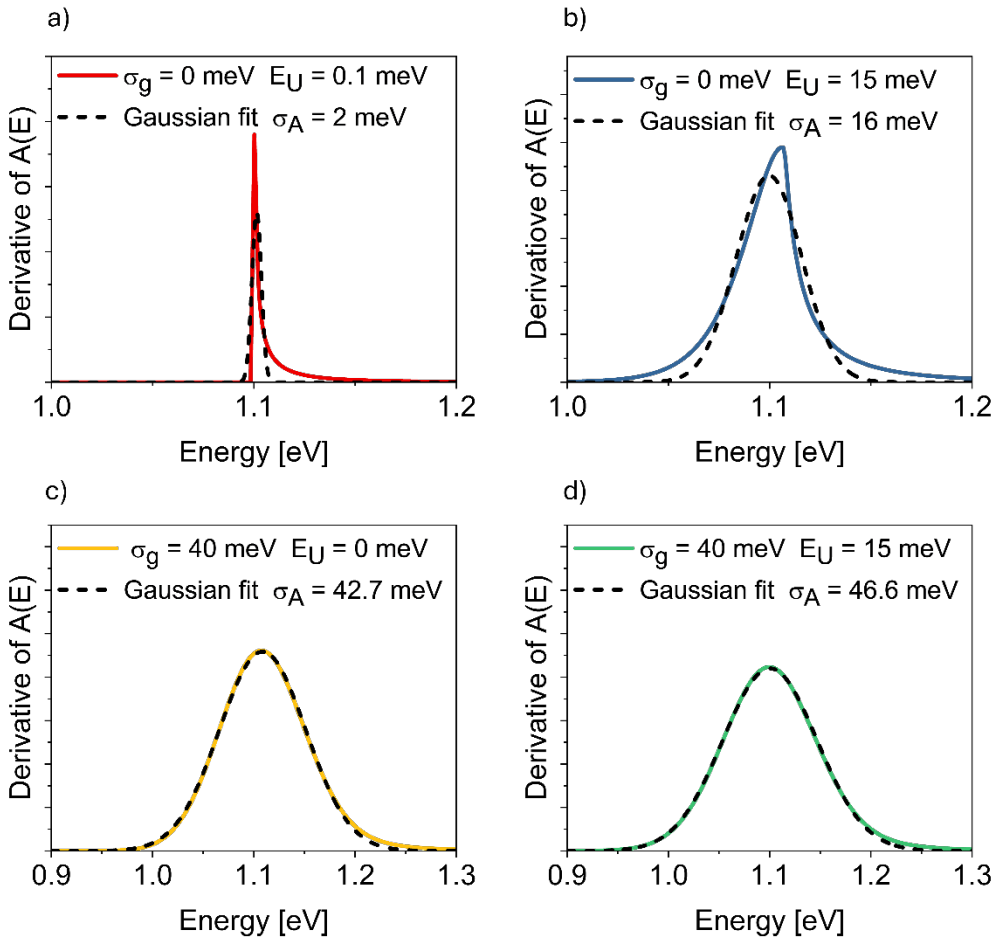

Fig 4. 8. The derivative of simulated $A(E)$ spectra in **Fig 4. 7**, along with corresponding Gaussian fits for the cases: **a)** $\sigma_g = 0$ meV and $E_U = 0.1$ meV, **b)** $\sigma_g = 0$ meV and $E_U = 15$ meV, **c)** $\sigma_g = 40$ meV and $E_U = 0$ meV and **d)** $\sigma_g = 0$ meV with $E_U = 15$ meV. These simulations were performed for absorber thickness of 2 µm and considering $\overline{E_g} = 1.1\ eV$.

In **Fig 4. 8 a**, it can be observed that when Urbach tails are extremely small and there are no band gap fluctuations, the $A(E)$ spectrum still exhibits a broadening of approximately 2 meV.

Obviously, the derivative curve of $A(E)$ deviates significantly from the Gaussian function. However, the Gaussian fit can still give insights about the degree of broadening σ_A. This broadening here mainly results from the square root dependence of the $\alpha(E)$ (See Eq 4.23). Later in the subsequent section, I will show that this broadening is also influenced by absorbers thickness.

In the second case, when the $E_U = 15\ meV$ is introduced, the σ_A increases significantly (**Fig 4. 8 b**). In this case, it can be also seen that the first derivative curve of $A(E)$ deviates substantially from the Gaussian fit.

Furthermore, **Fig 4. 8 c** and **d** illustrate that introducing the fluctuation parameter (σ_g) has more pronounced effect on the σ_A compared to the tail states. In the **Fig 4. 8 c** and **d**, the derivative of $A(E)$ along with Gaussian fits are presented for two last cases with $\sigma_g = 40$ meV, one considering with Urbach tails and another without. Notably, it can be observed that unlike the previous two initial models without fluctuations, the $A(E)$ derivative shows better agreement with Gaussian fits. Additionally, similar to **Fig 4. 4**, **Fig 4. 8 d** also indicates that introduction of Urbach tails leads to a slight increase in σ_A compared to the case where only band gap fluctuations are present.

Overall, at the end of this section, it can be concluded that broadening of the absorption edge is affected by both Urbach tails and Gaussian band gap inhomogeneities. However, their contribution to final σ_A is not identical. The simulations indicated that when the fluctuation parameter σ_g is significantly larger than E_U, the Gaussian band gap fluctuations have dominant effect on the $A(E)$ broadening. On the other hand, in the range of Urbach energies for CIGSe absorbers, the Urbach tails contribute to much lesser extent, and their effect is primarily in the energies deep into the band gap. Generally, increase in both E_U and σ_g would result in higher $\delta\Delta\mu^{rad}$ and lower values for $\Delta\mu^{rad}$, which in turn reduces the V_{OC} of the final device, ultimately decreasing its overall efficiency (see **Fig 4. 3** and **Fig 4. 5**).

4.2.3 Effect of absorber thickness on the $A(E)$ broadening

In previous discussions, all simulations have been conducted with a fixed absorber thickness of $d = 2\ \mu m$. However, as mentioned earlier, the absorber thickness can also have additional contribution to the absorption edge softening. In this section, the thickness effect is investigated

in more detail. Two different cases are studied here: in the first case, simulations are performed for different absorber thicknesses by considering $\sigma_g = 0$ meV (i.e., no fluctuations). In the second approach, the $\sigma_g = 40$ meV is introduced. For simplicity, in both cases, the effect of Urbach tails is excluded (i.e., $E_U = 0$ meV).

Here, the influence of thickness can be related to the effect of a band gap gradient. As demonstrated in **Fig 2. 11** and discussed in **Section 2.5.2**, when a band gap gradient is present, the absorption onset is determined by the minimum band gap position (notch), and the notch width dictates the effective absorption thickness for photons with energies near the minimum band gap energy.

In samples with a V-shaped band gap profile, the effective absorption thickness is restricted to the narrow notch region, meaning that near band edge light absorption is limited to relatively thin section within the absorber. In contrast, for absorbers without any gradient, the effective absorption thickness spans to the entire depth of the material (see again **Fig 2. 11**).

It is worth mentioning that the upcoming simulations offer a simplified representation of the gradient effect, which considers only the influence of notch width and ignores the light absorption at higher energies by other parts of absorber. A more accurate modeling approach has been presented in previous published work of Carron et al [176], where $QE(E)/A(E)$ spectra of CIGSe solar cells with different gradient profiles were simulated using the transfer matrix method.

For the first step of simulations, a simple case of a direct semiconductor is considered with no band gap fluctuations and no Urbach tails (i.e $\sigma_g = 0$ meV and $E_U = 0$ meV). In this particular case, the *α(E)* only exhibits a square root increase above the band gap energy with no sub band gap states (see Eq 4.23). Therefore, the $A(E)$ spectrum can be solely defined by the Beer-Lambert's law (Eq 4.24), and there is no need to solve the complicated integral in Eq 4.20 since there is no band gap distribution (i.e., $\sigma_g = 0$ meV). In **Fig 4. 9,** the $A(E)$ spectra for this simplified case are presented for different absorber thicknesses. It can be observed that for small thicknesses, the $A(E)$ spectra exhibit a gradual increase from the band gap energy (here 1.1 eV) towards higher energy ranges. Once again I have to mention that this behavior is because of the square-root increase of the *α(E)* (see Eq 4.23). Furthermore, as the absorber

thickness increases, the exponential term in Beer-Lambert's law (Eq 4.24) goes to zero. Therefore, $A(E)$ spectrum approaches the step-function, resembling the SQ model. The step function model can also be obtained by having significantly large values of *α(E)*; similar to the thickness effect, with the increase in *α(E)*, the $A(E)$ spectrum would progressively approach the ideal SQ step function model (see again Eq 4.24).

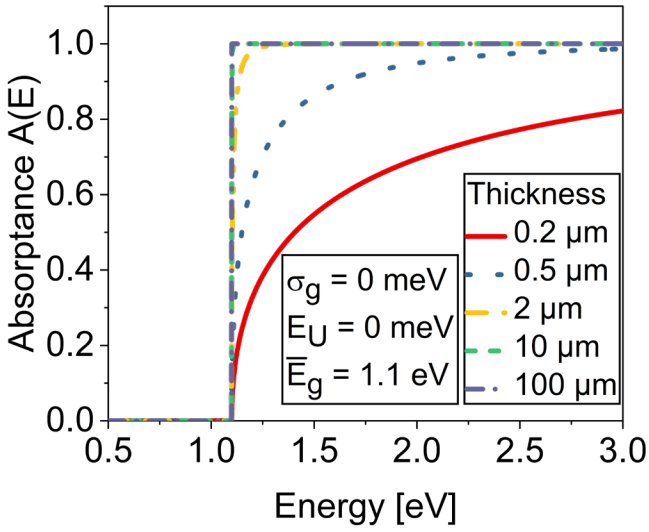

Fig 4. 9 Illustrates the influence of increase in the thickness on the shape and broadening of $A(E)$. This simulated $A(E)$ spectra are obtained considering $\sigma_g =$ 0 meV and $E_U = 0\ meV$, using absorption coefficient of direct semiconductor that exhibits square-root increase above the band gap (see Eq 4.23 and Eq 4.24).

From this simulation, it can be concluded that achieving the ideal SQ model for $A(E)$ would either need a significantly thick absorber or a very large *α(E)* values, while also there should be no influence of Urbach tails and band gap fluctuations (i.e., $\sigma_g = 0$ meV and $E_U = 0\ meV$).

In the next case, the fluctuation parameter σ_g is introduced into the simulations, and the previously discussed model for $A(E)$, which combines the effects of the direct band gap absorption coefficient and band gap fluctuations (see **Section 4.2.2**), is employed for simulations. As a reminder, it is still assumed that $E_U = 0$ meV.

Fig 4. 10 a depicts the simulated $A(E)$ spectra for $\sigma_g = 40$ meV and $\overline{E_g} = 1.1\ eV$, considering effective absorption thicknesses of 0.5 µm , 2 µm and 100 µm. Additionally, in **Fig 4. 10 b** the

first derivative of each spectrum is shown, along with the σ_A obtained from the corresponding Gaussian fit for each case.

One important observation is that when the thickness is small, the broadening of $A(E)$ spectrum (σ_A) extracted from Gaussian fit is larger than the defined fluctuation parameter (σ_g) (i.e. $\sigma_A > \sigma_g$). Additionally, the $A(E)$ inflection point deviates from the defined average band gap $\overline{E_g} = 1.1\ eV$ (see **Fig 4. 10 b**). It can be also seen that the derivative of simulated $A(E)$ spectrum deviates significantly from the Gaussian shape when the thickness is small. However, as the thickness increases, the $A(E)$ converges to the error function model for. For thickness of 100 µm, the $A(E)$ derivative shows perfect Gaussian shape with $\sigma_A = \sigma_g = 40$ meV and inflection point same as $\overline{E_g} = 1.1\ eV$.

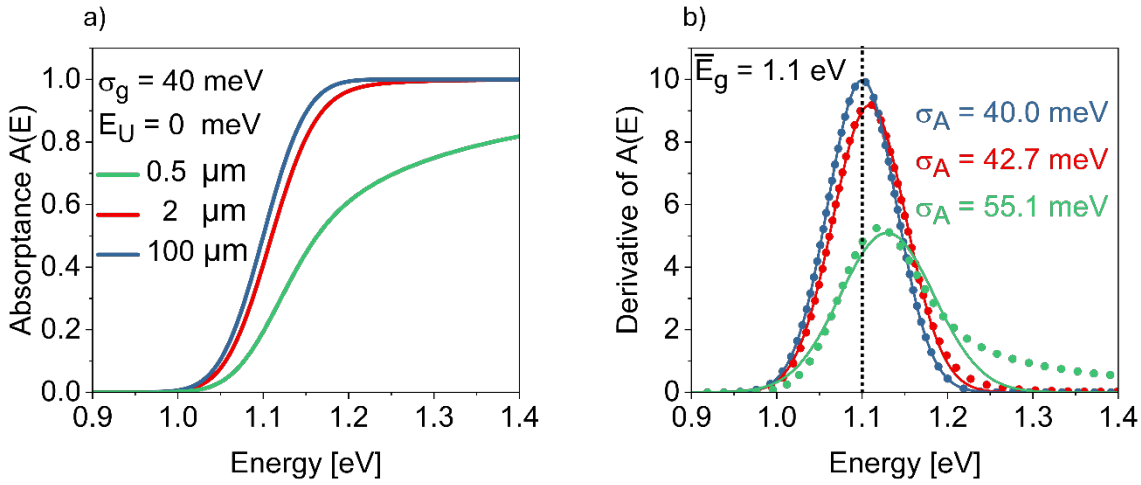

Fig 4. 10 a) $A(E)$ spectra simulated using combined effect of Gaussian band gap fluctuations and absorption coefficient of direct semiconductor with $E_U = 0$ meV (See **Section 4.2.2**), for the cases with 0.5 µm, 2 µm and 100 µm thicknesses. A specific color code is assigned to each thickness **b)** The first derivative of the simulated $A(E)$ spectra (dotted lines) along with the σ_A values extracted from Gaussian fit to each derivative. Gaussian fits are represented by continuous lines, and the $\overline{E_g}$ position is indicated with black dotted line.

According to these simulated spectra, it becomes evident that limited absorber thicknesses can introduce additional broadening to the $A(E)$ spectrum. Nevertheless, as the thickness increases, this effect vanishes, and the broadening of $A(E)$ becomes primarily dominated by the fluctuation parameter, σ_g.

This simplified approach provides insights into the impact of notch thickness on the absorption edge broadening effect. In CIGSe thin-film solar cells, the absorbers thickness is typically around 2 μm. However, in the presence of a Ga gradient, the notch, which determines the near band edge absorption, has much smaller width (around 200 nm to 500 nm). As shown in the simulations (**Fig 4. 10**), even with a 2 μm thickness, the finite thickness effect still contributes to absorption edge broadening.

Once again, I have to mention that these simulations consider very simplified model for the notch absorption effect, where the absorption effect of high band gap energy regions within the absorber is not considered.

In the **Chapter 5**, experimental results and a meta-analysis of existing literature data will further confirm this hypothesis, showing that absorbers with a graded band gap profile and narrow notch width exhibit a stronger broadening compared to those with uniform band gap profile across the depth.

4.3 Summary and conclusion of Chapter 4

At the beginning of this chapter, the generalized detailed balance model was introduced. This model enables the determination of the radiative limit (both $\Delta\mu^{rad}$ and V_{OC}^{rad}) for absorbers and solar cells with non-step-like $A(E)/QE(E)$ spectra. Additionally, this model enables the quantification of $\Delta\mu/V_{OC}$ loss components associated with absorption edge broadening, incomplete absorption, and collection losses.

Subsequently, simulations were conducted to explore the impact of band gap inhomogeneities (fluctuations) and Urbach tails on the shape of $A(E)$. Furthermore, generalized detailed balance formulas were employed to quantify the $\Delta\mu^{rad}$ and $\delta\Delta\mu^{rad}$ for each simulated $A(E)$ spectrum.

Overall, it was observed that both Urbach tails and band gap inhomogeneities (fluctuations) can cause broadening of the $A(E)$ spectum and increase $\delta\Delta\mu^{rad}$. However, influence of fluctuations is dominant and contributes more strongly to the $A(E)$ broadening. On the other hand, Urbach tails have minimal effect on the shape of $A(E)$ within the range of E_U values for CIGSe absorbers. The influence of tail states are only noticeable at significantly lower energies well below the band gap, and their contribution to $\delta\Delta\mu^{rad}$ is also small.

At the end, influence of absorber thickness was investigated. It was observed that a decrease in the thickness would enhance the broadening of the absorption edge.

While this chapter totally focused on theoretical analysis, **Chapter 5** will primary focus on the experimental quantification of $\Delta\mu$ and V_{OC} losses.

5 Experimental quantification of V_{OC} losses in CIGSe solar cells

In **Chapter 4**, the theory of the generalized detailed balance model was introduced. It was shown that $V_{OC}/\Delta\mu$ losses can be separated into distinct loss components: (i) radiative losses resulting from the broadening of the absorption edge, (ii) generation and short-circuit losses due to light absorption losses and incomplete charge collection, and (iii) non-radiative losses caused by the presence of non-radiative recombination channels, such as deep defects in the band gap or interface/surface recombination activities.

In this chapter, the theoretical formulas discussed in **Chapter 4** will be applied to the experimentally measured $A(E)$ and $QE(E)$ spectra, and all $\Delta\mu$ /V_{OC} loss components will be quantified for both absorber thin films and complete devices.

This chapter consists of three main sections.

Section 5.1 of this chapter focuses on the experimental quantification of $\Delta\mu$ losses using generalized detailed balance model based on optical approach (discussed in **Section 4.1.1**). It is worth mentioning again that thin-film absorbers alone are sufficient for $\Delta\mu$ loss analysis, and there is no need to make functional devices. In this section, the $A(E)$ spectra of CIGSe absorbers are first determined through a combination of PL and photospectometric measurements. Using the obtained $A(E)$ spectra, $\Delta\mu^{rad}$ and all $\Delta\mu$ loss components, including radiative losses ($\delta\Delta\mu^{rad}$), generation losses ($\delta\Delta\mu^{Gen}$), and non-radiative losses ($\delta\Delta\mu^{nr}$) are quantified for CIGSe absorbers. It is important to note that, since absolute PL measurements are carried out in this thesis, $\delta\Delta\mu^{nr}$ for each sample is determined using the extracted Y_{PL} (see Eq 4.10).

This loss analysis ultimately results in the final $\Delta\mu$ values. Notably, it will be demonstrated that the $\Delta\mu$ values extracted from this method are in excellent agreement with those obtained directly from a linear fit to the high-energy wing of Planck's generalized law [29, 34, 77].

Section 5.2 of this chapter uses optoelectrical measurements to determine V_{OC} losses for complete solar cells (see **Section 4.1.2**). By employing both absolute EL and direct $QE(E)$ measurements, the V_{OC} losses are quantified for CIGSe devices. It is important to emphasize

that for non-radiative loss analysis, all EL measurements were performed under absolute condition. Consequently, the non-radiative V_{OC} losses can be reliably determined using the Y_{EL} extracted from these measurements (see Eq 4.17).

In this chapter, the emphasis is on the influence of the band gap gradient on radiative losses (both $\delta\Delta\mu^{rad}$and δV_{OC}^{rad}). In **Sections 2.5.2** and **4.2.3**, it was mentioned that the presence of the gradient can reduce the effective absorption thickness. This effect can potentially enhance the broadening of $A(E)$ and, thus, increase the $\delta\Delta\mu^{rad}$.

It is worth mentioning that the band gap gradient is not exclusive to CIGSe solar cell technology. CdSeTe [177, 178] and emerging CZTSSe [179] technologies also employ graded band gap technology to suppress the surface recombination and enhance device performance. Therefore, understanding the impact of band gap gradient on the final V_{OC} of solar cells is essential. To investigate this, comprehensive $V_{OC}/\Delta\mu$ loss analyses are conducted on CIGSe samples with and without a Ga gradient. In particular, it will be shown that CIGSe samples with a Ga gradient exhibit a broader $A(E)/QE(E)$ spectrum and can experience up to 16 meV of additional radiative losses compared to the non-graded absorbers.

The final section of this chapter, **section 5.3**, explores the origins of the radiative losses and absorption edge broadening in CIGSe absorbers. This section presents an analytical analysis of 19 samples, exploring how variations in CGI and GGI concentrations, as well as Urbach tails, influence the broadening of the absorption onset in samples with and without a Ga compositional gradient. Additionally, a literature review and meta-analysis of published CIGSe data are presented. This meta-analysis study demonstrates that the $A(E)$ broadening is directly linked to the steepness of the Ga gradient profile in the absorbers. Specifically, when the minimum band gap region is sufficiently thick and extends significantly through the depth, the broadening of $A(E)/QE(E)$ is weaker compared to the samples where the minimum band gap position is restricted within a narrow region in the absorber thickness.

Furthermore, our colleagues from Cambridge University have conducted high-spatial-resolution cathodoluminescence (CL) analyses on selected CIGSe absorbers. These analyses provide detailed microscopic insights into the depth-dependent band gap variations, as well as an assessment of in-plane lateral band gap fluctuations. The CL results revealed that Ga-graded

samples not only exhibit the expected band gap variations through their thickness and a narrower absorption region, but also show indications of stronger lateral band gap inhomogeneities compared to samples with a uniform Ga distribution.

At the time of writing this thesis, the results presented in this chapter have been submitted for publication. A preprint of the prepared manuscript is available online [149]. All the figures, tables, and results are reproduced from this preprint under **CC BY 4** license. The upcoming discussions follows my manuscript structure.

5.1 $\Delta\mu$ analysis for samples deposited on SLG

5.1.1 $\Delta\mu$ extraction from generalized detailed balance model

At the beginning of the experimental section, I start the $\Delta\mu$ loss analysis for several absorbers deposited on transparent soda-lime glass (SLG). More details regarding the deposition process of these samples have already been explained in **Section 3.1**.

To prevent surface oxidation and degradation, all samples were covered with a CdS buffer layer (see **Section 3.2**), and all upcoming $A(E)$ and PL measurements were performed on CdS-covered absorbers.

These absorbers cannot be processed into complete working devices, since they are missing the window layer and metallic back contact. However, because they are deposited on the transparent SLG substrates, their $A(E)$ can be reliably measured over a wide spectral range using UV-Vis photospectrometer (see **Section 3.6**). Later, I will demonstrate that these UV-Vis measurements become unreliable in the sub-band gap absorption region. To overcome this limitation, additional PL measurements need to be employed to reconstruct the low-energy edge of $A(E)$.

With the use of the full range $A(E)$ spectra, the generalized detailed balance model based on the optical approach (outlined in **Section 4.1.1**) can be employed for $\Delta\mu$ loss analysis. Additionally, this approach enables a detailed analysis of optical losses with excluding effects of non-ideal charge transport and carrier collection losses that may occur in the complete devices.

In this section, five samples from different processes are investigated. **Table 5.1** summarizes the key properties of these absorbers, including their names, the presence of a Ga gradient, as well as CGI and GGI values obtained from EDX measurements. For simplicity, samples with a non-graded band gap profile are labeled as **NG**, while those with a band gap gradient are labeled as **BGG**.

For some selected samples, SIMS measurements were performed to investigate the Ga gradient profile through the depth (see **Appendix B1**). The presence of a V-shape Ga gradient in the E-BGG sample and a uniform Ga profile in the D-NG absorber were confirmed by these SIMS measurements.

Table 5.1 Name, CGI, GGI and presence of Ga gradient for absorbers deposited on transparent SLG substrate. CGI and GGI were determined from EDX using acceleration voltage of 20 KV.

Sample Name	***CGI***	***GGI***	***Gradient***
A-NG	*0.90*	*0.20*	*No*
B-NG	*0.94*	*0.26*	*No*
C-BGG	*0.88*	*0.30*	*Yes*
D-NG	*0.88*	*0.25*	*No*
E-BGG	*0.94*	*0.20*	*Yes*

To obtain the $A(E)$ profile for each sample, transmittance and reflectance measurements were carried out separately using UV-Vis photospectrometer. In **Section 3.6**, the details of the these measurements were discussed. It was shown that using a UV-Vis spectrometer, the transmittance $T(E)$ and reflectance $R(E)$ spectra can be measured for each sample independently. Subsequently, the $A(E)$ spectra can be obtained using the simple equation $A(E) = 1 - T(E) - R(E)$.

As shown in **Fig 3. 11**, the transmittance (T) and reflectance (R) measurements cover a wide spectral energy range, enabling accurate extraction of the $A(E)$ profile across most of the

photon energy ranges. However, these measurements are less reliable in the low-energy decay region (i.e., energies below the band gap) [175]. In **Fig 3. 11**, it can be seen that the $A(E)$ spectra extracted from the spectrometer is distorted and do not exhibit the expected decay at low energies; instead, they level off at low energy region. This effect is likely due to light scattering from the rough CIGSe surface and/or the possible influence of the CIGSe/SLG interface.

On the other hand, the extraction of $\Delta\mu^{rad}$ and $\delta\Delta\mu^{rad}$ requires detailed knowledge of the $A(E)$ shape across the entire spectral range, including both low-energy decay and high-energy region.

To calculate $\Delta\mu^{rad}$ and $\delta\Delta\mu^{rad}$, the radiative saturation flux density (F_0^{rad}) needs to be determined (see Eq 4.3 and Eq 4.8). For the F_0^{rad} calculation, the $A(E)$ spectrum is multiplied by the blackbody radiation spectrum ($\Phi_{BB}(E)$). Since the $\Phi_{BB}(E)$ spectrum increases substantially at the low-energy range, any inaccuracies or a non-decreasing $A(E)$ in this region are heavily weighted in the F_0^{rad} integral, leading to unrealistically large values for F_0^{rad}. Therefore, an accurate determination of the $A(E)$ profile across the entire spectral range is essential for precise F_0^{rad} calculation.

To address this limitation, additional photoluminescence (PL) measurements are employed to reconstruct the low-energy decay portion of the $A(E)$ spectrum. In contrast to photospectrometry measurements, PL measurements are highly sensitive in the low-energy decay slope, making them ideal for extracting ultra-low values of $A(E)$ in this part of the spectrum [38, 68, 169, 175].

By considering the Planck's generalized law (Eq 2.52), and using the PL emission spectra (Φ_{PL}) of each absorber, the non-absolute $A(E)$ spectra from PL measurements can be obtained using the following relation:

$$A^{PL}(E) \propto \frac{\Phi_{PL}}{\Phi_{BB}} \qquad (\boldsymbol{Eq\ 5.1})$$

Here, $A^{PL}(E)$ denotes the $A(E)$ spectrum obtained from PL measurements.

Subsequently, in specific energy ranges where both $A^{PL}(E)$ and the directly measured $A^{dir}(E)$ provide reliable values, the $A^{PL}(E)$ spectrum can be scaled to match $A^{dir}(E)$. This approach enables the reconstruction of the full range $A(E)$ spectrum, extending from low to high energy ranges.

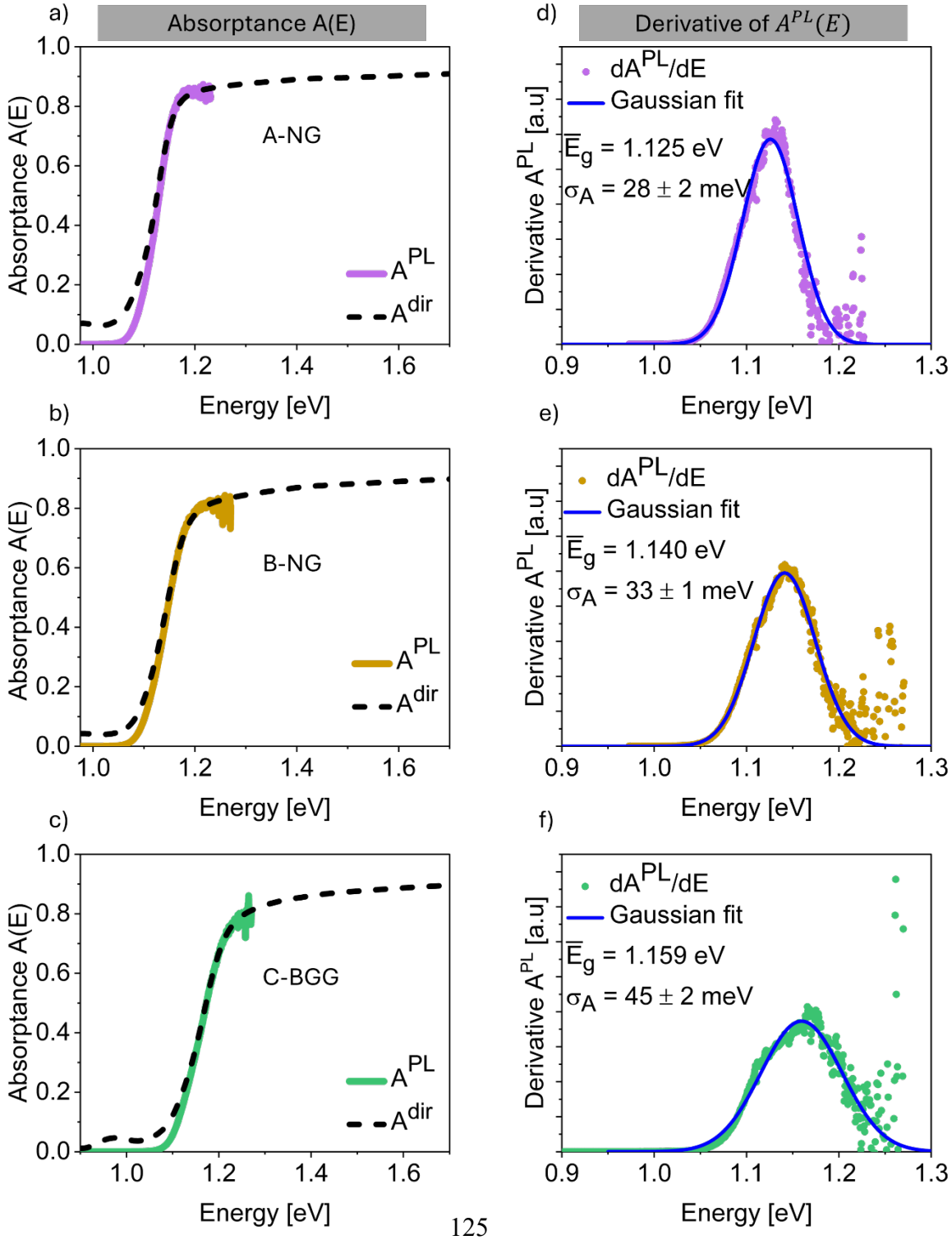

Fig 5. 1 a), b), and **c)** illustrate the $A(E)$ spectra for CIGSe A-NG, B-NG and C-BGG samples, respectively. These spectra were obtained from PL measurements ($A^{PL}(E)$) and direct photospectrometric measurements ($A^{dir}(E)$). **d)**, **e)** and, **f)** depicts the first derivative of the $A^{PL}(E)$ spectra for A-NG, B-NG and C-BGG samples (see **Table 5.1**), respectively. The $\overline{E_g}$ and σ_A here for each case are extracted from Gaussian fit to this first derivative. The σ_A values are extracted from multiple fitting ranges covering the low energy and high energy sides, and average σ_A is presented along with error bars indicating standard deviation. To enhance visualization, smoothed $A^{PL}(E)$ profiles were used to extract these derivatives.

It is important to highlight that obtaining the non-absolute $A^{PL}(E)$ does not require any knowledge about $\Delta\mu$ value. In Planck's generalized law (Eq 2.52), the exponential term containing $\Delta\mu$ acts only as a scaling factor. Therefore, even without knowing the numerical $\Delta\mu$ values, the shape of the non-absolute $A^{PL}(E)$ can still be obtained using the PL spectrum and the measurements temperature. It is important to mention that, for all upcoming analysis, the temperature of these absorbers was measured separately using thermometer and thermal camera, and it was 296 K.

In **Fig 5. 1** the left column presents the $A(E)$ spectra obtained from both $A^{PL}(E)$ and $A^{dir}(E)$ measurements for A-NG, B-NG and C-BGG absorbers (see **Table 5.1)**. Additionally, the $A(E)$ measurements of two other samples are illustrated in **Appendix B2**. It can be observed that, within certain energy ranges, the $A^{PL}(E)$ spectrum has perfect agreement with the directly measured $A^{dir}(E)$. However, in the low energy region, $A^{dir}(E)$ becomes already distorted and unreliable, while in the high-energy range, the $A^{PL}(E)$ spectrum is affected by measurement noise due to a decrease in the PL counts.

By combining these two spectra and excluding their unreliable parts, the full-range of $A(E)$ spectrum can be reconstructed. In the next steps, this full range spectrum is used for the upcoming $\Delta\mu$ loss calculations.

At this stage, with the use of complete $A(E)$ spectrum and measurement temperature (T), the $\Delta\mu^{rad}$ can be already determined using Eq 4.3. However, it is important to emphasize once again that having $A(E)$ alone is not sufficient for calculating the relative $\Delta\mu$ losses. These losses must be evaluated with respect to the SQ limit of the reference band gap (E_g) [28, 31] (see Eq 4.7 and Eq 4.8). Therefore, for precise loss analysis, it is crucial to determine the band

gap energy. Subsequently, all $\Delta\mu$ losses can be obtained using this band gap energy as a reference point for calculations.

Published reports propose various methods for the band gap energy extraction, such as using a Tauc plot method [31], approximating it from the PL maximum emission energy [29], and, in cases where the derivative of $A(E)$ exhibits a symmetrical shape, the band gap can be identified from the inflection point of the $A(E)$ spectrum [28, 31]. In this thesis, the latter approach is adopted, where the band gap of the absorbers is extracted from the inflection point of the $A(E)$ spectrum, and all $\Delta\mu$ losses are subsequently evaluated with respect to the SQ limit of this inflection point.

In this method, a Gaussian fit is applied to the derivative of each measured $A(E)$ spectrum, with the maximum point of this fit taken as the reference band gap point for further calculations. Additionally, the broadening of the $A(E)$ spectra, σ_A, is determined from the width parameter obtained from this Gaussian fit.

This method is very similar to the error function approach discussed in **Section 4.2.1**, where the $A(E)$ spectra are described by a complementary error function model, and their derivatives show a Gaussian distribution centered at the average band gap energy ($\overline{E_g}$) (see also Eq 4.22 and **Fig 4. 2**). Therefore, similar to the calculations performed for the error function model, the SQ limit of this $\overline{E_g}$ can be used as a reference point for a reliable quantification of $\Delta\mu$ losses.

It is worth mentioning once again that the error function model was initially developed for the case of lateral band gap fluctuations (see **Section 4.2.1** and references [166, 167]), where σ_A was same as the defined fluctuation parameter σ_g (i.e., $\sigma_g = \sigma_A$), and it quantifies the extent of band gap inhomogeneities (fluctuations) (see again **Fig 4. 2**).

However, in reality, the CIGSe samples exhibit not only lateral band gap fluctuations due to In–Ga alloy disorder, but also inhomogeneities through the depth. These depth inhomogeneities can arise from an intentionally introduced Ga gradient in the material or unintentional effects such as compositional fluctuations.

Moreover, as discussed in the **Sections 4.2.2** and **4.2.3**, the σ_A can also depend on multiple other factors such as Urbach tails and absorber thickness. Therefore, in this context, this error

function model is used only as a practical tool to determine the average band gap energy ($\overline{E_g}$), and the obtained σ_A indicates how the broadening of the measured $A(E)$ deviates from the ideal SQ step function.

It is thus crucial to clarify that, in this case, σ_A does not directly reflect the extent of lateral band gap inhomogeneities. Instead, the Gaussian fit just represents the distribution of step-function-like band gaps. Even in some cases where the original $A(E)$ derivatives slightly from the Gaussian shape, still valuable information can be obtained by using this Gaussian fit approach.

Later in **Section 5.3**, the contributions of different factors to σ_A will be discussed in more details.

The right column in **Fig 5. 1** presents the first derivative of the $A^{PL}(E)$ spectra for A-NG, B-NG, and C-BGG samples. The Gaussian fit, along with the extracted $\overline{E_g}$ and σ_A values for each spectrum are displayed in the inset of each figure. Additionally, the derivative of $A^{PL}(E)$, $\overline{E_g}$, and σ_A values for two other samples, D-NG and E-BGG, are illustrated in **Appendix B2**.

It is crucial to mention that, for the purpose of band gap and broadening extraction, I used the derivative of $A^{PL}(E)$ rather than $A^{dir}(E)$. This is because the $A^{dir}(E)$ spectra tend to become distorted near the absorption onset energy. In **Appendix B2**, I show that although the inflection point $\overline{E_g}$ can also be extracted reliably from the $A^{dir}(E)$, quantification of σ_A remains challenging with these measurements, as they get already distorted in the energy ranges very close to the absorption edge.

At this stage, the accurate shape of $A(E)$ across the entire spectral range, as well as the $\overline{E_g}$ for each sample, have been determined. This information can now be used to conduct further calculations and extract the $\Delta\mu$ losses.

It is crucial to note that determining the band gap energy with 1 meV accuracy can be tricky with this Gaussian fit approach. However, in this analysis, the band gap values serve only as a reference point for performing loss calculations. For the minimal errors in the band gap determination, the resulting $\Delta\mu$ losses and the SQ limit would compensate for each other, ensuring that the final $\Delta\mu^{rad}$ remains unchanged, as it is independent of the defined band gap

and only depends on $A(E)$ and temperature (see Eq 4.3). Nonetheless, as will be demonstrated later, this approach provides a reliable tool for quantifying $\Delta\mu$ losses and comparing different absorbers.

According to Eq 4.4, to quantify the $\Delta\mu$ and its losses, the first step involves calculating qV_{OC}^{SQ} of the reference band gap (here $\overline{E_g}$) using the Eq 2.47.

Once again it is important to highlight that all PL analysis were conducted at room temperature (here 296 K). Therefore, the corresponding calculations for SQ limit and $\Delta\mu$ losses are all performed at T = 296 K. The values of the $\overline{E_g}$ and corresponding qV_{OC}^{SQ} for each samples are summarized in **Table 5.2** .

In the next step, the $\delta\Delta\mu^{Gen}$ and $\delta\Delta\mu^{rad}$ are quantified using Eq 4.7 and Eq 4.8, respectively, and their values are also presented in **Table 5.2** .

Table 5.2 Illustrates σ_A, average band gap energy ($\overline{E_g}$), and $\Delta\mu$ with its associated losses for samples deposited on transparent SLG substrate. $\Delta\mu$ values were determined using the generalized detailed balance model (see Eq 4.9).

Sample Name	$\boldsymbol{\sigma_A}$ ***(meV)***	$\overline{\boldsymbol{E_g}}$ ***(eV)***	$\boldsymbol{qV_{OC}^{SQ}}$ ***(meV)***	$\boldsymbol{\delta\Delta\mu^{rad}}$ ***(meV)***	$\boldsymbol{\delta\Delta\mu^{Gen}}$ ***(meV)***	$\boldsymbol{\Delta\mu^{rad}}$ ***(meV)***	$\boldsymbol{\delta\Delta\mu^{nr}}$ ***(meV)***	$\boldsymbol{\Delta\mu}$ ***(meV)***
A-NG	*28 ± 2*	*1.125*	*885.0*	*13.5*	*2.8*	*868.7*	*207.1*	*661.6*
B-NG	*33 ± 1*	*1.140*	*898.8*	*13.0*	*3.3*	*882.5*	*220.5*	*662.0*
C-BGG	*45 ± 2*	*1.159*	*916.4*	*22.9*	*3.3*	*890.2*	*213.2*	*677.0*
D-NG	*36 ± 1*	*1.131*	*890.5*	*15.8*	*3.4*	*871.3*	*212.2*	*659.1*
E-BGG	*40 ± 2*	*1.109*	*869.9*	*19.0*	*3.8*	*847.1*	*225.6*	*621.5*

As mentioned earlier, the $\delta\Delta\mu^{rad}$ mainly depends on the broadening of $A(E)$ (i.e, deviation from step function). In **Sections 4.2.1** and **4.2.2,** it was shown that the $\delta\Delta\mu^{rad}$ increases with increasing σ_A.

Fig 5. 2 illustrates the relationship between σ_A and the extracted $\delta\Delta\mu^{rad}$ for each sample. Despite some scatter, a broader $A(E)$ spectrum (i.e, larger σ_A) results in a higher values for $\delta\Delta\mu^{rad}$.

As an initial observation, the C-BGG and E-BGG samples, which have a Ga compositional gradient through their thickness, exhibit larger values of σ_A and $\delta\Delta\mu^{rad}$. In the upcoming sections, more details regarding the contribution of Ga gradient to this broadening will be discussed.

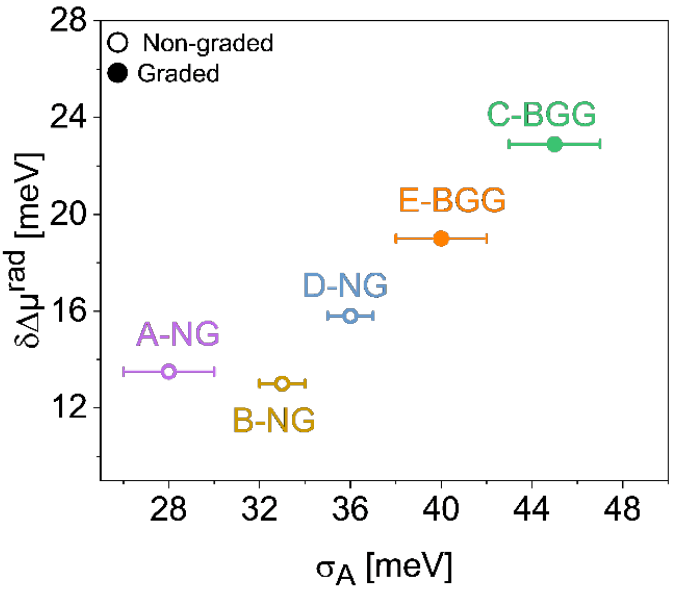

Fig 5. 2 Illustrates calculated $\delta\Delta\mu^{rad}$ versus σ_A for samples deposited on transparent SLG substrate. The σ_A and $\delta\Delta\mu^{rad}$ values for each sample are summarized in **Table 5.2** .

Furthermore, $\delta\Delta\mu^{Gen}$ is mainly attributed to the photon absorption losses (see Eq 4.7). As shown in **Fig 3. 11**, UV-Vis measurements for B-NG sample indicate that at energies significantly above the band gap, the reflection is around 10% to 15%. A similar reflectance was observed for four other absorbers. In **Fig 5. 1**, it can be observed that all $A(E)$ spectra tend to plateau at values between 0.85 to 0.9 for energies well above the $\overline{E_g}$, and all samples reach

to similar plateau levels. Consequently, $\delta\Delta\mu^{Gen}$ values for these samples fall within a similar range of approximately 3 meV to 4 meV (see **Table 5.2**).

To obtain the final $\Delta\mu$ value, in the last step, the most important loss mechanism in the most solar cells, the non-radiative $\Delta\mu$ losses ($\delta\Delta\mu^{nr}$), are determined using the measured photoluminescence quantum yield (Y_{PL}) (see Eq 4.10 and Eq 4.11).

It is important to note that under laboratory conditions, Y_{PL} is measured using monochromatic laser light rather than solar spectrum. Therefore, the Eq 4.11 is transformed to the following form:

$$Y_{PL} = \frac{\int_0^\infty \Phi_{\mathrm{PL}}(E)\,dE}{F_{Gen}^{Sun}} = \frac{\int_0^\infty \Phi_{\mathrm{PL}}(E)\,dE}{F_{Gen}^{Laser}} \qquad (\boldsymbol{Eq\ 5.2})$$

Here, F_{Gen}^{Laser} represents the generation laser flux density (i.e., the absorbed laser flux density).

Section 3.3.1 provides details regarding the laser intensity calibration. For extracting the $\Delta\mu$ and its associated losses, the laser intensity was calibrated to have an incident flux (F_{inc}^{Laser}) equivalent to 1 sun SQ flux density for a defined band gap. (i.e., $F_{inc}^{Laser} \approx F_{Gen}^{SQ} = \int_{E_g}^{\infty} \Phi_{Sun} dE$). As the $A(E)$ spectra of each sample is separately measured with UV-Vis measurements, thus $A(E)$ value at the laser energy $A(E_{laser})$ is known. Therefore, the F_{Gen}^{Laser} (i.e., absorbed Flux density) can be determined using $F_{Gen}^{Laser} = A(E_{laser})F_{inc}^{Laser}$.

It is crucial to mention that using monochromatic laser light instead of solar irradiance can introduce potential discrepancies in the $\delta\Delta\mu^{nr}$ calculations and final $\Delta\mu$ extraction. This is because the solar spectrum spans over a broad spectral range (see **Fig 2. 2**), and therefore, the absorptance of solar photons varies with energy. On the other hand, the laser light is emitted at a single energy. However, it is shown in the **Appendix B3** that this discrepancy is extremely small and does not affect the final results.

This Y_{PL} was measured for each sample independently under one sun incident laser flux density. Subsequently, respective non-radiative $\Delta\mu$ losses ($\delta\Delta\mu^{nr}$) for each sample were quantified using Eq 4.10. The corresponding $\delta\Delta\mu^{nr}$ values for all investigated samples are summarized in the **Table 5.2** .

It is worth mentioning that for CIGSe absorbers, it is crucial to obtain the Y_{PL} under 1 sun laser incident flux. The Y_{PL} of CIGSe absorbers depends on the excitation laser flux and varies under different incident laser intensities [55, 106, 180, 181]. In **Fig 5. 3 a** , intensity dependent PL measurements for B-NG sample is displayed for laser intensities ranging from 0.5 sun to 8 sun. similar measurements were performed for all other samples, and at each intensity the Y_{PL} were calculated using Eq 5.2**.** In **Fig 5. 3b**, It can be clearly seen that the Y_{PL} is not constant under different excitation fluxes. As the laser intensity increases, the Y_{PL} in CIGSe samples also rises, confirming its dependence on the incident laser excitation flux.

The Y_{PL} of a CIGSe sample depends on the optical diode factor (ODF). For a p-type doped semiconductor, an ODF of unity is expected [106, 180, 181]. However, it is well known that CIGSe absorbers exhibit ODF values greater than one (ODF > 1) [55, 106, 180, 181]. The ODF > 1 would result in the increased Y_{PL} with excitation. This behavior is primarily related to the presence of metastable defects in the CIGSe absorbers [106, 180, 181].

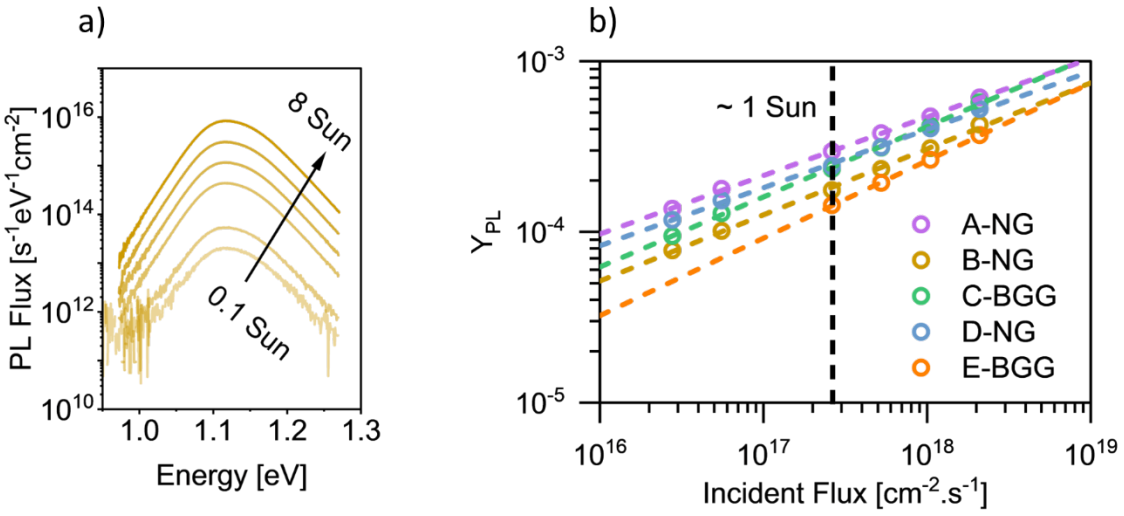

Fig 5. 3 a) Intensity dependent PL spectra for CIGSe B-NG sample. The arrow direction illustrates increase in the incident laser flux. **b)** Y_{PL} values extracted for all samples deposited on SLG under increased laser intensity.

Nevertheless, in **Chapter 4**, it was illustrated that the generalized detailed balance model for both optical and optoelectrical approaches considers one sun excitation flux density. Therefore,

for experimental quantification of $\Delta\mu$ losses, it is necessary to use Y_{PL} and $\delta\Delta\mu^{nr}$ under one sun laser excitation condition.

At this stage, $\Delta\mu^{rad}$ and all $\Delta\mu$ loss components for each absorber have been quantified. In the next step, by applying Eq 4.9, the final $\Delta\mu$ values for each sample are calculated, and the results are summarized in **Table 5.2** .

Furthermore, **Fig 5. 4** provides an overview of the share of each loss mechanism to the total $\Delta\mu$ of each sample.

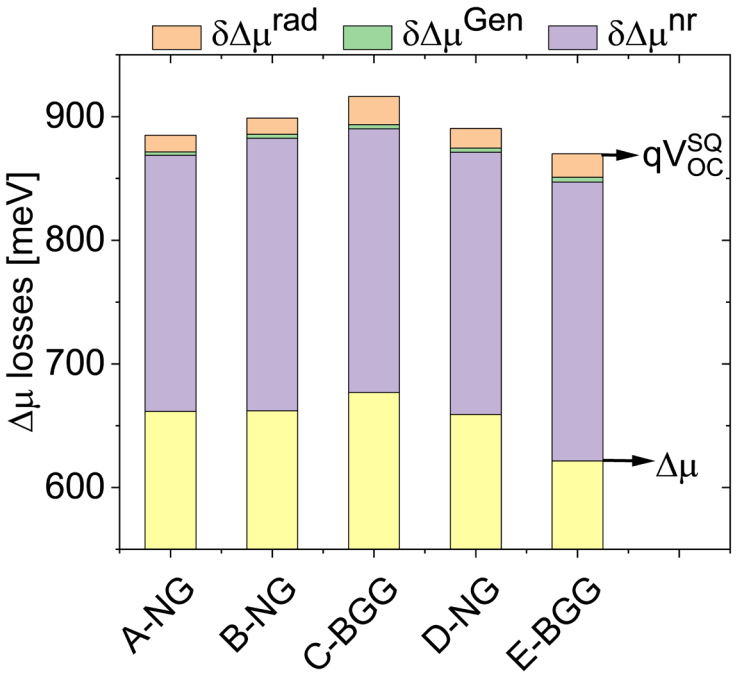

Fig 5. 4 $\Delta\mu$ losses obtained for samples deposited on SLG substrate. All the losses and final $\Delta\mu$ values are summarized in **Table 5.2** .

Overall, it can be observed that the main loss mechanism that pushes the final $\Delta\mu$ far below than SQ limit is non-radiative losses ($\delta\Delta\mu^{nr}$) (see **Fig 5. 4** and **Table 5.2**). These non-radiative losses ($\delta\Delta\mu^{nr}$) primarily occur within the bulk of the material or at the surface and interfaces regions.

As mentioned in **Section 2.5.2**, a Ga gradient in CIGSe solar cells is necessary to mitigate the non-radiative recombination at the back interface. However, since these samples are deposited

on SLG substrates, the back surface is effectively passivated for all cases, regardless of the presence or absence of a Ga back gradient. This is because SLG is a high band gap material, and SLG/CIGSe interface exhibits significantly lower recombination activities compared to the cases where CIGSe is in direct contact with metallic Mo back contact [106]. Consequently, it can be observed that presence of Ga gradient has almost no effect on the non-radiative losses, and all samples show similar values for $\delta\Delta\mu^{nr}$. In contrast, in the upcoming **Section 5.2**, I will show that, unlike the samples on SLG substrates, those deposited on Mo require a backside Ga gradient to effectively suppress the non-radiative recombination activities at the back interface.

In any case, it is important to mitigate the non-radiative recombination activities to achieve higher $\Delta\mu$ in the CIGSe absorbers. For state of the art CIGSe absorbers, this $\delta\Delta\mu^{nr}$ is less than 120 meV [11, 29, 33].

Significant reduction in non-radiative losses can be achieved by performing heavy alkali PDT after the CIGSe growth process [11, 33, 111]. In **Chapter 6**, strategies based on heavy alkali PDT will be discussed, showing their effectiveness in enhancing the $\Delta\mu$ by reducing $\delta\Delta\mu^{nr}$.

On the other hand, the contribution of $\delta\Delta\mu^{rad}$ and $\delta\Delta\mu^{Gen}$ to overall losses are much smaller compared to $\delta\Delta\mu^{nr}$. In the case of radiative losses ($\delta\Delta\mu^{rad}$), it can be observed that it falls within the range of 13 meV to 23 meV.

Initial observations indicate that samples with a Ga compositional gradient exhibit slightly higher $\delta\Delta\mu^{rad}$ values compared to the absorbers with uniform Ga distribution. This is because they have slightly higher values for σ_A (see **Fig 5. 2**). This behavior may be associated with the small notch region in the graded absorbers, as discussed in **Section 4.2.3**. However, as mentioned earlier in **Chapter 4**, σ_A can also be influenced by multiple other factors, including alloy fluctuations, tail states and Cu poor composition. In the upcoming discussions in **Section 5.3**, the correlation between the band gap gradient and broadening will be explored in more detail.

The generation losses $\delta\Delta\mu^{Gen}$ are approximately 3 meV to 4 meV, which are almost negligible in all cases. To further mitigate this loss mechanism, it is essential to eliminate the 15%

reflection at energies above the band gap (see **Fig 3. 11**). For this purpose, an antireflection coating can be used to reduce the reflection effect and enhance the light absorption.

5.1.2 $\Delta\mu$ from linear fit to Planck's Generalized law

Up to this stage, the final $\Delta\mu$ values for a set of samples prepared on SLG have been determined through loss analysis based on the generalized detailed balance model. However, the discussed approach is not the only method for extracting $\Delta\mu$ from PL measurements.

A widely used alternative method in $\Delta\mu$ extraction involves performing a linear fit to the high-energy slope of the PL spectrum [29, 33, 77, 106, 111, 182]. In this section, this linear fit approach is discussed in detail. The $\Delta\mu$ values of the samples in **Table 5.1** will be extracted using the linear fit to high energy slope of PL spectrum, and the results will be compared to those obtained from the loss analysis.

The aim here is to check if the $\Delta\mu$ values derived from generalized detailed balance model are complete and consistent with previously established methods.

By employing Boltzmann approximation (i.e., $E - \Delta\mu \gg k_B T$), the Planck's generalized law (Eq 2.52) can be rearranged into the following form [29]:

$$ln\left(\frac{\Phi_{PL} h^3 c^2}{2\pi A(E) E^2}\right) = -\frac{E - \Delta\mu}{k_B T} \qquad (\boldsymbol{Eq\ 5.3})$$

With detailed knowledge of the $A(E)$ spectrum and transforming the PL spectra according to this Eq 5.3, the $\Delta\mu$ can be extracted by applying a linear fit to the high-energy slope of this equation. The intercept on the vertical axis of this fit provides the $\Delta\mu$ value, while its slope corresponds to $1/k_B T$. Consequently, from the slope of this linear fit, the absorber temperature (i.e., the measurement temperature) can be determined.

According to Eq 5.3, determining accurate values for $\Delta\mu$ requires precise knowledge of both the shape and numerical values of $A(E)$ spectra.

The linear fit for $\Delta\mu$ extraction is performed in energy ranges well above the band gap. In this range, the $A^{dir}(E)$ spectra can be obtained reliably using photospectrometric measurements for samples deposited on SLG (see **Fig 5. 1**). Therefore, by directly using the measured spectrum $A^{dir}(E)$ and substituting it for $A(E)$ in Eq 5.3, the $\Delta\mu$ can be reliably extracted from the linear fit to the high energy flank of this equation.

However, in the absence of measured $A(E)$ spectra, a simplified approximation can be employed. For example, as shown in references [29, 33, 77, 106, 182, 183], at energy ranges significantly higher than the band gap, it is commonly assumed that $A(E) = 1$, implying that all incident photons are fully absorbed by the material. Using this assumption, the PL spectrum can be transformed by replacing $A(E)$ in Eq 5.3 with unity. Subsequently, a linear fit can be applied to high-energy range to determine the $\Delta\mu$.

As an example, **Fig 5. 5 a** and **b** illustrate the transformed PL spectra of B-NG sample using modified Planck's generalized law according to Eq 5.3, considering both cases: (ii) the measured $A^{dir}(E)$, (ii) and using the approximation $A(E) = 1$.

Once again, it is important to clarify that these $A^{dir}(E)$ measurements are reliable only in the high-energy range above the bandgap. Therefore, transformed PL spectrum (Eq 5.3) has only reliable values in the high-energy region. Ideally, if the exact shape of $A(E)$ was known across all energy ranges, including both low and high energies, the transformed PL spectrum would be a straight line with a slope corresponding to $1/k_BT$ (not shown here).

For an accurate $\Delta\mu$ extraction, the appropriate selected fitting range is typically chosen around 100 meV above the maximum PL emission [29, 33]. In this region, $A^{dir}(E)$ can be precisely determined (see **Fig 5. 1**), thus $\Delta\mu$ can be obtained reliably from linear fit approach. It is also important to avoid fitting ranges around the measurement noise, as they can introduce errors in the extracted $\Delta\mu$ and temperature.

As an example, in **Fig 5. 5a** and **b**, the $\Delta\mu$ of the B-NG sample is extracted from a linear fit using $A(E) = 1$ and $A(E) = A^{dir}(E)$, respectively.

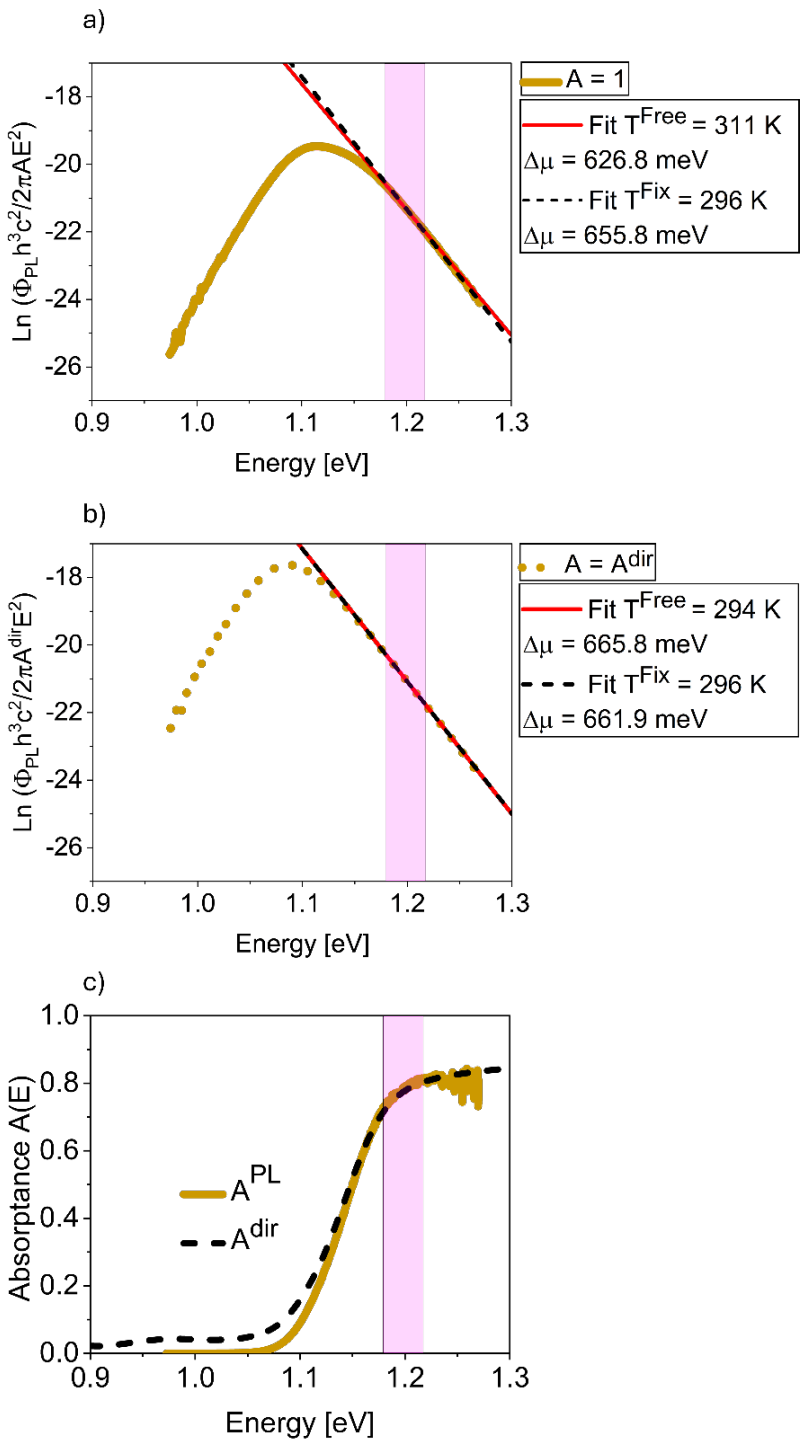

Fig 5. 5 a) and **b)** Illustrating the transformed PL spectra of sample B-NG using modified Planck's generalized law according to Eq 5.3 with considering $A(E) = 1$ and $A(E) = A^{dir}\ (E)$ cases, respectively. The Δμ in both cases were extracted from linear fit with fixed and free slope conditions, and the $\Delta\mu$ values are illustrated in each figure inset. The highlighted region shows the fitting range. c) Linear fitting range illustrated on the $A(E)$ profile of B-NG sample.

It is crucial to mention that when $A(E)$ remains constant within the fitting range, assuming a constant $A(E)$ value (i.e., $A(E) = 1$) should yield an extracted temperature from the slope of this linear fit that matches the actual measurement temperature (here ~296 K) [2]. However, if the $A(E)$ spectrum continues to rise without leveling off, this approximation leads to unrealistically high extracted temperatures and significantly underestimated $\Delta\mu$ values [2, 11]. To solve this issue, the temperature can be fixed to 296 K (i.e., fixing the slope). With this approach, the $A(E) = 1$ condition is enforced, leading to more accurate values for $\Delta\mu$ [29, 184]. More details are provided in the following discussions.

In **Fig 5. 5 a**, linear fits to the high-energy slope of the transformed PL spectrum (Eq 5.3) are performed for B-NG sample with using the assumption $A(E) = 1$. The linear fits are applied under two conditions: a free slope fit and a fit with a fixed slope (i.e fixed temperature at 296 K). It can be observed that when the fit is performed using free slope condition, the extracted temperature is approximately 16 K above the actual measurement temperature. This discrepancy arises mainly because, within the chosen fitting range, the $A(E)$ spectrum does not reach a constant value but continues to increase (see **Fig 5. 5 c**). As a result, assuming a constant $A(E)$ (i.e., $A(E) = 1$) leads to this deviation.

Furthermore, comparing the $\Delta\mu$ values extracted from these fits to those obtained from generalized detailed balance calculations in **Table 5.2** , it can be observed that when the slope is fixed, the $\Delta\mu$ shows reasonably good agreement with those values reported in **Table 5.2** . However, it still remains approximately 6 meV lower. In contrast, when the fit is performed with a free slope, the extracted $\Delta\mu$ shows unrealistically much smaller values compared to the values in **Table 5.2** .In the next stage, the case with $A(E) = A^{dir}(E)$ is investigated.

Fig 5. 5 b illustrates the modified PL spectrum (Eq 5.3) under the condition $A(E) = A^{dir}(E)$. Here, also a linear fit is performed to extract the $\Delta\mu$ within the same fitting range as used in **Fig 5. 5 a** .

For the case of $A(E) = A^{dir}(E)$, the free slope fit results in a temperature very close to the measurement temperature (294 K). However, later it will be shown that this extracted temperature can be affected by the measurements noise, and depending on the fitting ranges that I choose, the linear fit can result temperatures of around 296 ± 2 K . To avoid this problem,

the $\Delta\mu$ here is also extracted under fixed slope condition. It can be observed that for B-NG sample, when the slope is fixed at the measurement temperature (here 296 K), the $\Delta\mu$ would be almost same as the values obtained from the loss analysis (see **Fig 5. 5 b** and **Table 5.2**).

For a more detailed understanding of the sensitivity of the fitting range, it is often helpful to analyze the derivative of the modified PL spectra at high energy ranges (i.e., the derivative of Eq 5.3). From this derivative, the local slope at each corresponding energy point can be determined. This approach allows the examination of variations in the extracted temperature across the full spectrum and helps assess how different fitting ranges influence the extracted temperatures.

Therefore, the concept of differential temperature (T^{diff}) is introduced here. T^{diff} is simply obtained by taking the derivative of the transformed PL spectra (i.e., derivative of Eq 5.3**)** and multiplying its inverse by k_B. In fact, the T^{diff} represents the temperature extracted from the local slope at each distinct energy point.

Fig 5. 6 a and **b**, illustrates the differential temperature (T^{diff}) extracted for sample B-NG under the conditions of $A(E) = 1$ and $A(E) = A^{dir}(E)$, respectively. In both cases, the highlighted region indicates the linear fit range, as illustrated in.

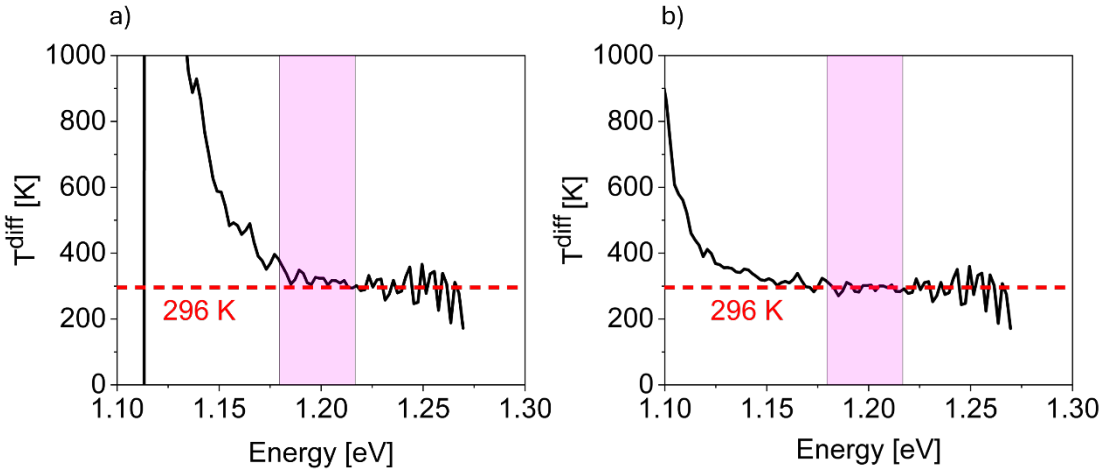

Fig 5. 6 Differential temperature T^{diff} for B-NG sample extracted from the transformed PL spectrum using Eq 5.3 by considering **a)** $A(E) = 1$ and **b)** $A(E) = A^{dir}(E)$.

It can be seen that in **Fig 5. 6 a**, for the case of $A(E) = 1$, the T^{diff} within the linear fitting range does not stabilize and continues to decrease. This explains why the temperature from the free slope fit shows higher values than measurement temperature in the highlighted fitting ranges (see **Fig 5. 5 a)**

Moreover, it can be observed that changes in the fitting range can have influence on this extracted temperature. If the fitting ranges is shifted slightly toward lower energies, the free slope fit would result in a temperature that is higher than measurement temperature of 296 K.

On the other hand, when $A(E) = A^{dir}(E)$ is considered in Eq 5.3, T^{diff} plateaus around 296 K, suggesting a more reliable temperature extraction.

Furthermore, using differential temperature plot is a good way to find a suitable fitting range for $\Delta\mu$ extraction. in **Fig 5. 6 a** and **b**, fluctuations in T^{diff} can be observed for both cases. Notably, these fluctuations become stronger at high energy ranges. This effect is caused by variations in the local slope of the PL spectrum and might be attributed to the measurement noise. At high energy ranges, as the PL counts decrease, the local slope becomes more effected by measurement noise, and thus these fluctuations become stronger. As a result, the temperature obtained from the slope of this linear fit tends to be less reliable in this range. Consequently, linear fit should be performed in a region where it is less effected by the slope fluctuations and measurement noises.

Overall, for all samples, the $\Delta\mu$ values are extracted using the linear fit method under both conditions: $A(E) = 1$ and $A(E) = A^{dir}(E)$, using the fixed temperature of 296 K. In **Fig 5. 7,** a comparison of $\Delta\mu$ values extracted from loss analysis (**Table 5.2**) and linear fit methods is displayed, while the corresponding $\Delta\mu$ values are summarized in **Table B4.1** in **Appendix B4**.

From **Fig 5. 7**, it can be observed that when the $A(E) = A^{dir}(E)$ is considered, the obtained $\Delta\mu$ from linear fit shows excellent agreement within range of 1-2 meV with those values calculated from the loss analysis. In contrast, assuming $A(E) = 1$ leads to approximately 5 meV to 7 meV underestimation in the obtained $\Delta\mu$. The comparison of numerical values for $\Delta\mu$ values extracted from different methods are presented in **Appendix B4**. This discrepancy occurs because, in reality, the actual $A(E)$ is less than unity within the fitting region. For instance, in sample B-NG, **Fig 5.5 c** shows that $A(E)$ remains below 1 in the energy ranges where the linear fit is performed, with numerical values around 0.7 to 0.8. Consequently,

approximating the $A(E)$ with unity results in underestimation of the final $\Delta\mu$ value by approximately 6 meV.

It is worth mentioning that the $\Delta\mu$ values reported here are obtained from a single measured point on each sample, and statistical errors due to sample inhomogeneities are not presented.

The purpose of this study is to show that all significant loss mechanisms are covered by generalized detailed balance calculations, and by subtracting all losses from the SQ limit (qV_{OC}^{SQ}), the final $\Delta\mu$ of the samples can be determined according to Eq 4.9. Additionally, I wanted to show also that the extracted $\Delta\mu$ values obtained from the linear fits align perfectly with those extracted from the loss analysis, and assuming $A(E) = 1$ introduces a systematic error, resulting in a small underestimation of the $\Delta\mu$ by few meV.

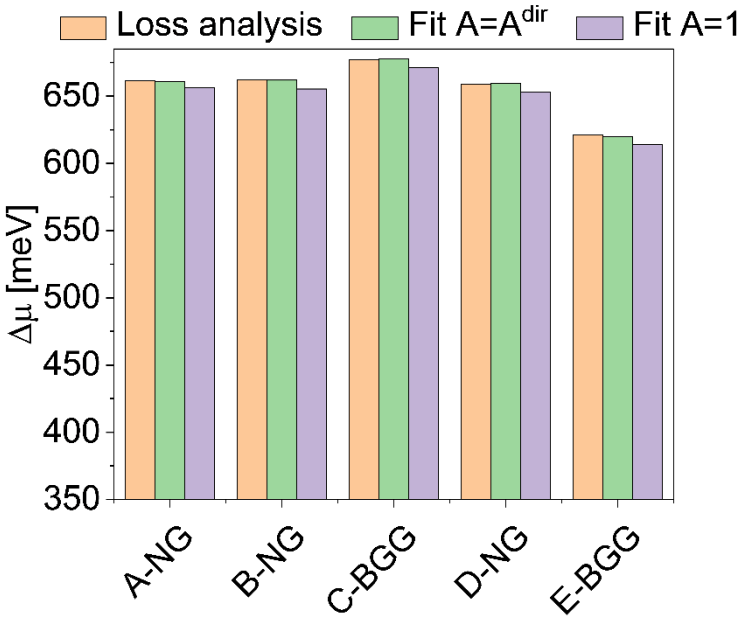

Fig 5. 7 Illustrates the comparison between extracted $\Delta\mu$ values using loss analysis and linear fit to the high energy slope of modified PL spectrum according to Eq 5.3, with both $A(E) = 1$ and $A(E) = A^{dir}(E)$ conditions. For numerical values please see **Appendix B4**.

However, it is also important to note that inhomogeneities through the sample can cause small variations in Y_{PL} and PL maximum emission from point to point. This variations can introduce an uncertainty of approximately ± 5 meV in the final $\Delta\mu$. This, in turn, will affect the final $\Delta\mu$ values if different points on the absorbers are compared.

In addition to inhomogeneities, errors in temperature measurement can impact the accuracy of the final $\Delta\mu$ values. However, it is important to clarify that when referring to temperature errors, I do not mean that $\Delta\mu$ values are extracted at different temperatures for different methods. Instead, I am referring to inaccuracies in the thermometer or thermal camera readings.

In all cases, a consistent temperature should be used for each method, as the same measured PL spectra for each sample are used across all described methods. Using a slightly different temperature would shift the extracted $\Delta\mu$ values in both the loss analysis and linear fit methods. Because both methods depend similarly on the chosen temperature, the resulting $\Delta\mu$ would still be comparable.

Furthermore, it is crucial to note that the systematic error arising from the assumption $A(E) = 1$ is independent of temperature. This error originates from the fact that $A(E)$ is typically less than 1 (around 0.8) within the fitting range (see **Fig 5. 2**). As a result, approximating $A(E)$ as unity leads to an underestimation of the extracted $\Delta\mu$ values.

In the energy ranges where the linear fitting is performed, incomplete absorption is mainly because of the surface reflection (see **Fig 3. 11**). For samples deposited on Mo (an opaque substrate), the *A(E)* value cannot be directly obtained using UV-Vis measurements, as transmittance measurements cannot be performed. However, in such cases, the reflectance (R) can still be measured reliably. In the cases where the reflectance is around 15-20%, instead of simple assumption of $A(E) = 1$, one can apply the approximation $A(E) \approx 1 - R(E)$, or use a constant value like $A(E) = 0.80$. Subsequently, the $\Delta\mu$ can be obtained from the linear fit with fixed slope under this new assumption. This approach accounts for the absorption losses, providing more accurate values for the extracted $\Delta\mu$.

5.2 V_{OC} losses for complete solar cell device

Up to this stage, the experimental analysis has focused on the optical approach, using PL and $A(E)$ measurements for $\Delta\mu$ analysis. However, as outlined in the **Section 4.1.2**, analogous calculations can also be performed using combination of $QE(E)$ and EL measurements to determine the relative V_{OC} losses for the completed devices.

It is often essential to investigate the properties of complete devices, rather than focusing solely on the absorbers. First of all, if a sample shows a high Y_{PL} and $\Delta\mu$, does not necessarily mean that it would also have a very good performance. Charge collection losses and charge transport non-idealities can impact J_{SC}, ultimately reducing the overall efficiency of the device. Additionally, ohmic and contact losses, as well as interface recombination effects, can further reduce the V_{OC} below its $\Delta\mu$. These effects are primarily related to the electrical properties of the devices and cannot be identified with performing optical investigations alone.

Moreover, CIGSe solar cells are typically fabricated on Mo-coated substrates. In such cases, determining the exact numerical values of $A(E)$ remains challenging. The Mo substrates prevents transmittance measurements, making it impossible to obtain the $A(E)$ spectrum with conventional UV/Vis transmittance/reflectance spectrometry. Alternative techniques such as ellipsometry, also present challenges due to surface roughness [171, 185] and the presence of a band gap gradient. Accurate interpretation of ellipsometry analysis requires specialized modeling that accounts for both roughness and gradient effects.

Additionally, the optical properties of the final devices can be different from the unprocessed absorbers. Factors such as reflection from the window layer, parasitic absorption in the window layer (free carrier absorption) [186-188] can alter the optical characteristics of the absorbers in the final device, making them different from the absorber material alone. Therefore, investigation of the final processed solar cells, instead of absorbers alone, can provide additional information regarding the performance limitations.

In this section, the optoelectrical approach is employed to evaluate the V_{OC} losses using combination of absolute EL and direct $QE(E)$ measurements.

The optoelectrical approach for quantifying the V_{OC} losses in the photovoltaic devices is a well-established method. Number of previously published reports investigated this effect for different technologies, including CIGSe [28, 30, 31, 164, 172]. However, in this thesis, the focus is on comparing the graded and non-graded CIGSe absorbers. Additionally, in the published reports, non-radiative losses are usually quantified using the difference between measured V_{OC} and its radiative limit [28, 31]. Nevertheless, here, the non-radiative losses are obtained using absolute EL emission spectra.

In this section, three different devices are investigated: Sample F-BGG, which exhibits a Ga gradient throughout its thickness, and samples G-NG and H-NG, both of which have a uniform band gap profile. The deposition process of samples with and without the band gap gradient has been already explained in **Section 3.1.1**.

In **Table 5.3** , key properties of these absorbers, including CGI , GGI , presence of gradient are presented.

Table 5.3 Summarizes the properties of F-BGG, G-NG and H-NG absorbers. Including name, CGI and GGI values determined by EDX measurements with 20 kV acceleration voltage, presence of band gap gradient and device parameters of the solar cell with highest efficiency on each absorber.

Sample name	***Gradient***	***CGI***	***GGI***	***Voc (mV)***	***Jsc (mA/cm^2)***	***FF***	***PCE(%)***
F-BGG	*Yes*	*0.93*	*0.25*	*648*	*35.5 (35.1*)*	*76.7*	*17.6*
G-NG	*No*	*0.94*	*0.27*	*608*	*33.7 (33.4*)*	*76.1*	*15.6*
H-NG	*No*	*0.99*	*0*	*474*	*40.8 (40.4*)*	*71.1*	*13.7*

* Obtained by integrating the AM 1.5g solar spectrum over $QE(E)$ spectrum (see Eq 2.35).

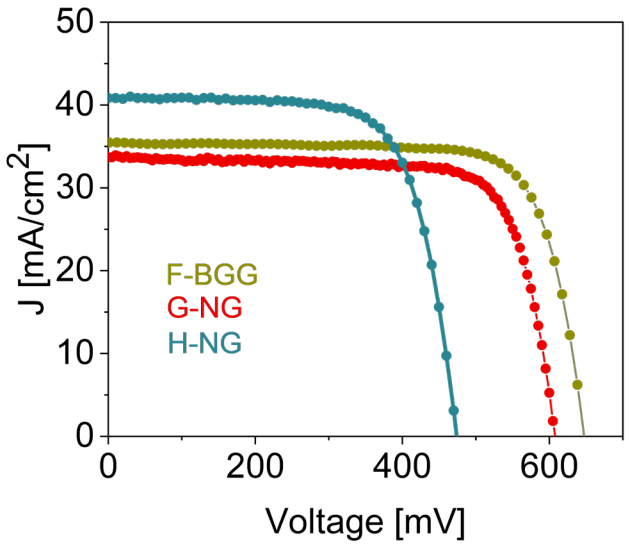

Fig 5. 8 The representative J-V curves of the solar cells with highest efficiency made from absorbers F-BGG, G-NG and H-NG. The device parameters are summarized in **Table 5.3**

F-BGG and H-NG samples were deposited using 3-stage deposition process. H-NG is pure CISe and contains no Ga, therefore no gradient in band gap is possible for this particular sample.

G-NG is a CIGSe device with a uniform Ga distribution, prepared using Cu-rich-off (CURO) process,

SIMS measurements were performed on the F-BGG and G-NG samples, confirming that the F-BGG absorber exhibits a graded Ga distribution, while the G-NG sample displays a relatively uniform Ga profile along its thickness.

A total of 5 to 8 distinct devices were fabricated on each absorber. The J-V characteristics of the highest-efficiency devices are presented in **Fig 5. 8**, with the corresponding photovoltaic parameters listed in **Table 5.3** . Furthermore, the statistical distribution of all photovoltaic parameters from the fabricated solar cells is provided in **Appendix B5**.

As discussed earlier in **Section 4.1.2**, and mentioned in references [28, 30, 31, 172], obtaining the radiative V_{OC} limit (V_{OC}^{rad}) and analyzing corresponding V_{OC} losses, require precise knowledge of the quantum efficiency $QE(E)$ spectrum across the entire spectral energy range. Therefore, similar to the optical approach is **Section 5.1.1**, the first step for V_{OC} loss analysis is to obtain the full $QE(E)$ spectrum for each sample.

In **Section 3.7**, it was shown that the $QE(E)$ spectrum of a solar cell can be determined through **direct measurements** using a dedicated $QE(E)$ equipment. These measurements requires measuring the current density of a device at different incident photon energies. The direct $QE(E)$ measurements (denoted here as $QE^{dir}(E)$) provide a reliable spectrum over a wide spectral range. However, they are known to be less sensitive in the low-energy slope (sub-bandgap energies), where detecting small currents become challenging [30, 31]. Consequently, in the low-energy sub-band gap decay region, $QE^{dir}(E)$ measurements are typically unreliable, and the $QE^{dir}(E)$ spectrum tends to flatten rather than showing the expected decay behavior.

To overcome these limitations, similar approach to optical measurements in Eq 5.1 can be employed to reconstruct the low-energy portion of the $QE(E)$ spectrum. This approach

involves using EL emission spectrum to construct the sub-band gap part of $QE(E)$. Unlike the direct measurements, the EL measurements provide very high accuracy in the sub band gap decay region.

Analogous to generalized Planck's law, where the $A(E)$ is connected to $\Delta\mu$ and PL spectra, the optoelectrical reciprocity equation (Eq 2.52) links the $QE(E)$ spectrum of a solar cell to its V_{in} and EL emission spectrum (Φ_{EL}) [69]. Again, same as $\Delta\mu$ in the optical approach, V_{in} in the exponential term of Eq 2.52 acts only as a scaling factor. Therefore, the $QE(E)$ shape can be reliably obtained through EL measurements without any knowledge about the numerical values of V_{in}, simply by using the following correlation (see Eq 5.1 for comparison):

$$QE^{EL}(E) \propto \frac{\Phi_{EL}(E)}{\Phi_{BB}(E)} \qquad (\boldsymbol{Eq\ 5.4})$$

Here, the $QE^{EL}(E)$ refers to $QE(E)$ spectrum obtained from EL spectra.

Subsequently, same as the approach that was used for optical case in **Fig 5. 1**, in the energy ranges where both $QE^{dir}(E)$ and $QE^{EL}(E)$ have reliable values, the $QE^{EL}(E)$ spectra can be scaled to match the directly measured $QE^{dir}(E)$ spectrum. With this approach, full range of $QE(E)$ spectrum can be effectively constructed, and this spectrum can be subsequently used for V_{OC} loss quantifications.

In **Fig 5. 9 a**, combination of direct and EL measurements were used to obtain the full range of $QE(E)$ spectra for samples F-BGG, G-NG, and H-NG. In all cases, it can be observed that $QE^{dir}(E)$ levels off at the $QE(E)$ values around 10^{-3}. However, from EL measurements the low energy decay portion can be quantified reliably. For all these three samples, the EL spectra used for $QE(E)$ determination are illustrated in **Fig B6.1** in **Appendix B6**.

Fig 5. 9 a illustrates that within a specific energy range, the rescaled $QE^{EL}(E)$ values show excellent agreement with the direct measurements, confirming the validity of the reconstruction approach. In the subsequent steps, all V_{OC} losses are calculated using the full reliable range of $QE(E)$ spectra reported in **Fig 5. 9 a**.

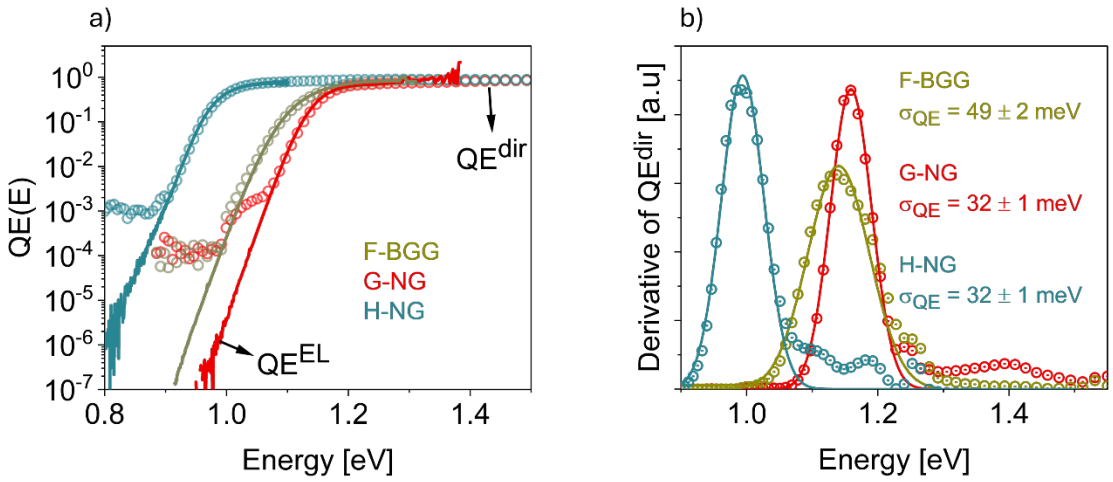

Fig 5. 9 a) The $QE(E)$ spectra for F-BGG, G-NG, and H-NG solar cells, obtained by combining direct $QE(E)$ and EL measurements. **b)** The first derivative of the $QE^{dir}(E)$ spectrum for each sample is shown with its corresponding Gaussian fit. The reported σ_{QE} is the average value extracted from multiple Gaussian fits using different fitting ranges, and errors represent the standard deviation.

Here, similarly to the optical approach, a Gaussian fit is employed to the derivative of the $QE(E)$ spectra to extract the mean band gap energy ($\overline{E_g}$) and the corresponding broadening parameter (σ_{QE}). In **Fig 5. 9 b**, the first derivative of the directly measured $QE^{dir}(E)$ spectra is used for this purpose. Notably, unlike the optical measurements, both the $QE^{dir}(E)$ and $QE^{EL}(E)$ can be used here. In **Fig B6.4** in **Appendix B6**, an example for the F-BGG demonstrates that the derivatives of these two $QE(E)$ spectra exhibit similar broadening values, indicating that both EL and direct measurements can be utilized to assess the $QE(E)$ onset.

The σ_{QE} for these samples along with the $\overline{E_g}$ values are all summarized in **Table 5.4**.

As outlined in **Section 2.2.1**, the $QE(E)$ and $A(E)$ spectra are linked through the charge collection function. In the low energy range, where the material's absorption coefficient has small values, this collection function behaves as a constant scaling factor that scales the $A(E)$ to $QE(E)$ [30]. Therefore, in this region, $A(E)$ has similar profile as $QE(E)$ spectra, and the broadening of $QE(E)$ represents the broadening of the absorption edge. In **Fig B6.2** in **Appendix B6**, as an example for F-BGG sample, it is shown that the PL spectrum of the solar cell and its EL spectrum have similar shape. Consequently, $A(E)$ and $QE(E)$ show identical profile in the energy ranges where EL and PL are measured.

So far, with the knowledge of the accurate $QE(E)$ spectrum in the entire spectral range, and reference band gap energy, all V_{OC} losses of these samples can be quantified according to equations in **Section 4.1.2.**

Same as the optical approach, the first step involves the determination of SQ limit (V_{OC}^{SQ}) using Eq 2.47. Here also, the reference SQ limit is calculated for the average band gap $\overline{E_g}$, which is determined from Gaussian fit to the first derivative of $QE(E)$. Subsequently, V_{OC} losses are obtained by considering this $\overline{E_g}$ as a reference band gap.

Corresponding V_{OC}^{SQ} limit of each sample is presented in **Table 5.4**. It is important to once again mention that all the calculations are carried out at the room temperature (here 296 K). Therefore, in all calculations fixed T = 296 K is used.

Table 5.4. Summarizes $\overline{E_g}$, σ_{QE} and all V_{OC} losses for F-BGG, G-NG and H-NG solar cells. Here, the statistical errors due to inhomogeneities in Y_{EL} and setup calibration errors are included in both δV_{OC}^{nr} and V_{in}.

Sample Name	σ_{QE} ***(meV)***	$\overline{E_g}$ ***(eV)***	V_{OC}^{SQ} ***(mV)***	δV_{OC}^{rad} ***(mV)***	δV_{OC}^{SC} ***(mV)***	V_{OC}^{rad} ***(mV)***	δV_{OC}^{nr} ***(mV)***	V_{in} ***(mV)***
F-BGG	*49 ± 2*	*1.140*	*898.8*	*25.8*	*5.1*	*867.9*	*213.4 ± 11.0*	*654.5 ± 11.0*
G-NG	*32 ± 1*	*1.159*	*916.4*	*10.0*	*5.8*	*900.6*	*282.5 ± 7.0*	*618.1 ± 7.0*
H-NG	*32 ± 1*	*0.994*	*762.8*	*10.0*	*4.6*	*748.2*	*258.4 ± 9.0*	*489.8 ± 9.0*

In the next stage, calculations are performed based on Eq 4.14 and Eq 4.15 to quantify the δV_{OC}^{SC} and δV_{OC}^{rad}, respectively.

The δV_{OC}^{SC} here is analogous to the $\delta\Delta\mu^{Gen}$, and it arises primarily due to the reduction of the J_{SC} value with respect to the SQ limit. Part of this reduction can result from incomplete light absorption or parasitic absorption in window, which decreases the photogenerated charge carrier density. Moreover, charge collection losses can also have further contribution to this loss.

The δV_{OC}^{rad}, on the other hand, is caused by the broadening of the $QE(E)$ edge. Therefore, samples with larger σ_{QE} values are expected to show higher δV_{OC}^{rad}.

In **Table 5.4**, it can be observed that the δV_{OC}^{SC} have values around 5 mV for all samples. Same as $\delta\Delta\mu^{Gen}$ (in **Section 5.1.1**), this loss mechanism has almost negligible contribution to the overall V_{OC} losses compared to non-radiative loss component.

On the other hand, the δV_{OC}^{rad} lies within the range of 10 mV to 26 mV. The G-NG and H-NG samples, which have uniform band gap profile and identical σ_{QE} values, both show a δV_{OC}^{rad} of 10 mV. However, the F-BGG sample, which has Ga gradient and exhibits around 20 meV larger σ_{QE}, shows approximately 16 mV higher δV_{OC}^{rad} compared to the two other samples.

Furthermore, to determine the final V_{in} values, the last and most important loss mechanism—non-radiative V_{OC} losses (δV_{OC}^{nr})—are quantified using absolute EL measurements. For this purpose, under an injected current density of J_{SC} (corresponding to one-sun current density), the Y_{EL} of each sample is obtained according to Eq 4.17. Subsequently, using Eq 4.16, the non-radiative losses (δV_{OC}^{nr}) are quantified.

For all performed calculations in **Section 4.1.2**, the one sun spectral emission was used (See **Fig 2. 2**). This emission leads to one-sun J_{SC} in the device. Therefore, same as the PL measurements in **Section 5.1.1**, it is crucial here to determine Y_{EL} under injection current density equal to one-sun J_{SC}. As demonstrated in **Appendix B7**, Y_{EL} varies with increasing injected current density. Therefore, using J_{SC} injected current is crucial for accurate δV_{OC}^{rad} quantification.

In **Table 5.4**, the average δV_{OC}^{nr} value for each sample is reported, along with the errors arising due to inhomogeneities in Y_{EL} and setup calibration uncertainties.

For these samples, additional absolute PL measurements were also conducted to determine ($\delta\Delta\mu^{nr}$). Notably, it was observed that $\delta\Delta\mu^{nr}$ values for samples covered with CdS and CdS/Window have a reasonable agreement with the EL extracted δV_{OC}^{nr}, with differences falling within the error bars. These measurements are provided in **Appendix B8**.

In **Table 5.4** and **Appendix B8**, one notable observation is that, unlike the samples on SLG, the ungraded absorbers exhibit significantly higher non-radiative losses compared to the graded F-BGG sample, with differences reaching up to ~70 eV. This is because, in contrast to the SLG substrate, the Mo/CIGSe interface shows higher recombination activity than the SLG/CIGSe interface [106, 108]. Therefore, incorporating a Ga gradient is essential to suppress the back-interface recombination velocity. The presence of Ga gradient near the rear side drives the minority carriers (electrons) away from the back contact, reducing back-surface recombination and consequently lowering δV_{OC}^{nr} . More details regarding the effect of Ga gradient on back surface recombination has already been provided in **Section 2.5.2** and references [3, 100].

Furthermore, at this stage by having the V_{OC}^{SQ} and respective V_{OC} losses, the final V_{in} values can be obtained by adding up these losses separately for each sample. The extracted V_{in} for each sample is also presented in **Table 5.4**.

In **Fig 5. 10**, the extracted V_{in} values are compared to the applied bias voltages (V_{bi}) and measured V_{OC} of devices. The numerical values for all three parameters are summarized in **Table B7.1** in **Appendix B7**.

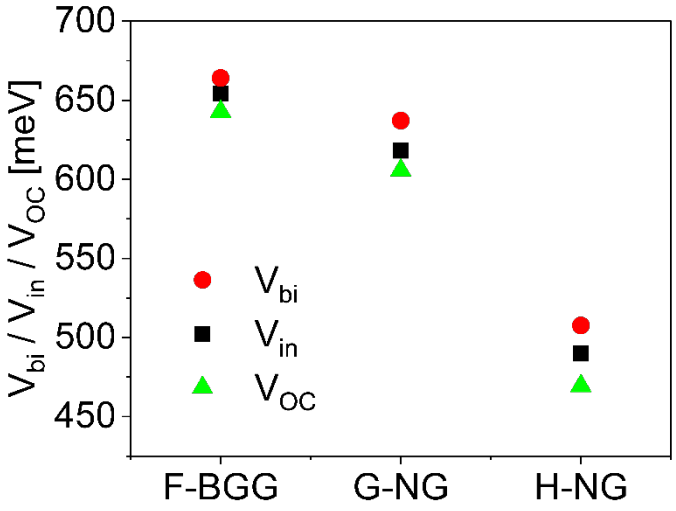

Fig 5. 10. Illustrates the comparison between V_{bi} , V_{in} and measure V_{OC} values for F-BGG, G-NG and H-NG samples. V_{in} here is extracted from generalized detailed balance model (Eq 4.16). The measurements were carries out from different cells and average value for each parameter is presented here. For numerical values and error bars see **Table B7.1** in **Appendix B7.**

It can be observed that V_{bi} has 10-20 meV larger values than V_{in}, and V_{in} exceeds the V_{OC} by approximately 5-10 meV. However, it is important to mention that comparing these three parameters is not straightforward. In an ideal scenario for solar cells, where the light J–V curve has the same shape as the dark J–V, but is simply shifted downward by the short-circuit current density (J_{SC}) (see Eq 2.34 and its related discussions), and assuming there are no transport and interface losses, V_{bi}, V_{in}, and V_{OC} would all have the same values.

However, in reality, the situation is more complicated. the EL analysis is performed under dark condition, in this condition, the applied bias voltage V_{bi} has higher values than V_{in}. This is because charge transport losses and interface recombination can reduce V_{in} below V_{bi}.

Furthermore, in thin film solar cells, such as CIGSe devices, the illuminated and dark J–V characteristics exhibit different diode behavior. In such cases, the light J-V cannot be simply represented as a shifted version of the dark J–V [3].

In **Appendix B7**, I show that light and dark J-V curves can crossover. Therefore, V_{in} cannot be directly compared to V_{OC} and understanding the correlation between V_{in} and V_{OC} needs detailed knowledge regarding the differences in dark and light diode curves for each solar cell.

Overall, to summarize V_{OC} loss analysis for these three samples, it can be observed that the dominant V_{OC} loss mechanism in the CIGSe solar cells remains non-radiative loss component (δV_{OC}^{nr}). This loss mechanism can be partly suppressed using a Ga gradient. However, it is also well established that using heavy alkali PDT can further reduce this loss mechanism by passivating interface and bulk recombination centers, as well as by increasing the net doping level of absorbers [22, 65, 129, 130, 189]. In **Chapter 6**, the reduction in non-radiative losses with heavy alkali incorporation will be discussed in more detail.

The δV_{OC}^{rad} is the second contributor to the V_{OC} losses, with values around 10 mV for non-graded samples and around 26 mV for the Ga graded F-BGG sample. Similar to the samples deposited on SLG, the graded sample here also show larger broadening, and therefore additional δV_{OC}^{rad} compared to the non-graded samples (see **Table 5.4** and **Table 5.2** for

comparison). In the upcoming **Section 5.3**, the effect of gradient on the broadening will be explored extensively.

Finally, the δV_{OC}^{SC} loss remains small in all cases, around 5 mV. However, its numerical value is approximately 1 mV higher compared to the $\frac{\delta \Delta \mu^{Gen}}{q}$ of absorbers deposited on SLG (see **Table 5.4** and **Table 5.2**). To further minimize this loss mechanism, both absorption and collection losses should be mitigated. The absorption loss can be reduced by using an anti-reflection coating, while the charge collection losses can be mitigated by improving the collection function. This can be achieved by having a material with significantly long diffusion length or by enhancing junction properties, such as extending the space charge region width, which can improve the drift component of charge collection [3, 190].

5.3 Why do graded samples show larger broadening?

So far, initial observations from the experimental results indicate that samples with a Ga gradient exhibit a larger broadening at the absorption edge compared to those without a gradient. This increased broadening leads to additional radiative losses (i.e., higher δV_{OC}^{rad} and $\delta \Delta \mu^{rad}$).

However, as discussed earlier in **Chapter 4** and references [41, 167, 173], broadening can be influenced by multiple other factors, including tail states, lateral band gap inhomogeneities, and non-stoichiometric composition.

In this section, more detailed discussions regarding the origin of this broadening will be provided.

First, to investigate the microscopic origins of the broadening, high-resolution cathodoluminescence (CL) measurements will be shown for samples deposited on Mo. Subsequently, a detailed analysis will be presented on 19 samples from our laboratory —both with and without a Ga gradient—to assess the impact of tail states, CGI, GGI, and presence of a Ga gradient on broadening of the absorption edge.

Finally, at the end of this section, a literature study and meta-analysis of published reports on graded and non-graded CIGSe samples will be presented. In this section, the broadening

observed in the CIGSe samples will also be compared with the broadening values of other photovoltaic technologies.

5.3.1 Microscopic Origin of broadening

To gain a deeper understanding regarding the origins of the $A(E)/QE(E)$ broadening, our colleagues from Cambridge University have conducted high-spatial-resolution cathodoluminescence (CL) measurements on F-BGG, G-NG, and H-NG samples (see **Table 5.3**).

In the previous section, it was shown that the F-BGG sample, which has a Ga gradient, exhibits a 20 meV larger σ_{QE} and 16 mV additional higher δV_{OC}^{rad} compared to the two other non-graded samples (see again **Table 5.3**).

The CL measurements were carried out on bare absorbers (without buffer and window layer), and these measurements were performed on both the planar surface and on the cross-section of the samples. Details of the CL measurements can be found in **Section 3.10**.

It is important to highlight that the CL peak position offers useful insights about the near-band-edge recombination process. Consequently, monitoring the CL peak emission map can reveal valuable information regarding the degree of lateral bandgap fluctuations and depth-dependent variations in the bandgap.

Fig 5. 11 a presents the panchromatic cross-section images of the F-BGG sample. It can be observed that this image is slightly bended. This bending results from charging-induced drift effects occurring during the CL measurements. Corresponding SEM images for these measurements are provided in **Appendix B9**.

In any case, to track changes in CL emission, a line scan was conducted through the absorber's depth. The evolution of the normalized CL emission spectrum along the scan is shown in **Fig 5. 11 b**. The same spectral evolution is presented in **Fig 5. 11 c** as a heat map, which also highlights changes in CL intensity along the line scan. Similar measurements were conducted on the other two samples, with the results presented in the **Appendix B9**. The SEM measurements of all these samples are also summarized in **Appendix B9**.

It can be observed that in the F-BGG sample, which has a Ga gradient, the CL peak emission exhibits a continuous blue shift from the surface to the back contact (**Fig 5. 11 a** and **c**). In contrast, for other two samples, a constant emission peak position is observed through the depth (see **Appendix B9**).

These observations align perfectly with the performed SIMS analyses. The SIMS profiles of samples F-BGG and G-NG are presented in **Appendix B1**. The SIMS analyses confirm that in the F-BGG sample, the Ga concentration steadily increases toward the Mo back contact, whereas in the G-NG sample, the Ga distribution remains uniform throughout its thickness. Consequently, it is expected that the F-BGG sample would exhibit continuous increase in the band gap toward the back contact, while the G-NG sample would maintain a constant bandgap across its depth. More details regarding the effect of Ga concentration on band gap energy can be found in **Section 2.5.1**.

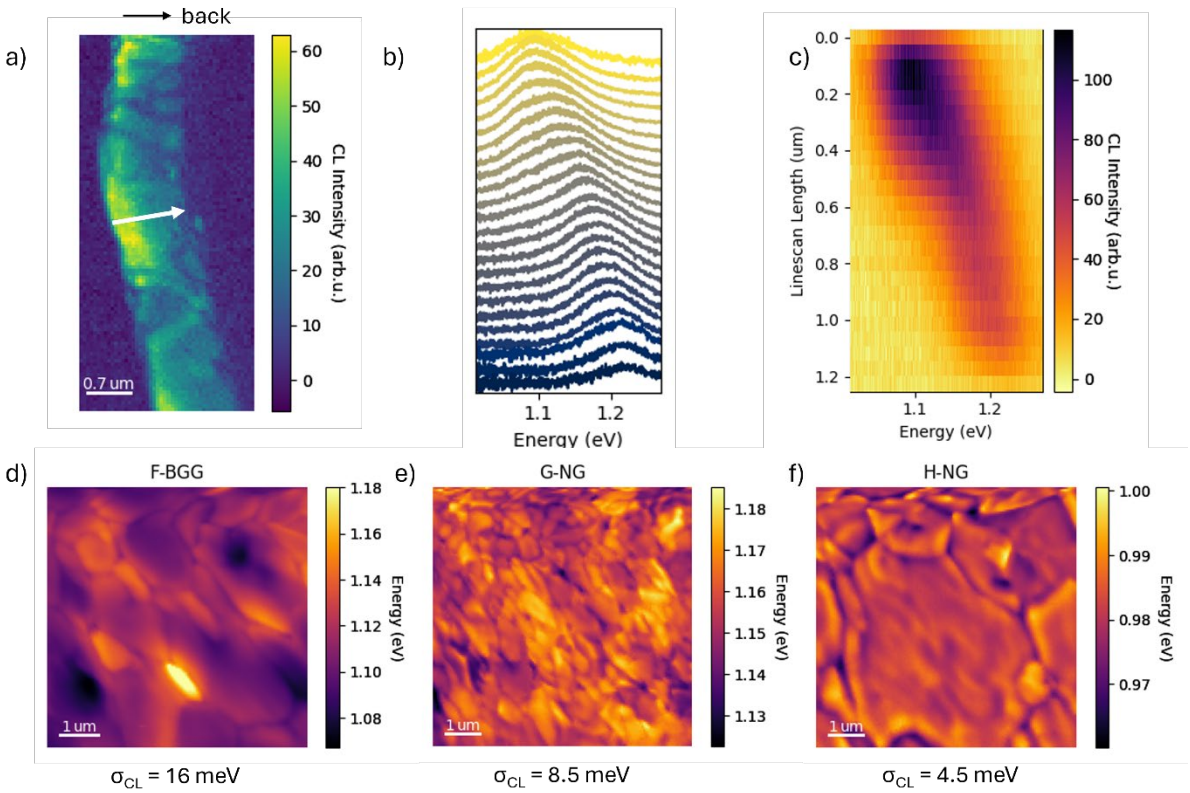

Fig 5. 11 a) Panchromatic cross section CL intensity image of the F-BGG sample, the white arrow indicates the line scan area. **b)** Illustrates the change in the PL emission spectra in the direction of this line scan. **c)** Heatmap showing the shift of CL maximum emission towards higher energies in the direction of the line scan. **d)** ,**e)** and **f)** Showing the maximum CL emission energy on each point at

the surface of samples F-BGG, G-NG and H-NG samples respectively. The parameter σ_{CL} indicates the standard deviation of the distribution of peak energies. These measurements were provided by Yucheng Hu from Cambridge University.

For the H-NG sample, SIMS measurements were not performed. This sample contains no Ga and it is pure CISe absorber; therefore, no compositional gradient is possible for this absorber.

Cross-sectional CL analysis combined with SIMS measurements indicate that in the F-BGG sample, which exhibits a bandgap gradient, the minimum bandgap is located in a narrow region near the surface of the absorber. Once again, it is important to emphasize that the absorption onset is determined from this minimum bandgap region (i.e., notch). As discussed in **Section 4.2.3**, and illustrated in published works by Carron et al. [176], a reduction in the thickness of this notch region would lead to increased broadening in the absorption onset.

On the other hand, in the two other samples, the minimum bandgap region extends throughout the entire thickness of the absorber, resulting in an effective absorption thickness that spans to the full depth of the material.

To evaluate the degree of lateral band gap inhomogeneities, and to further investigate the origin of this enhanced absorption edge broadening, planar CL mapping measurements were conducted on these three samples.

Fig 5. 11 d-f presents the planar CL maps of the F-BGG, G-NG, and H-NG samples. These maps display the energy of the maximum CL emission peak at each point. Additionally, a standard deviation parameter (σ_{CL}) is defined here for each sample; this parameter represents the width of the distribution of CL peaks. This σ_{CL} parameter is also shown for each CL map in **Fig 5. 11 d-f**. Furthermore, for all these samples panchromatic CL surface map and SEM images are illustrated in **Appendix B9**.

This standard deviation parameter provides important information on both grain-to-grain bandgap inhomogeneities, as well as bandgap variations within individual grains. Thus, it offer useful insights regarding the lateral bandgap inhomogeneities across these samples.

In **Fig 5. 11 d-f**, it can be observed that the H-NG sample, which is pure CISe, exhibits the smallest σ_{CL} values, which stems mostly from a lower emission energies near the grain boundary region.

Furthermore, introducing Ga into the material in the G-NG sample, slightly increases the σ_{CL} parameter. This observation is expected, as Ga and In alloy disorder can enhance bandgap inhomogeneities. Moreover, the F-BGG sample, which has a graded Ga profile, exhibits significantly higher σ_{CL} compared to the two other non-graded absorbers—nearly twice the σ_{CL} value of the G-NG sample. This suggests that the F-BGG sample experiences stronger lateral bandgap inhomogeneities compared to the ungraded samples.

In **Section 4.2.1**, using Gaussian distribution model for band gaps, it was shown that stronger lateral bandgap fluctuations can enhance the absorption edge broadening. Based on these CL measurements, it can be concluded that this enhanced broadening in the F-BGG sample is at least partially due to the enhanced degree of lateral bandgap inhomogeneities.

However, it is important to note that this observation cannot be applied universally to all graded CIGSe absorber, as only three samples have been studied here. To confirm with certainty that graded samples exhibit a stronger degree of lateral bandgap fluctuations, a broader statistical analysis must be performed with more samples.

Overall, these observations help partially explain why graded samples exhibit larger σ_{QE}/σ_A values compared to the ungraded samples. First, in the graded samples, the effective absorption thickness is confined to the small notch thickness (see also **Section 2.5.2**). Additionally, there are indications that the graded samples suffer from a higher degree of lateral band gap inhomogeneity, which may further contribute to the softening of the absorption edge.

However, more samples are required to fully explain the observed broadening of the $QE(E)/A(E)$ spectrum in the graded samples. Further analysis in upcoming **Section 5.3.2** on graded and non-graded absorbers are performed to find dominant contribution to the $A(E)/QE(E)$ broadening.

5.3.2 Analytical study and Meta-analysis of graded and non-graded absorbers

So far, a comprehensive analysis with combination of PL, EL, direct $QE(E)$, and photospectrometric measurements has shown that samples with a bandgap gradient exhibit enhanced broadening of the absorption edge and increased radiative losses in both $\Delta\mu$ and V_{OC}. Additionally, SIMS measurements, together with cross-sectional CL mapping, have

demonstrated that in the graded samples, the effective absorption thickness (i.e notch region) is limited to a narrow thickness within the absorber (see **Fig 5. 11 b** and **Appendix B1** and **Appendix B8**).

Furthermore, planar CL maps in **Fig 5. 11 d-f** suggest that graded samples may also exhibit a higher degree of lateral bandgap inhomogeneities along the absorber surface

However, determining whether the dominant factor contributing to $A(E)/QE(E)$ broadening is the bandgap gradient itself still requires further investigation. In this section, the effects of deviations in CGI and GGI, Urbach tails, and presence of the gradient is investigated for these samples.

To identify the key factors responsible for absorption edge broadening in our CIGSe absorbers, an analytical analysis is first conducted on 19 samples from different processes (including samples investigated in **Section 5.1** and **5.2**).

Fig 5. 12 presents the broadening parameters σ_{QE}/σ_A for CIGSe samples with different CGI, GGI, and Urbach energies, including both for graded and non-graded CIGSe absorbers. These samples were prepared either on Mo or SLG substrates, and broadening parameter of them are either extracted from $A(E)$ or $QE(E)$ spectra.

In **Appendix B6**, it is illustrated that in the energy ranges where the broadening of $QE(E)/A(E)$ is extracted, both $QE(E)$ and $A(E)$ spectra show identical shape (see **Fig B6.2** in **Appendix B6**). Consequently, similar broadening is expected for both spectra. Therefore, the σ_{QE} and σ_A are not distinct in this context and are used interchangeably to compare all samples.

Furthermore, to see the potential contribution of the Urbach tails to the $A(E)/QE(E)$ broadening, the Urbach energy for each sample is extracted from separate EL or PL measurements.

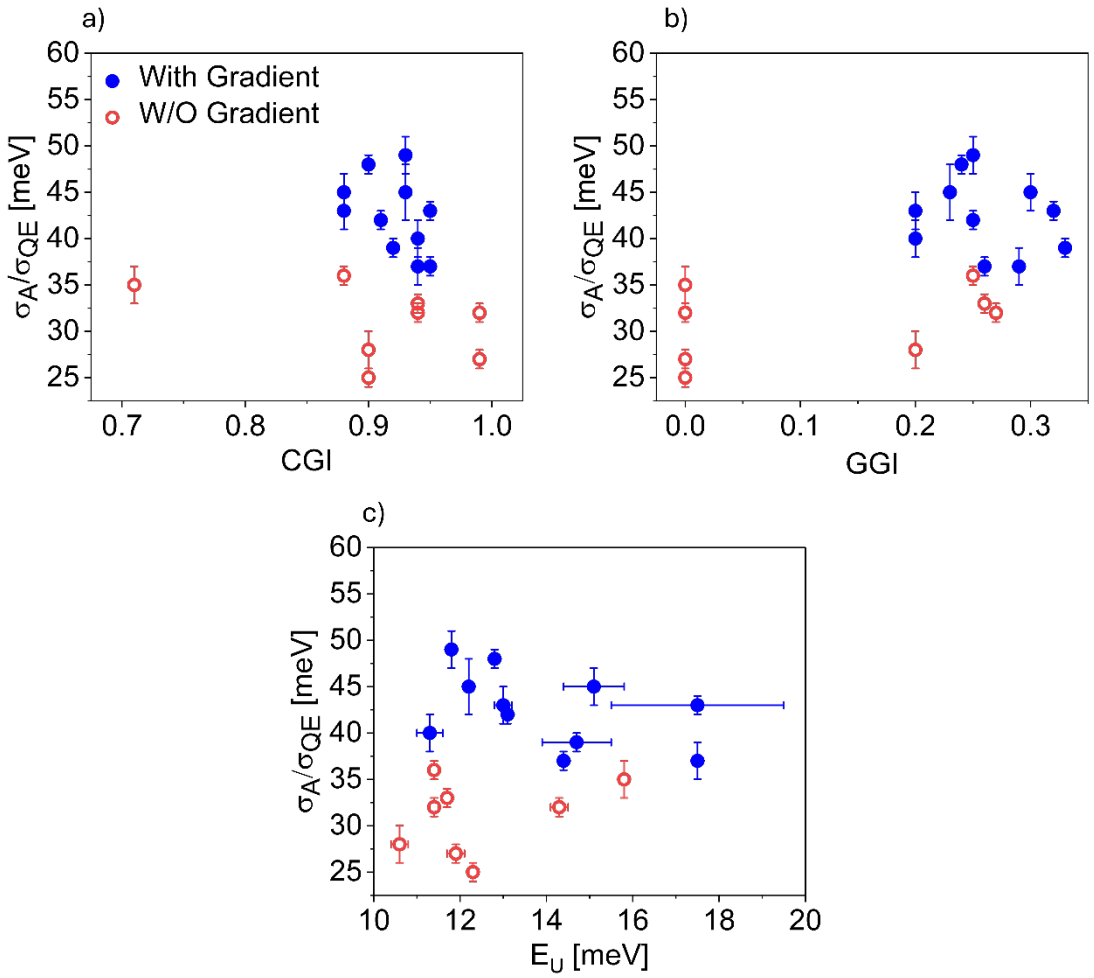

Fig 5. 12 Illustrates the effect of **a)** CGI, **b)** GGI, and **c)** Urbach tails on the σ_{QE}/σ_A for 19 samples from different processes.

It was shown in Eq 2.13 and Eq 2.39, that both $A(E)$ and $QE(E)$ spectra are related to *α(E)* via Beer-Lambert's law. Consequently, *α(E)* can be extracted using the measured $A(E)$ and $QE(E)$ spectra. Subsequently, the E_U can be quantified from the exponential decay of the *α(E)* below the band gap energy.

As an example, the Urbach energy extraction for F-BGG sample is presented in **Fig B6.3** in the **Appendix B6**.

All the analyzed samples in **Fig 5. 12** have a Cu-poor composition (i.e., CGI < 1), with the GGI values varying between 0 to 0.35.

Fig 5. 12 a and **b** illustrate the broadening parameter of investigated CIGSe absorbers with different Cu and Ga concentration. It can be seen that there is no evident correlation between variations in CGI and GGI and an increase in the broadening parameters.

A similar trend is seen for Urbach tails, where larger Urbach energies do not necessarily correspond to a larger broadening parameter (**Fig 5. 12 c**).

However, in all three figures, a clear boundary can be identified that separates the graded and non-graded samples. Absorbers with a Ga gradient consistently exhibit a larger degree of broadening parameter compared to non-graded samples, with σ_{QE}/σ_A values larger than 35 meV are exclusively observed in samples with graded band gap profile.

These observations suggest that, within this set of samples, the main factor responsible for the enhanced broadening in the $A(E)/QE(E)$ edge is the presence of the Ga gradient across the absorber thickness.

Furthermore, to determine if this observation is specific to my samples or represents a general trend, a meta-analysis was performed using published $A(E)/QE(E)$ data from CIGSe and other photovoltaic technologies.

This meta-analysis data was either directly obtained from the reported σ_{QE}/σ_A values in the published works, or extracted through digitization of $QE(E)/A(E)$ profiles when the broadening values was not explicitly provided. This approach enabled to evaluate the $A(E)/QE(E)$ broadening of each reported solar cell.

For the meta-analysis, three different categories of CIGSe samples were examined:

1. **Non-graded (NG) samples**, which have a constant band gap throughout their thickness.
2. **Band gap graded (BGG) absorbers**, which exhibit significant variations in the band gap across their depth.
3. **Hockey stick band gap (HSG) samples**, which maintain a uniform band gap throughout their depth but show a sharp increase in band gap near the Mo back contact.

The details of these band gap profiles have already been discussed in **Section 2.5.2**, and a schematic representation of the profiles is illustrated in **Fig 2. 11**.

Notably, the Hockey stick band gap (HSG) profile has gained popularity in recent years for back surface/interface passivation [11, 168]. At the time of writing this thesis, the highest-efficiency CIGSe cell, with 23.6 % power conversion efficiency, was fabricated using this HSG band gap profile [11].

Fig 5. 13 compares the published CIGSe σ_{QE}/σ_A values. Additionally, the CIGSe samples were also compared to other inorganic photovoltaic technologies, including wafer based Si technology and thin film GaAs, $Cu(Zn,Sn)S_4$ (CZTS), and Cd(Se,Te) absorbers. It is important to note that the broadening parameters were extracted from samples demonstrating very good performance in each technology.

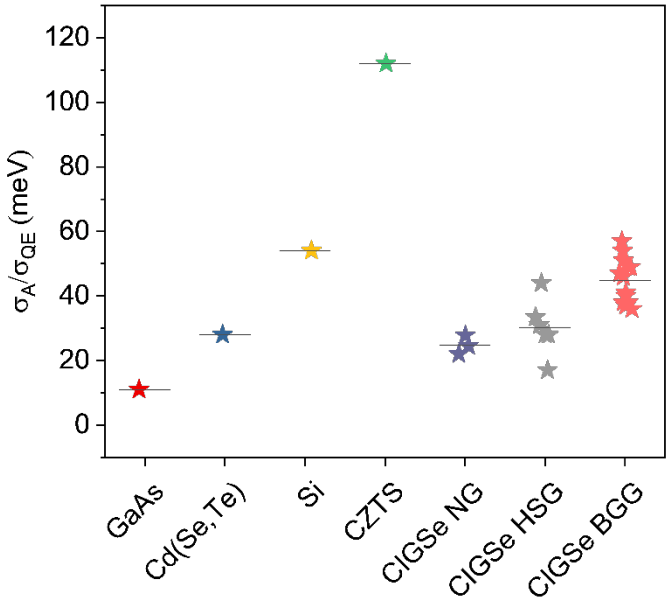

Fig 5. 13 Presents the meta-analysis of published data for comparing the (σ_{QE}/σ_A) of different photovoltaic technologies. This meta-analysis includes GaAs [191], Cd(Se,Te) [192], Si [193], Cu (Zn,Sn)S_4 CZTS [194], CIGSe samples with hockey-stick gradient (HSG) band gap profile [11, 71, 108, 168], CIGSe absorbers with non-graded (NG) band gap profile [6, 108], and CIGSe absorbers featuring a band gap graded (BGG) profile [46, 77, 107, 132, 168].

In **Fig 5. 13,** it can be seen that NG and HSG absorbers show a smaller broadening parameter compared to the BGG absorbers. This difference can be attributed to the distribution of the minimum band gap within the absorber.

In NG and HSG samples, the minimum band gap position spans significantly through the absorber's depth —sometimes extending 1 to 2 micrometers in the depth [11]. In contrast, in BGG absorbers the minimum band gap region is limited to a much thinner thickness within the absorber.

This observation once again confirms that the softening of the $A(E)/QE(E)$ edge is strongly related to the steepness of the band gap gradient profile. Particularly, a smaller thickness of the notch width leads to a larger broadening.

This observation aligns well with my own analysis (see **Fig 5. 12**), where BGG samples were found to have higher σ_{QE}/σ_A values than NG samples.

Additionally, at the end, I would like to compare the CIGSe technology to other inorganic photovoltaic technologies. In **Fig 5. 13**, the σ_{QE}/σ_A of a GaAs, Si, CdTe and CZTSe absorbers are also illustrated.

Among all presented σ_{QE}/σ_A values, the GaAs absorber exhibits the sharpest absorption onset, with a broadening values near 11 meV. This value is around 6 meV lower than the smallest broadening observed in CIGSe samples.

CdTe absorbers, on the other hand, show a broadening of approximately 28 meV, which is comparable to the average values of σ_{QE}/σ_A observed in NG and HSG CIGSe samples. In contrast, BGG CIGSe samples display broadening similar to those of silicon (Si) technology. However, it is important to note that silicon is an indirect semiconductor, where significant broadening is expected due to its absorption coefficient properties. Compared to the direct semiconductor, in indirect semiconductors, the absorption coefficient increases more gradually at the absorption onset. As a result, broader absorption edges are typically observed in indirect semiconductors.

The highest broadening value is observed in CZTS absorbers, reaching up to 110 meV. It was previously reported that Kieserite CZTSSe absorbers show stronger broadening compared to the other photovoltaic technologies [195]. This enhanced broadening can be attributed to severe band gap inhomogeneities and a high density of tail states [67, 195].

Overall, the meta-analysis results, combined with my own observations, once again indicate that the primary contributor to the broadening of $QE(E)/A(E)$ spectra in CIGSe absorbers is the presence of a compositional gradient.

5.4 Summary and conclusion of Chapter 5

In this chapter, the generalized detailed balance model was employed to experimentally quantify the V_{OC} and $\Delta\mu$ losses in CIGSe samples. In **Section 5.1.1**, the $\Delta\mu$ losses for absorbers deposited on SLG were calculated using optical measurements, where $A(E)$ and PL emission spectra were used to assess the $\Delta\mu$ and its associated losses. In this section, it was found that samples with the presence of Ga gradient show slightly larger broadening in the absorption edge and additional radiative losses compared to the samples with non-graded Ga distribution.

Subsequently, in **Section 5.1.2**, alternative method bases on linear fit to Planck's generalized law was used to determine the $\Delta\mu$ values **(**see Eq 5.3). Notably, the extracted $\Delta\mu$ using this linear fit method aligns excellently with ones calculated from detailed balance model (i.e., loss analysis). This observation indicates that loss analysis is complete and aligns with previously established approaches for $\Delta\mu$ extraction.

Additionally, In **Section 5.2**, Generalized detailed balance analysis was extended to solar cells, where optoelectrical characterization methods were used to investigate the V_{OC} losses in CIGSe devices.

Similar to absorber materials, solar cells with graded Ga profile illustrate larger absorption edge broadening and higher radiative losses compared to non-graded ones.

Overall, both analysis on solar cells and on absorbers indicate that presence of Ga compositional gradient can enhance the radiative losses by 5 meV to 16 meV.

To further explore the origins of this enhanced broadening in the graded absorbers, in **Section 5.3** a combination of microscopic, analytical, and meta-analysis studies were conducted.

cathodoluminescence (CL) analysis along with the SIMS measurements, confirmed that in the graded samples, the region of the minimum bandgap (i.e., notch) is confined to a small thickness. Previously, in **Section 2.5.2** and **4.2.3**, it was shown that this narrow notch region can increase the broadening of $A(E)/QE(E)$.

Moreover, CL surface mapping indicated that graded absorbers might also experience a higher degree of lateral band gap inhomogeneities compared to ungraded ones, which could further contribute to the broadening.

Furthermore, both analytical studies conducted on in-house samples and a meta-analysis of published data strongly suggest that the enhanced broadening of the absorption edge in CIGSe samples is mainly due to the presence of a bandgap gradient. These findings suggests that, to mitigate radiative losses, it is crucial to prepare samples with a uniform bandgap profile.

However, in the absence of Ga gradient, back surface recombination must be effectively suppressed to prevent performance degradation due to increased recombination at the Mo/CIGSe interface. Effective passivation strategies, such as using a hockey-stick gradient (HSG) profile near the Mo back contact [11, 24, 100, 106] or using a selective hole transport contact [100, 108, 109], can significantly mitigate the back surface recombination and thereby enhance the efficiency and performance of next-generation CIGSe solar cells.

6 Grain boundaries and Urbach tails in CIGSe absorbers

So far, in **Chapter 4**, the contribution of Urbach tails to the broadening of $A(E)$ and radiative losses were quantified. It was shown that Urbach tails increase both absorption edge broadening and radiative losses, which in turn leads to drop in the final $\Delta\mu$ and V_{OC} values (see **Fig 4. 4** and **Fig 4. 5**). Additionally, previous reports have indicated that Urbach tails also enhance non-radiative recombination via SRH recombination processes, further contributing to the V_{OC} and overall efficiency losses [33].

The concept of Urbach tails has already been covered in **Section 2.3**. It was mentioned that both structural disorders and thermal vibrations can introduce a density of states (DOS) into the band gap. Moreover, some structural defects can become charged. These charged defects can interact electrostatically through Coulombic forces, causing fluctuations in both conduction band and valance band edges, this effect can have additional contribution to the Urbach tails [34].

Furthermore, in **Section 2.5.3**, the effect of alkalis on the tail states of CIGSe absorbers have been discussed. It is widely known that alkali ions can suppress Urbach tails in the CIGSe absorbers [18, 33, 34, 65, 117]. Some studies attribute this effect to the passivation and neutralization of charged defects at the grain boundary (GB) regions [65], a hypothesis supported by some published KPFM measurements that showed a substantial reduction in the band bending across the GBs upon alkali ions incorporation [65, 127]. However, KPFM results remain somehow controversial. Most studies have used amplitude modulation (AM) mode of KPFM for CIGSe GBs investigation [65, 127, 152-154]. As discussed earlier in **Section 3.8** and references [133, 134], employing AM-mode for rough, polycrystalline surfaces can be significantly affected by surface morphology and geometrical features, leading to experimental errors, artifacts and distortions in the measured band bending values [133, 134]. Consequently, using AM-mode for GB analysis on rough surfaces can possibly result in the misinterpretation of KPFM measurements. Therefore, for more reliable data extraction, it is recommended to use the frequency modulation (FM) mode of the KPFM measurements for the band bending analysis. Unlike the AM-mode, the FM mode is less affected by topographical features [133].

Moreover, the most recent studies on the single-crystalline CIGSe absorbers—with no GBs — have also shown that both light alkali (Na) and heavier ones (K) can effectively suppress the tail states and reduce the Urbach energies (E_U) [34].

All these observations collectively suggest that GBs in CIGSe absorbers need further investigations to see if there are any relationship between GB band bending and Urbach tails.

This chapter investigates the potential contribution of GBs to the formation of tail states, and explores the origin of these tails in the CIGSe absorbers.

In this chapter, CIGSe absorbers without alkali elements, with sodium (Na), and with both sodium and rubidium (Na + Rb) are investigated. The Urbach energies of these samples are quantified through PL analysis. Additionally, my colleague **Muhammad Uzair Farooq**, from the Scanning Probe Microscopy (SPM) laboratory, analyzed the potential barriers (band bending) at the GBs of these absorbers using more reliable frequency modulation (FM) mode of the KPFM measurements. The details of KPFM measurements has been briefly explained in **Section 3.8**. Additional information regarding these measurements can be found in refences [133, 134].

It is important to note that the presented results in this chapter have already been published as an open-access paper with **CC BY 4.0** license [132]. With some small modifications, all the graphs, tables and results in the main text and in the appendixes are taken from this published paper. The following discussions follow more or less this published paper structure.

6.1 Investigated samples, $\Delta\mu$ and device performance

In this chapter, five different samples are studied. These samples were prepared at PVcomB HZB. As previously mentioned in **Section 3.1.2**, the growth processes were optimized to obtain a smooth surface morphology, which is crucial for an accurate KPFM characterization.

The investigated samples include alkali-free absorbers, absorbers with Na alone, and absorbers containing both Na and Rb (Na+Rb). **Table 6.1** provides an overview of the main characteristics of these samples. The investigated samples are classified into two series, A and B series, each label corresponding to a different growth recipe. The A1 sample, that contains no alkali elements, was grown on a substrate with Na barrier layer (SLG/Na-barrier/Mo

substrates). Although it was prepared using the same deposition recipe as A2 and A3, the composition of this sample, particularly the GGI, is slightly higher from the other two. This difference is likely due to the presence of the Na-blocking layer and/or the absence of Na during growth, which might have influence on the final composition. On the other hand, For Na-containing absorbers, the Mo-coated soda-lime glass (SLG) was used as a substrate, thus, the Na introduction into these absorbers is through diffusion from SLG during the growth process. Additionally, for samples containing Rb, the Rb was introduced through RbF-PDT using two different approaches: ex-situ and in-situ methods. The A2 absorbers received an in-situ RbF PDT, whereas the B2 sample underwent an ex-situ RbF PDT. More details regarding the growth and PDT processes has already been explained in the **Section 3.1.2** of this thesis.

Table 6.1 also shows the $(\frac{Cu}{Ga+In})$ CGI and $(\frac{Ga}{Ga+In})$ GGI values of all investigated absorbers. The CGI and GGI of these samples were determined using EXD measurements with acceleration voltage of 20kV. It is important to note that prior to the EDX analysis, all samples underwent ammonia cleaning procedure to remove possible oxides [151] and RbF traces from the surface (see **Appendix C1**).

Table 6.1 shows that all absorbers exhibit a Cu-poor composition, with CGI ratio below unity. The GGI ratio for samples containing Na is around 0.2-0.23. However, the A1 sample, grown on a substrate with a Na-barrier (i.e, with no alkali), shows slightly higher GGI ratio compared to four other absorbers. The GGI ratio of A1 sample is around 0.28.

Table 6.1 Illustrates the samples names, presence of alkali, PDT process methods, CGI and GGI values determined from EDX measurements. Adapted from Ghrabeiki et al [132].

Series	***Sample Name***	***Alkali***	***PDT***	***CGI***	***GGI***
A	*A1*	*None*	*No*	*0.95*	*0.28*
	A2	*Na*	*No*	*0.97*	*0.21*
	A3	*Na+Rb*	*RbF in-situ*	*0.98*	*0.20*
B	*B1*	*Na*	*No*	*0.97*	*0.23*
	B2	*Na+Rb*	*RbF ex-situ*	*0.96*	*0.22*

To evaluate the $\Delta\mu$ of each sample, absolute PL measurements under 1 sun incident laser flux were conducted. It is important to mention that all measurements are performed on CdS covered absorbers. The CdS layer is required to protect the sample surface from surface oxidation.

Fig 6. 1 a illustrates the absolute PL spectrum of sample A3, and in **Fig 6. 1 b**, the corresponding transformed PL spectrum according to modified Planck's Generalized law (Eq 5.3) is illustrated. Here, assumption of $A(E) = 1$ was used to transform the PL spectrum according to Eq 5.3.

At first glance, it can be seen that the PL spectrum shows distinct peaks. It is important to note that these peaks are not associated with any defect luminescence; rather, they stem from thin-film interference effects. The presence of interference peaks can be confirmed by performing a rotation test during PL measurements: as the laser hits the sample at different angles, the interference peaks are displaced to different energy positions [196].

Similar interference effects have been reported in previous studies for thin film absorbers [77, 196-198]. Later in **Fig 6. 6**, it will be demonstrated that these interference fringes can be effectively suppressed by depositing Polystyrene (PS) spheres on the top surface of the absorbers.

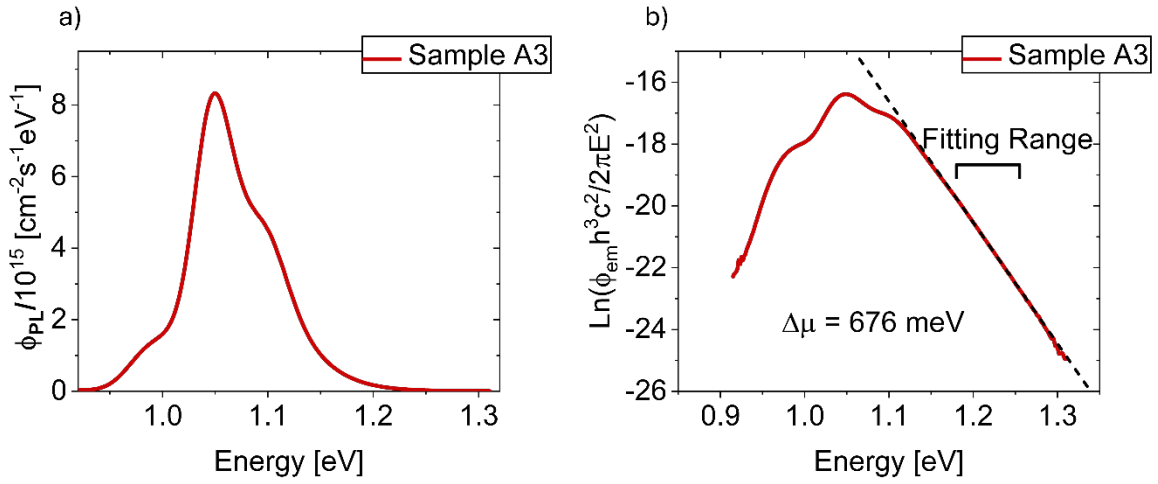

Fig 6. 1 a) The absolute PL emission spectrum of sample A3 containing both Na and Rb. **b)** Transformed PL emission spectrum using Eq 5.3, The $\Delta\mu$ here is quantified through the linear fit to high energy slope of this modified PL spectrum. Fixed temperature T= 296 K is considered for the $\Delta\mu$ determination. Adapted from Ghrabeiki et al [132].

In **Fig 6. 1 b**, the $\Delta\mu$ extraction of A3 sample from a linear fit to Planck's generalized law is illustrated. Here, the $\Delta\mu$ is determined using linear fit at fixed temperature of 296 K to high energy flank of transformed PL spectrum (according to Eq 5.3) under assumption of $A(E) = 1$. More details regarding the $\Delta\mu$ extraction has already been explained in **Section 5.1.2**.

For these samples the reflectance measurements indicate that in the ranges where linear fit is performed, the CdS covered absorbers show a reflectance of around 17% (See **Appendix C2)**, the influence of surface reflection and absorption losses on the $\Delta\mu$ has been discussed extensively in **Section 5.1.2**. It is obvious that these reflection effect push the $A(E)$ below unity. For 17% reflection, it can be expected that linear fit method, under $A(E) = 1$ assumption, will cause ~ 5 meV underestimation in the final extracted $\Delta\mu$ values (see **Section 5.1.2** for more details).

Similarly, absolute PL measurements were carried out on four other samples as well. **Fig 6. 2** presents the $\Delta\mu$ and Y_{PL} values for all investigated absorbers.

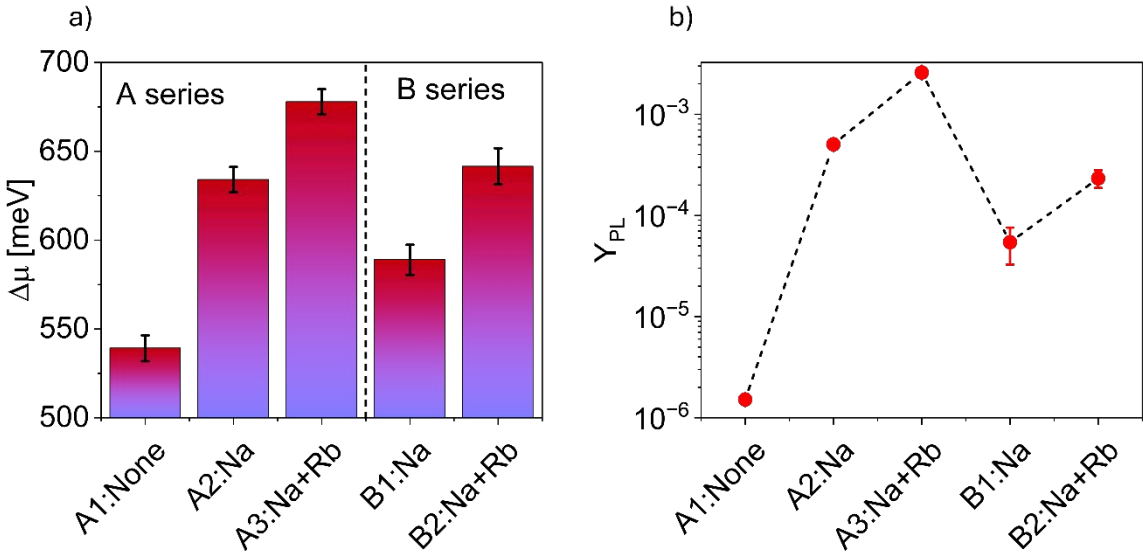

Fig 6. 2 Presenting **a)** $\Delta\mu$ values and **b)** Y_{PL} for both A-series and B-series samples (see **Table 6.1**). Measurements were performed from different points on the absorbers, the average $\Delta\mu$ and Y_{PL} is presented here. The error bars for Y_{PL} is representing standard deviation due to inhomogenieties. For $\Delta\mu$ the errors arise from inhomogeneities in the sample and PL calibration errors.

In **Fig 6. 2**, it can be observed that the A1 sample, which contains no alkali elements, exhibits the lowest $\Delta\mu$ and Y_{PL} values. With the introduction of Na into the absorber, both $\Delta\mu$ and Y_{PL}

increase. Furthermore, with the addition of Rb into the Na-containing absorbers, a further increase in both parameters is observed across each distinct series. This observed improvement in both $\Delta\mu$ and Y_{PL} with the introduction of Na and heavy alkali (here Rb) is completely in agreement with previous reports [33, 34, 65, 77, 111, 199]. The improvement of Y_{PL} indicates that alkali elements primarily mitigate the non-radiative losses in the CIGSe absorbers (see Eq 4.10).

In **Section 2.5.3**, it was mentioned that alkali ions can contribute to the enhancement of $\Delta\mu$ through two different mechanisms: The first mechanism is passivation of SRH non-radiative losses (i.e increase in the carrier lifetime), and the second mechanism is increase in the net carrier concentration.

Notably, in my case, these samples show improvements in both doping concentration and lifetime. More details regarding the lifetime measurements and extraction of doping concentration is provided in upcoming **Section 6.2**.

Furthermore, all absorbers are completed into solar cells. In **Table 6.2**, photovoltaic parameters for the device with highest efficiency on each sample are summarized.

Table 6.2. Device parameters corresponding to the highest-efficiency solar cell for each absorber. Adapted from Ghrabeiki et al [132].

Series	*Sample Name*	*Alkali*	*PDT*	V_{OC} *(mV)*	J_{SC} *(mA/cm²)*	*FF (%)*	*PCE (%)*
A	*A1*	*None*	*No*	*526*	*34*	*66.4*	*11.8*
	A2	*Na*	*No*	*621*	*35.9*	*73.6*	*16.4*
	A3	*Na+Rb*	*RbF in-situ*	*673*	*36.1*	*77.4*	*18.8*
B	*B1*	*Na*	*No*	*587*	*34.6*	*71.7*	*14.5*
	*B2**	*Na+Rb*	*RbF ex-situ*	-----	-----	-----	-----

* sample B2 is shunted

Fig 6. 3 presents the J-V measurements of the solar cell with the highest power conversion efficiency in the A series absorbers. Moreover, statistical distribution of photovoltaic parameters for all fabricated solar cells from the A series absorbers are all illustrated in **Fig 6. 4**. Additionally, numerical values of these parameters are summarized in **Appendix C3** .

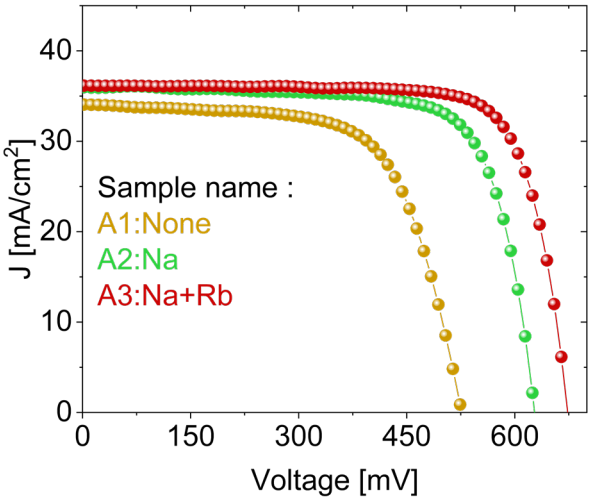

Fig 6. 3 Champion solar cell performance. the J–V curve of the highest-efficiency device on A series absorbers. Device parameters are presented in **Table 6.2**. Adapted from Ghrabeiki et al [132].

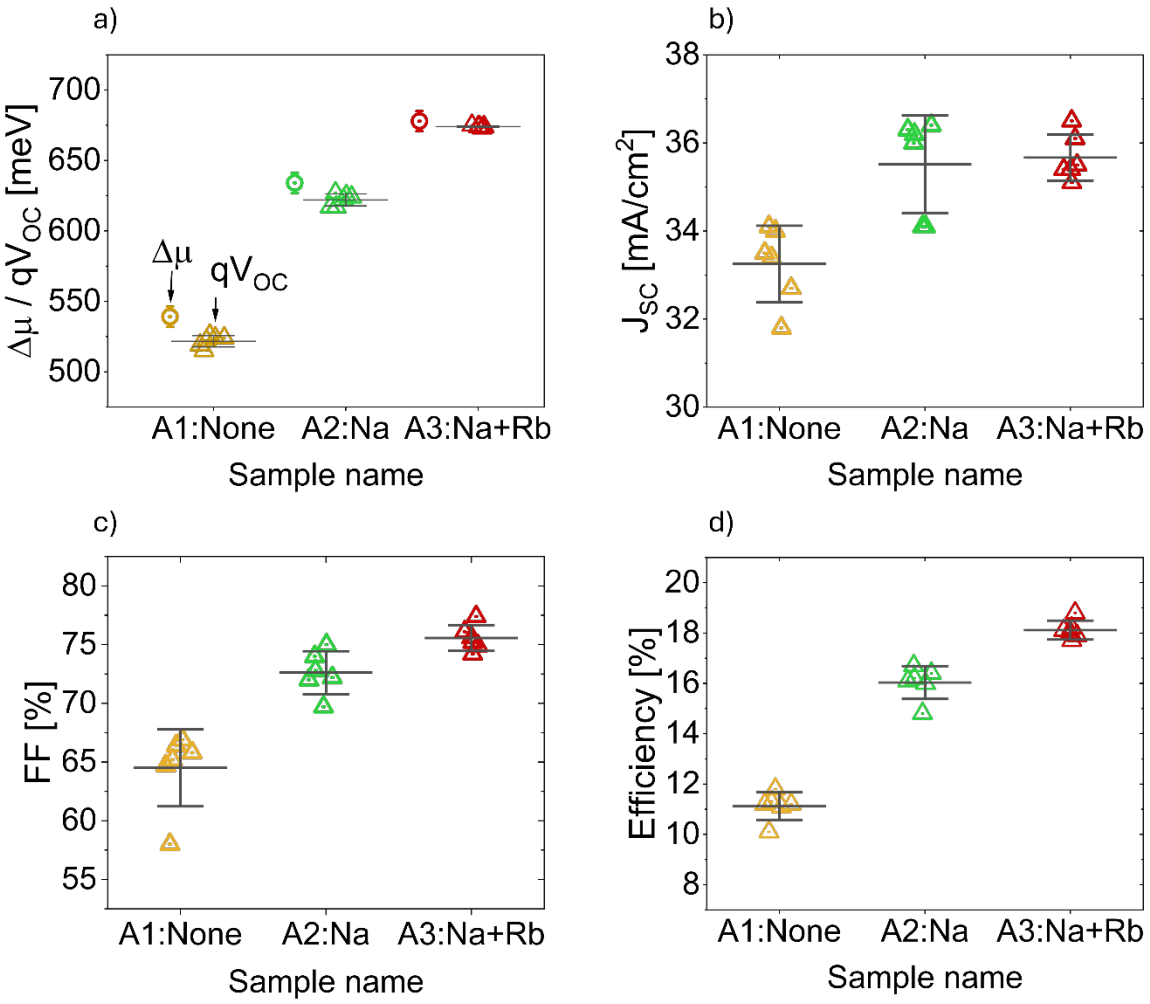

Fig 6. 4 a) compares all the measured V_{OC} with the extracted $\Delta\mu$. **b)**, **c)**, and **d)** present the distributions of J_{SC}, FF, and power conversion efficiency, respectively. Error bars indicate the standard deviation across all measured devices. Adapted from Ghrabeiki et al [132].

Additionally, the J–V measurement of B1 sample is also provided in **Appendix C3** . Unfortunately, devices fabricated from the B2 absorber, which received ex-situ RbF-PDT, resulted in shunted solar cells. Therefore, the device parameters for this particular sample are not presented.

In **Fig 6. 4 a**, the extracted $\Delta\mu$ and qV_{OC} distributions of A-series devices are presented. It can be observed that measured qV_{OC} values follow a similar trend to the $\Delta\mu$ values. However, their average values remain around 10 meV to 5 meV lower than $\Delta\mu$. As explained earlier in **Section 2.2.1**, this discrepancy between two quantities is possibly associated with the non-radiative recombination losses at the surface and interface regions, or to the presence of transport losses.

Once again it is worth mentioning that the $\Delta\mu$ translates to the upper limit of the V_{OC}. In the ideal scenario, where the surface and interface recombination is effectively mitigated, and also charge transport losses are minimal, the qV_{OC} would be equal to $\Delta\mu$. However, in the presence of the interfacial non-radiative recombination, and additional transport losses, the qV_{OC} falls below the $\Delta\mu$ limit. Further details regarding the effect of interface recombination and transport losses on the V_{OC} have already been explained in **Sections 2.2.1** and **5.2**. Additional information regarding these losses can be found in references [29, 53-55, 200].

In **Fig 6. 4 b**, it can be seen that FF values also show improvement with the introduction of alkali ions into the material. This improvement can be explained with the improvements in V_{OC}. Eq 2.47 indicates that the FF is directly linked to the V_{OC}, and enhancements in V_{OC} would result in a higher FF values for solar cells.

Regarding the J_{SC}, **Fig 6. 4 c** shows that the A2 and A3 samples show J_{SC} in the similar range with average values around 36 mA/cm^2. On the other hand, the average J_{SC} of A1 sample is around 3 mA/cm^2 lower compared to the A2 and A3. This lower J_{SC} can be related to the slightly higher band gap energy of A1 sample compared to the two other ones. The band gap energy of these absorbers will be discussed later in **Section 6.2**.

Furthermore, the power conversion efficiencies of A-series solar cells are presented in **Fig 6. 4 c**. Overall, it can be seen that alkali ions lead to an enhancement in the efficiency of these solar cells. The highest efficiency of around 18.8% is observed in the A3 sample containing both Na and Rb.

The observed gain in the efficiency of these CIGSe solar cells is in strong agreement with previous studies [18, 33, 65, 111], where alkali ions were shown to enhance overall device performance, primarily due to improvements in V_{OC}.

6.2 Tail states with alkali incorporation

Up to this section, the $\Delta\mu$ values for all absorbers has been quantified independently using absolute PL spectrum. Moreover, the device performances have been presented for both A-series and B-series absorbers (see **Table 6.2** and **Fig 6. 4**). In this section, the PL analysis is used to quantify the Urbach energies for these samples.

In **Fig 6. 1**, it was illustrated that the PL spectra of the CIGSe samples are distorted by thin-film interference emission peaks. The observed interference peaks appear because of the smooth surface of these absorbers. The low surface roughness primarily results in specular reflections of the emitted PL light beams at the interfaces and surfaces. Depending on the phase difference between the reflected beams, constructive or destructive interferences can occur. A detailed explanation of the underlying mechanism responsible for these interference fringes is provided in the PhD thesis of **Dr. Max Wolter** [77].

In the high energy side of the PL spectrum, where the absorption is high enough, these interference peaks do not appear. However, in the low energy ranges with small absorption, the interference peaks distort the sub band gap decay wing of the spectrum. Therefore, for the Urbach energy measurements it is necessary to effectively correct the PL spectrum and remove the interference fringes.

To eliminate the interference effect, I used a method previously employed by **Dr. Max Wolter** [77]. In this method, before performing PL measurements, the CIGSe absorbers are covered with polystyrene (PS) microspheres.

These PS spheres were acquired from Across organics. They are dissolved in ethanol and their average size is around 1 µm. **Fig 6. 5** illustrates the deposition process of the PS spheres on the top of CdS covered absorbers. The deposition process is straightforward: a few drops of the ethanol solution containing PS spheres are pipetted onto the absorber surface, and within a few minutes, the droplets dry, leaving the surface covered with white PS beads.

It is very important to note that PL measurements on the PS-covered samples are no longer absolute, as the exact absorbed laser flux is unknown. However, for Urbach energy extraction, only the PL spectrum shape is needed. Therefore, even without absolute spectrum, the E_U can be extracted reliably.

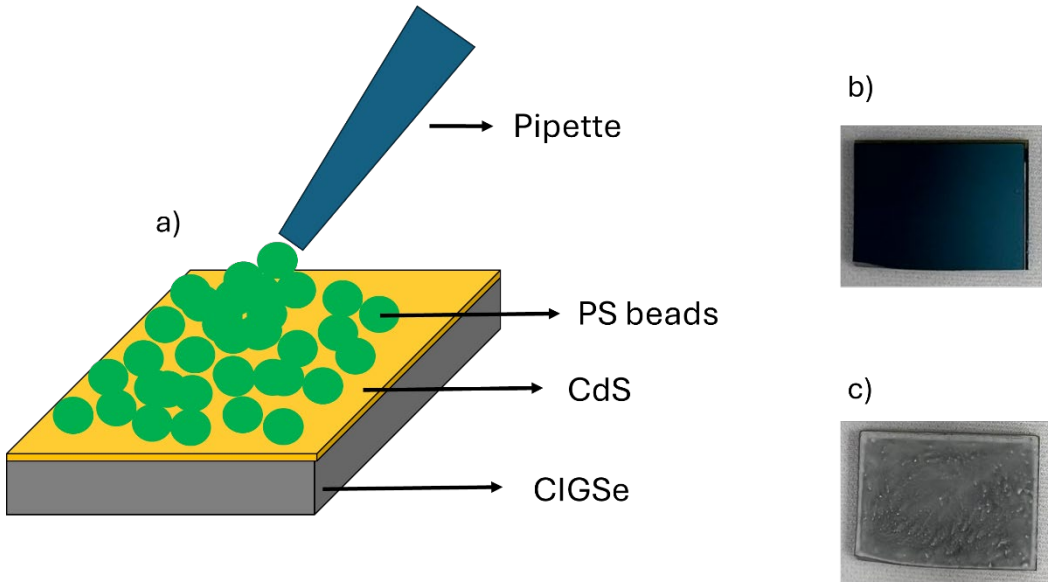

Fig 6. 5 a) Schematic image showing deposition process of PS beads on the top of the absorbers. **b)** showing samples without PS beads. **c)** showing samples covered with PS microbeads.

Additionally, it is crucial to mention that an optical lens is used during the Urbach energy measurements to reduce the laser spot radius from 1.1 mm to 70 µm. It will be shown in the upcoming **Section 6.3.3** that using this lens is essential for performing intensity-dependent measurements.

Fig. 6. 6 a illustrates the transformed PL spectra of A3 sample using modified Planck's generalized law (according to Eq 5.3). Both PL spectra with and without the presence of PS spheres are presented. In this figure, the PL spectrum of the PS-covered samples has been rescaled to match the absolute PL spectrum of the absorber without PS coating.

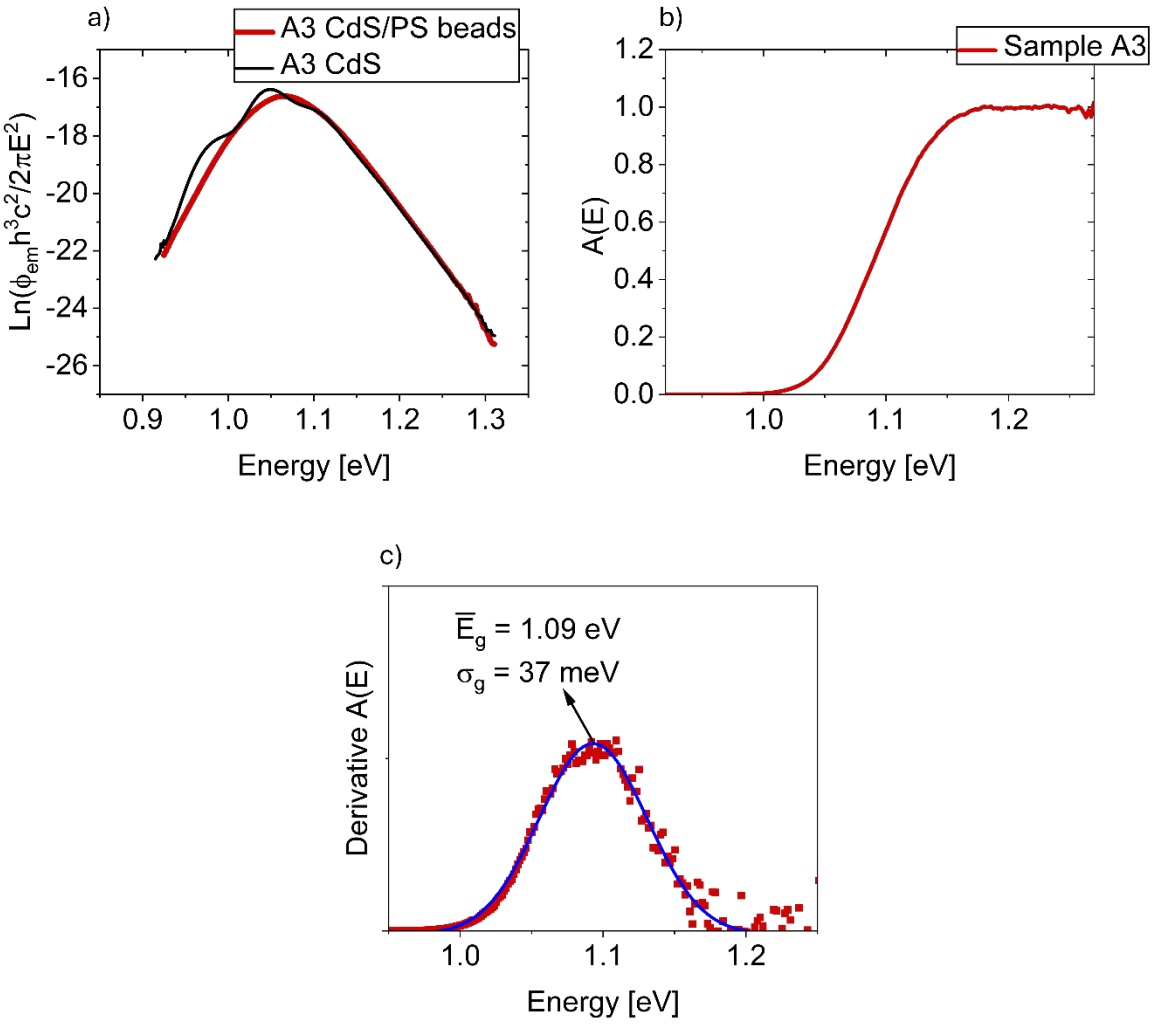

Fig. 6. 6 a) Transformed (PL) spectra based on Eq 5.3 and the assumption $A(E) = 1$, comparing absorbers with and without polystyrene (PS) spheres. The PL spectrum for the sample with PS spheres has been scaled to the reference sample without PS. **b)** Extracted $A^{PL}(E)$ spectrum from PL measurements performed on samples coated with PS microspheres. **c)** Corresponding first derivative of $A^{PL}(E)$, along with an applied Gaussian fit. Adapted from Ghrabeiki et al [132].

In **Fig 6.6 a**, It can be seen that the high energy slope remains unchanged after the PS coating. On the other hand, in the low energy side, the interference fringes are effectively suppressed.

The presence of PS spheres artificially increases the surface roughness, this effect reduces the mirror-like specular reflection and promotes diffusive reflectance. As a result, the emitted PL beams reflect at various angles from surfaces. Unlike the specular reflectance, the diffusive reflection prevents formation of the constructive and destructive interferences because the reflected beams have random phases.

For these samples, additional reflectance measurements were performed (see **Appendix C2**). Absorbers with no PS coating show strong interference peaks in the reflectance spectrum. In contrast, reflectance spectrum on samples covered with PS microspheres show significant decrease in the amplitude of interference peaks. Moreover, in **Fig 6. 6 b**, the $A^{PL}(E)$ spectrum for A3 sample was extracted using the PL spectrum of the PS-covered absorber (See Eq 5.1). Additionally, **Fig 6. 6 c** shows the first derivative of $A^{PL}(E)$ spectrum. Similar to **Fig 5. 1**, here also the average band gap energy ($\overline{E_g}$) and broadening of the absorption edge (σ_A) are determined using the Gaussian fit approach.

Similar measurements were performed on the four other samples. In **Table 6.3** , the average band gap energy of each absorber along with its corresponding qV_{OC}^{SQ} limit is presented. In the upcoming discussions, this SQ limit will be used to evaluate the $\Delta\mu$ deficit for each sample.

Table 6.3 Presents average band gap energy ($\overline{E_g}$) and qV_{OC}^{SQ} for investigates samples in this chapter. The SQ limit is calculated using Eq 2.47 with temperature of 296 K. Reproduced from Ghrabeiki et al [132].

Sample name	Eg (eV)	qV_{OC}^{SQ} (meV)
A1	1.15	908
A2	1.10	861.3
A3	1.09	851.9
B1	1.11	870.7
B2	1.11	870.7

It can be observed that sample A1, which contains no alkali elements (i.e., deposited on a substrate with Na barrier), exhibits approximately 40 meV to 60 meV higher band gap energy values compared to the other samples. This small increase in the band gap is possibly

associated with slightly higher Ga concentration of this sample (see also **Table 6.1** for composition).

Furthermore, using Beer–Lambert's law (Eq 2.13 with $R(E) = 0$), the absorption coefficient *α(E)* for each sample was determined from extracted $A^{PL}(E)$ spectrum. **Fig 6. 7 a** and **Fig 6. 7 b** present the *α(E)* for the A and B series absorbers, respectively.

Additionally, the E_U values for each sample were quantified from the exponential decay of *α(E)* at the energies well below the band gap ($\alpha(E) = \exp(E/E_U)$). All numerical E_U values are summarized in **Fig 6. 7 a** and **Fig 6. 7 b** inset.

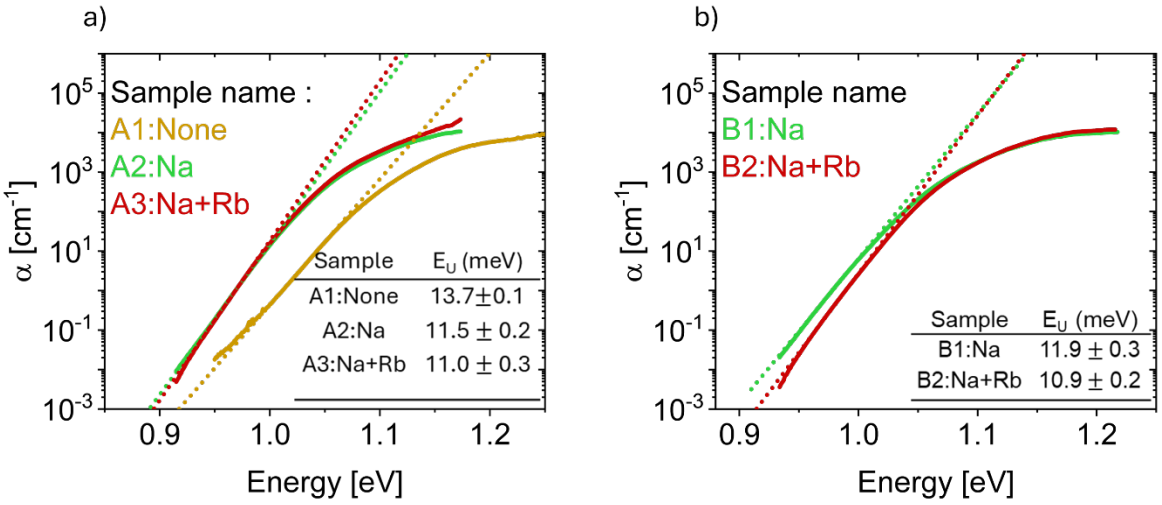

Fig 6. 7 Absorption coefficient *α(E)* derived from the $A^{PL}(E)$ spectrum for **a)** A-series and **b)** B-series absorbers. These figures include examples of linear fits used for E_U determination. Various fitting ranges were employed for E_U extraction, and the average values, along with the errors corresponding to standard deviations, are provided in each figure inset. Adapted from Ghrabeiki et al [132].

It can be observed that the introduction of the light alkali ion Na can effectively suppress the Urbach tails, reducing the E_U values from approximately 13.7 meV to below 12 meV. Furthermore, addition of the heavier alkali element Rb to Na-containing samples leads to a further reduction in E_U for the A3 sample, by around 0.5 meV. The effect of RbF PDT is more pronounced in the B2 sample, where the E_U decrease of about 1 meV. In both A and B series, the Rb introduction brings the E_U values close to 11 meV.

This observation is perfectly consistent with the previously published reports. Earlier studies have also demonstrated that Urbach tails can be effectively suppressed by the addition of Na,

with even greater reductions in the Urbach tails were observed when additional RbF PDT is performed on the Na-containing absorbers [18, 33, 34].

Furthermore, as mentioned earlier in **Section 2.5.4**, the most recent reports have identified an empirical linear relationship between the V_{OC} deficit (V_{OC}^{def}) and E_U in the state-of-the-art (SOA) CIGSe devices[33].

Analogous to the V_{OC}^{def}(Eq 2.56), the $\Delta\mu$ deficit ($\Delta\mu^{def}$) can also be defined according to the following formula:

$$\Delta\mu^{def} = qV_{OC}^{SQ} - \Delta\mu \qquad (\boldsymbol{Eq\ 6.1})$$

As previously mentioned in **Section 2.2.1**, since the $\Delta\mu$ and V_{OC} can be treated similarly, the $\Delta\mu^{def}$ would be analogous to the V_{OC}^{def}deficit, and it can be used to compare absorbers effectively.

In **Fig 6. 8**, the modified version of **Fig 2. 12** is presented. Here, the qV_{OC}^{def} and E_U for state-of-the-art (SOA) CIGSe absorbers are compared with the $\Delta\mu^{def}$ of A and B series absorbers. The SOA samples here are presented with gray points, while A and B series absorbers are presented with symbols, and the presence of alkalis is indicated using color codes.

It can be clearly seen that the A and B series absorbers do not follow the empirical trend of SOA samples. Instead, they exhibit higher $\Delta\mu^{def}$ values compared to the qV_{OC}^{def} of SOA solar cells.

For both A and B series, it is observed that the addition of Na leads to a reduction in the $\Delta\mu^{def}$, and the corresponding data points in the figure are moving closer to the empirical line with Na addition. A further decrease in $\Delta\mu^{def}$ is observed in the absorbers with both Na and Rb. Among these samples, the A3 sample lies closest to the empirical line. However, it still shows approximately 50 meV additional $\Delta\mu^{def}$ compared to the SOA sample with comparable E_U.

For SOA solar cells, it was proposed that tail states are the main limiting factor of the V_{OC} [33]. This simply means that both radiative and non-radiative recombination via Urbach tails are the dominant contributors to the V_{OC}^{def}. Therefore, the data points that are located above the empirical line indicate that, in addition to the losses in the Urbach tails, other mechanisms are

likely responsible for further lowering the $\Delta\mu$ and V_{OC} below their SQ-limit. This discrepancy may be attributed to a lower p-type doping concentration compared to samples that follow the empirical trend, or the presence of additional SRH recombination sites beyond the tail states, such as presence of bulk deep defects or surface/interface recombination centers.

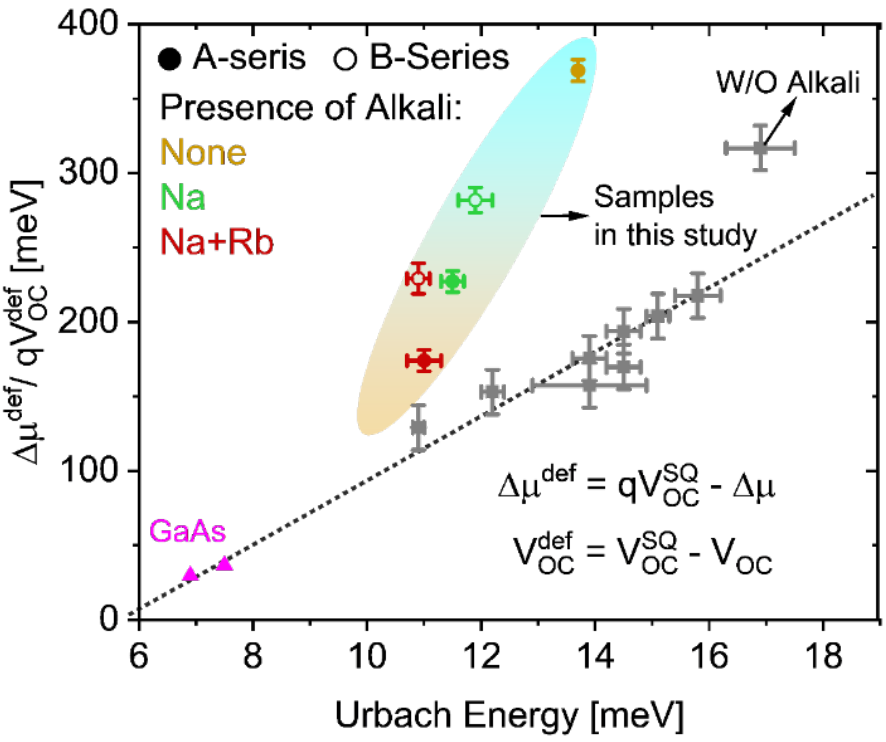

Fig 6. 8 Comparison between the V_{OC}^{def} values of state-of-the-art (SOA) solar cells and the $\Delta\mu^{def}$ values of the samples studied in this thesis. This figure is an adapted version of Fig 4 from reference [33] reproduced using the **CC BY 4.0** license. This figure was also used in my published work [132].

As presented earlier in **Fig 6. 2 b**, alkali ions lead to a reduction in the non-radiative losses and an improvement in the Y_{PL}. Once again, it is important to highlight that alkali ions decrease the non-radiative losses by suppressing the SRH recombination activities (i.e., increasing lifetime), and by increasing hole concentration (i.e., enhancing p-type doping level).

To get deeper insights regarding the origins of this decrease in the non-radiative losses (i.e., improvement in Y_{PL}), TRPL measurements were performed to extract the effective lifetime

τ_{eff}. The details of the TRPL measurements and extraction of τ_{eff} has already been presented in **Section 3.11**.

Fig 6. 9 a and **b** present the TRPL decay profile for A series and B series absorbers, respectively. Furthermore, the effective lifetime is extracted for each sample using biexponential fit to each decay profile (see **Section 3.11**). Numerical values of τ_{eff} are summarized in **Table 6.4**.

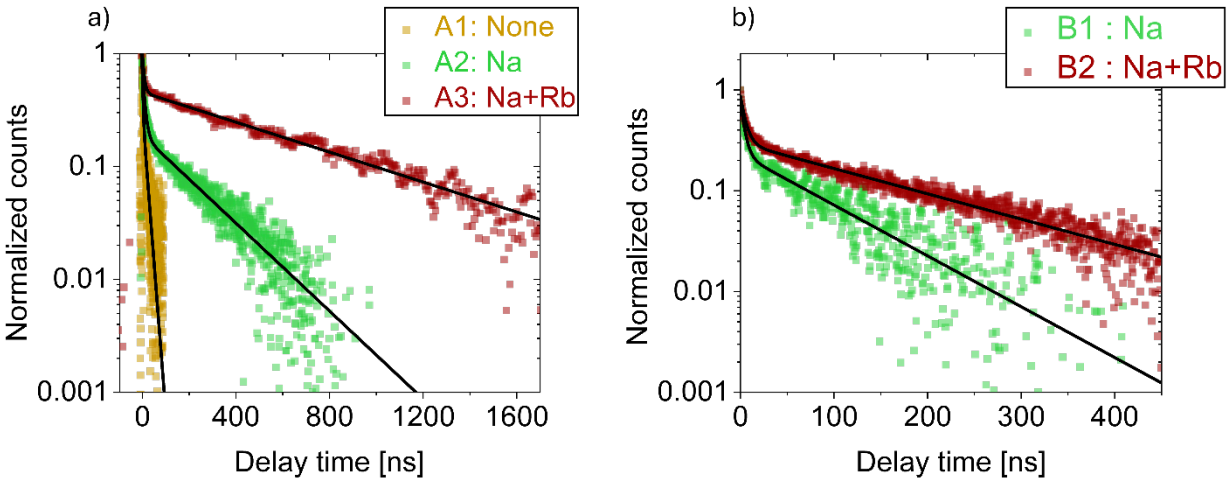

Fig 6. 9 TRPL decay profiles for **a)** A-series and **b)** B-series absorbers, shown together with bi-exponential fits (black curves) used for effective lifetime analysis. Adapted from Ghrabeiki et al [132].

Table 6.4 Presence effective lifetime τ_{eff} for A series and B series absorbers extracted from TRPL measurements. τ_{eff} here is the long decay component of biexponential fit.

Sample Name	τ_{eff} (ns)
A1	16
A2	223
A3	655
B1	86
B2	173

The TRPL measurements indicate that the Na presence significantly improves the carrier lifetime. Additionally, further enhancement in the lifetime can be achieved by Rb addition.

The increase in the lifetime indicates that SRH recombination rate has been effectively suppressed through alkali incorporation.

Notably, for some similarly processed absorbers, I conducted low-temperature PL measurements. The results for low temperature PL are presented in **Appendix C4**. These measurements reveal that the sample without any alkali elements exhibits a pronounced deep defect PL emission at low energies. However, this defect is effectively suppressed and no longer detectable when Na is present in the material. These analysis clearly demonstrate that Na can possibly neutralize the deep defects in these absorbers, leading to an increase in carrier lifetime.

It is very important to once again mention that the TRPL measurements presented here are more reliable for qualitative comparison of absorbers. For quantitative lifetime assessment, and to extract detailed lifetime values, however, more complicated measurements are needed, including excitation-dependent and temperature-dependent analysis [159, 161].

Additionally, to assess the doping level in these absorbers, capacitance–voltage (CV) measurements were performed on devices fabricated from the A series samples. For more details regarding the CV analysis please see **Section 3.5**.

Fig 6. 10 illustrates the C-V profile of the A series solar cells. Moreover, the carrier concentration for each absorber is determined from the minimum point of the C-V profile, and the values are summarized in **Table 6.5** .

These measurements show a significant enhancement in the doping concentration with Na incorporation, followed by a smaller additional increase after RbF-PDT.

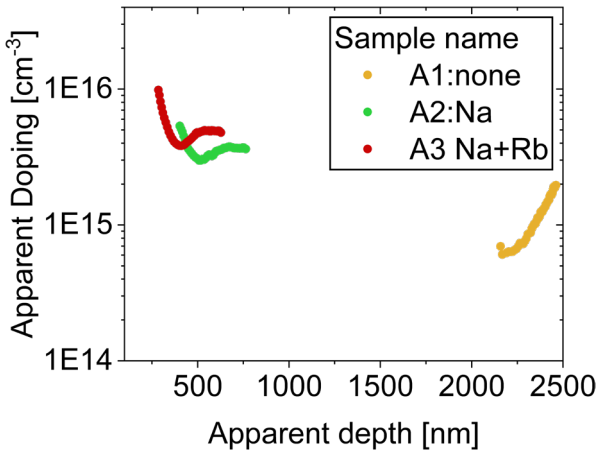

Fig 6. 10 Apparent oping profile vs apparent depth obtained from low temperature CV measurements. Adapted from Ghrabeiki et al [132].

Table 6.5 Doping concentration extracted from minimum point of C-V profile in **Fig 6. 10**. Errors are due to 0.01 cm^2 uncertainty in the device area.

Sample Name	Doping CV (cm^{-3})
A1	6 (± 0.50) × 10^{14}
A2	3 (± 0.28) × 10^{15}
A3	3.8 (± 0.36) × 10^{15}

It is important to highlight that Kodalle et al. [22] previously reported CV measurements for similarly prepared absorbers. Their extracted carrier concentration show a slightly stronger increase upon Rb addition. However, their reported doping values are in the same range with my reported values in **Table 6.5** [22].

Among all investigated samples, the highest doping concentration is observed in the A3 sample (with Na+Rb), which has a carrier concentration of approximately 3.8×10^{15} cm^{-3}. On the other hand, for high efficiency CIGSe samples with similar band gap energies but higher V_{OC} values, one order of magnitude higher doping concentrations have been reported by C-V measurements [11, 45, 46, 71]. This difference suggests that the additional $\Delta\mu^{def}$ observed in the **Fig 6. 8** for samples in this thesis might primarily result from the low doping concentrations.

Unfortunately, the doping concentration of the B series absorbers cannot be compared here, as the devices made from B2 sample were shunted, which could not be used for C-V measurements.

In any case, the absorbers investigated in this thesis show the expected behavior upon alkali addition. In both A and B series, suppression of Urbach tails and increase in the $\Delta\mu$ can be seen with alkali incorporation. In the following sections, the main focus will be on the origins of these tail states.

6.3 Origin of the Urbach tails in CIGSe absorbers

So far, it was observed that Urbach tails in the CIGSe absorbers can be suppressed upon alkalis addition. This observation is not something new, and it has been already reported multiple times in previous studies [18, 33, 34].

In this section the primary reason behind the effect of alkalis and decrease in the Urbach tails are discussed.

This section is divided into 3 sub sections: in **Section 6.3.1** the possible correlation between Urbach tails and grain boundaries (GBs) is investigated. In **Section 6.3.2** intensity dependent PL measurements were performed to analyze the effect of electrostatic potential fluctuations to the tail states. Finally, **Section 6.3.3** provides discussions and hypothesis regarding the origin of the decrease in the E_U with alkali addition.

6.3.1 Grain boundary contribution to E_U

To gain deeper insights into the influence of the GBs, FM-KPFM measurements were employed to monitor changes in the potential barrier at the GBs of each absorber. Details of the KPFM measurements and band bending extraction methods have already been discussed in **Section 3.8** and references [133, 134].

As mentioned earlier in **section 3.8**, the band bending (i.e., electronic potential barrier) at the GBs can be quantified by monitoring the changes in the contact potential differences (ΔCPD) across the GBs.

In previous discussions in **Section 3.8**, an example of downward band bending was illustrated for a selected GB. Here, In **Fig 6. 11**, an example of upward band bending is illustrated for a selected GB from A2 absorber.

Similar to **Fig 3. 13**, first the GB position is identified from topography map (**Fig 6. 11a**). Subsequently, using the KPFM map the changes in work function (corresponding to ΔCPD) are extracted from the same area (**Fig 6. 11 b**).

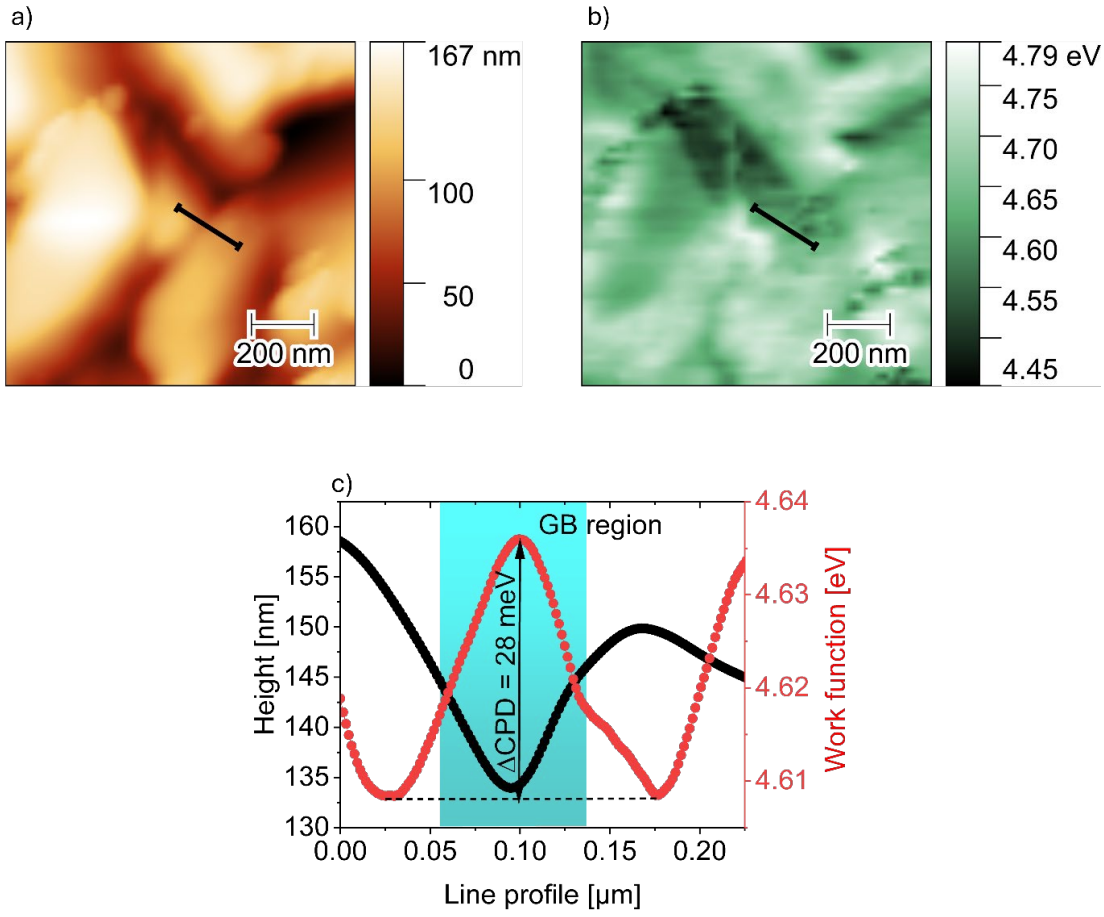

Fig 6. 11 a) and **b)** illustrates an example of a selected GB from sample A2. This GB is marked with black line. **a)** presents the AFM topography map, while **b)** shows the simultaneously measured KPFM map. **c)** Illustrates the height and work function changes along this selected GB (i.e, black line), this GB shows an positive potential barrier (i.e, upward band bending) with ΔCPD = 28 meV. Adapted from Ghrabeiki et al [132].

In the line profile shown in **Fig 6. 11c**, the topography measurement of this particular GB shows a drop followed by a rise in the measured height across the GB, forming a valley-like

pattern that corresponds to the GB position. The corresponding change in the work function along the same line is also presented in **Fig 6. 11c**, showing an increase followed by a decrease across the GB. This observed change in the work function indicates that this selected grain boundary exhibits an upward band bending profile.

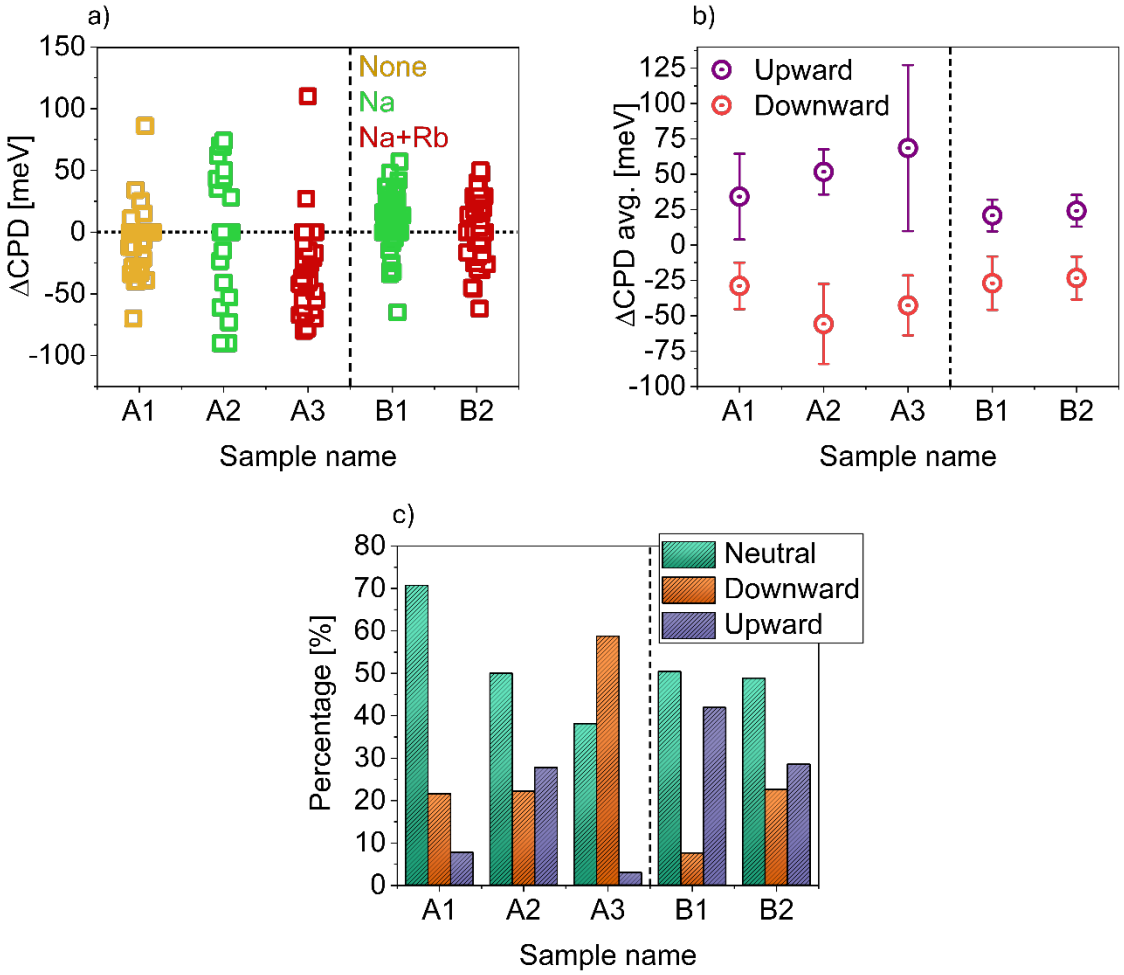

Fig 6. 12 a) Overview of the all obtained band bending values for all samples. **b)** Mean band bending values across all GBs for absorbers with the presence of various alkali ions. **c)** Bar chart summarizing the distribution of the positive, negative and neutral GB types for all investigated samples. Adapted from Ghrabeiki et al [132].

Overall, to have reliable statistical results, the potential barriers of more than 340 GBs were investigated.

Fig 6. 12 a illustrates the statistical distribution of all measured band bending values (ΔCPD) for each distinct absorber. Positive ΔCPD values correspond to upward band bending, resulting

from accumulation of negative charges (i.e., electron barrier), while negative ΔCPD values correspond to downward band bending due to accumulation of positive charges (i.e, hole barrier). GBs with ΔCPD values near zero, or those GBs with work function variations attributed to facet-dependent effects, are classified as electrically neutral (ΔCPD = 0).

Furthermore, **Fig 6. 12 b** illustrates the mean band bending values (i.e., average ΔCPD) for both upward and downward band bending for each absorber. Notably, these mean ΔCPD values remain very small for all analyzed samples —around the thermal energy at room temperature (26 meV)— with only minimal variations observed across different absorbers. Considering the error bars and associated uncertainties, the presence or absence of alkali elements does not significantly affect the mean band bending values.

Additionally, **Fig 6. 12 c** shows the portion of GBs exhibiting positive, negative, or neutral band bending for each sample. In sample A1, with the absence of alkali elements, most of the GBs are electrically neutral (i.e., ΔCPD = 0). The incorporation of Na leads to a noticeable rise in the share of GBs with positive potential barrier (i.e., positive band bending), although neutral GBs with ΔCPD = 0 still represent the majority. This observed trend aligns with earlier studies, which suggest that Na segregation at GBs promotes the formation of upward band bending [90, 123].

Furthermore, B2 and A3 absorbers, which contain Rb, show a significant increase in the number of GBs with negative potential barrier, accompanied by a clear reduction in the share of GBs with positive potential barrier.

Up to now, with the use of the KPFM results and Urbach energy measurements, it can be seen that KPFM data do not indicate any correlation between tail states and charged GBs. In **Fig 6. 7**, it was observed that introduction of alkalis leads to noticeable decrease in the E_U values. However, KPFM analysis show that the magnitude of band bending remains very small for all samples. Even in A1 sample, which contains no alkali ions, only very small band bending was detected at the GBs, with neutral GBs being dominant.

Furthermore, with alkali incorporations, the number of neutral GBs decreases. This observation clearly show that presence of alkali ions results in an increase in the share of charged GBs.

If Urbach tails were directly linked to the GBs, it would be expected to see reduced band bending and fewer charged GBs in the alkali-containing absorbers—which is not observed here.

However, it is very important to mention that the KPFM analysis are surface sensitive measurements, and the extracted data primarily reflect the properties of absorber surface.

Overall, combination of PL and KPFM measurements leads to the conclusion that the suppression of tail states with alkali incorporation is not primarily linked to the charged GBs.

This statement is further supported by previous findings of **Dr. Omar Ramirez**, where he observed that alkalis can also decrease the E_U in the single-crystalline CIGSe films with no GBs [34].

6.3.2 Electrostatic fluctuations in CIGSe absorbers

In **section 2.3**, where the tail states are first introduced, it was briefly mentioned that Urbach tails originate from disorders within the semiconductor material. This disorders stem partly from lattice vibrations associated with thermal effects and partly from disorders in the material. The latter case can be further categorized into two types: (i) static disorder or frozen-in defects, such as band gap variations caused by alloy composition fluctuations, and (ii) charged defects, which induce Coulombic electrostatic potential fluctuations that lead to distortions in the band edges.

Cody et al. [63] proposed following equation that can describe the E_U in a semiconductor with the presence of lattice vibrations and static disorders [59, 63, 64]:

$$E_U = S_0 k \theta_E \left(\frac{1+X}{2} + \frac{1}{\exp\left(\frac{\theta_E}{T}\right) - 1} \right) \qquad (\boldsymbol{Eq\ 6.2})$$

Here, S_0 is a constant, T represents the semiconductor's temperature, k_B is the Boltzmann constant, and θ_E denotes the Einstein characteristic temperature, which is related to the phonon vibration effects. The parameter X is dimensionless and independent of temperature; this parameter reflects the strength of static, frozen-in disorders. A larger value of X indicates a higher degree of static disorder within the material and result in the higher values of E_U. In an ideal crystal structure, free from static disorders, X would be equal to zero.

However, this equation does not provide any information regarding the behavior of E_U in the presence of charged defects. Unlike the static disorder, charged defects can have interaction with free carriers. As the temperature of the absorber increases, thermally generated free carriers can effectively screen these charged defects, thereby reducing the magnitude of electrostatic potential fluctuations and the Urbach energy [34, 66]. Similarly, an increase in the incident laser intensity leads to a higher density of photogenerated mobile carriers, which can also screen the charged defects, consequently reducing the strength of the electrostatic fluctuations and decreasing the extent of the Urbach tails [34, 67].

Fig 6. 13 a schematically represents the effect of incident light intensity on the strength of electrostatic fluctuations. Here, both conduction band and valance band edges are deformed because of electrostatic fluctuations. As the incident laser flux increases, the screening effect reduces the strength of these fluctuations.

Multiple reports have demonstrated the presence of electrostatic potential fluctuations in the CIGSe absorbers [34, 66, 77]. As discussed in **Section 2.5.1**, CIGSe is a compensated semiconductor, containing both acceptor states such as V_{Cu} and donor states like In_{Cu}. These defect states can become charged and interact with each other, leading to electrostatic fluctuations in the band edges. Notably, previous studies have shown that the strength of these fluctuations and magnitude of E_U are strongly influenced by the Cu concentration [34, 66, 96]. Cu-poor materials exhibit stronger electrostatic potential fluctuations and higher E_U [34, 66, 96].

These fluctuations are more pronounced at low temperature [34, 66], while the increase in the temperature significantly reduces the magnitude of these electrostatic fluctuations, in the Cu-poor materials, even at the room temperature (here 296 K), these electrostatic fluctuations are present to some extent [34, 66].

To investigate the influence of electrostatic potential fluctuations on the Urbach tails, intensity-dependent PL measurements were performed on the CIGSe samples. For these measurements, it is crucial to change the incident flux substantially to see the effect of fluctuations. With the small changes in the flux, this effect cannot be revealed. Therefore, an optical lens was employed to reduce the laser beam radius from 1.1 mm to approximately 70 μm. By reducing

the laser beam size, higher incident photon fluxes can be achieved without increasing the total laser power.

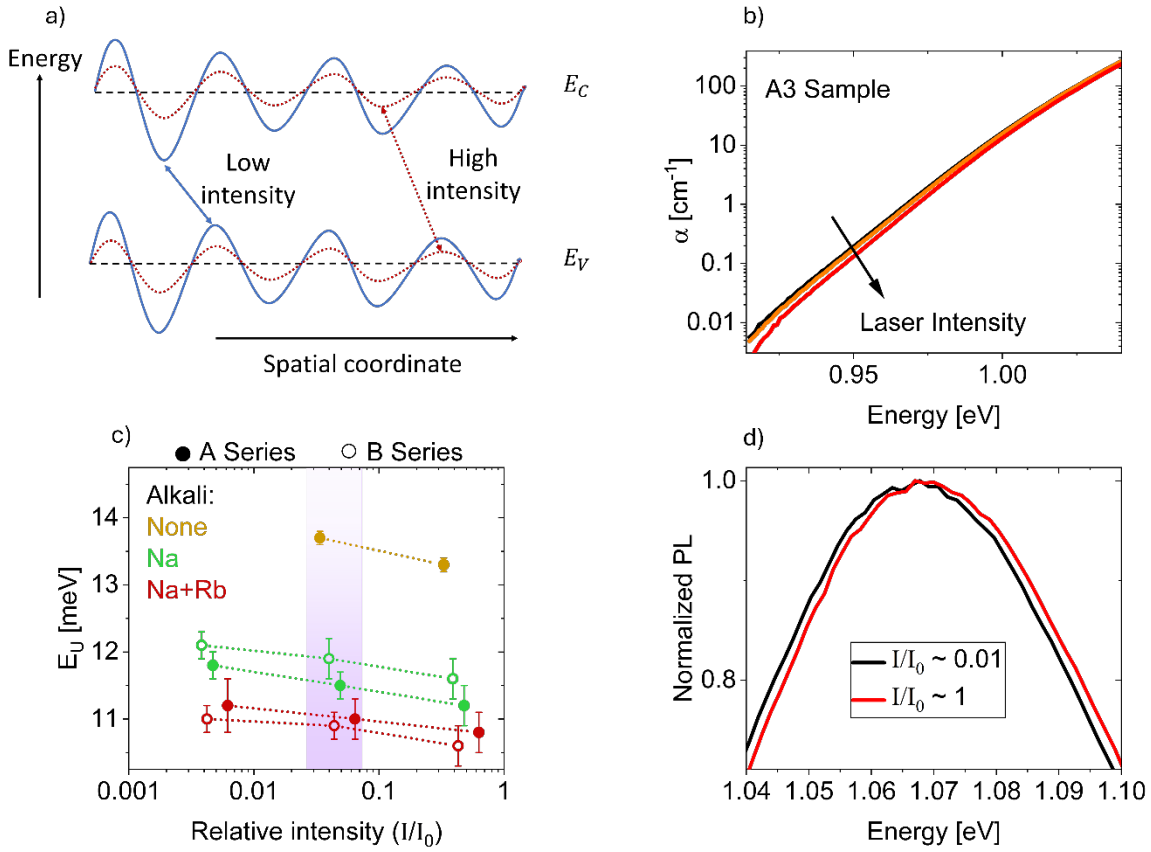

Fig 6. 13 a) Schematic figure illustrating that extent of electrostatic fluctuations diminish with increase in laser excitation flux. **b)** *α(E)* of sample A3 derived from intensity dependent PL analysis. **c)** Average E_U values obtained at various laser excitation fluxes. As explained in the main text, the rescaling factor is multiplied to each laser intensity. The E_U values highlighted region has been already illustrated in **Fig 6. 7**. **d)** Normalized PL emission spectra of sample A3, illustrating a small shift to the high energies with increase in laser flux. Adapted from Ghrabeiki et al [132].

It is important to mention that low temperature intensity dependent measurements have been reported previously for CIGSe absorbers [34, 66]. However, here, I performed these measurements at the room temperature. The main purpose of these measurements is to confirm the presence of electrostatic fluctuations at significantly higher temperatures.

Fig 6. 13 b illustrates the intensity-dependent E_U measurements for A3 sample. These analysis were carried out at a constant room temperature (296 K), and the incident laser flux was

increased by an order of magnitude at each step. At each intensity level, a PL spectrum was recorded, and the E_U was extracted using the method described earlier in **Section 6.2**. It is worth mentioning that the absorber temperature remained stable throughout the intensity-dependent measurements. Additional details regarding the influence of laser intensity on the sample temperature are discussed in **Appendix C5**.

In **Fig 6. 13 b**, it is evident that as the laser intensity increases, the low energy side of the $\alpha(E)$ becomes steeper, resulting in the lower E_U values. A similar trend was also observed for four other samples. **Fig 6. 13 c** presents a comparison of E_U values for all samples under increased laser intensity. It is very important to note that, because the samples are covered with PS spheres, and the coated PS layer is not identical for all absorbers, the absorbed laser flux is different for each sample. To ensure a valid comparison, a rescaling factor needs to be applied to the incident laser fluxes. This factor was determined by measuring the PL spectra of the absorbers both before and after the PS coating. The PL spectra of the PS-coated absorbers were then rescaled to align with those of the uncoated samples (as shown in **Fig 6. 6**), and the scaling factor was calculated individually for each sample. This factor was then applied to the incident laser intensities in **Fig 6. 13 c** to facilitate the comparison between the samples.

This observed decrease in the E_U with increasing laser flux show that electrostatic potential fluctuations are responsible for the formation of Urbach tails to some extent. Higher laser fluxes generate more charge carries, which can screen the charged defects and flatten these fluctuations, thereby reducing the magnitude of Urbach tails (**Fig 6. 13 a**).

Furthermore, as the laser flux increases, the PL spectrum exhibits a shift toward higher energies (i.e., a blue shift). As illustrated in the **Fig 6. 13 b** for the A3 sample, higher laser intensity leads to a slight blue shift in the PL spectrum. This blue shift is also associated with the screening effect of charged impurities and the resulting flattening of the electrostatic fluctuations, which results to higher-energies for radiative transitions [34, 66]. Similar behavior was also observed for other absorbers.

If the band gap fluctuations were caused solely by static disorders, such as alloy fluctuations, an increase in the laser excitation flux would not cause a blue shift in the PL peak and decrease in E_U.

Overall, these observations indicate that the electrostatic potential fluctuations exist in the CIGSe absorbers even at the room temperature, and these fluctuations partly contribute to the formation density of states (DOS) within the band gap.

Previously published temperature-dependent PL investigations have observed that the strength of electrostatic fluctuations decreases in the presence of alkali ions [34, 77]. In the next section, further details and hypotheses regarding the suppression of these fluctuations with the alkali ion introduction will be discussed.

6.3.3 Why E_U decreases with alkali incorporation?

As discussed earlier in **Section 6.3.2**, the presence of charged defects are responsible for the electrostatic fluctuations in the material.

Shklovsky and Efros [201] proposed the following equation that gives the mean depth of these electrostatic fluctuations γ_{el}:

$$\gamma_{el} = \frac{q^2}{4\pi\varepsilon_0\varepsilon}\frac{N_I^{\frac{2}{3}}}{p^{\frac{1}{3}}} \qquad (\boldsymbol{Eq\ 6.3})$$

In this equation, the N_I represents the number of charged impurities, q represents the elementary charge, ε is the CIGSe relative permittivity, and p is the mobile carrier concentration. The p here can be expressed as [98]:

$$p = p_0 + \delta p + \delta n \qquad (\boldsymbol{Eq\ 6.4})$$

Where p_0 is net doping concentration (i.e, hole concentration) of the CIGSe semiconductor, while δp and δn represent the photogenerated hole and electron concentrations, respectively. As discussed in **Section 2.1.2**, since the electrons and holes are generated in pairs under illumination, the δp would be same as δn (i.e., $\delta p = \delta n$).

The decrease in the amplitude of electrostatic fluctuations with increasing laser flux can be explained using Eq 6.3. As the excitation flux increases, more mobile charge carriers are generated within the semiconductor, which results in a increase in both δp and δn. This increase, in turn, decreases the average amplitude of electrostatic fluctuations γ_{el} [34, 98].

Furthermore, similar behavior can be expected when the net carrier concentration (p_0) of the material increases [34]. Similarly, with the increase in p_0, the charged impurities are screened, leading to a smaller magnitude of electrostatic potential fluctuation according to Eq 6.3.

This model offers insight into why the introduction of alkali ions leads to a reduction in the E_U of CIGSe absorbers. As previously shown in **Section 2.5.3**, the introduction of Na increases the doping concentration of the absorbers, and even additional enhancement in doping is observed with the involvement of heavier alkali ions.

This enhancement in the p type doping level with alkalis incorporation can effectively screen the charged defects, thereby reducing the mean depth of electrostatic potential fluctuations, γ_{el}.This reduction, in turn, leads to a decrease in the extent of Urbach tails.

Notably, Dr. Omar Ramirez proposed this hypothesis to explain the decrease in the Urbach energy with alkali addition in single crystalline CIGSe samples [34]. Here, to get further insights regarding this mechanism, some simple simulations are performed using Eq 6.3.

Let's assume the case for a p-type compensated semiconductor where all acceptor states and donor states are charged and contribute to the overall doping of the semiconductor. In this case for p_0 and N_I, it can be written:

$$p_0 = N_A - N_D \qquad (\boldsymbol{Eq\ 6.5})$$

$$N_I = N_A + N_D \qquad (\boldsymbol{Eq\ 6.6})$$

In this case the Eq 6.3 can be transformed into the following form:

$$\gamma_{el} = \frac{q^2}{4\pi\varepsilon_0\varepsilon}\frac{(N_A + N_D)^{\frac{2}{3}}}{(N_A - N_D)^{\frac{1}{3}}} \qquad (\boldsymbol{Eq\ 6.7})$$

Furthermore, the degree of compensation K can be defined by following formula:

$$K = \frac{N_D}{N_A} \qquad (\boldsymbol{Eq\ 6.8})$$

Notably, CIGSe absorbers are known to be heavily compensated. Some studies have reported K values up to 0.99 for CGSe absorbers [99].

In **Section 2.5.3** it was mentioned that alkalis can increase the doping concentration by promoting the formation of acceptor states such as V_{Cu}, or by neutralizing donor states like In_{Cu}.

Now let's simulate the first case, where only the acceptor states are introduced in the absorbers. In **Fig 6. 14**, the effect of increasing net doping concentration and reduction in the compensation was simulated by varying the acceptor concentrations N_A while keeping the donor concentration N_D constant. As N_A increases, leads to a rise in the net doping concentration, resulting in a decrease in the γ_{el} values due to screening effect (see Eq 6.3 and Eq 6.7).

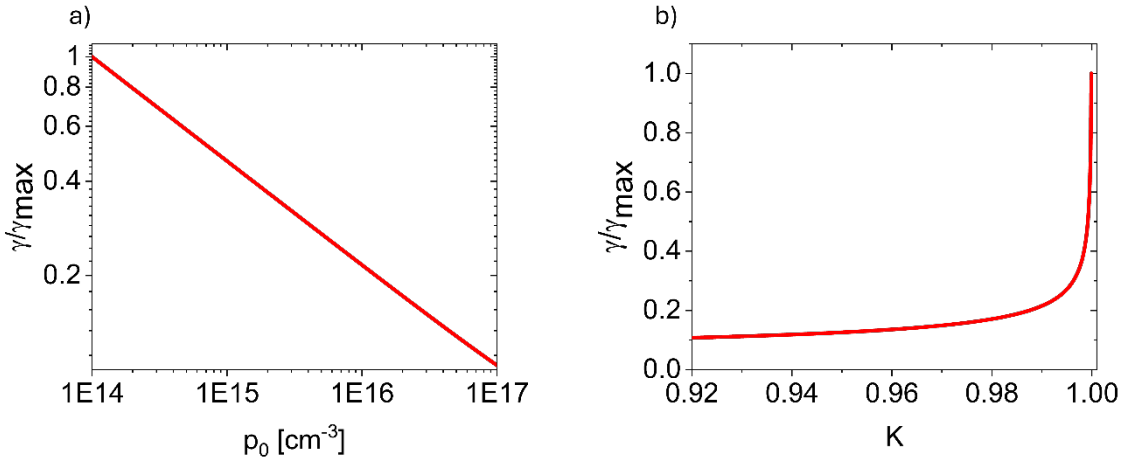

Fig 6. 14 Modeling the effect of increased p-type doping resulting from increase acceptor defects (i.e, increase in N_A) : A reduction in γ_{el} as **a)** the doping concentration rises, and **b)** when compensation ratio K decreases. (For Simulation parameters See **Appendix C6**). Adapted from Ghrabeiki et al [132].

In the next step, the other mechanism is illustrated, where the N_A is kept constant and N_D is reduced, similarly in **Fig 6. 15** it can be seen that the depth of fluctuations γ_{el} decreases with the decrease in N_D and K.

For these two cases, all simulation parameters are presented in **Appendix C6**.

In any case, regardless the mechanism behind the increase in the doping with alkalis, according to the Eq 6.3 and assumptions in Eq 6.5 and Eq 6.6, both increase in the number of acceptor states and passivation of the donor states can lead to decrease in the magnitude of γ_{el}. This

effect provides a possible explanation for the observed reduction in the Urbach tails upon the involvement of alkali ions.

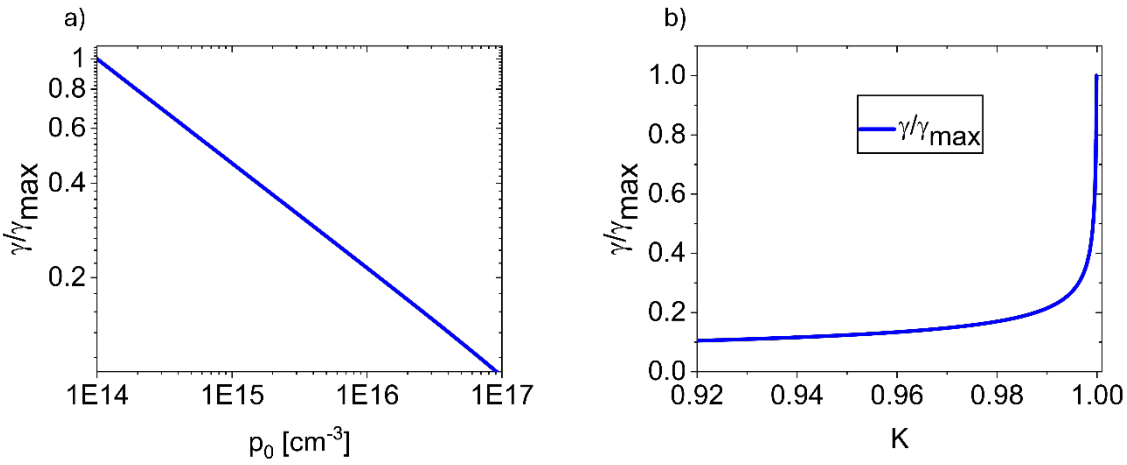

Fig 6. 15 Simulations presenting the impact of increased p-type doping due to a rise in the donor defects (i.e., increase in N_D), showing a reduction in γ_{el} both as the **a)** doping concentration increases and **b)** as the K decreases. (For simulation parameters, see **Appendix C6**). Adapted from Ghrabeiki et al [132].

Additionally, the most recent conductive atomic force microscopy (C-AFM) study by Sharma et al. (C-AFM) [45] has shown that in addition to the increase the p-type doping level, alkali ions also promote a more homogeneous doping distribution profile across the CIGSe absorbers. In the **Appendix C7**, I show that this observation can be linked to a reduction in the amplitude of electrostatic potential fluctuations. When γ_{el} decreases, a more uniform doping profile is expected within the sample.

6.4 Conclusion and summary of Chapter 6

This chapter primarily focused on studying the origin of tail states in CIGSe absorbers. In particular, it investigated the potential role of charged GBs in the formation of tail states within the band gap. PL analysis indicated that Urbach tails are significantly suppressed upon the incorporation of alkali elements. However, KPFM results did not support the hypothesis that charged GBs are responsible for the reduction of tail states. Specifically, the electronic barriers at the GBs remained small, and it was found that alkali incorporation increases the number of charged GBs.

Moreover, excitation-dependent PL measurements clearly showed that E_U decreases, and the PL emission shifts to higher transition energies as the excitation flux increases. This behavior is attributed to the screening effect of charged impurities through the generation of mobile free carriers, which can diminish the extent of electrostatic fluctuations.

Moreover, increase in the hole concentration can also lead screening of charged defects and decrease in the amplitude of γ_{el}. Notably, the alkali-induced enhancement in hole concentration contributes to this screening, effectively mitigating the impact of these charged defects and thereby lowering the extent of electrostatic fluctuations and Urbach tails.

7 Summary and conclusion

The main objective of this thesis was to investigate the limitations in the V_{OC} of CIGSe devices and to explore the relationship between tail states and grain boundaries. In this final chapter, I summarize the key findings and overall results of this thesis.

In **Section 4.1** of **Chapter 4**, the generalized detailed balance model was introduced using both optoelectrical and purely optical formalisms.

Once again, I have to mention that optoelectrical measurements have been widely applied in previous studies to investigate the V_{OC} limitations in solar cells [28, 30, 31]. On the other hand, the optical model has not received significant attention.

With the use of analogy between optoelectrical reciprocity (Eq 2.52) and Planck's generalized law (Eq 2.54), the generalized detailed balance model was extended to purely optical analysis, where the $A(E)$ and absolute PL spectrum was used to identify the radiative $\Delta\mu$ limit and all $\Delta\mu$ losses.

Overall, using the generalized detailed balance formalism allows us to quantify the V_{OC} and $\Delta\mu$ losses relative to the idealized SQ limit.

Both V_{OC} and $\Delta\mu$ losses can be divided into different categories:

(i) Radiative losses (both $\delta\Delta\mu^{rad}$ and δV_{OC}^{rad}) are induced due to the broadening of the $A(E)/QE(E)$ onset (see Eq 4.8 and Eq 4.15)

(ii) Generation $\Delta\mu$ loss ($\delta\Delta\mu^{Gen}$) in the thin-film absorbers originate from the reduction in the generation flux density compared to the SQ generation flux density i.e. $F_{Gen}^{sun} < F_{Gen}^{SQ}$. (see Eq 4.7). Similarly, short-circuit V_{OC} losses (δV_{OC}^{SC}) in complete devices occurs due to decrease in the J_{SC} compared to the SQ-J_{SC} limit i.e. $J_{SC} < J_{SC}^{SQ}$ (see Eq 4.14)

(iii) Non-radiative losses (both $\delta\Delta\mu^{nr}$ and δV_{OC}^{nr}) arise due to undesirable non-radiative recombination activities within the absorber/devices (see Eq 4.10 and Eq 4.16)

Following the introduction of theoretical formalism, in **Section 4.2,** detailed simulations have been conducted to explore the influence of band gap inhomogeneities (fluctuations), sub-band gap Urbach tails and limited absorber thickness on the $A(E)$ broadening and radiative losses.

Notably, the effect of tail states and Gaussian band gap distributions are combined together in these simulations. The results indicate that increase in the Urbach energy and stronger lateral band gap inhomogeneities can both enhance the $A(E)$ broadening and induce radiative losses (**Fig 4. 4** and **Fig 4. 5**). However, in the range of Urbach energies typically observed for CIGSe absorbers, sub-band gap tail states have only a minor influence on the $A(E)$ broadening. On the other hand, band gap fluctuations are the dominant factor contributing to the broadening of $A(E)$ spectrum. Additionally, decrease in the material thickness can further enhance this broadening and radiative losses (**Fig 4. 10**).

Subsequently, in **Chapter 5**, I used the generalized detailed balance formulas to quantitatively assess all V_{OC} and $\Delta\mu$ losses for thin-film CIGSe samples.

In **Section 5.1**, with the use of directly extracted $A(E)$ and absolute PL spectra, all the radiative, generation and non-radiative $\Delta\mu$ losses were quantified for number of CIGSe absorbers both with and without Ga compositional gradient (see **Table 5.2**).

Moreover, experimental results demonstrated that the final $\Delta\mu$ of the absorbers can be determined using the generalized detailed balance model by adding up the radiative, generation, and non-radiative losses (see again **Table 5.2**).

The quantified values of $\Delta\mu$ from loss analysis have been compared with those extracted independently from linear fit to high energy slope of PL spectrum. Notably, this comparison shows that the numerical $\Delta\mu$ values extracted from both methods exhibit very good agreement (see **Fig 5. 7**).

Similar analysis were conducted on CIGSe devices where V_{OC} losses and final internal voltage (V_{in}) was determined using combination of absolute EL and direct *QE(E)* analysis.

Overall, both optoelectrical and purely optical analysis show that absorbers containing Ga compositional gradient can show approximately 10 meV to 20 meV increase in the absorption

edge broadening. This enhanced broadening, in turn, induces 5 meV to 16 meV additional radiative losses (see **Table 5.2** and **Table 5.4**)

The observed increase in both broadening and radiative losses in graded absorbers can be associated with the narrow width of notch region.

Moreover, CL analysis in **Fig 5. 11** revealed that graded CIGSe absorbers might possibly show more pronounced lateral band gap inhomogeneities compared to the ungraded ones.

My own observation was further confirmed by the literature review and metanalysis of literature data, where meta-analysis results in **Fig 5. 13** showed that gradient is the main contributor to the $A(E)/QE(E)$ broadening.

The meta-analysis results also indicate that band gap graded (BGG) absorber have average broadening parameter around 45 meV. This average broadening values is further decreased to around 30 meV with employing hockey stick gradient (HSG) profile, and even a slightly smaller values can be seen for absorbers with no gradient (see aging **Fig 5. 13**).

In CIGSe absorbers, both in this study and in state-of-the-art technology, the non-radiative loss component remains the primary loss that reduces the V_{OC}.

In **Chapter 5**, for the best case, the non-radiative loss was around 200 meV. On the other hand, the record CIGSe solar cell show non-radiative losses around 100 meV [11].

It is important to note that considerable work is still needed to further reduce the contribution of non-radiative recombination. However, this does not mean that mitigating radiative losses is less important.

For the latest record efficiency CIGSe device, I found a broadening parameter of around 30 meV from published $QE(E)$ data. Simulations based on the error function model show that this amount of broadening would induce approximately 18 meV radiative losses (see **Fig 4. 3**). If this broadening can be reduced to values close to GaAs technology with $\sim$ 10 meV broadening parameter (see **Fig 5. 13**), approximately 15 meV can be gained in the V_{OC}. This amount of V_{OC} increase can directly result in 0.5 % efficiency improvement in these devices.

Overall, from the **Chapter 5** results, it can be concluded that if we want to mitigate the radiative losses, next generation CIGSe solar cells should feature with uniform band gap profile.

However, in the absence of gradient, it is important to use alternative passivation approaches for the back surface recombination. The most recent works of **Dr. Taowen Wang**, shows that effective back surface passivation can be successfully achieved by employing a selective hole transport contact [100, 109, 180]. With the use of this selective contact, we can avoid the band gap gradient, and prepare samples with uniform band gap profile with effectively passivated back interface.

The last chapter of this thesis primarily studies the effect of alkali ions on the Urbach tails and grain boundaries of CIGSe absorbers. Although in **Chapter 4** I showed that tail states have only a small influence on the radiative losses, they can further reduce the V_{OC} of devices by contributing to the detrimental non-radiative SRH recombination process.

Recent studies proposed that the radiative and non-radiative losses through Urbach tails are the primary limiting mechanism for the performance of state-of-the-art CIGSe devices [33].

In **Chapter 5**, the discussions were mainly focused on the origin of these Urbach tails.

Consistent with previous reports, my measurements also demonstrate that alkali ions reduce the Urbach energy and lead to increase in V_{OC} and efficiency [33, 77, 111]. PL analysis revealed that, with the presence of Na and Rb, the Urbach energy can approach to values as low as 11 meV (**Fig 6. 7**).

However, FM-KPFM analysis did not confirm the idea that the reduction of Urbach tails is caused by grain boundary passivation effect. The band bending in all samples, both with and without alkali incorporation, showed only small values. Furthermore, alkali incorporation neither reduced the magnitude of band bending nor decreased the number of charged grain boundaries (**Fig 6. 12**).On the other hand, excitation-dependent PL measurements showed that higher laser intensities result in lower Urbach energies.

This observation clearly indicates that electrostatic potential fluctuations contribute to the formation of tail states in CIGSe absorbers (**Fig 6. 13**).The reduction of the Urbach energy can be explained using previously proposed mechanism based on increase in the p-type doping level [34]. According to this mechanism, the enhanced carrier concentration leads to screening of charged defects and flattening of these electrostatic fluctuations, thereby reducing the Urbach tails.

List of Publications and presentations

First Author Publications:

- **Gharabeiki, Sevan**, Michele Melchiorre, and Susanne Siebentritt. "Influence of NaF and KF Post-Deposition Treatment on the Sub-Band Gap Absorption of Cu (In, Ga) Se 2 Absorber Layers." In *2023 IEEE 50th Photovoltaic Specialists Conference (PVSC)*, pp. 1-3. IEEE, 2023.

- **Gharabeiki, Sevan**, Muhammad Uzair Farooq, Taowen Wang, Mohit Sood, Michele Melchiorre, Christian A. Kaufmann, Alex Redinger, and Susanne Siebentritt. "Grain boundaries are not the source of Urbach tails in Cu (In, Ga) Se2 absorbers." *Journal of Physics: Energy* 6, no. 3 (2024): 035008.

- **Gharabeiki, Sevan**, Francesco Lodola, Tilly Schaaf, Taowen Wang, Michele Melchiorre, Nathalie Valle, Jérémy Niclout et al. "The effect of a band gap gradient on the radiative losses in the open circuit voltage of solar cells." *Under review, PRX ENERGY* (2025).

Co-authored Publications:

- Siebentritt, Susanne, Uwe Rau, **Sevan Gharabeiki**, Thomas P. Weiss, Aubin Prot, Taowen Wang, Damilola Adeleye, Marwan Drahem, and Ajay Singh. "Photoluminescence assessment of materials for solar cell absorbers." *Faraday discussions* 239 (2022): 112-129.

- Singh, Ajay, Jeremy Hieulle, Joana Ferreira Machado, **Sevan Gharabeiki**, Weiwei Zuo, Muhammad Uzair Farooq, Himanshu Phirke, Michael Saliba, and Alex Redinger. "Coevaporation stabilizes tin-based perovskites in a single Sn-oxidation state." *Nano Letters* 22, no. 17 (2022): 7112-7118.

- Finn Babbe, Nicoleta Nicoara, Harvey Guthrey, Nathalie Valle, Omar Ramirez Sanchez, Damien Aureau, Hossam Elanzeery, Deepanjan Sharma, José Luís Virtuoso, Jean-Nicolas Audinot, Anastasiya Zelenina, **Sevan Gharabeiki**, Tom Wirtz, Susanne Siebentritt, Phillip J Dale, Sascha Sadewasser, Diego Colombara. "Vacuum-healing of grain boundaries in sodium-doped CuInSe2 solar cell absorbers." *Advanced Energy Materials* 13, no. 17 (2023): 2204183.

- Phirke, H., **S. Gharabeiki**, A. Singh, A. Krishna, S. Siebentritt, and A. Redinger. "Quantifying recombination and charge carrier extraction in halide perovskites via hyperspectral time-resolved photoluminescence imaging." *APL Energy* 2, no. 1 (2024).

- Wang, Taowen, Longfei Song, **Sevan Gharabeiki**, Mohit Sood, Aubin JC M. Prot, Ricardo G. Poeira, Michele Melchiorre et al. "Shifting the paradigm: a functional hole-selective transport layer for chalcopyrite solar cells." *Solar RRL* 8, no. 12 (2024): 2400212.

- Zhang, Yan-Song, Hasan Arif Yetkin, Hakam Agha, **Sevan Gharabeiki**, Rijeesh Kizhakidathazhath, Lena Merges, Ricardo G. Poeira, Jan PF Lagerwall, and Phillip J. Dale. "Arbitrary and active colouring of solar cells with negligible loss of efficiency." *Energy & Environmental Science* 18, no. 2 (2025): 884-896.

- Farooq, Muhammad Uzair, **Sevan Gharabeiki**, Ding Yong, Joana Ferreira Machado, Jean-Nicolas Audinot, Tom Wirtz, Mohammad Khaja Nazeeruddin, Susanne Sienbentritt, and Alex Redinger. "Impact of processing atmosphere on nanoscale properties of highly efficient Cs 0.05 MA 0.05 FA 0.9 PbI 3 perovskite solar cells." *Nanoscale* 17, no. 14 (2025): 8861-8871.

- Prathapani, Sateesh, **Sevan Gharabeiki**, Jakob Lauche, René Schwiddessen, Pablo Reyes-Figueroa, Nikolaus Weinberger, Michele Melchiorre, Rutger Schlatmann, Iver Lauermann, and Christian Alexander Kaufmann. "Impact of Minimal Silver Incorporation on Chalcopyrite Absorbers—Origins for Improved Open-Circuit Voltages in (Ag, Cu)(In, Ga) Se2 Solar Cells." *Solar RRL* 9, no. 5 (2025): 2400863.

Presentations and Talks:

- **Sevan Gharabeiki**, Taowen Wang, Ajay Singh, Alex Redinger and Susanne Siebentritt, Exact determination of Quasi-Fermi Level splitting from absolute photoluminescence and absorptance spectra. DPG Focus session: Perspectives in Cu(In,Ga)Se_2, Regensburg, Germany, September 2022. (Oral presentation. Presented by **Dr. Taowen Wang**)

- **Sevan Gharabeiki**, Mohit Sood, Michele Melchiorre and Susanne Siebentritt, Influence of NaF and KF post-deposition treatment on the Urbach energy of Cu(In,Ga)Se_2 absorber layers, Poster presentation, IEEE PVSEC conference, Puerto Rico, USA, June 2023 (Poster presentation. Presented by **Prof. Susanne Siebentritt**)

- **Sevan Gharabeiki**, Mohit Sood, Valentina Serrano Escalante, Taowen Wang, and Susanne Siebentritt, Beneficial impact of KF post-deposition treatment on non-radiative recombination of CIGSe absorbers. DPG Spring meeting, Dresden, Germany, March 2023 (Oral presentation)

- **Sevan Gharabeiki**, Muhammad Uzair Farooq, Taowen Wang, Mohit Sood, Michele Melchiorre, Christian A. Kaufmann, Alex Redinger and Susanne Siebentrirr, Grain

boundaries are not the source of Urbach tails in Cu(In,Ga)Se2. 34th Asian PVSEC, Shenzhen, China, November 2023 (Oral presentation)

- **Sevan Gharabeiki**, Tilly Schaff , Francesco Lodola, Taowen Wang, Michele Melchiorre and Susanne Siebentritt, Effect of the Band Gap Gradient on the Open Circuit voltage limit of the Cu(In,Ga)Se2 Absorbers, IEEE PVSEC conference, Seattle, USA, June 2024 (Poster presentation. Presented by **Prof. Susanne Siebentritt**)

- **Sevan Gharabeiki**, Tilly Schaaf, Francesco Lodola, Taowen Wang , Michele Melchiorre, and Susanne Siebentritt. The effect of a band gap gradient on the radiative loss in open circuit voltage of solar cells, European Material Research Society (E-MRS) fall meeting, September 2024 (Oral presentation)

- **Sevan Gharabeiki**, Francesco Lodola, Taowen Wang, Michele Melchiorre, Nathalie Valle, Jérémy Niclout , Manha Ali, Yucheng Hu, Gunnar Kusch, Rachel A.Oliver and Susanne Siebentritt . Radiative voltage losses induced by band gap fluctuations, Urbach tails and compositional gradients, IEEE PVSEC, Montreal, Canade, June 2025 (Accepted for oral presentation, finalist for best student presentation award)

Acknowledgement

Completing this project would have not been possible without the support and encouragement I received along the way. Over the past four years, I had the opportunity to work with many wonderful people. Here, I would like to thank everyone who supported me through this journey.

First and foremost, I would like to express my deepest gratitude to Prof. Susanne Siebentritt, my supervisor, for giving me the opportunity to join her research group. Her continuous support, insightful discussions, and valuable guidance were instrumental throughout the course of my PhD. I am specially thankful for the resources and facilities that she provided, which enabled me to carry out my research efficiently.

I would also like to thank Prof. Alex Redinger and Muhammad Uzair Farooq for their collaboration to this work. The grain boundary and surface analyses presented in Chapter 6 were performed by Uzair under the supervision of Prof. Redinger. I am also grateful to Prof. Redinger for being a member of my CET committee and the jury of my doctoral defense. His constructive feedback and insightful discussions during our meetings were highly valuable and played a key role in enhancing the quality of my research.

Special thanks to Prof. Jürgen Christen for his participation as a CET committee member and jury member for my PhD defense. I would also like to warmly thank Prof. Thomas Kirchartz and Prof. Selina Olthof for being jury members of my PhD defense.

I am also thankful to Dr. Christian Kaufmann and PVcomB team at HZB for providing samples used in the analysis of Urbach tails and grain boundaries.

I extend my sincere thanks to Dr. Michele Melchiorre for processing the solar cells and for depositing the buffer and window layers. I am also deeply grateful to Thomas Schuler for his technical support in maintaining and repairing laboratory equipment.

A special thanks goes to Prof. Rachel A. Oliver, Dr. Gunnar Kusch and Yucheng Hu from GaN centre at the University of Cambridge for performing and analyzing the cathodoluminescence measurements.

I would like to thank my colleagues in the LPV, LEM, and SPM groups. In particular, I wish to acknowledge Prof. Philip Dale, Taowen, Omar, Aubin, and offer special thanks to Saeed, Francesco, Aline, Boaz, Penda, Adriana, Mohit, Damilola, Zhuangyi, Paul, Clara, Patricia, Thomas Weiss, Alessandro, Elham, Tien, Kulwinder, Arivu, Ricardo, Joana, Hasan, Tilly, and Alice. I am grateful to all who supported me throughout this journey.

A very special thanks to my family—my parents, Klaris and Yourik, and my sister, Naeira—for their support throughout these four years. Your love, encouragement, and belief in me have meant everything and helped me persevere through every challenge.

I would also like to thank the Luxembourg National Research Fund (FNR) for supporting my research through the following grant numbers: C20/MS/14735144/TAILS.

I would like to acknowledge the assistance of OpenAI's ChatGPT for providing English language editing support, including help with grammar, punctuation, and word choice, which contributed to improving the clarity of my own written content.

Lastly, to anyone I may have forgotten—thank you as well for your contribution and support. I am sincerely grateful to all who played a role in this work.

Appendix of Chapter 4

Appendix A1. Solution to error function integral

In this part, solution to the integral in Eq 4.20 where the $A^{loc}\left(E, E_g^{loc}\right)$ is defined by step function (Eq 4.21**)** is presented.

For the Gaussian distribution of local band gap $P\left(E_g^{loc}\right)$ (Eq 4.18), the lower limit of the integral can be reliably extended to $-\infty$. This is because the Gaussian function approaches to zero in the range from $-\infty$ to 0. Therefore, its contribution to the integral is negligible.

With this approach, the Eq 4.20 can be written as:

$$A(E) = \int_{-\infty}^{\infty} A^{loc}\left(E, E_g^{loc}\right) P\left(E_g^{loc}\right) dE_g^{loc} \qquad (\boldsymbol{Eq\ A1.1})$$

By considering Eq 4.18 and Eq 4.21**,** the equation above **(**Eq A1.1**)** transforms to the following form [166, 167]**:**

$$A(E) = \int_{-\infty}^{E} \frac{1}{\sigma_g\sqrt{2\pi}} \exp\left(-\frac{\left(E_g^{loc} - \overline{E_g}\right)^2}{2\sigma_g^2}\right) dE_g^{loc} \qquad (\boldsymbol{Eq\ A1.2})$$

Now, by defining $x = \frac{E_g^{loc} - \overline{E_g}}{\sigma_g}$, the Eq A1.2 can be written as:

$$A(E) = \int_{-\infty}^{\frac{E-\overline{E_g}}{\sigma_g}} \frac{1}{\sqrt{2\pi}} \exp\left(-\frac{x^2}{2}\right) dx \qquad (\boldsymbol{Eq\ A1.3})$$

Subsequently, the integral above (A1.3) can be broken into the following form:

$$A(E) = \int_{-\infty}^{0} \frac{1}{\sqrt{2\pi}} \exp\left(-\frac{x^2}{2}\right) dx + \int_{0}^{\frac{E-\overline{E_g}}{\sigma_g}} \frac{1}{\sqrt{2\pi}} \exp\left(-\frac{x^2}{2}\right) dx \qquad (\boldsymbol{Eq\ A1.4})$$

The first term of Eq A1.4 is integral over Gaussian distribution (i.e., probability distribution), if the full integral range is considered (i.e., from $-\infty$ to $+\infty$), this result would be 1. However, here only integral extends from $-\infty$ to 0. Therefore, its result would be $\frac{1}{2}$.

Furthermore, according to error function definition (i.e., $\mathrm{erf}(z) = \int_0^z \frac{2}{\sqrt{\pi}} \exp(-z^2)\, dz$), the second term would be $\frac{1}{2}\mathrm{erf}\left(\frac{E-\overline{E_g}}{\sqrt{2}\sigma_g}\right)$.

Therefore, the overall result of Eq A1.4 can be written into the following form:

$$A(E) = \frac{1}{2} + \frac{1}{2}\mathrm{erf}\left(\frac{E - \overline{E_g}}{\sqrt{2}\sigma_g}\right) \qquad (\boldsymbol{Eq\ A1.5})$$

Considering the fact that erf is an odd function, the equation A1.5 can be rearranged into:

$$A(E) = \frac{1}{2} - \frac{1}{2}\mathrm{erf}\left(\frac{\overline{E_g} - E}{\sqrt{2}\sigma_g}\right) \qquad (\boldsymbol{Eq\ A1.6})$$

$$= \frac{1}{2}\mathrm{erfc}\left(\frac{\overline{E_g} - E}{\sqrt{2}\sigma_g}\right)$$

The equation above is complementary error function (erfc) from, which is same as Eq 4.22 in the main text.

Appendix A2. Radiative limit from Rau-Werner method

Rau and Werner [166] proposed equations to calculate the V_{OC}^{rad} by considering a Gaussian band gap distribution (according to Eq 4.18).

$$V_{OC}^{rad} = \overline{E_g} - \frac{{\sigma_g}^2}{2kT} - kTln\left(\frac{J_{00}}{J_{SC}}\right) \qquad (\boldsymbol{Eq\ A2.1})$$

Here the J_{00} is defined according to the following formula:

$$J_{00} = \frac{2\pi q}{h^3c^2}\left[2(2kT)^3 + 2(kT)^2\overline{E_g} + kT\overline{E_g}^2 - 2{\sigma_g}^2\overline{E_g} - {\sigma_g}^2kT + \frac{{\sigma_g}^4}{kT}\right] \qquad (\boldsymbol{Eq\ A2.2})$$

And J_{SC} is simply defined by:

$$J_{SC} = q\int_0^\infty A(E)\Phi_{Sun}dE \qquad (\boldsymbol{Eq\ A2.3})$$

Eq A2.3 assumes no collection loss, therefore $A(E) = QE(E)$. In this context the V_{OC}^{rad} would be same as $\Delta\mu^{rad}$.

In this appendix, I compare my calculations results for $\Delta\mu^{rad}$ (here same as qV_{OC}^{rad}) in **Fig 4.3** with the values extracted from the Eq A2.1. Although they also used a Gaussian distribution model for the band gap to perform the calculations for V_{OC}^{rad}, their calculation models differ slightly from the approach presented in **Section 4.1.1**.

By using these equations, the $\Delta\mu^{rad}$, was calculated for σ_g in the range of 0 meV to 100 meV. Here also $\overline{E_g} = 1.1\ eV$ and T = 296 K is considered.

Fig A2.1 illustrates the calculated $\Delta\mu^{rad}$ using the Eq A2.1. It can be observed that the obtained results completely align with the values that were reported in **Fig 4.3**.

Furthermore, some studies use simplified approximation to obtain the $\Delta\mu^{rad}$, which involves using the following assumption for SQ limit [46, 167, 173]:

$$qV_{OC}^{SQ} \approx E_g - k_BTln\left(\frac{J_{00}}{J_{SC}}\right) \qquad (\boldsymbol{Eq\ A2.4})$$

And by using this assumption and Eq A2.1 the $\Delta\mu^{rad}$ can be estimated as [173]:

$$\Delta\mu^{rad} \approx qV_{OC}^{SQ} - \frac{{\sigma_g}^2}{2k_BT} \qquad (\boldsymbol{Eq\ A2.5})$$

In **Fig A2.1** the $\Delta\mu^{rad}$ values are also compared for this simplified case with the exact calculated results. It is evident that as the σ_g increases, these simple approximations lead to the underestimation in $\Delta\mu^{rad}$. This is because the Eq A2.4 is only a good approximation for small σ_g values, and as σ_g increases, the right-hand side of Eq A2.4 gets larger than the qV_{OC}^{SQ}, therefore approximating it with qV_{OC}^{SQ} would result in underestimation of $\Delta\mu^{rad}$.

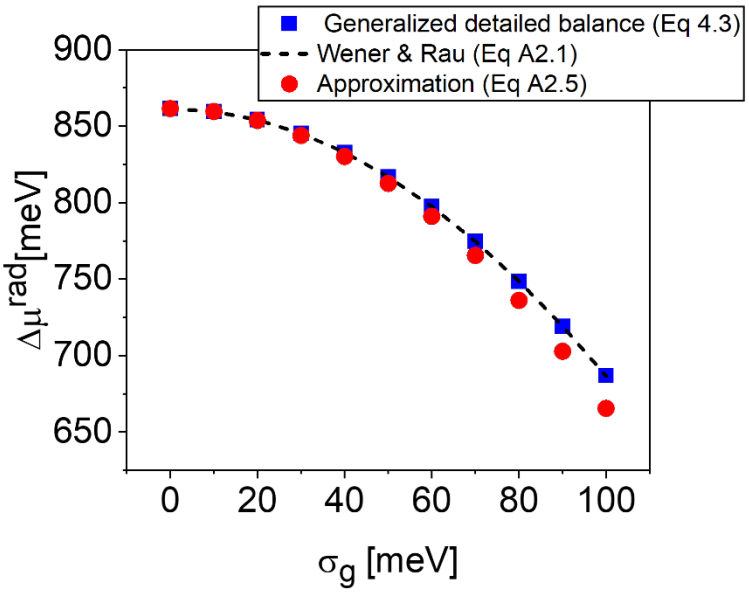

Fig A2.1 Comparison of the $\Delta\mu^{rad}$ calculated from Eq 4.3 (in main text), Eq A2.1 and Eq A2.5. Her Gaussian distribution of band gaps were assumed (see Eq 4.18)

Appendix of Chapter 5

Appendix B1. SIMS measurements for F-BGG, G-NG, E-BGG and D-NG samples

SIMS measurements were performed on the selected CIGSe to evaluate the Ga distribution across the thickness. The details of SIMS measurements has already been provided in **Section 3.12**.

In **Fig B1.1**, for samples F-BGG and G-NG, it can be observed that the SIMS measurements are completely in agreement with the cross sectional CL analysis. The CL measurements of F-BGG **Fig 5. 11,** and CL measurements of G-NG sample can be found in **Appendix B9**, respectively.

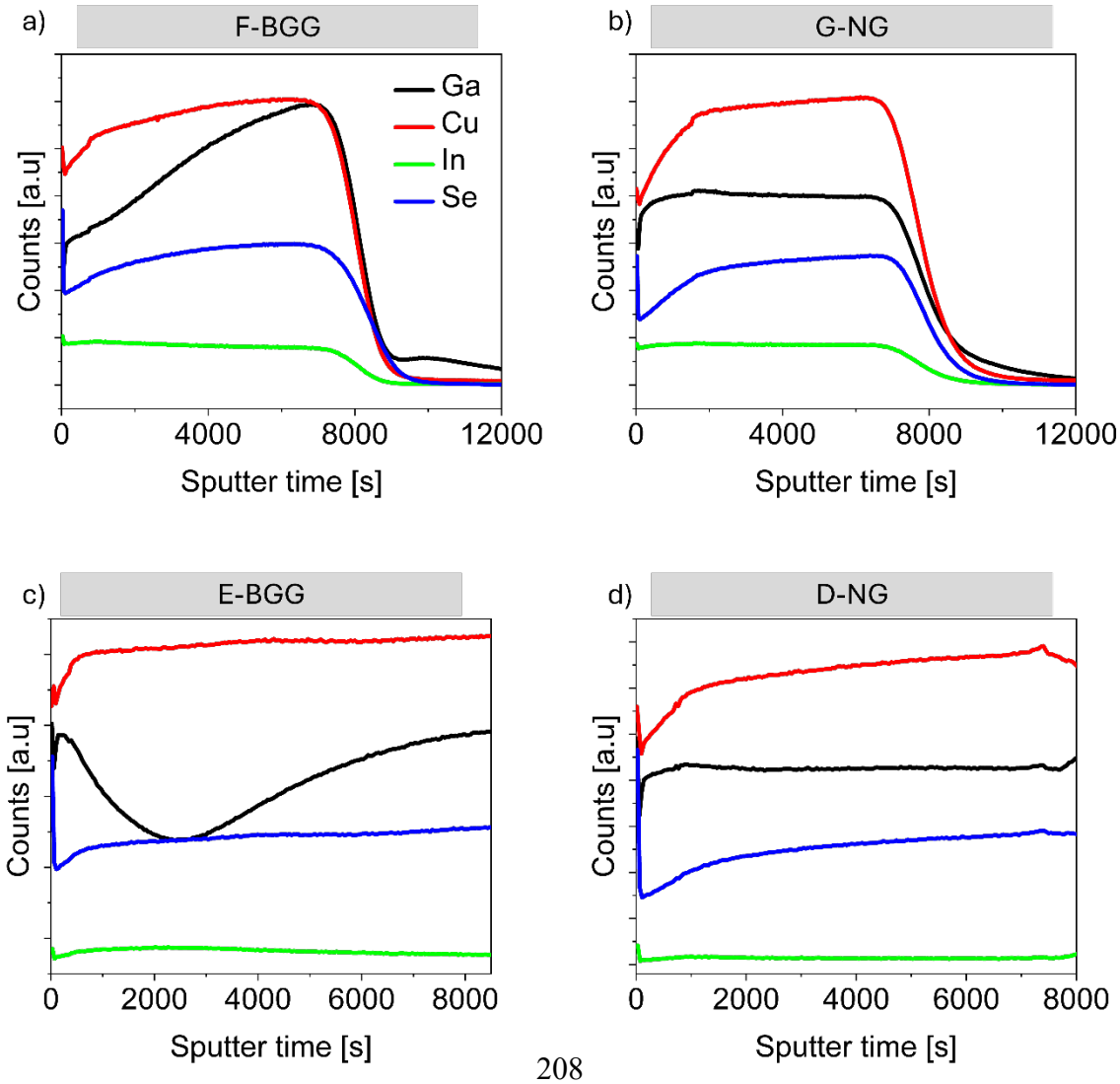

Fig B1.1. SIMS measurements showing Cu, In, Ga and Se distribution profile over the absorbers depth for **a)** F-BGG, **b)** G-NG, **c)** E-BGG and **d)** D-NG absorbers. The F-BGG and G-NG absorbers are prepared on Mo substrate, while E-BGG and D-NG samples are prepared on SLG. (The samples surface is at sputter time = 0)

In **Fig 5. 11**, for F-BGG sample, it was observed that CL emission peak shifts to higher energies when moving toward the back contact, confirming the presence of Ga gradient. On the other hand, in **Fig B9.1** in **Appendix B9,** for G-NG sample, it can be seen that the CL emission peak remains nearly unchanged through the depth.

Appendix B2. Absorptance spectra for the D-NG and E-BGG absorbers

The $A(E)$ spectra extracted from PL and direct measurements for samples D-NG and E-BGG are presented in the following **Fig B2.1**. These samples are introduced in **Table 5.1** .

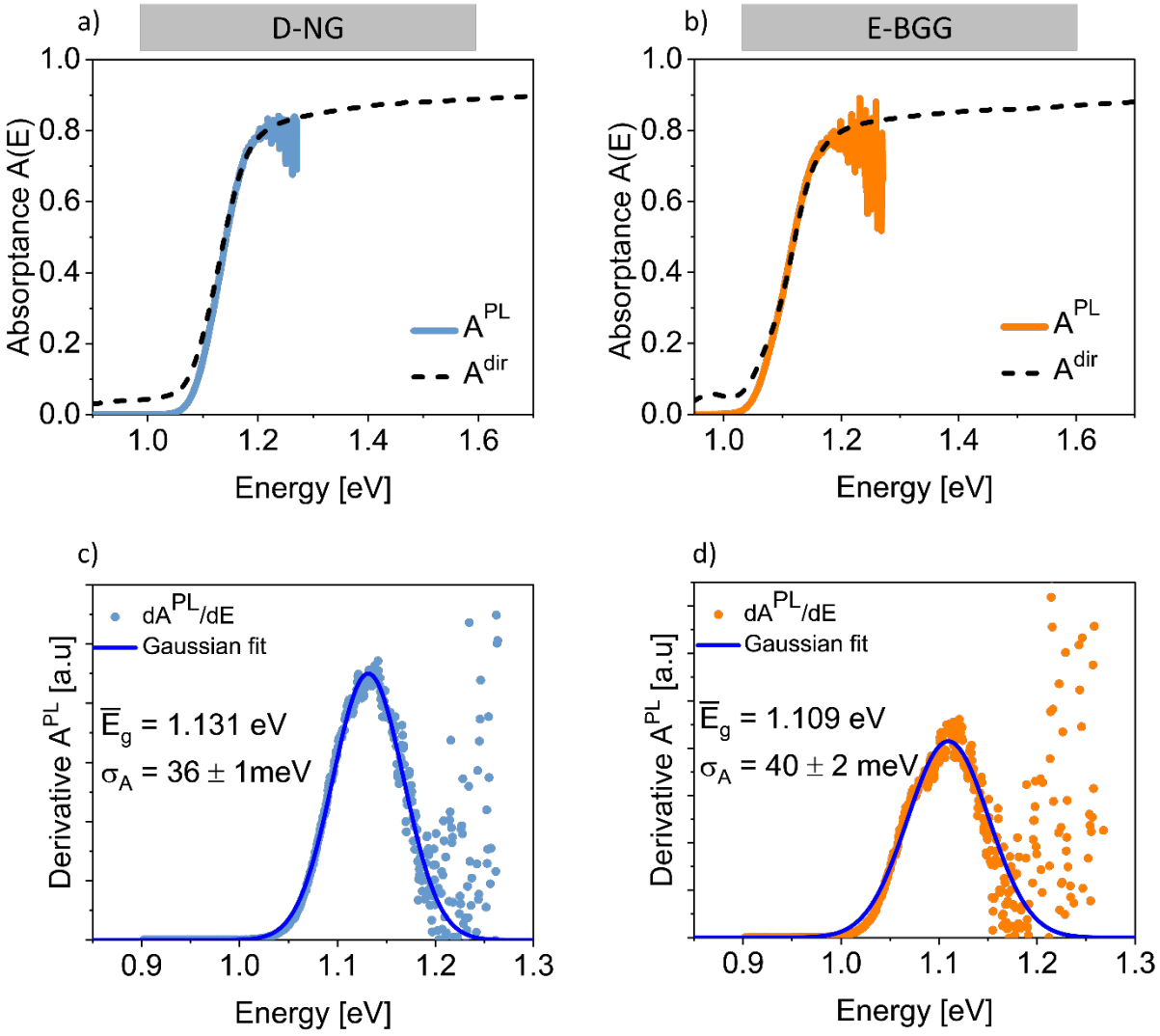

Fig B2.1. a) and **b)** Illustrating the absorptance spectra for D-NG and E-BGG absorbers. **c)** and **d)** shows the 1st derivative of $A^{PL}(E)$ spectra along with the $\overline{E_g}$ and σ_A for D-NG and E-BGG samples.These derivatives are extracted from smoothed $A^{PL}(E)$ curves. These samples were prepared on SLG substrate (See **Table 5.1**).

Additionally, as an example, **Fig B2.2** compares the first derivative of *A(E)* for B-NG absorber, obtained from both $A^{dir}(E)$ and $A^{PL}(E)$ measurements.

It can be observed that both derivative curves have the same maximum position (i.e same values of $\overline{E_g}$). However, the curve derived from $A^{dir}(E)$ falls lower than $A^{PL}(E)$, and becomes distorted at lower energies. This deviation occurs because $A^{dir}(E)$ becomes already distorted and unreliable near the onset energy (see **Fig 3. 11**). Therefore, in all previous figures, only $A^{PL}(E)$ has been used to assess the broadening, as it provides a more reliable shape.

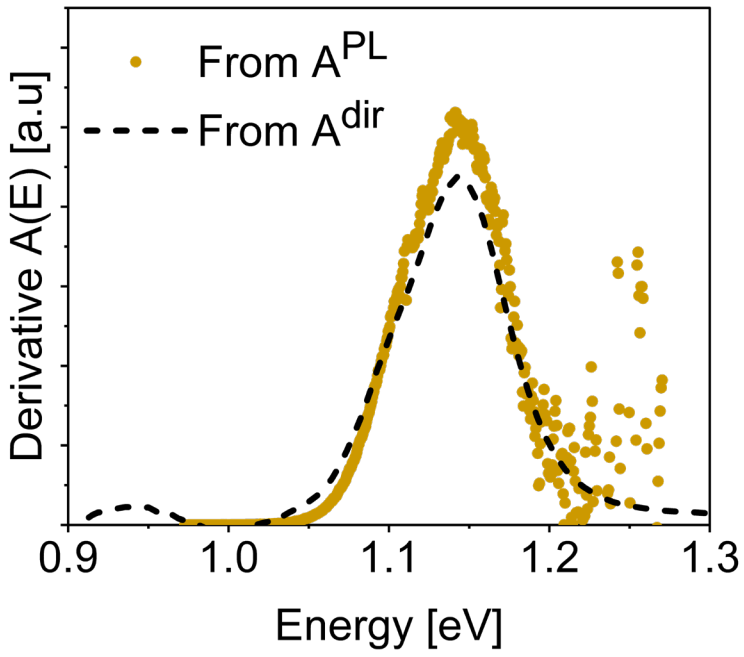

Fig B2.2. Illustrates the first derivative of $A^{PL}(E)$ and $A^{dir}(E)$ spectra for B-NG absorber.

Appendix B3: Comparison between laser generation flux and Sun generation flux

In **Chapter 4**, all equations for generalized detailed balance model were presented by considering the on sun radiation spectrum AM 1.5 g [40] (see also **Fig 2. 2**). However, in **Chapter 5**, the Y_{PL} was obtained using incident laser light rather than sun radiation. By considering the fact that sun spectrum covers the wide energy range and laser emission is monochromatic emission in a single wavelength, the final absorbed flux for a sample can be different under sun emission and laser emission. Here, it will be shown that this discrepancy is very small for CIGSe samples, and has almost no influence on the final values of obtained $\Delta\mu$.

As mentioned earlier in **Section 5.1.1**, the incident laser flux (F_{inc}^{Laser}) is calibrated to have flux equal to one sun SQ generation flux (F_{Gen}^{SQ}). Therefore, for F_{inc}^{Laser}, it can be written:

$$F_{inc}^{Laser} \approx F_{Gen}^{SQ} = \int_{Eg}^{\infty} \Phi_{Sun} dE \qquad (\boldsymbol{Eq\ B3.1})$$

As explained in **Section 5.1.1**, by having the *A(E)* spectra of samples, the laser generation flux (F_{Gen}^{Laser}) would be:

$$F_{Gen}^{Laser} = A(E_{laser}) F_{inc}^{Laser} \qquad (\boldsymbol{Eq\ B3.2})$$

Here, the $A(E_{laser})$ is the numerical value of *A(E)* at the laser emission energy.

On the other hand, the sun generation flux for a sample with known *A(E)* was given by Eq 2.19 ($F_{Gen}^{Sun} = \int_0^{\infty} A(E)\Phi_{Sun} dE$):

Since for samples prepared on SLG substrate, separate transmittance and reflectance measurements are performed, and the $A(E_{laser})$ can be independently determined through these measurements (see **Fig 3. 11**).

Furthermore, as already been explained in **Section 5.1.1,** the full range $A(E)$ can be reconstructed by combination of photospectrometric and PL measurements (see **Fig B3.1** and **Fig 5. 1**)

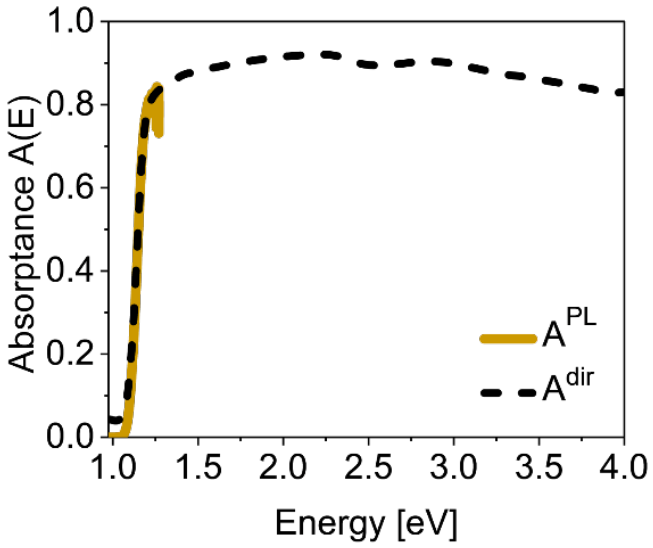

Fig B3.1. Full range $A(E)$ extracted from direct photospectometric measurements $A^{dir}(E)$ and PL measurements $A^{PL}(E)$.

With using the full range $A(E)$ in **Fig B3.1**, and AM 1.5 g [40] emission spectrum (**Fig 2. 2**), the F_{Gen}^{Sun} is calculated according to Eq 2.19**.** For this particular sample, the F_{Gen}^{Sun} has value of 2.35×10^{17} $(\frac{photons}{cm^{-2}s^{-1}})$.

On the other hand, by having the calibrated incident laser flux of ~ 2.62×10^{17} $(\frac{photons}{cm^{-2}s^{-1}})$ and $A(E_{laser}) = 0.91$, the F_{Laser}^{Gen} would be 2.38×10^{17} $(\frac{photons}{cm^{-2}s^{-1}})$ according to Eq B3.2,

By comparing the sun generation flux and laser generation flux, it can be written:

$$\frac{F_{Gen}^{Laser}}{F_{Gen}^{Sun}} \approx 1.01 \qquad (\boldsymbol{Eq\ B3.3})$$

It can be seen that the difference is small, and considering the fact that the logarithmic term of Y_{PL} is calculated for $\delta\Delta\mu^{nr}$, this extremely small discrepancy is negligible in final result.

Appendix B4. $\Delta\mu$ values from linear fit method and from generalized detailed balance analysis

Table B4.1. Numerical values of $\Delta\mu$ calculated from Eq 5.3 by considering both $A(E) = 1$ and $A(E) = A^{dir}(E)$. Additionally, $\Delta\mu$ values extracted from generalized detailed balance model using loss analysis according to **Section 5.1.1**

Sample Name	$\Delta\mu$ extracted method		
	Fit $A(E) = 1$	Fit $A(E) = A^{dir}(E)$	Loss analysis
A-NG	656.6	660.9	661.6
B-NG	655.8	661.9	662.0
C-BGG	671.0	678.0	677.0
D-NG	653.0	659.4	659.1
E-BGG	614.0	620.1	621.5

Appendix B5. Device performance for F-BGG, G-NG and H-NG samples

The statistical distribution of photovoltaic parameters for devices made from F-BGG, G-NG and H-NG absorbers are presented in the following tables. As a reminder, the J-V curve of the solar cell with highest efficiency on each individual sample is presented in **Fig 5. 8**.

Table B5.1 Statistical distribution of photovoltaic parameters for sample F-BGG

Sample No	*V_{OC}(mV)*	*J_{SC}(mA/cm^{-2})*	*FF*	*PCE (%)*
F-1	*637*	*35.0*	*76.7*	*17.1*
F-2	*642*	*34.3*	*78.9*	*16.9*
F-3	*642*	*34.8*	*75.1*	*16.8*
F-4	*642*	*32.9*	*76.8*	*16*
F-5	*643*	*35.3*	*77.2*	*17.5*
F-6	*648*	*35.5*	*76.7*	*17.6*
F-7	*643*	*33.5*	*75.9*	*16.4*
F-8	*646*	*31.1*	*76.3*	*15.3*

Table B5.2 Statistical distribution of photovoltaic parameters for sample G-NG.

Sample No	*V_{OC} (mV)*	*J_{SC} (mA/cm^{-2})*	*FF*	*PCE (%)*
G-1	*607*	*31.2*	*76.0*	*14.4*
G-2	*606*	*33.0*	*74.6*	*14.9*
G-3	*607*	*33.4*	*75.3*	*15.3*
G-4	*607*	*30.8*	*75.2*	*14.1*
G-5	*608*	*33.7*	*76.1*	*15.6*
G-6	*604*	*33.7*	*75.8*	*15.4*
G-7	*602*	*32.7*	*75.6*	*14.9*
G-8	*604*	*30.6*	*75.3*	*13.9*

Table B5.3 Statistical distribution of photovoltaic parameters for sample H-NG.

Sample No	*V_{OC} (mV)*	*J_{SC} (mA/cm^{-2})*	*FF*	*PCE (%)*
H-1	*474*	*40.8*	*71.1*	*13.7*
H-2	*473*	*39.9*	*71.7*	*13.5*
H-3	*460*	*38.6*	*70.8*	*12.5*
H-4	*468*	*39.8*	*68.3*	*12.7*
H-5	*472*	*36.2*	*71.1*	*12.1*

Appendix B6. EL spectra, Absorptance and broadening analysis

The EL spectra used for low energy $QE(E)$ reconstruction in **Fig 5. 9** is presented in the following **Fig B6.1**.

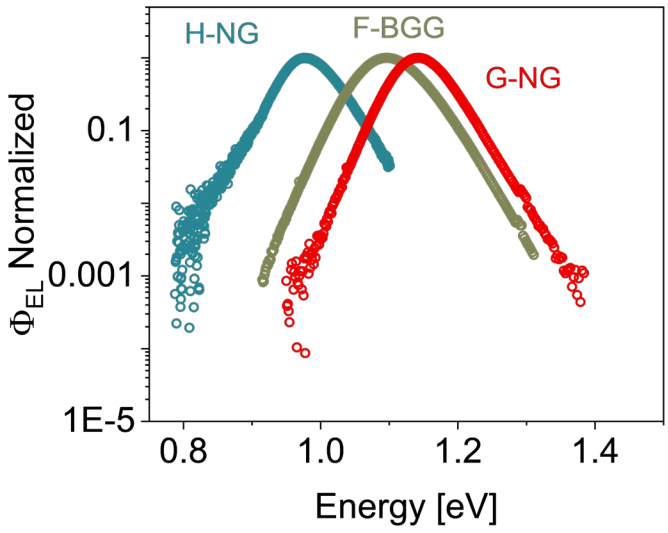

Fig B6.1. Normalized EL emission of samples F-BGG, G-NG and H-NG.

Additionally, as mentioned previously in **Section 5.2**, within the energy range where PL and EL measurements are performed, the PL and EL emission spectra exhibit a similar shape. Consequently, the $QE^{EL}(E)$ and $A^{PL}(E)$ spectra for these solar cells also have the same spectral shape.

As an example, **Fig B6.2** illustrates the normalized PL and EL spectra for the F-BGG sample, while **Fig B6.3** presents the rescaled $A^{PL}(E)$spectra to $QE^{EL}(E)$ for the same sample.

Since $A^{PL}(E)$ and $QE^{EL}(E)$ share the same spectral profile, the broadening of the $QE(E)$ spectra is expected to be same as the $A(E)$ broadening.

Furthermore, this characteristic allows for a reliable extraction of the Urbach energy using Beer-Lambert's law (see Eq 2.13 and Eq 2.39). Given that the $QE(E)$ follows the same decay profile as $A(E)$, thus, it can be written:

$$A(E) \propto QE(E) \propto 1 - exp(-\alpha d)$$

Furthermore, by analyzing the decay profile of the extracted α in the sub band gap region, the Urbach energy can be obtained from exponential decay of α in the energy ranges deep within the bandgap (see **Fig B6.3**)

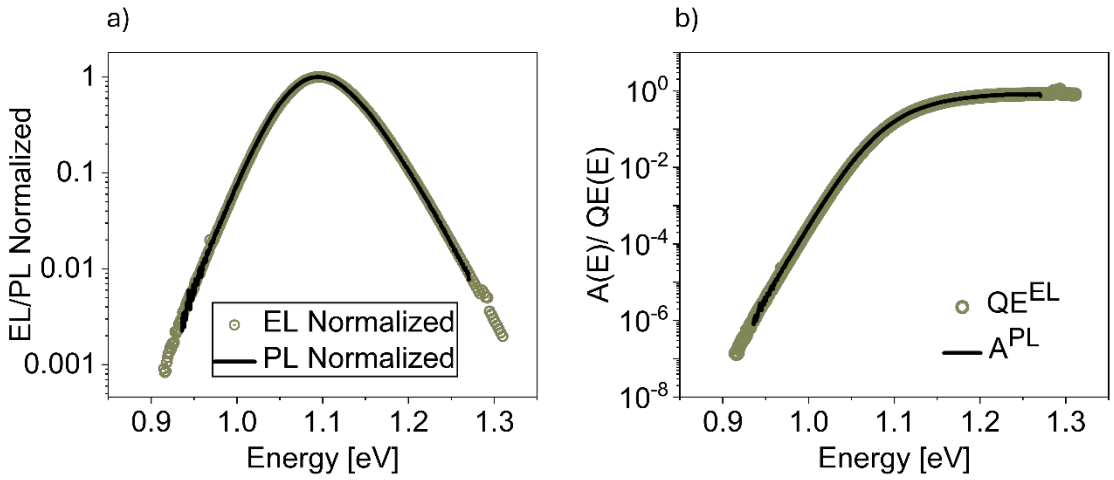

Fig B6.2 a) Normalized PL and EL spectra for F-BGG sample, and **b)** $A^{PL}(E)$ rescaled to $QE(E)$ for same F-BGG sample. The PL measurements here is performed from sample covered by CdS/Window using PL setup 2 (see **section 3.1.1**)

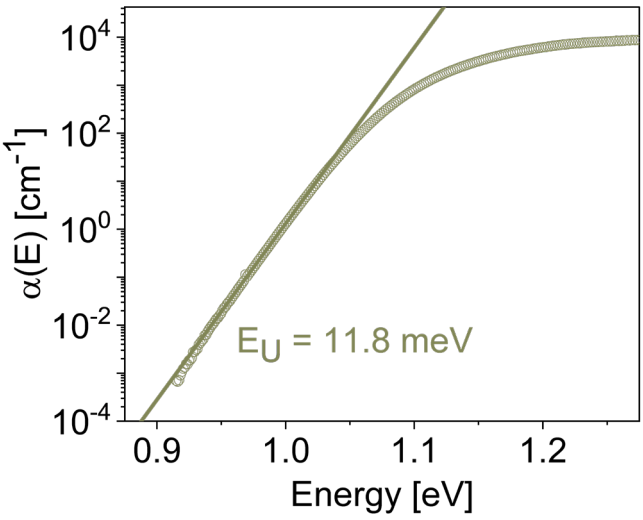

Fig B6.3. Illustrates the Urbach energy E_U extracted from $QE^{EL}(E)$ measurements

In **Fig B6.4** the first derivative of $QE^{EL}(E)$ and $QE^{dir}(E)$ for a solar cell from F-BGG sample is illustrated, where a Gaussian fit is performed to demonstrate that the broadening values are similar.

It is important to note that, in the discussions related to **Fig 5. 9 b**, the average value of σ_{QE} was presented. Where this average σ_{QE} was extracted using multiple Gaussian fits over various fitting ranges, with the standard deviation representing the errors bars. However, here, in **Fig B6.4**, only a single fit is shown for comparison purposes.

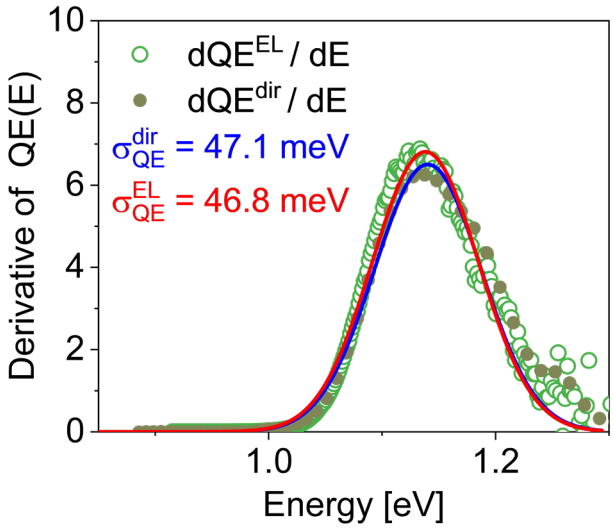

Fig B6.4. First derivative of $QE^{EL}(E)$ and $QE^{dir}(E)$ along with the Gaussian fits.

Appendix B7. EL under different injection

It was previously shown that it is essential to measure the Y_{PL} under one sun illumination intensity (see **Fig 5. 3**). Here, it will be shown that for Y_{EL} measurements, it is also crucial to use an injected current corresponding to J_{SC} (one-sun current).

Here, in this appendix, the EL measurement under different injected current density is discussed. First, In the **Fig B7.1**, the representative dark and illuminated J-V curves are illustrated. The dark J-V measurements are performed in the solar simulator setup and also separately in the EL setup (see **Section 2.4.2**). It can be seen that the dark J-V characteristics obtained from the EL setup closely matches those measured using the solar simulator. However, small discrepancies are always possible due to differences in the contact resistance between the two setups.

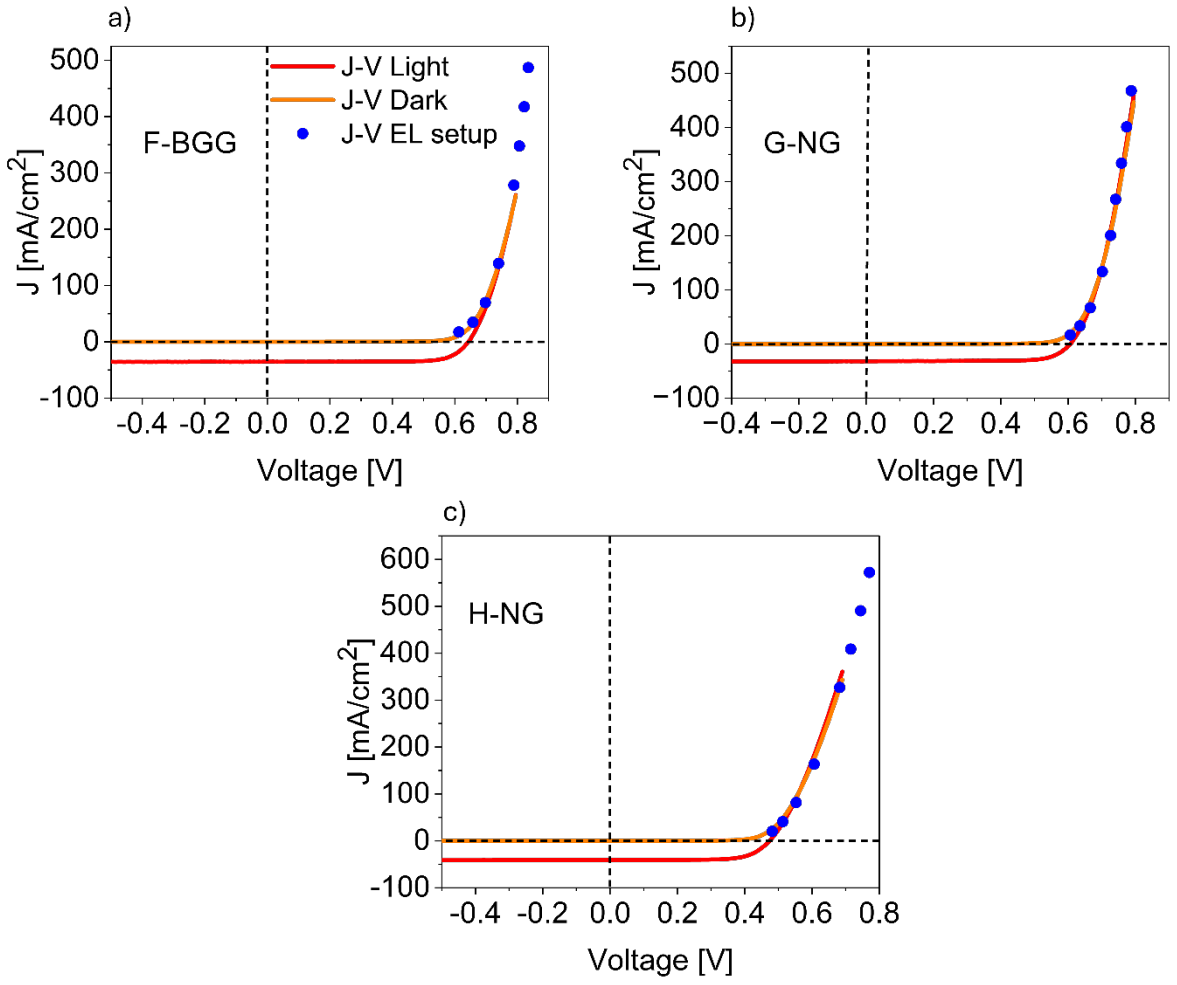

Fig B7.1 a), **b)**, and **c)** show representative J-V curves for samples F-BGG, G-NG, and H-NG, measured under dark and illuminated conditions using a solar simulator, as well as dark J-V measurements from the EL setup. EL measurements shown here were performed on cells F-5, G-3 and H-1 from **Table B5.1**, **Table B5.2** and **Table B5.3** respectively.

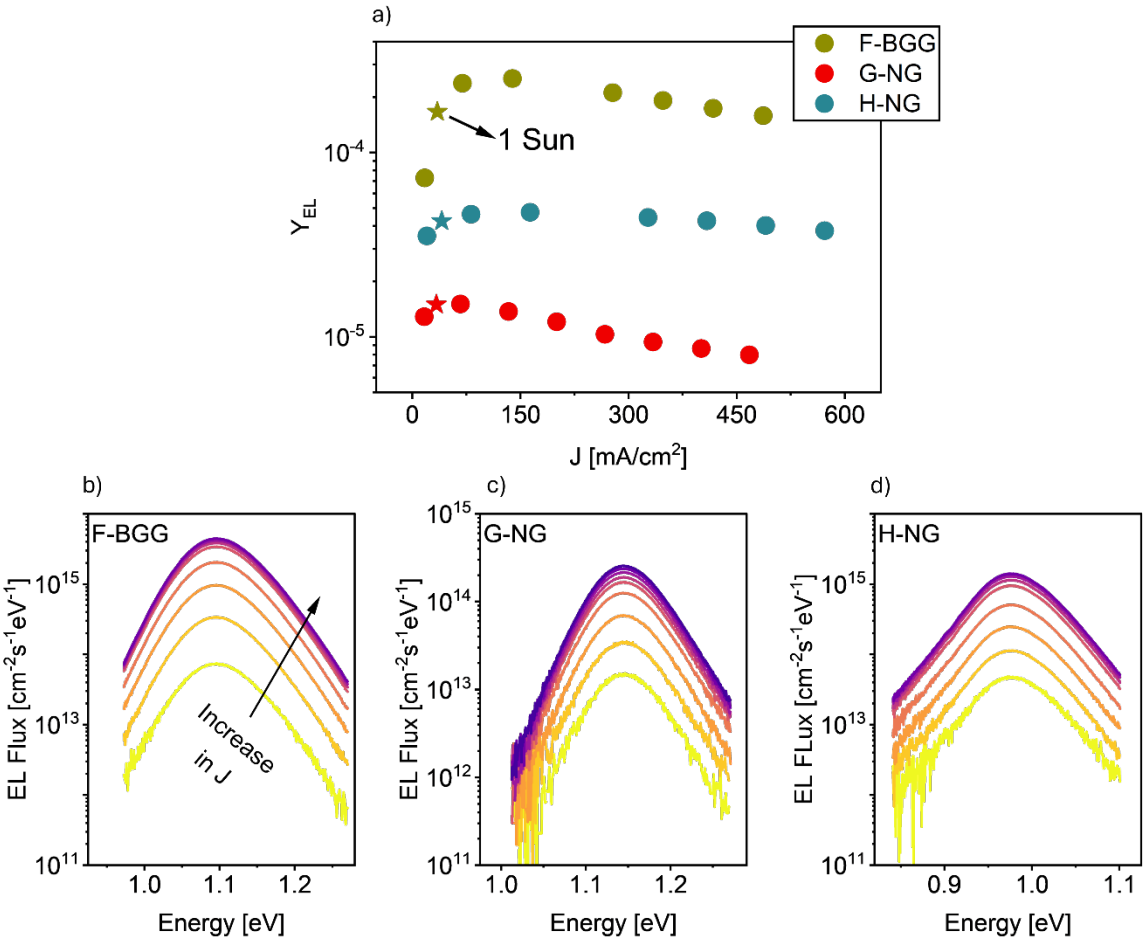

Fig B7.2 a) Y_{EL} as a function of increasing injection current density. One sun injection (J_{SC}) for each sample is shown by star symbol. **b)**, **c)**, and **d)** EL spectra under increasing injection current density for samples F-BGG, G-NG, and H-NG, respectively. The arrow indicates the direction of increase in the injection current density. EL spectra from just single point is illustrated here and statistical errors due to inhomogeneities are not included.

At each injected current density (J), the Y_{EL} is calculated using the Eq 4.17. In these measurements, the one-sun equivalent injection corresponds to the short-circuit current density (J_{SC}) injection. In the **Fig B7.2 a**, the Y_{EL} is displayed as a function of increasing injection

current density,. Meanwhile, in **Fig B7.2 b-d** the corresponding EL spectra for each sample under increased injection current density are presented. In contrast to the PL measurements for CIGSe absorbers, where a continuous increase in Y_{PL} is observed with rising excitation intensity (**Fig 5. 3**), here, in **Fig B7.2**, it can be observed that Y_{EL} initially increases, reaches a maximum point, and then decreases as the injection current density (J) continues to rise.

The origin of this behavior requires further investigation. However, it can be speculated that this observation is probably due to increase in the internal series resistance with increase in injection current as reported by Rau et al. [200].

In **Fig 5. 10** in the main text the V_{bi}, V_{in} and V_{OC} of investigated solar cells were presented. Here, in the following **Table B7.1** the numerical values of V_{bi}, V_{in} and V_{OC} for investigated solar cells are presented.

Table B7.1 Comparison of V_{bi}, V_{in} and V_{OC}. The measurements were performed on different cells. The table presents average values Errors in V_{in} are due to Y_{EL} inhomogeneities and EL calibration errors.

Sample Name	V_{bi} *(meV)*	V_{in} *(meV)*	V_{OC} *(meV)*
F-BGG	*664.1 ± 6.1*	*654.5 ± 11.0*	*642.8 ± 3.0*
G-NG	*637.1 ± 6.3*	*618.1 ± 7.0*	*605.6 ± 2.0*
H-NG	*507.6 ± 5.0*	*489.8 ± 9.0*	*469.4 ± 5.1*

Appendix B8. PL measurements on CIGSe/Cds and CIGSe/CdS/Window configuration

To enable a more accurate comparison between PL and EL analyses, additional PL analysis were carried out on CIGSe/CdS and CIGSe/CdS/Window stacks for F-BGG, G-NG, and H-NG samples. The samples with a window layer (but without Ni:Al grids) were measured using PL setup-2 with a beam expander. For more details regarding the PL setup and PL measurements see **Section 3.3.1**.

The non-radiative losses extracted from both EL and PL measurements (δV_{OC}^{nr} and $\delta\Delta\mu^{nr}$) are presented in **Fig B8.1**.

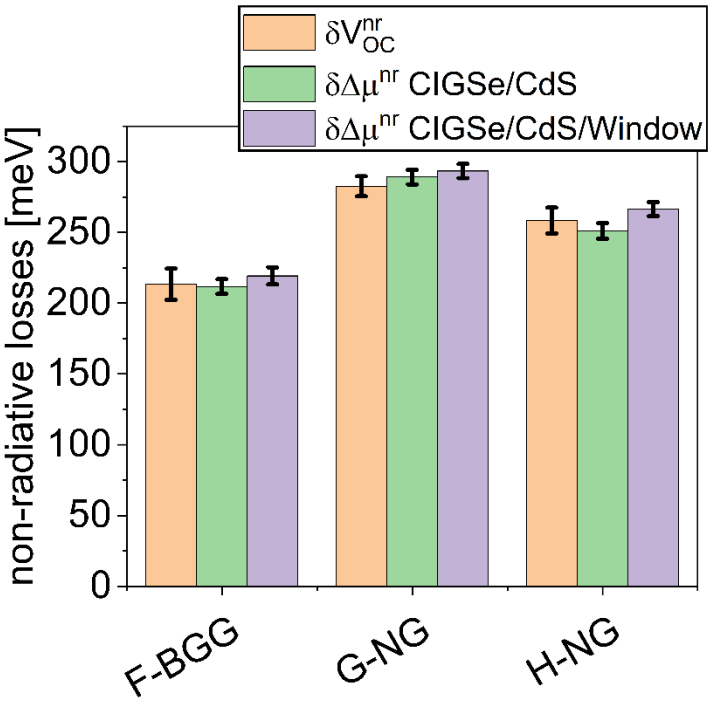

Fig B8.1. Non-radiative losses (δV_{OC}^{nr} and $\delta\Delta\mu^{nr}$) extracted from EL and PL measurements. Errors in δV_{OC}^{nr} are due to inhomogeneities and also calibration errors.

For PL measurements, Eq 4.11 and Eq 4.10 were used to calculate the Y_{PL} and ($\delta\Delta\mu^{nr}$), respectively. In Eq 4.11 it is clear that for accurate YPL determination, the numerical value of $A(E)$ is needed. Since, I did the measurements with red laser, here the $A(E) = A(E_{laser})$.

However, since the samples were prepared on Mo, transmittance measurements could not be performed to directly extract $A(E_{laser})$. Instead, it was estimated using $A(E_{laser}) \approx 1 - R(E_{laser})$ approximation.

The $1 - R(E)$ spectra for CdS covered samples are illustrated in **Fig B8.2**, while for Cd/window configuration, the $1 - R(E)$ profile along with the full range $QE(E)$ of the devices are presented in **Fig B8.3**.

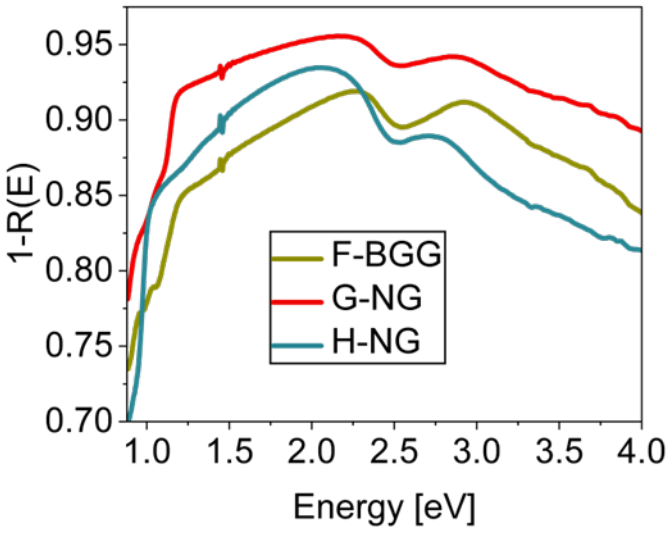

Fig B8.2. $1 - R(E)$ measured for CdS covered absorbers

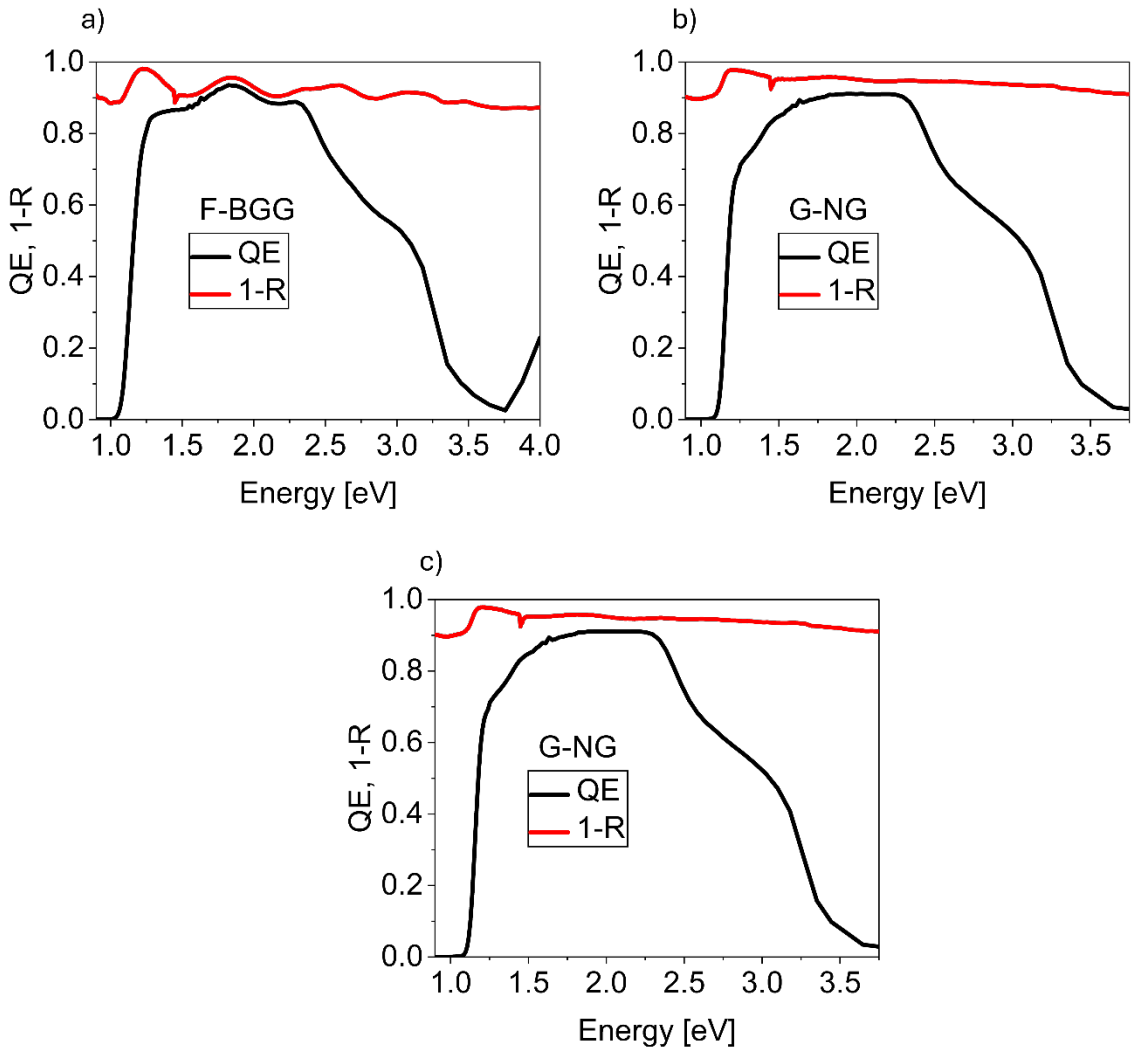

Fig B8.3. $QE(E)$ and $1-R(E)$ profile for **a)** F-BGG, **b)** G-NG and **c)** H-NG samples. $1-R(E)$ was measured from CIGSe/CdS/Window configuration.

Appendix B9. SEM and CL measurements

For sample F-BGG, the panchromatic PL image and a depth line scan were shown in **Fig 5. 11**.

In this appendix, the panchromatic CL image, depth line scan, and the evolution of CL spectra through the absorber depth are presented for G-NG and H-NG samples in **Fig B9.1** and **Fig B9.2** respectively.

Unlike, the F-BGG sample, both non graded G-NG and H-NG samples show constant CL emission peak through their entire depth.

Additionally, **Fig B9.3** and **Fig B9.4** illustrates the surface and cross-sectional SEM images, along with the corresponding panchromatic CL map from the same regions of F-BGG, G-NG and H-NG samples.

All the following measurements are provided by **Yucheng Hu** from Cambridge University.

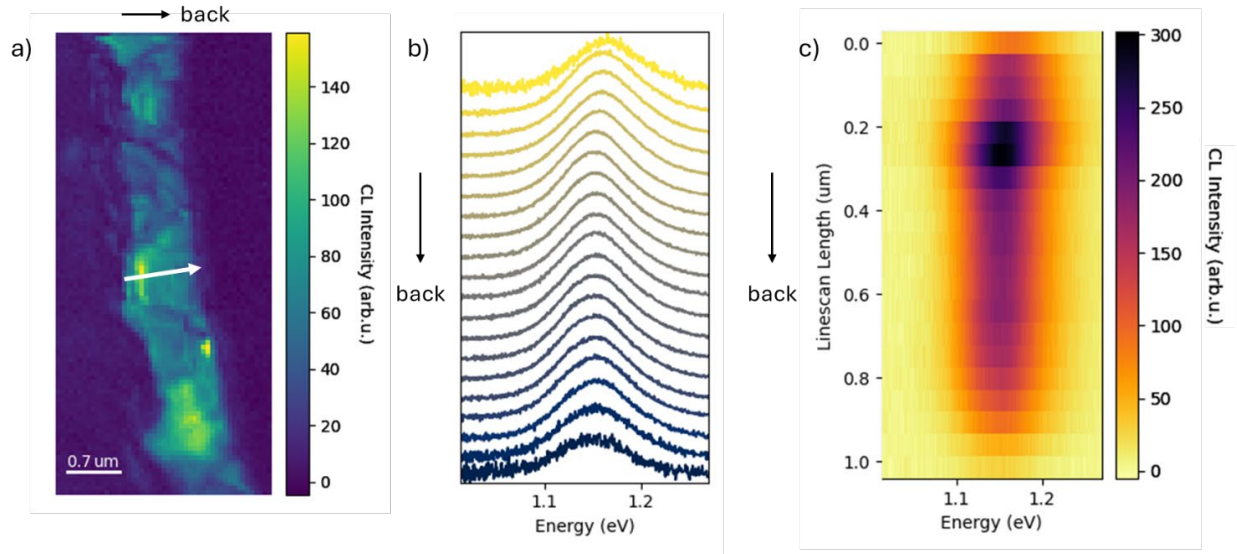

Fig B9.1. a) Illustrates panchromatic cross section CL intensity image for G-NG absorber, line scan direction and area is shown by white arrow. b) CL emission spectra through the line scan. c) Heat map indicating the CL emission peak evolution through the direction of line scan arrow.

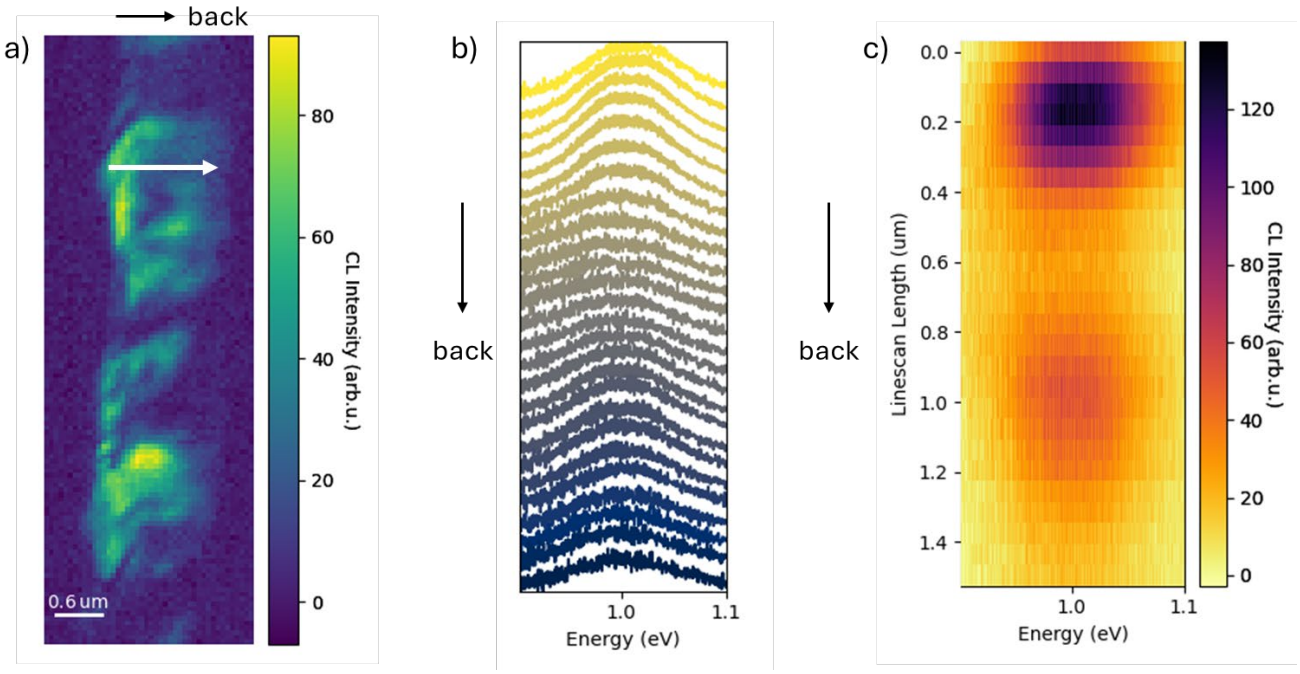

Fig B9.2. Same as previous figure, **a)** shows panchromatic cross section CL intensity image of the H-NG absorber, with the line scan direction and area indicated by a white arrow. **b)** CL emission spectra along the line scan. **c)** Heat map illustrating the CL emission peak position and its intensity along the line scan arrow direction.

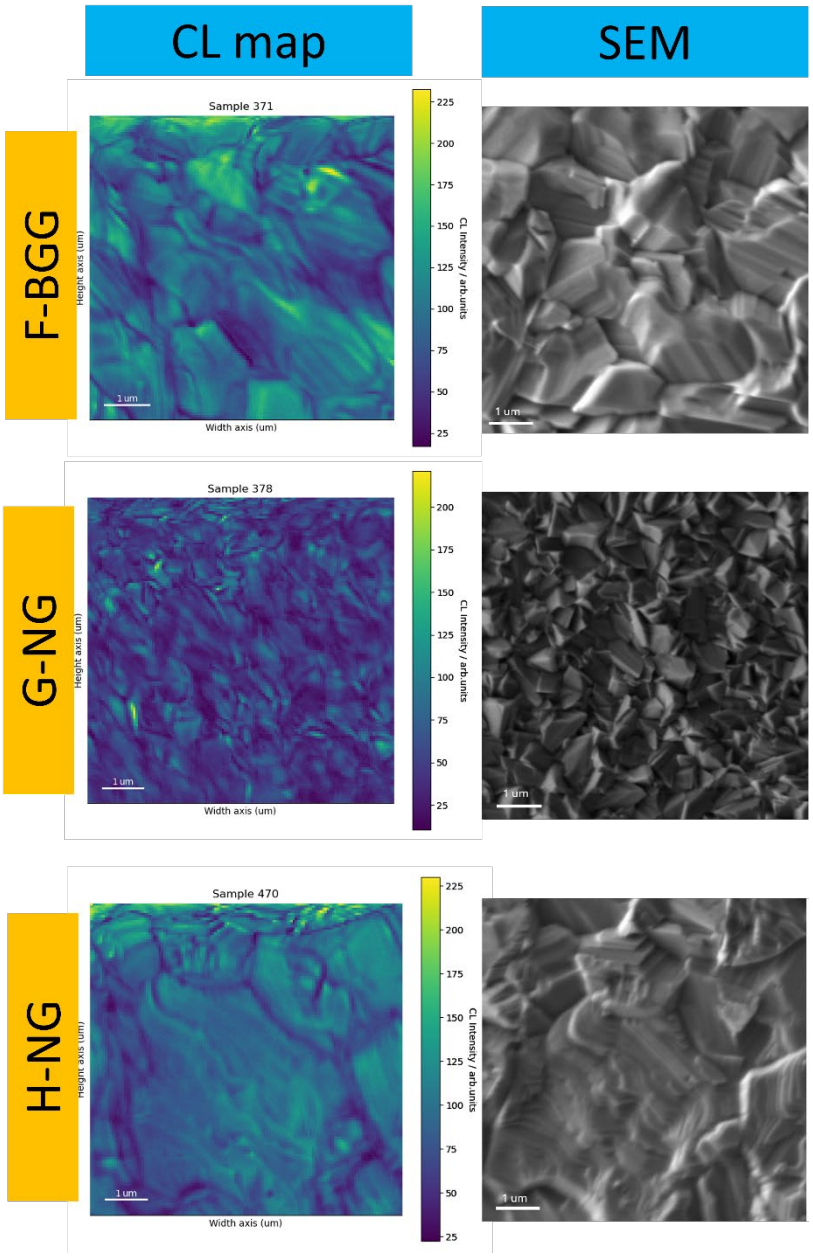

Fig B9.3. Illustrates the surface SEM images and the corresponding panchromatic CL intensity maps for F-BGG, G-NG and H-NG samples deposited on Mo.

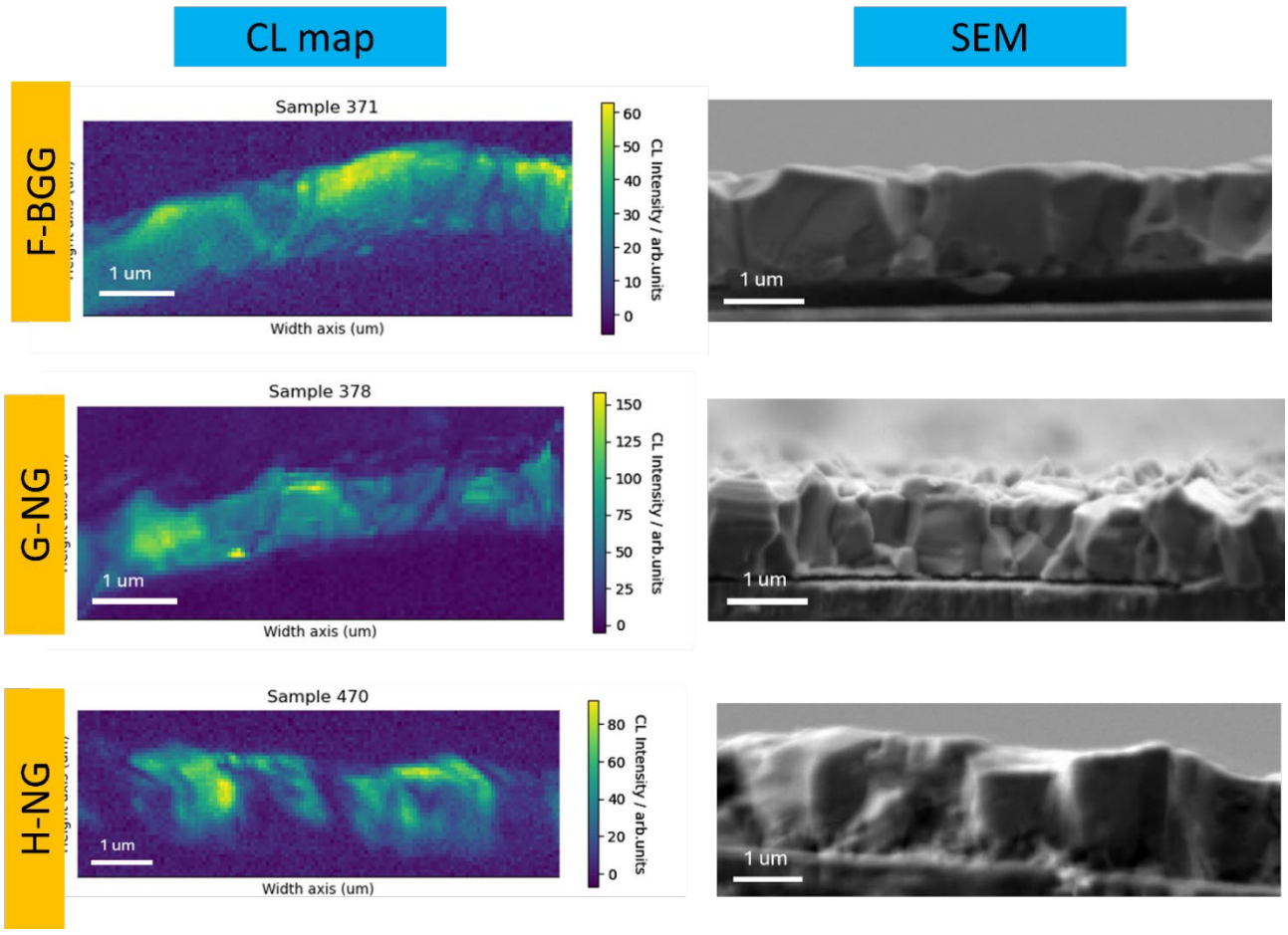

Fig B9.4. The cross-sectional SEM image and the corresponding panchromatic CL intensity map from same area for samples deposited on Mo are illustrated. Variations between the patterns observed in the panchromatic CL and SEM images are noticeable (bending). According to our colleagues from Cambridge university, this bendings are due to charge induced drift effects occurring during the long duration of measurements.

Appendix of Chapter 6

Appendix C1. Ammonia cleaning effect

Fig C1.1 illustrates the (SEM) images of the A3 sample before and after ammonia etching. Prior to the etching process, surface traces, can be observed on the sample. These traces are possibly RbF residues.

However, after cleaning with ammonia, the surface appeared significantly cleaner, indicating the effectiveness of the ammonia etching in removing residual surface contaminants.

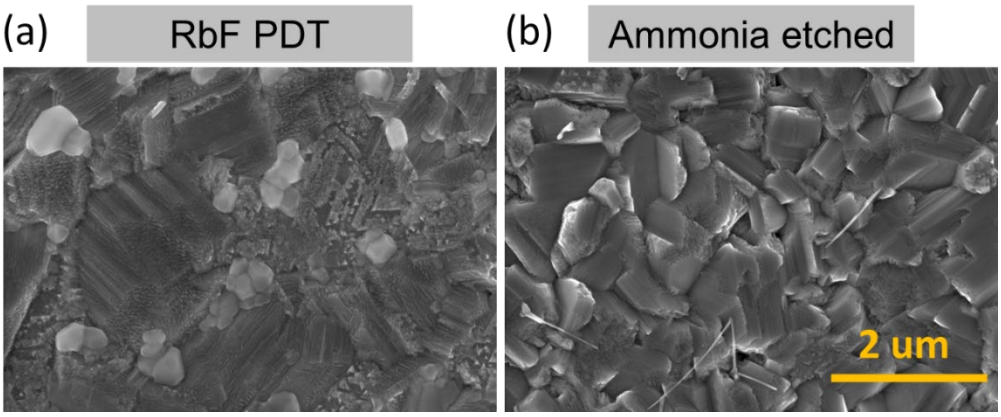

Fig C1.1 FESEM image illustrating that ammonia etching removes surface residual from RbF PDT. This figure is taken from Ghrabeiki et al [132].

Appendix C2. Reflectance measurements:

Fig C2.1 presents the reflectance measurements for absorbers with and without PS microbeads. Interference fringes are visible in both cases; however, their amplitude is reduced when the PS beads are used. Additionally, an overall increase in reflectance is observed for the PS-coated samples, which can be attributed to the enhanced diffuse reflection caused by the white PS layer.

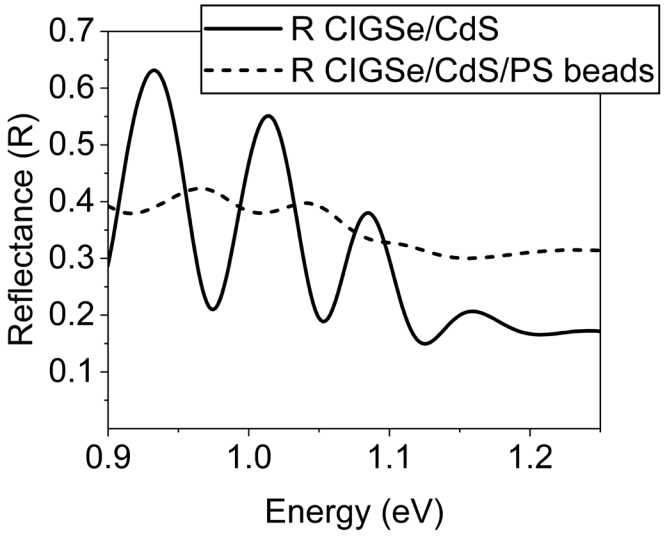

Fig C2.1. Reflectance measurements for CdS covered absorbers with and without PS spheres.

Appendix C3 .Device performance of A1,A2,A3 and B1 samples

All the devices parameters investigated in chapter 6 are summarized in the following tables.

All the following tables are taken from my published work under **CC BY 4** license [132].

Table C3.1 Photovoltaic parameters for A1 solar cells.

Cell No	*V_{OC} (mV)*	*J_{SC} (mA/cm^2)*	*FF*	*PCE (%)*
A1-1	*515*	*34.1*	*58*	*10.1*
A1-2	*526*	*34.0*	*66.4*	*11.8*
A1-3	*522*	*33.4*	*65.2*	*11.3*
A1-4	*524*	*32.7*	*65.8*	*11.2*
A1-5	*519*	*33.5*	*64.7*	*11.2*
A1-6	*524*	*31.8*	*66.9*	*11.1*

Table C3.2 Photovoltaic parameters for A2 solar cells.

Cell No	*V_{OC} (mV)*	*J_{SC} (mA/cm^2)*	*FF*	*PCE (%)*
A2-1	*622*	*34.1*	*69.7*	*14.7*
A2-2	*627*	*36.0*	*74*	*16.7*
A2-3	*625*	*34.1*	*75*	*16*
A2-4	*624*	*36.4*	*72.2*	*16.4*
A2-5	*617*	*36.2*	*72.8*	*16.2*
A2-6	*617*	*36.3*	*72*	*16.1*

Table C3.3 Photovoltaic parameters for A3 solar cells.

Cell No	*V_{OC} (mV)*	*J_{SC} (mA/cm^2)*	*FF*	*PCE (%)*
A3-1	*673*	*36.1*	*77.4*	*18.8*
A3-2	*674*	*35.5*	*74.9*	*17.9*
A3-3	*675*	*35.4*	*76.1*	*18.1*
A3-4	*674*	*35.4*	*75.6*	*18*
A3-5	*674*	*35.1*	*75.2*	*17.7*
A3-6	*674*	*36.5*	*74.2*	*18.2*

Table C3.4 Photovoltaic parameters for B1 solar cell. For JV curve see **Fig C2.1**

Cell No	V_{OC} *(mV)*	J_{SC} *(mA/cm²)*	*FF*	*PCE (%)*
B1-1	*587*	*34.6*	*71.7*	*14.5*

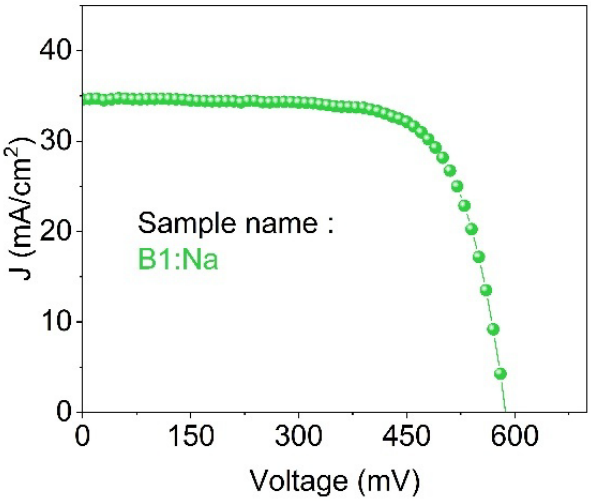

Fig C3.1. J-V measurement of the solar cell made from B1 sample. The parameters has already been illustrated in **Table C3.4.** Reproduced from Ghrabeiki et al [132].

Appendix C4. Na incorporation and defect passivation

Fig C4.1 illustrates the low temperature PL spectrum of samples with no Na and containing Na. These samples had similar deposition process to the ones that I have already discussed in the main text. But they are not from A and B series.

In any case, it can be observed absorbers without Na show a deep level defect, and Na leads to passivation of the deep level defect.

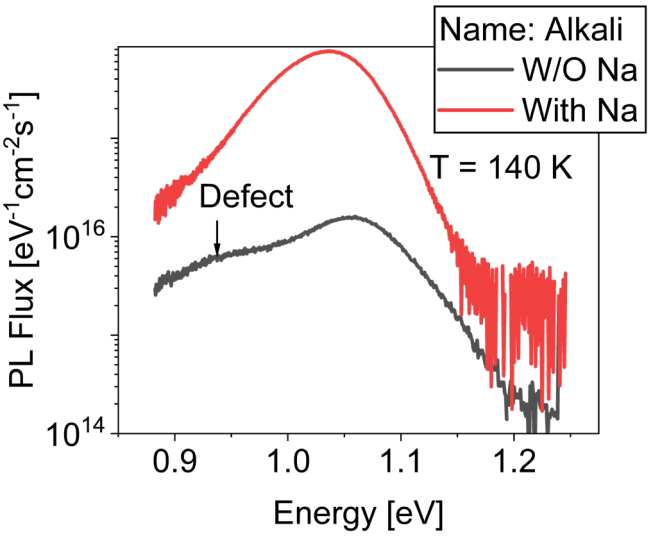

Fig C4.1 PL measurements at 140 K were conducted on samples both with and without sodium (Na) incorporation. These analysis were conducted on absorbers covered with PS microspheres (See **Fig 6. 5**)

Appendix C5. Laser intensity and Temperature

As discussed in **Section 5.1.2**, the temperature of the absorbers can be estimated by monitoring the high-energy slope of the modified photoluminescence (PL) spectrum, as described by Eq 5.3.

In this section, the high-energy slope of the PL spectra of sample A3 is investigated under varying laser intensities. All the following PL measurements were done on absorbers covered with PS-spheres. Similar investigations have also been done for four other samples.

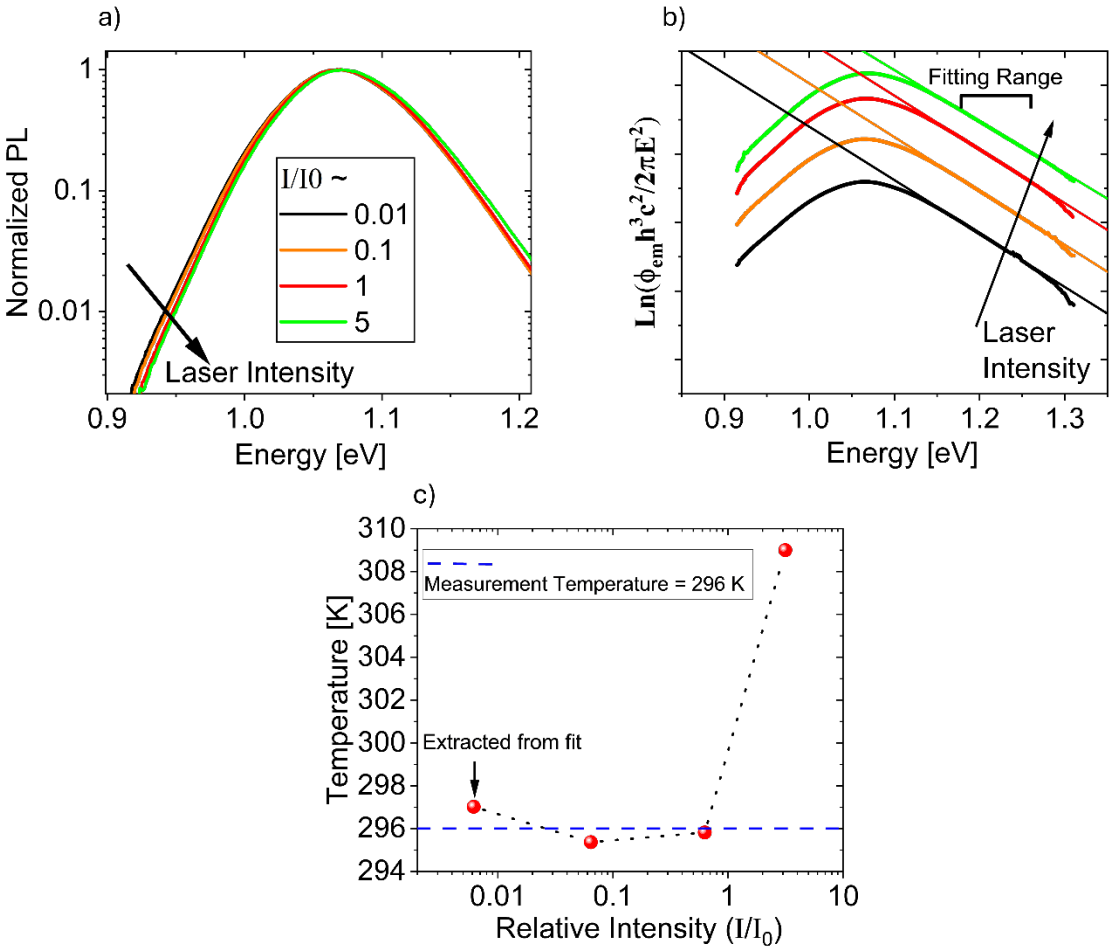

Fig C5.1 a) Normalized PL spectra of the A3 sample measured under increased laser intensities, (I/I_0) ranging from 0.01 to 5. **b)** PL spectra transformed according to the modified Planck's generalized law (Eq 5.3), with linear fits applied to the high-energy slopes for temperature extraction. **c)** Extracted temperatures as a function of relative laser intensity, obtained from the linear fits shown in part **(b)**.

All these measurements are performed on samples covered with polystyrene (PS) layer (see **Fig 6. 5**). Adapted from Ghrabeiki et al [132].

In **Fig C5.1 a**, the normalized PL spectra of sample A3 are presented under increased laser intensities. Here, the relative laser intensity (I/I0) is increased from 0.01 to 5. It is important to mention that in the main text, only spectra corresponding to I/I_0 between 0.01 and 1 were discussed in **Fig 6. 13**.

From the normalized spectra, a shift of the PL peak toward higher energies is observed as the laser intensity increases. Additionally, at $I/I_0 = 5$, a noticeable flattening of the high-energy slope can be seen.

In **Fig C5.1 b**, the PL spectra are plotted based on the modified Planck's generalized law (Eq 5.3). To assess the temperature, a linear fit is applied to the high-energy region of each spectrum. Subsequently, from the slope of this linear fit the temperature is extracted (See **Section 5.1.2** for more details).

In **Fig C5.1 c**, the extracted temperature values obtained from the linear fits are presented for each laser intensity. It is observed that when the relative intensity (I/I_0) is in the range of 0.01 to 1, the temperature remains close to room temperature (approximately 296 K). However, as the intensity increases to $I/I_0 = 5$, the temperature rises by approximately 14 K. A similar trend has been observed for other samples as well.

Therefore, based on this analysis, it can be concluded that in the intensity range used for evaluating the Urbach energies in the main text (**Fig 6. 13**), the absorber temperature remains effectively constant.

Appendix C6. Simulation parameters

In **Section 6.3.3** simulations have been performed to show the impact of increase in the p type doing level on the magnitude of electrostatic potential fluctuations. Two separate cases were presented:

Table C6.1 represents the simulation parameters for the first case, where the donor concentration(N_D) is fixed and acceptor concentration (N_A) increases (See **Fig 6. 14**).

In this case N_D has constat concentration of 1×18 cm^{-3}, while N_A increases from 1.0001×18 cm^{-3} with the steps of 1×14 cm^{-3}.

Table C6.1 Illustrates simulation parameters for γ_{el}, for the case when N_D is constant and N_A increases. Reproduced from Gharabeiki et al[132]

Parameters			comments
Acceptor density	N_A	----------	Starting with 1.0001×18 cm-3, increase with the steps of 1×14 cm^{-3}
Donor density	N_D	1×18 cm^{-3}	Constant value
Doping concentration	p_0	N_A-N_D	
Charged defect concentration	N_I	N_A+N_D	
Degree of compensation	K	$K = \frac{N_D}{N_A}$	

In the second case, for **Fig 6. 15**, the N_A is assumed to stay constant at 1.0001×18 cm^{-3}, while the N_D is decreasing from 1 ×18 cm^{-3} with steps of 1×14 cm^{-3}. In **Table C6.2** the simulation parameters for this case are summarized .

Table C6.2 Illustrates simulation parameters for γ_{el}, for the case when N_A is constant and N_D decreases. Reproduced from Gharabeiki et al[132]

Parameters			comments
Acceptor density	N_A	1.0001×18 cm-3	constant
Donor density	N_D	----------	Starting with 1 ×18 cm-3, decrease with the steps of 1×14 cm^{-3}
Doping concentration	p_0	N_A-N_D	
Charged defect concentration	N_I	N_A+N_D	
Degree of compensation	K	$K = \frac{N_D}{N_A}$	

Appendix C7. Homogeneity in doping with alkali incorporation

Previous studies have illustrated that the incorporation of alkali ions can result in a more homogeneous doping concentration profile for CIGSe absorber [45]. This observation can be explained with the model of electrostatic potential fluctuations. In the following discussions it will be shown that the reduction in the mean depth of electrostatic potential fluctuations (γ_{el}) results more uniform doping profile.

Fig C7.1 presents the electrostatic potential fluctuations within the absorber, here both the valence band edge (E_V) and conduction band edge (E_C) fluctuate spatially. Here, two adjacent points (point 1 and 2) are illustrated within the absorber, this neighboring points can be either between two separate grains or inside a single grain. This adjacent points exhibit a potential difference of Γ in their band gap. This Γ, is directly linked to the average depth of electrostatic fluctuations γ_{el}. A reduction in Γ is therefore expected to result in a lower γ_{el}, and vice versa.

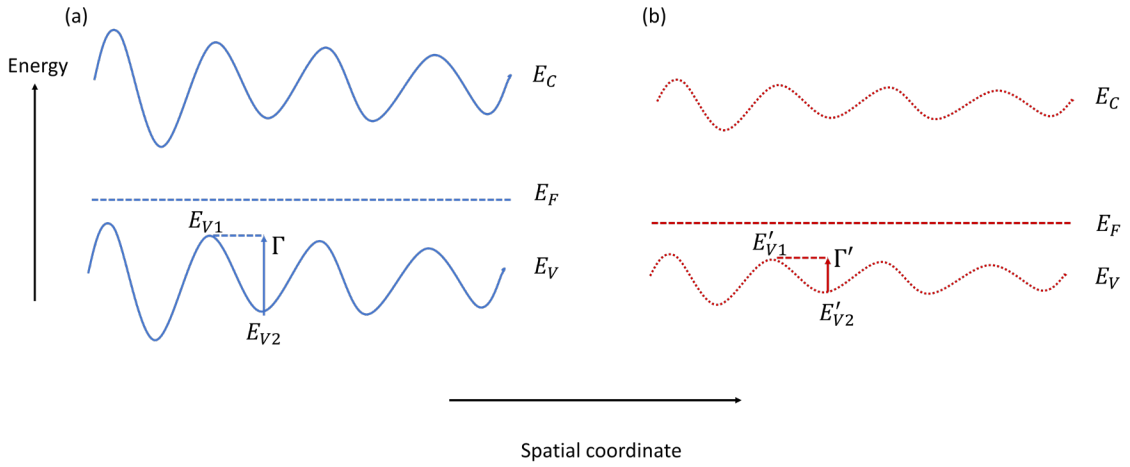

Fig C7.1 Illustration of electrostatic potential fluctuations in an absorber material **a)** before increase in the doping. **b)** after increase in the doping. This figure is reproduced from Ghrabeiki et al [132].

In **Fig C7.1** a, the E_{V1} and E_{V2} are valence band edge for point 1 and 2 respectively before increase in doping, and **Fig C7.1 b** presents the $E'_{V1}$and E'_{V2} the valence band edge of point 1 and point 2 after increase in doping.

Fig C7.1 b presents the case where overall doping concentration increases, in this case Fermi level shifts down toward valence band. As discussed in the main text, enhancements in the

carrier concentration leads to reduction in average amplitude of electrostatic fluctuations γ_{el}, which would subsequently lower Γ values between two points (see **Section 6.3.3**).

Under this simplified scenario, using Eq 2.2, the hole concentration (i.e., p-type doping level) at each point can be expressed as:

$$p_1 = N_V \exp\left(\frac{E_{V1} - E_F}{k_B T}\right) and\ p_2 = N_V \exp\left(\frac{E_{V2} - E_F}{k_B T}\right) \qquad (\boldsymbol{Eq\ C7.1})$$

Here, p_1 and p_2 represent the hole concentrations at points 1 and 2, respectively. E_{V1} and E_{V2} are the valence band energies at those points. The potential difference between the two (Γ)can be expressed as:

$$\Gamma = E_{V1} - E_{V2} \qquad (\boldsymbol{Eq\ C7.2})$$

Taking the ratio of the hole concentrations yields:

$$\frac{p_1}{p_2} = \exp\left(\frac{E_{V1} - E_{V2}}{k_B T}\right) = \exp\left(\frac{\Gamma}{k_B T}\right) \qquad (\boldsymbol{Eq\ C7.3})$$

This equation clearly shows that a smaller potential difference Γ, leads to a smaller $\frac{p_1}{p_2}$ ratio, which translates to more homogeneous doping profile throughout the absorber material.

Bibliography

[1] E. Çam, M. Casanovas, and J. Moloney, "Electricity 2025: Analysis and Forecast to 2027," 2025. [Online]. Available: https://policycommons.net/artifacts/18291196/electricity2025/19191668/.

[2] F. I. a. W. W. Dr. Simon Philipps, PSE Projects GmbH. "Photovoltaics Report." https://www.ise.fraunhofer.de/en/publications/studies/photovoltaics-report.html (accessed 2025).

[3] R. Scheer and H.-W. Schock, *Chalcogenide photovoltaics: physics, technologies, and thin film devices*. John Wiley & Sons, 2011.

[4] A. Adhikari *et al.*, "Review on the developments in copper indium gallium diselenide (CIGSe)-based thin film photovoltaic devices," *Journal of Materials Science: Materials in Electronics,* vol. 35, no. 15, p. 1016, 2024.

[5] S. Siebentritt and T. Weiss, "Chalcopyrite solar cells—state-of-the-art and options for improvement," *Science China Physics, Mechanics & Astronomy,* vol. 66, no. 1, p. 217301, 2023.

[6] J. Zhang *et al.*, "Highly efficient narrow bandgap Cu (In, Ga) Se2 solar cells with enhanced open circuit voltage for tandem application," *Nature Communications,* vol. 15, no. 1, p. 10365, 2024.

[7] M. Jošt *et al.*, "21.6%-efficient monolithic perovskite/Cu (In, Ga) Se2 tandem solar cells with thin conformal hole transport layers for integration on rough bottom cell surfaces," *ACS Energy Letters,* vol. 4, no. 2, pp. 583-590, 2019.

[8] S. Ishizuka, "CuGaSe2 thin film solar cells: challenges for developing highly efficient wide-gap chalcopyrite photovoltaics," *physica status solidi (a),* vol. 216, no. 15, p. 1800873, 2019.

[9] M. Powalla *et al.*, "Advances in cost-efficient thin-film photovoltaics based on Cu (In, Ga) Se2," *Engineering,* vol. 3, no. 4, pp. 445-451, 2017.

[10] NREL. "Best Research-Cell Efficiency Chart." https://www.nrel.gov/pv/cell-efficiency (accessed 2025).

[11] J. Keller *et al.*, "High-concentration silver alloying and steep back-contact gallium grading enabling copper indium gallium selenide solar cell with 23.6% efficiency," *Nature Energy,* no. 9, pp. 467–478 2024, doi: 10.1038/s41560-024-01472-3.

[12] A. M. Gabor *et al.*, "Band-gap engineering in Cu (In, Ga) Se2 thin films grown from (In, Ga) 2Se3 precursors," *Solar energy materials and solar cells,* vol. 41, pp. 247-260, 1996.

[13] T. Feurer *et al.*, "Progress in thin film CIGS photovoltaics–Research and development, manufacturing, and applications," *Progress in Photovoltaics: Research and Applications,* vol. 25, no. 7, pp. 645-667, 2017.

[14] V. Nadenau *et al.*, "Solar cells based on CuInSe2 and related compounds: material and device properties and processing," *Progress in photovoltaics: research and applications,* vol. 3, no. 6, pp. 363-382, 1995.

[15] D. J. Schroeder and A. A. Rockett, "Electronic effects of sodium in epitaxial CuIn 1− x Ga x Se 2," *Journal of Applied Physics,* vol. 82, no. 10, pp. 4982-4985, 1997.

[16] V. Probst *et al.*, "The impact of controlled sodium incorporation on rapid thermal processed Cu (InGa) Se/sub 2/-thin films and devices," in *Proceedings of 1994 IEEE*

1st World Conference on Photovoltaic Energy Conversion-WCPEC (A Joint Conference of PVSC, PVSEC and PSEC), 1994, vol. 1: IEEE, pp. 144-147.

[17] A. Chirila *et al.*, "Potassium-induced surface modification of Cu(In,Ga)Se2 thin films for high-efficiency solar cells," *Nat Mater,* vol. 12, no. 12, pp. 1107-11, Dec 2013, doi: 10.1038/nmat3789.

[18] R. Carron *et al.*, "Advanced alkali treatments for high-efficiency Cu (In, Ga) Se2 solar cells on flexible substrates," *Advanced Energy Materials,* vol. 9, no. 24, p. 1900408, 2019.

[19] P. Jackson, R. Wuerz, D. Hariskos, E. Lotter, W. Witte, and M. Powalla, "Effects of heavy alkali elements in Cu(In,Ga)Se2 solar cells with efficiencies up to 22.6%," *physica status solidi (RRL) – Rapid Research Letters,* vol. 10, no. 8, pp. 583-586, 2016, doi: 10.1002/pssr.201600199.

[20] M. Nakamura, K. Yamaguchi, Y. Kimoto, Y. Yasaki, T. Kato, and H. Sugimoto, "Cd-free Cu (In, Ga)(Se, S) 2 thin-film solar cell with record efficiency of 23.35%," *IEEE Journal of Photovoltaics,* vol. 9, no. 6, pp. 1863-1867, 2019.

[21] A. Czudek, A. Urbaniak, A. Eslam, R. Wuerz, and M. Igalson, "Potassium versus Sodium in Cu (In, Ga) Se2—Similarities and Differences in the Electrical Characteristics of Solar Cells and Thin Films after NaF or KF Postdeposition Treatment," *physica status solidi (RRL)–Rapid Research Letters,* vol. 16, no. 1, p. 2100459, 2022.

[22] T. Kodalle *et al.*, "Elucidating the mechanism of an RbF post deposition treatment in CIGS thin film solar cells," *Solar RRL,* vol. 2, no. 9, p. 1800156, 2018.

[23] S.-H. Wei, S. Zhang, and A. Zunger, "Effects of Na on the electrical and structural properties of CuInSe 2," *Journal of applied physics,* vol. 85, no. 10, pp. 7214-7218, 1999.

[24] T. Feurer *et al.*, "RbF post deposition treatment for narrow bandgap Cu (In, Ga) Se2 solar cells," *Thin Solid Films,* vol. 670, pp. 34-40, 2019.

[25] M. Ochoa, S. C. Yang, S. Nishiwaki, A. N. Tiwari, and R. Carron, "Charge carrier lifetime fluctuations and performance evaluation of Cu (In, Ga) Se2 absorbers via time-resolved-photoluminescence microscopy," *Advanced Energy Materials,* vol. 12, no. 3, p. 2102800, 2022.

[26] W. Shockley and H. J. Queisser, "Detailed Balance Limit of Efficiency of p-n Junction Solar Cells," *Journal of Applied Physics,* vol. 32, no. 3, pp. 510-519, 1961, doi: 10.1063/1.1736034.

[27] S. Rühle, "Tabulated values of the Shockley–Queisser limit for single junction solar cells," *Solar energy,* vol. 130, pp. 139-147, 2016.

[28] U. Rau, B. Blank, T. C. M. Müller, and T. Kirchartz, "Efficiency Potential of Photovoltaic Materials and Devices Unveiled by Detailed-Balance Analysis," *Physical Review Applied,* vol. 7, no. 4, p. 044016, 2017, doi: 10.1103/PhysRevApplied.7.044016.

[29] S. Siebentritt, T. P. Weiss, M. Sood, M. H. Wolter, A. Lomuscio, and O. Ramirez, "How photoluminescence can predict the efficiency of solar cells," *Journal of Physics: Materials,* vol. 4, no. 4, p. 042010, 2021.

[30] T. Kirchartz and U. Rau, "Electroluminescence analysis of high efficiency Cu (In, Ga) Se2 solar cells," *Journal of applied physics,* vol. 102, no. 10, p. 104510, 2007.

[31] L. Krückemeier, U. Rau, M. Stolterfoht, and T. Kirchartz, "How to report record open-circuit voltages in lead-halide perovskite solar cells," *Advanced energy materials,* vol. 10, no. 1, p. 1902573, 2020.
[32] T. Kirchartz, *Generalized detailed balance theory of solar cells*. Forschungszentrum Jülich, 2009.
[33] M. H. Wolter *et al.*, "How band tail recombination influences the open-circuit voltage of solar cells," *Progress in Photovoltaics: Research and Applications,* pp. 702–712, 2021, doi: 10.1002/pip.3449.
[34] O. Ramírez *et al.*, "On the Origin of Tail States and Open Circuit Voltage Losses in Cu (In, Ga) Se2," *Solar RRL,* vol. 7, no. 13, p. 2300054, 2023.
[35] M. Grundmann, *Physics of semiconductors*. Springer, 2010.
[36] B. G. Streetman and S. Banerjee, *Solid state electronic devices*. Prentice hall New Jersey, 2000.
[37] S. M. Sze, Y. Li, and K. K. Ng, *Physics of semiconductor devices*. John wiley & sons, 2021.
[38] P. Würfel and U. Würfel, *Physics of solar cells: from basic principles to advanced concepts*. John Wiley & Sons, 2016.
[39] J. A. Nelson, *The physics of solar cells*. World Scientific Publishing Company, 2003.
[40] "ASTM G173-03 Reference Spectra http://rredc.nrel.gov/solar/spectra/am1.5/." NREL. (accessed 2025).
[41] J. H. Werner, J. Mattheis, and U. Rau, "Efficiency limitations of polycrystalline thin film solar cells: case of Cu(In,Ga)Se2," *Thin Solid Films,* vol. 480-481, pp. 399-409, 2005, doi: 10.1016/j.tsf.2004.11.052.
[42] T. P. Weiss *et al.*, "Time-resolved photoluminescence on double graded Cu (In, Ga) Se2–Impact of front surface recombination and its temperature dependence," *Science and technology of advanced materials,* vol. 20, no. 1, pp. 313-323, 2019.
[43] W. Van Roosbroeck and W. Shockley, "Photon-radiative recombination of electrons and holes in germanium," *Physical Review,* vol. 94, no. 6, p. 1558, 1954.
[44] T. P. Weiss, B. Bissig, T. Feurer, R. Carron, S. Buecheler, and A. N. Tiwari, "Bulk and surface recombination properties in thin film semiconductors with different surface treatments from time-resolved photoluminescence measurements," *Scientific reports,* vol. 9, no. 1, p. 5385, 2019.
[45] D. Sharma, N. Nicoara, P. Jackson, W. Witte, D. Hariskos, and S. Sadewasser, "Charge-carrier-concentration inhomogeneities in alkali-treated Cu (In, Ga) Se2 revealed by conductive atomic force microscopy tomography," *Nature Energy,* pp. 1-9, 2024.
[46] M. Krause *et al.*, "Microscopic origins of performance losses in highly efficient Cu (In, Ga) Se2 thin-film solar cells," *Nature communications,* vol. 11, no. 1, p. 4189, 2020.
[47] S. Puttnins *et al.*, "Effect of sodium on material and device quality in low temperature deposited Cu (In, Ga) Se2," *Solar energy materials and solar cells,* vol. 119, pp. 281-286, 2013.
[48] W. Shockley and W. Read Jr, "Statistics of the recombinations of holes and electrons," *Physical review,* vol. 87, no. 5, p. 835, 1952.
[49] R. N. Hall, "Electron-hole recombination in germanium," *Physical review,* vol. 87, no. 2, p. 387, 1952.

[50] M. Govoni, I. Marri, and S. Ossicini, "Auger recombination in Si and GaAs semiconductors: Ab initio results," *Physical Review B—Condensed Matter and Materials Physics,* vol. 84, no. 7, p. 075215, 2011.
[51] D. Matsakis, A. Coster, B. Laster, and R. Sime, "A renaming proposal:“The Auger–Meitner effect”," *Physics Today,* vol. 72, no. 9, pp. 10-11, 2019.
[52] T. Tiedje, E. Yablonovitch, G. D. Cody, and B. G. Brooks, "Limiting efficiency of silicon solar cells," *IEEE Transactions on electron devices,* vol. 31, no. 5, pp. 711-716, 1984.
[53] M. Sood *et al.*, "Passivating Surface Defects and Reducing Interface Recombination in CuInS2 Solar Cells by a Facile Solution Treatment," *Solar RRL,* vol. 5, no. 4, 2021, doi: 10.1002/solr.202100078.
[54] M. Sood *et al.*, "Near surface defects: Cause of deficit between internal and external open-circuit voltage in solar cells," *Progress in Photovoltaics: Research and Applications,* vol. 30, no. 3, pp. 263-275, 2022.
[55] F. Babbe, L. Choubrac, and S. Siebentritt, "The optical diode ideality factor enables fast screening of semiconductors for solar cells," *Solar RRL,* vol. 2, no. 12, p. 1800248, 2018.
[56] J. I. Pankove, *Optical processes in semiconductors*. Courier Corporation, 1975.
[57] O. RAMIREZ SANCHEZ, "OPTOELECTRONIC PROPERTIES OF CU (IN, GA) SE2 SINGLE CRYSTALS WITH ALKALI POSTDEPOSITION TREATMENTS," 2022.
[58] F. Urbach, "The long-wavelength edge of photographic sensitivity and of the electronic absorption of solids," *Physical review,* vol. 92, no. 5, p. 1324, 1953.
[59] S. Johnson and T. Tiedje, "Temperature dependence of the Urbach edge in GaAs," *Journal of applied physics,* vol. 78, no. 9, pp. 5609-5613, 1995.
[60] S. Wasim *et al.*, "Effect of structural disorder on the Urbach energy in Cu ternaries," *Physical Review B,* vol. 64, no. 19, p. 195101, 2001.
[61] M. Ledinsky *et al.*, "Temperature Dependence of the Urbach Energy in Lead Iodide Perovskites," *J Phys Chem Lett,* vol. 10, no. 6, pp. 1368-1373, Mar 21 2019, doi: 10.1021/acs.jpclett.9b00138.
[62] C. K. G. Kwok, N. Masuko, S. Ishizuka, R. Scheer, M. M. Islam, and T. Sakurai, "Recombination Effects of Urbach Tails as Trap States in Cu (In, Ga) Se2 Solar Cells Probed by Temperature-Dependent Junction-Transient Spectroscopies," *Solar RRL,* p. 202400925, 2025.
[63] G. Cody, T. Tiedje, B. Abeles, B. Brooks, and Y. Goldstein, "Disorder and the optical-absorption edge of hydrogenated amorphous silicon," *Physical Review Letters,* vol. 47, no. 20, p. 1480, 1981.
[64] M. Beaudoin, A. DeVries, S. R. Johnson, H. Laman, and T. Tiedje, "Optical absorption edge of semi-insulating GaAs and InP at high temperatures," *Applied Physics Letters,* vol. 70, no. 26, pp. 3540-3542, 1997.
[65] S. Siebentritt *et al.*, "Heavy Alkali Treatment of Cu(In,Ga)Se2 Solar Cells: Surface versus Bulk Effects," *Advanced Energy Materials,* vol. 10, no. 8, 2020, doi: 10.1002/aenm.201903752.
[66] J. K. Larsen, K. Burger, L. Gütay, and S. Siebentritt, "Temperature dependence of potential fluctuations in chalcopyrites," in *2011 37th IEEE Photovoltaic Specialists Conference*, 2011: IEEE, pp. 000396-000401.

[67] G. Rey *et al.*, "On the origin of band-tails in kesterite," *Solar Energy Materials and Solar Cells,* vol. 179, pp. 142-151, 2018.
[68] P. Wurfel, "The chemical potential of radiation," *Journal of Physics C: Solid State Physics,* vol. 15, no. 18, p. 3967, 1982.
[69] U. Rau, "Reciprocity relation between photovoltaic quantum efficiency and electroluminescent emission of solar cells," *Physical Review B,* vol. 76, no. 8, p. 085303, 2007.
[70] J. Keller, L. Stolt, O. Donzel-Gargand, A. F. Violas, T. Kubart, and M. Edoff, "Bifacial Wide-Gap (Ag, Cu)(In, Ga) Se2 Solar Cell with 13.6% Efficiency Using In2O3: W as a Back Contact Material," *Solar RRL,* vol. 8, no. 15, p. 2400430, 2024.
[71] M. Krause, S. Moser, C. Mitmit, S. Nishiwaki, A. N. Tiwari, and R. Carron, "Precise Alkali Supply during and after Growth for High-Performance Low Bandgap (Ag, Cu) InSe2 Solar Cells," *Solar RRL,* vol. 8, no. 10, p. 2400077, 2024.
[72] D. Adeleye, A. Lomuscio, M. Sood, and S. Siebentritt, "Lifetime, quasi-Fermi level splitting and doping concentration of Cu-rich CuInS2 absorbers," *Materials Research Express,* vol. 8, no. 2, p. 025905, 2021.
[73] S. Shukla *et al.*, "Over 15% efficient wide-band-gap Cu (In, Ga) S2 solar cell: Suppressing bulk and interface recombination through composition engineering," *Joule,* vol. 5, no. 7, pp. 1816-1831, 2021.
[74] N. Barreau *et al.*, "Investigation of co-evaporated polycrystalline Cu (In, Ga) S2 thin film yielding 16.0% efficiency solar cell," *EPJ Photovoltaics,* vol. 13, p. 17, 2022.
[75] T. P. Weiss, M. Sood, A. Vanderhaegen, and S. Siebentritt, "CuIn (Se, Te) 2 absorbers with bandgaps< 1 eV for bottom cells in tandem applications," *Progress in Photovoltaics: Research and Applications,* vol. 33, no. 2, pp. 253-264, 2025.
[76] J. Jaffe and A. Zunger, "Electronic structure of the ternary chalcopyrite semiconductors CuAl s 2, CuGa s 2, CuIn S 2, CuAl se 2, CuGa se 2, and CuIn Se 2," *Physical Review B,* vol. 28, no. 10, p. 5822, 1983.
[77] M. H. Wolter, "WOLTER, M. (2019). Optical investigation of voltage losses in high-efficiency Cu(In,Ga)Se2 thin-film solar cells [Doctoral thesis, Unilu - University of Luxembourg]. ORBilu-University of Luxembourg. https://orbilu.uni.lu/handle/10993/39611," 2019.
[78] S. H. Wei and A. Zunger, "Band offsets and optical bowings of chalcopyrites and Zn-based II-VI alloys," *Journal of Applied Physics,* vol. 78, no. 6, pp. 3846-3856, 1995.
[79] A. Klein, "Energy band alignment in chalcogenide thin film solar cells from photoelectron spectroscopy," *Journal of physics: Condensed matter,* vol. 27, no. 13, p. 134201, 2015.
[80] S. Chen, X. Gong, and S.-H. Wei, "Band-structure anomalies of the chalcopyrite semiconductors CuGa X 2 versus AgGa X 2 (X= S and Se) and their alloys," *Physical Review B—Condensed Matter and Materials Physics,* vol. 75, no. 20, p. 205209, 2007.
[81] J. Boyle, B. McCandless, W. Shafarman, and R. Birkmire, "Structural and optical properties of (Ag, Cu)(In, Ga) Se2 polycrystalline thin film alloys," *Journal of Applied Physics,* vol. 115, no. 22, 2014.
[82] Z. J. L. Kao, T. Kobayashi, and T. Nakada, "Modeling of the surface sulfurization of CIGSe-based solar cells," *Solar energy,* vol. 110, pp. 50-55, 2014.
[83] D. Lee *et al.*, "Direct evidence of void passivation in Cu (InGa)(SSe) 2 absorber layers," *Applied Physics Letters,* vol. 106, no. 8, 2015.

[84] S. Ishizuka *et al.*, "Physical and chemical aspects at the interface and in the bulk of CuInSe 2-based thin-film photovoltaics," *Physical Chemistry Chemical Physics,* vol. 24, no. 3, pp. 1262-1285, 2022.
[85] G. Hu, X. Cai, and Y. Rong, *Materials Science* (Volume 1 Structure). Berlin, Boston: De Gruyter, 2021.
[86] J. Dietrich *et al.*, "Origins of electrostatic potential wells at dislocations in polycrystalline Cu (In, Ga) Se2 thin films," *Journal of Applied Physics,* vol. 115, no. 10, 2014.
[87] J. Dietrich, D. Abou-Ras, T. Rissom, T. Unold, H.-W. Schock, and C. Boit, "Compositional Gradients in Cu (In, Ga) Se $ _ {\bf 2} $ Thin Films for Solar Cells and Their Effects on Structural Defects," *IEEE Journal of Photovoltaics,* vol. 2, no. 3, pp. 364-370, 2012.
[88] A. J. M. Prot *et al.*, "Improved sequentially processed Cu (In, Ga)(S, Se) 2 by Ag alloying," *Solar RRL,* 2024.
[89] A. J. Prot *et al.*, "Composition variations in Cu (In, Ga)(S, Se) 2 solar cells: Not a gradient, but an interlaced network of two phases," *APL Materials,* vol. 11, no. 10, p. 101120, 2023.
[90] Y. Yan, C.-S. Jiang, R. Noufi, S.-H. Wei, H. Moutinho, and M. Al-Jassim, "Electrically benign behavior of grain boundaries in polycrystalline CuInSe 2 films," *Physical review letters,* vol. 99, no. 23, p. 235504, 2007.
[91] U. Rau, K. Taretto, and S. Siebentritt, "Grain boundaries in Cu (In, Ga)(Se, S) 2 thin-film solar cells," *Applied Physics A,* vol. 96, pp. 221-234, 2009.
[92] J. Y. Seto, "The electrical properties of polycrystalline silicon films," *Journal of Applied Physics,* vol. 46, no. 12, pp. 5247-5254, 1975.
[93] D. Abou-Ras *et al.*, "No Evidence for Passivation Effects of Na and K at Grain Boundaries in Polycrystalline Cu(In,Ga)Se2 Thin Films for Solar Cells," *Solar RRL,* vol. 3, no. 8, 2019, doi: 10.1002/solr.201900095.
[94] S. Siebentritt, M. Igalson, C. Persson, and S. Lany, "The electronic structure of chalcopyrites—bands, point defects and grain boundaries," *Progress in Photovoltaics: Research and Applications,* vol. 18, no. 6, pp. 390-410, 2010.
[95] C. Spindler *et al.*, "Electronic defects in Cu (In, Ga) S e 2: Towards a comprehensive model," *Physical Review Materials,* vol. 3, no. 9, p. 090302, 2019.
[96] S. Siebentritt, L. Gütay, D. Regesch, Y. Aida, and V. Deprédurand, "Why do we make Cu(In,Ga)Se2 solar cells non-stoichiometric?," *Solar Energy Materials and Solar Cells,* vol. 119, pp. 18-25, 2013, doi: 10.1016/j.solmat.2013.04.014.
[97] H. Elanzeery *et al.*, "Challenge in Cu-rich CuInSe 2 thin film solar cells: Defect caused by etching," *Physical review materials,* vol. 3, no. 5, p. 055403, 2019.
[98] S. Siebentritt, N. Papathanasiou, and M. C. Lux-Steiner, "Potential fluctuations in compensated chalcopyrites," *Physica B: Condensed Matter,* vol. 376-377, pp. 831-833, 2006, doi: 10.1016/j.physb.2005.12.208.
[99] S. Schuler *et al.*, "Self-compensation of intrinsic defects in the ternary semiconductor CuGaSe 2," *Physical Review B,* vol. 69, no. 4, p. 045210, 2004.
[100] T. WANG, "Comprehending and Mitigating Backside Recombination in Cu (In, Ga) Se2 Solar Cells," 2023.
[101] A. Chirilă *et al.*, "Highly efficient Cu (In, Ga) Se2 solar cells grown on flexible polymer films," *Nature materials,* vol. 10, no. 11, pp. 857-861, 2011.

[102] P. Jackson *et al.*, "New world record efficiency for Cu (In, Ga) Se2 thin-film solar cells beyond 20%," *Progress in photovoltaics: research and applications,* vol. 19, no. 7, pp. 894-897, 2011.
[103] B. S. Yadav, S. R. Dey, and S. R. Dhage, "Effective ink-jet printing of aqueous ink for Cu (In, Ga) Se2 thin film absorber for solar cell application," *Solar Energy,* vol. 179, pp. 363-370, 2019.
[104] S. M. McLeod, C. J. Hages, N. J. Carter, and R. Agrawal, "Synthesis and characterization of 15% efficient CIGSSe solar cells from nanoparticle inks," *Progress in Photovoltaics: Research and Applications,* vol. 23, no. 11, pp. 1550-1556, 2015.
[105] V. B. Chu *et al.*, "Waste-and Cd-free inkjet-printed Zn (O, S) buffer for Cu (In, Ga)(S, Se) 2 thin-film solar cells," *ACS Applied Materials & Interfaces,* vol. 13, no. 11, pp. 13009-13021, 2021.
[106] T. Wang *et al.*, "Diode factor in solar cells with metastable defects and Back contact recombination," *Advanced Energy Materials,* vol. 12, no. 44, p. 2202076, 2022.
[107] S. Thomas *et al.*, "Role of Ag Addition on the Microscopic Material Properties of (Ag, Cu)(In, Ga) Se2 Absorbers and Their Effects on Losses in the Open-Circuit Voltage of Corresponding Devices," *Progress in Photovoltaics: Research and Applications,* vol. 32, no. 12, pp. 930-940, 2024.
[108] T. Wang *et al.*, "Shifting the paradigm: a functional hole selective transport layer for chalcopyrite solar cells," *Solar RRL,* vol. 8, no. 12, p. 2400212, doi: 10.1002/solr.202400212.
[109] T. Wang *et al.*, "Sub-micron Cu (In, Ga) Se2 solar cell with efficiency of 18.2% enabled by a hole transport layer," *arXiv preprint arXiv:2505.03253,* 2025.
[110] J. Keller, S. Mudgal, C. Hägglund, K. Kiselman, and M. Edoff, "Ultrathin AlOx Films for Back Contact Passivation in Bifacial Wide-Gap (Ag, Cu)(In, Ga) Se2 Solar Cells," *Solar RRL,* p. 202500101, 2025.
[111] M. H. Wolter *et al.*, "Influence of sodium and rubidium postdeposition treatment on the quasi-fermi level splitting of Cu (In, Ga) Se 2 thin films," *IEEE Journal of Photovoltaics,* vol. 8, no. 5, pp. 1320-1325, 2018.
[112] D. Rudmann *et al.*, "Sodium incorporation strategies for CIGS growth at different temperatures," *Thin Solid Films,* vol. 480, pp. 55-60, 2005.
[113] F. Pianezzi *et al.*, "Unveiling the effects of post-deposition treatment with different alkaline elements on the electronic properties of CIGS thin film solar cells," *Phys Chem Chem Phys,* vol. 16, no. 19, pp. 8843-51, May 21 2014, doi: 10.1039/c4cp00614c.
[114] A. Rockett, "The effect of Na in polycrystalline and epitaxial single-crystal CuIn1− xGaxSe2," *Thin Solid Films,* vol. 480, pp. 2-7, 2005.
[115] D. Colombara, B. J. Stanbery, and G. Sozzi, "Revani diffusion model in Cu (In, Ga) Se 2," *Journal of Materials Chemistry A,* vol. 11, no. 48, pp. 26426-26434, 2023.
[116] Z. K. Yuan *et al.*, "Na-diffusion enhanced p-type conductivity in Cu (In, Ga) Se2: A new mechanism for efficient doping in semiconductors," *Advanced Energy Materials,* vol. 6, no. 24, p. 1601191, 2016.
[117] T. Kodalle, "Unraveling the structural and optoelectronic effects of Rb on chalcopyrite solar cells," Dissertation, Halle (Saale), Martin-Luther-Universität Halle-Wittenberg, 2020, 2020.

[118] S. Cheng *et al.*, "Effects of different Cs distribution in the film on the performance of CIGS thin film solar cells," *Solar Energy Materials and Solar Cells,* vol. 222, p. 110917, 2021.
[119] T. Kodalle, T. Bertram, R. Schlatmann, and C. A. Kaufmann, "Effectiveness of an RbF post deposition treatment of CIGS solar cells in dependence on the Cu content of the absorber layer," *IEEE Journal of Photovoltaics,* vol. 9, no. 6, pp. 1839-1845, 2019.
[120] E. Jarzembowski, F. Syrowatka, K. Kaufmann, W. Fränzel, T. Hölscher, and R. Scheer, "The influence of sodium on the molybdenum/Cu (In, Ga) Se2 interface recombination velocity, determined by time resolved photoluminescence," *Applied Physics Letters,* vol. 107, no. 5, 2015.
[121] J. Chantana *et al.*, "Effect of alkali treatment on photovoltaic performances of Cu (In, Ga)(S, Se) 2 solar cells and their absorber quality analyzed by urbach energy and carrier recombination rates," *ACS Applied Energy Materials,* vol. 3, no. 2, pp. 1292-1297, 2020.
[122] M. S. Mina, E. Enkhbayar, N. Otgontamir, S. Kim, and J. Kim, "Efficiency Improvement of Narrow Band Gap Cu (In, Ga)(S, Se) 2 Solar Cell with Alkali Treatment via Aqueous Spray Pyrolysis Deposition," *ACS Applied Materials & Interfaces,* vol. 15, no. 19, pp. 23199-23207, 2023.
[123] O. Cojocaru-Mirédin, M. Raghuwanshi, R. Wuerz, and S. Sadewasser, "Grain boundaries in Cu (In, Ga) Se2: a review of composition–electronic property relationships by atom probe tomography and correlative microscopy," *Advanced Functional Materials,* vol. 31, no. 41, p. 2103119, 2021.
[124] F. Couzinie-Devy, E. Cadel, N. Barreau, L. Arzel, and P. Pareige, "Atom probe study of Cu-poor to Cu-rich transition during Cu (In, Ga) Se2 growth," *Applied Physics Letters,* vol. 99, no. 23, 2011.
[125] A. Karami, M. Morawski, H. Kempa, R. Scheer, and O. Cojocaru-Mirédin, "Sodium in Cu (In, Ga) Se2 Solar Cells: To Be or Not to Be Beneficial," *Solar RRL,* vol. 8, no. 3, p. 2300544, 2024.
[126] P. Schöppe *et al.*, "Rubidium segregation at random grain boundaries in Cu (In, Ga) Se2 absorbers," *Nano Energy,* vol. 42, pp. 307-313, 2017.
[127] N. Nicoara *et al.*, "Direct evidence for grain boundary passivation in Cu (In, Ga) Se2 solar cells through alkali-fluoride post-deposition treatments," *Nature communications,* vol. 10, no. 1, p. 3980, 2019.
[128] N. Taguchi, S. Tanaka, and S. Ishizuka, "Direct insights into RbInSe2 formation at Cu (In, Ga) Se2 thin film surface with RbF postdeposition treatment," *Applied Physics Letters,* vol. 113, no. 11, 2018.
[129] C. K. Boumenou *et al.*, "Nanoscale Surface Analysis Reveals Origins of Enhanced Interface Passivation in RbF Post Deposition Treated CIGSe Solar Cells," *Advanced Functional Materials,* p. 2300590, 2023.
[130] A. Elizabeth *et al.*, "Surface Passivation and Detrimental Heat-Induced Diffusion Effects in RbF-Treated Cu (In, Ga) Se2 Solar Cell Absorbers," *ACS Applied Materials & Interfaces,* vol. 14, no. 29, pp. 34101-34112, 2022.
[131] S. De Wolf *et al.*, "Organometallic halide perovskites: sharp optical absorption edge and its relation to photovoltaic performance," *The journal of physical chemistry letters,* vol. 5, no. 6, pp. 1035-1039, 2014.

[132] S. Gharabeiki *et al.*, "Grain boundaries are not the source of Urbach tails in Cu (In, Ga) Se2 absorbers," *Journal of Physics: Energy,* vol. 6, no. 3, p. 035008, 2024.
[133] E. M. Lanzoni *et al.*, "The impact of Kelvin probe force microscopy operation modes and environment on grain boundary band bending in perovskite and Cu(In,Ga)Se2 solar cells," *Nano Energy,* vol. 88, 2021, doi: 10.1016/j.nanoen.2021.106270.
[134] E. Martin Lanzoni, "Grain boundaries and potassium post-deposition treatments in chalcopyrite solar cells," University of Luxembourg, Luxembourg, Luxembourg, 2022.
[135] M. Bär, S. Nishiwaki, L. Weinhardt, S. Pookpanratana, W. Shafarman, and C. Heske, "Electronic level alignment at the deeply buried absorber/Mo interface in chalcopyrite-based thin film solar cells," *Applied Physics Letters,* vol. 93, no. 4, 2008.
[136] D. Abou-Ras *et al.*, "Formation and characterisation of MoSe2 for Cu (In, Ga) Se2 based solar cells," *Thin Solid Films,* vol. 480, pp. 433-438, 2005.
[137] N. Barreau, J. Lähnemann, F. Couzinié-Devy, L. Assmann, P. Bertoncini, and J. Kessler, "Impact of Cu-rich growth on the CuIn1− xGaxSe2 surface morphology and related solar cells behaviour," *Solar Energy Materials and Solar Cells,* vol. 93, no. 11, pp. 2013-2019, 2009.
[138] W. Witte *et al.*, "Gallium gradients in Cu (In, Ga) Se2 thin-film solar cells," *Progress in Photovoltaics: Research and Applications,* vol. 23, no. 6, pp. 717-733, 2015.
[139] J. Kessler, J. Scholdstrom, and L. Stolt, "Rapid Cu (In, Ga) Se/sub 2/growth using" end point detection"," in *Conference Record of the Twenty-Eighth IEEE Photovoltaic Specialists Conference-2000 (Cat. No. 00CH37036)*, 2000: IEEE, pp. 509-512.
[140] T. Lepetit, L. Arzel, and N. Barreau, "Impact of maximum copper content during the 3-stage process on CdS thickness tolerance in Cu (In, Ga) Se2-based solar cell," *MRS Online Proceedings Library (OPL),* vol. 1538, pp. 33-38, 2013.
[141] R. Hunger *et al.*, "In situ deposition rate monitoring during the three-stage-growth process of Cu (In, Ga) Se2 absorber films," *Thin Solid Films,* vol. 431, pp. 16-21, 2003.
[142] K. Sakurai *et al.*, "In situ diagnostic methods for thin-film fabrication: utilization of heat radiation and light scattering," *Progress in Photovoltaics: Research and Applications,* vol. 12, no. 2-3, pp. 219-234, 2004.
[143] J. Kessler, C. Chityuttakan, J. Lu, J. Schöldström, and L. Stolt, "Cu (In, Ga) Se2 thin films grown with a Cu-poor/rich/poor sequence: growth model and structural considerations," *Progress in Photovoltaics: Research and Applications,* vol. 11, no. 5, pp. 319-331, 2003.
[144] R. Caballero *et al.*, "Cu deficiency in multi-stage co-evaporated Cu (In, Ga) Se2 for solar cells applications: Microstructure and Ga in-depth alloying," *Acta Materialia,* vol. 58, no. 9, pp. 3468-3476, 2010.
[145] R. Scheer, A. Neisser, K. Sakurai, P. Fons, and S. Niki, "Cu (In 1− x Ga x) Se 2 growth studies by in situ spectroscopic light scattering," *Applied physics letters,* vol. 82, no. 13, pp. 2091-2093, 2003.
[146] C. Kaufmann, A. Neisser, R. Klenk, and R. Scheer, "Transfer of Cu (In, Ga) Se2 thin film solar cells to flexible substrates using an in situ process control," *Thin Solid Films,* vol. 480, pp. 515-519, 2005.
[147] D. Abou-Ras, T. Kirchartz, and U. Rau, *Advanced characterization techniques for thin film solar cells*. Wiley Online Library, 2011.
[148] Perkinelmer. "https://resources.perkinelmer.com/lab-solutions/resources/docs/bro_lambda950850650americas.pdf." (accessed 2025).

[149] S. Gharabeiki *et al.*, "The effect of a band gap gradient on the radiative losses in the open circuit voltage of solar cells," *arXiv preprint arXiv:2503.14077,* 2025.
[150] M. SOOD, "Interface Open-Circuit Voltage Deficit In Cu (In, Ga) S2 Solar Cell: Characterization, Simulation and Mitigation," 2021.
[151] J. Lehmann *et al.*, "Reliable wet-chemical cleaning of natively oxidized high-efficiency Cu (In, Ga) Se2 thin-film solar cell absorbers," *Journal of Applied Physics,* vol. 116, no. 23, 2014.
[152] R. Baier *et al.*, "Electronic properties of grain boundaries in Cu (In, Ga) Se2 thin films with various Ga-contents," *Solar energy materials and solar cells,* vol. 103, pp. 86-92, 2012.
[153] R. Baier, C. Leendertz, D. Abou-Ras, M. C. Lux-Steiner, and S. Sadewasser, "Properties of electronic potential barriers at grain boundaries in Cu (In, Ga) Se2 thin films," *Solar energy materials and solar cells,* vol. 130, pp. 124-131, 2014.
[154] F. Babbe *et al.*, "Vacuum-Healing of Grain Boundaries in Sodium-Doped CuInSe2 Solar Cell Absorbers," *Advanced Energy Materials,* vol. 13, no. 17, p. 2204183, 2023.
[155] E. P. Francisco de la Peña, Vidar Tonaas Fauske, Jonas Lähnemann, Pierre Burdet, Petras Jokubauskas, Tom Furnival, Carter Francis, Magnus Nord, Tomas Ostasevicius, Katherine E. MacArthur, Duncan N. Johnstone, Mike Sarahan, Joshua Taillon, Thomas Aarholt, pquinn-dls, Vadim Migunov, Alberto Eljarrat, Jan Caron, … "hyperspy/hyperspy: v2.1.1 (v2.1.1)." *Zenodo,* 2024, doi: https://doi.org/10.5281/zenodo.12724131.
[156] J. Lähnemann *et al.*, "LumiSpy/lumispy: v0. 2.2," *Zenodo,* 2023, doi: 10.5281/zenodo.7747350.
[157] R. A. Carrasco *et al.*, "Photoluminescence and minority carrier lifetime of quinary GaInAsSbBi grown on GaSb by molecular beam epitaxy," *Applied Physics Letters,* vol. 120, no. 3, 2022.
[158] T. Kirchartz, J. A. Márquez, M. Stolterfoht, and T. Unold, "Photoluminescence-Based Characterization of Halide Perovskites for Photovoltaics," *Advanced Energy Materials,* vol. 10, no. 26, 2020, doi: 10.1002/aenm.201904134.
[159] A. Redinger, S. Levcenko, C. J. Hages, D. Greiner, C. A. Kaufmann, and T. Unold, "Time resolved photoluminescence on Cu (In, Ga) Se2 absorbers: Distinguishing degradation and trap states," *Applied Physics Letters,* vol. 110, no. 12, 2017.
[160] M. Maiberg, T. Hölscher, S. Zahedi-Azad, W. Fränzel, and R. Scheer, "Investigation of long lifetimes in Cu (In, Ga) Se2 by time-resolved photoluminescence," *Applied Physics Letters,* vol. 107, no. 12, 2015.
[161] A. J.-C. M. PROT, "Photoluminescence assessment of graded chacopyrite absorbers," 2024.
[162] M. Buffière *et al.*, "Surface Cleaning and Passivation Using (NH4)2S Treatment for Cu(In,Ga)Se2 Solar Cells: A Safe Alternative to KCN," *Advanced Energy Materials,* vol. 5, no. 6, 2014, doi: 10.1002/aenm.201401689.
[163] M. Maiberg, C. Spindler, E. Jarzembowski, and R. Scheer, "Electrical characterization of Cu (In, Ga) Se2-solar cells by voltage dependent time-resolved photoluminescence," *Thin Solid Films,* vol. 582, pp. 379-382, 2015.
[164] T. Kirchartz, A. Helbig, W. Reetz, M. Reuter, J. H. Werner, and U. Rau, "Reciprocity between electroluminescence and quantum efficiency used for the characterization of

silicon solar cells," *Progress in Photovoltaics: Research and Applications,* vol. 17, no. 6, pp. 394-402, 2009.
[165] E. O. Lawrence, "Transition probabilities: their relation to thermionic emission and the photo-electric effect," *Physical Review,* vol. 27, no. 5, p. 555, 1926.
[166] U. Rau and J. Werner, "Radiative efficiency limits of solar cells with lateral band-gap fluctuations," *Applied physics letters,* vol. 84, no. 19, pp. 3735-3737, 2004.
[167] U. R. J. Mattheis, and J. Werner, "Light absorption and emission on semiconductors with band gap fluctuations - a study on Cu(In,Ga)Se2 thin films," *J. Appl. Phys,* vol. 101, no. 11, p. 113519, 2007, doi: doi.org/10.1063/1.2721768.
[168] S. Thomas *et al.*, "Effects of material properties of band-gap-graded Cu (In, Ga) Se2 thin films on the onset of the quantum efficiency spectra of corresponding solar cells," *Progress in Photovoltaics: Research and Applications,* vol. 30, no. 10, pp. 1238-1246, 2022.
[169] E. Daub and P. Wurfel, "Ultralow values of the absorption coefficient of Si obtained from luminescence," *Phys Rev Lett,* vol. 74, no. 6, pp. 1020-1023, Feb 6 1995, doi: 10.1103/PhysRevLett.74.1020.
[170] M. A. Green and A. W. Ho-Baillie, "Pushing to the limit: radiative efficiencies of recent mainstream and emerging solar cells," *ACS Energy Letters,* vol. 4, no. 7, pp. 1639-1644, 2019.
[171] H. Fujiwara, "Effect of roughness on ellipsometry analysis," *Spectroscopic Ellipsometry for Photovoltaics: Volume 1: Fundamental Principles and Solar Cell Characterization,* pp. 155-172, 2018.
[172] T. Kirchartz and U. Rau, "Detailed balance and reciprocity in solar cells," *physica status solidi (a),* vol. 205, no. 12, pp. 2737-2751, 2008.
[173] D. Abou-Ras, "Microscopic origins of radiative performance losses in thin-film solar cells at the example of (Ag, Cu)(In, Ga) Se2 devices," *Journal of Vacuum Science & Technology A,* vol. 42, no. 2, p. 022803, 2024.
[174] Alex Redinger, José A. Márquez , and Thomas Unold. Quantitative Imaging of Non-radiative Losses in Thin Film Solar Cells.
[175] G. Rey *et al.*, "Absorption coefficient of a semiconductor thin film from photoluminescence," *Physical Review Applied,* vol. 9, no. 6, p. 064008, 2018.
[176] R. Carron *et al.*, "Refractive indices of layers and optical simulations of Cu (In, Ga) Se2 solar cells," *Science and Technology of advanced MaTerialS,* vol. 19, no. 1, pp. 396-410, 2018.
[177] X. Zheng *et al.*, "Recombination and bandgap engineering in CdSeTe/CdTe solar cells," *Apl Materials,* vol. 7, no. 7, p. 071112, 2019.
[178] M. A. Scarpulla *et al.*, "CdTe-based thin film photovoltaics: Recent advances, current challenges and future prospects," *Solar Energy Materials and Solar Cells,* vol. 255, p. 112289, 2023.
[179] Y. Zhao *et al.*, "Controllable double gradient bandgap strategy enables high efficiency solution-processed kesterite solar cells," *Advanced Functional Materials,* vol. 34, no. 8, p. 2311992, 2024.
[180] T. P. Weiss, F. Ehre, V. Serrano-Escalante, T. Wang, and S. Siebentritt, "Understanding performance limitations of Cu (In, Ga) Se2 solar cells due to metastable defects—a route toward higher efficiencies," *Solar RRL,* vol. 5, no. 7, p. 2100063, 2021.

[181] T. P. Weiss *et al.*, "Metastable defects decrease the fill factor of solar cells," *Physical Review Applied,* vol. 19, no. 2, p. 024052, 2023.
[182] F. Babbe, L. Choubrac, and S. Siebentritt, "Quasi Fermi level splitting of Cu-rich and Cu-poor Cu (In, Ga) Se2 absorber layers," *Applied Physics Letters,* vol. 109, no. 8, 2016.
[183] L. Gütay and G. Bauer, "Local fluctuations of absorber properties of Cu (In, Ga) Se2 by sub-micron resolved PL towards “real life” conditions," *Thin Solid Films,* vol. 517, no. 7, pp. 2222-2225, 2009.
[184] S. Siebentritt *et al.*, "Photoluminescence assessment of materials for solar cell absorbers," *Faraday Discuss,* vol. 239, no. 0, pp. 112-129, Oct 28 2022, doi: 10.1039/d2fd00057a.
[185] S. Siah, B. Hoex, and A. Aberle, "Accurate characterization of thin films on rough surfaces by spectroscopic ellipsometry," *Thin Solid Films,* vol. 545, pp. 451-457, 2013.
[186] G. Yin, P. Manley, and M. Schmid, "Light trapping in ultrathin CuIn1-xGaxSe2 solar cells by dielectric nanoparticles," *Solar Energy,* vol. 163, pp. 443-452, 2018.
[187] J. Chantana *et al.*, "Transparent electrode and buffer layer combination for reducing carrier recombination and optical loss realizing over a 22%-efficient Cd-free alkaline-treated Cu (In, Ga)(S, Se) 2 solar cell by the all-dry process," *ACS Applied Materials & Interfaces,* vol. 12, no. 19, pp. 22298-22307, 2020.
[188] M. Hála *et al.*, "Highly conductive ZnO films with high near infrared transparency," *Progress in Photovoltaics: Research and Applications,* vol. 23, no. 11, pp. 1630-1641, 2015.
[189] H. Tangara *et al.*, "Study of defect properties and recombination mechanism in rubidium treated Cu (In, Ga) Se2 solar cells," *Journal of Applied Physics,* vol. 129, no. 18, 2021.
[190] T. Nishimura, A. Doi, J. Chantana, A. Mavlonov, Y. Kawano, and T. Minemoto, "Silver-alloyed wide-gap CuGaSe2 solar cells," *Solar Energy,* vol. 230, pp. 509-514, 2021.
[191] M. A. Green, K. Emery, Y. Hishikawa, W. Warta, and E. D. Dunlop, "Solar cell efficiency tables (version 40)," *Progress in Photovoltaics: Research and Applications,* vol. 20, no. 5, pp. 606-614, 2012, doi: https://doi.org/10.1002/pip.2267.
[192] M. A. Green *et al.*, "Solar cell efficiency tables (version 65)," *Progress in Photovoltaics: Research and Applications,* vol. 33, no. 1, pp. 3-15, 2025.
[193] M. A. Green *et al.*, "Solar cell efficiency tables (Version 64)," *Progress in Photovoltaics: Research and Applications,* vol. 32, no. 7, pp. 425-441, 2024.
[194] K. Yin *et al.*, "Gradient bandgap enables> 13% efficiency sulfide Kesterite solar cells with open-circuit voltage over 800 mV," *arXiv preprint arXiv:2404.00291,* 2024.
[195] T. Gokmen, O. Gunawan, T. K. Todorov, and D. B. Mitzi, "Band tailing and efficiency limitation in kesterite solar cells," *Applied Physics Letters,* vol. 103, no. 10, p. 103506, 2013.
[196] M. H. Wolter, B. Bissig, P. Reinhard, S. Buecheler, P. Jackson, and S. Siebentritt, "Correcting for interference effects in the photoluminescence of Cu (In, Ga) Se2 thin films," *physica status solidi c,* vol. 14, no. 6, p. 1600189, 2017.
[197] J. K. Larsen *et al.*, "Interference effects in photoluminescence spectra of Cu2ZnSnS4 and Cu (In, Ga) Se2 thin films," *Journal of Applied Physics,* vol. 118, no. 3, 2015.

[198] R. Djemour, A. Redinger, M. Mousel, L. Gütay, and S. Siebentritt, "Erratum:“Multiple phases of Cu2ZnSnSe4 detected by room temperature photoluminescence”[J. Appl. Phys. 116, 073509 (2014)]," *Journal of Applied Physics,* vol. 118, no. 8, 2015.
[199] O. Ramírez *et al.*, "The Effect of Potassium Fluoride Postdeposition Treatments on the Optoelectronic Properties of Cu(In,Ga)Se2 Single Crystals," *Solar RRL,* vol. 5, no. 4, 2021, doi: 10.1002/solr.202000727.
[200] U. Rau, V. Huhn, and B. E. Pieters, "Luminescence analysis of charge-carrier separation and internal series-resistance losses in Cu (In, Ga) Se 2 solar cells," *Physical review applied,* vol. 14, no. 1, p. 014046, 2020.
[201] B. I. Shklovskii and A. L. Efros, *Electronic properties of doped semiconductors*. Springer Science & Business Media, 2013.